EQUIVALENT LINEAR MODEL BASED TORQUE CONTROL AND PERFORMANCE IMPROVEMENT FOR SWITCHED RELUCTANCE MOTOR (SRM) DRIVES

EQUIVALENT LINEAR MODEL BASED TORQUE CONTROL AND PERFORMANCE IMPROVEMENT FOR SWITCHED RELUCTANCE MOTOR (SRM) DRIVES

BY

GAOLIANG FANG, M.Eng.

A THESIS

SUBMITTED TO THE DEPARTMENT OF ELECTRICAL & COMPUTER ENGINEERING

AND THE SCHOOL OF GRADUATE STUDIES

OF MCMASTER UNIVERSITY

IN PARTIAL FULFILMENT OF THE REQUIREMENTS

FOR THE DEGREE OF

DOCTOR OF PHILOSOPHY

Doctor of Philosophy (2021) McMaster University

(Electrical & Computer Engineering) Hamilton, Ontario, Canada

TITLE:	Equivalent Linear Model Based Torque Control And Performance Improvement for Switched Reluctance Motor (SRM) Drives
AUTHOR:	Gaoliang Fang M.Eng. (Electrical Engineering), Northwestern Polytechnical University, Xi'an, China
SUPERVISOR:	Dr. Ali Emadi
NUMBER OF PAGES:	xxv, 198

Abstract

Switched reluctance machines (SRMs) are gaining increasing interest in industrial applications due to their low manufacturing cost, simple and robust structure, excellent fault-tolerant capability, and reliable operation in high-temperature operating environments. However, the inherent pulsative torque and radial force lead to the well-known torque ripples and acoustic noise issues. Although there are numerous advanced methods to address the above two issues, the high nonlinearity inevitably brings difficulties in controlling the SRMs.

Since the linear SRM voltage and toque equations are simple, it would be beneficial to explore the control algorithm by using such simple linear model. The application of the linear torque model is firstly explored. To utilize such simple model, the connections between the linear toque model and the nonlinear torque model are built through the mapping. The features of these mapping curves are studied in detail. Applying the linear torque equation to generate the reference currents in the optimization-based torque sharing function method shows a significant reduction of the time consumption in solving the bi-optimization problem.

Later, the complete equivalent linear SRM model is constructed by introducing the linear voltage equation and corresponding mapping. Since the linear model is easy to predict the behaviour of SRMs, it is beneficial to apply such model in the model

predictive torque control (MPTC) methods. The application of the equivalent linear model in the finite control set (FCS) MPTC method shows a low computational burden and occupies less storage space. Besides, the improved switching table in the proposed FCS MPTC method also enhances the torque control performance in high-speed operation conditions. To further reduce the torque ripples, the continuous control set (CCS) MPTC method is developed based on the constructed equivalent linear SRM model. The impossibility in analytically solving the optimization problem in the CCS MPTC method if using the original nonlinear SRM model is innovatively addressed by using the equivalent linear SRM model and properly modifying the cost function. Extensive simulation and experimental results prove the low-ripple feature of the proposed CCS MPTC method in a wide speed range.

The high nonlinearity also makes the current control of SRM drives difficult. An intersection-method-based current controller is presented to ensure good current tracking performance for SRMs. The employed adaptive flux-linkage observer makes this current controller show robust performance when there is a deviation on the employed flux-linkage characteristics.

Finally, the key but unmeasurable radial force information for the advanced acoustic reduction method is reconstructed based on the measured flux-linkage curves and some core relationship. This core relationship, which is between the square root of the radial force and the flux-linkage, is explored in detail. Simulation results reveal that the proposed method shows good radial force estimation accuracy when there is even 50% airgap length variation.

To my wife, Siqi Fu

To my parents and my parents-in-law

Acknowledgements

First of all, I would like to sincerely thank my supervisor Dr. Ali Emadi for giving me the valuable opportunity to be part of his world-leading research team in transportation electrification. Dr. Emadi is an outstanding expert in academics and an amazing leader in the industrial field. Without his continuous support, continuous guidance, and continuous encouragement in the past three years, I will not be able to finish this thesis.

I also would like to thank Dr. Jin Ye for her support and guidance on my publications and this thesis. Her insightful advice and comments have made a significantly positive impact on my research.

I also would like to thank my committee members, Dr. Babak Nahid-Mobarakeh and Dr. Bilgin Berker for their valuable and constructive suggestions in my supervisory committee meetings.

I also would like to thank all my colleagues at McMaster Automotive Resource Centre (MARC) for their accompaniment and concerns. Especially I would like to thank Dr. Zekun Xia and Dr. Dianxun Xiao for their support and suggestions for my research.

Finally, I would like to express my deepest gratitude to my parents, my wife, and my parents-in-law for their endless support. Especially, thank my wife, Siqi Fu, for

her accompaniment, support, and comfort during my Ph.D. period. Her company brings the happiness to my life, especially during the hard time of the pandemics.

Contents

Abstract **iii**

Acknowledgements **vi**

1 Introduction **1**

1.1 Motivation 1

1.2 Contributions 3

1.3 Outline of the Thesis 4

2 Switched Reluctance Motor (SRM) Drives and Advanced Torque Control Methods **7**

2.1 SRM Drive System 7

2.1.1 SRM model 7

2.1.2 Asymmetrical Half-Bridge inverter 10

2.2 Advanced Torque Control Methods 12

2.2.1 Indirect Method 13

2.2.2 Direct Method 22

2.2.3 Comparison of the torque control methods 27

3 Time-Efficient Torque Sharing Method for SRMs Based on Equivalent Linear Torque Model **30**

3.1 Introduction 30

3.2 Torque Mapping for SRMs 31

3.2.1 Torque Features and Torque Mapping Concept for SRMs . . . 31

3.2.2 Torque Mapping Properties for SRM 34

3.3 Proposed Time-Efficient TSF Method 39

3.3.1 TSF based on the equivalent linear torque model 40

3.3.2 Time-Efficient Parameter Selection 44

3.4 Simulation Verification 48

3.5 Experimental Verification 54

3.6 Conclusion 58

4 Computational-Efficient Model Predictive Torque Control for SRMs Based on Equivalent Linear SRM Model **59**

4.1 Introduction 59

4.2 LUT-Based MPTC with Improved Switching Table 61

4.2.1 Conventional LUT-Based MPTC 61

4.2.2 Improved LUT-Based MPTC 64

4.3 Proposed Linear-Model Based MPTC 67

4.3.1 Equivalent Linear SRM Model with Transformations 67

4.3.2 Linear-Model-Based MPTC 74

4.4 Experimental Validation 77

4.4.1 Execution Time and Storage Space Comparison 78

4.4.2 Torque Control Performance Comparison 81

4.4.3 Dynamic Performance Evaluation of the Linear-Model-Based MPTC . . . 88
4.5 Conclusion . . . 90

5 Low-Ripple Continuous Control Set Model Predictive Torque Control for SRMs Based on Equivalent Linear SRM Model 91
5.1 Introduction . . . 91
5.2 Merit and Challenge to Develop CCS MPTC . . . 92
5.3 Proposed CCS MPTC Method . . . 95
5.3.1 Equivalent Linear SRM Model . . . 95
5.3.2 Proposed CCS MPTC Method . . . 98
5.3.3 Wide Speed Operation of the Proposed CCS MPTC Method . 105
5.4 Simulation Validation . . . 108
5.5 Experimental Validation . . . 117
5.5.1 Steady-State Performance Comparison . . . 119
5.5.2 Dynamic-State Performance Comparison . . . 127
5.6 Conclusion . . . 129

6 A Predictive Current Controller for SRMs with Robust Tracking Performance 132
6.1 Introduction . . . 132
6.2 Drawbacks of the CCC Methods . . . 133
6.3 Proposed Current Controller . . . 136
6.3.1 PWM Duty Prediction Scheme . . . 136
6.3.2 Adaptive Flux-linkage Model . . . 142

6.3.3 Balanced Switching Operation 145
6.4 Experimental Validation 147
6.4.1 Model Mismatch Calibration Verification 149
6.4.2 Current Tracking Performance Evaluation 153
6.4.3 Balanced Switching Operation Verification 160
6.5 Conclusion 162

7 Lumped Radial Force Characteristics Estimation for SRMs 163
7.1 Introduction 163
7.2 Proposed Radial Force Estimation Method 165
7.2.1 Fundamentals of SRMs 165
7.2.2 Relationship Between Square Root of the Lumped Radial Force and the Flux-linkage 166
7.2.3 Radial Force Characteristics Estimation under Varied Airgap Length Condition 172
7.3 Simulation Verification 173
7.4 Conclusion 178

8 Conclusions and future work 179
8.1 Conclusions 179
8.2 Future work 181
8.3 Publications 182

References 184

List of Figures

2.1 Cross section of the typical (a) four phase 8/6 SRM and (b) three-phase 12/8 SRM. 8

2.2 Tangential and radial forces generated in a SRM. 10

2.3 Block diagram of the typical drive system for the four-phase 8/6 SRM. 11

2.4 Three operation modes of an AHB inverter: (a) magnetization mode, (b) freewheeling mode and (c) demagnetization mode. 11

2.5 Torque ripple illustration for SRMs. 12

2.6 General block diagram for indirect torque control. 13

2.7 Example waveforms of a torque sharing function based strategy. . . . 15

2.8 Illustration of the TSF method. (Note 1: f_{inc}, f_{out}, T_{inc}, and T_{out} represent the incoming phase torque distribution function, outgoing phase torque distribution function, incoming phase reference torque, and outgoing phase reference torque. Note 2: The dashed black and red lines in the last two columns represent the torque reference from the analytical TSF) 18

2.9 General block diagram for the harmonic current injection method. . . 20

2.10 General block diagram for DITC. 23

2.11 General block diagram for DTC. 25

2.12 General block diagram for MPTC. 26
3.1 Flux linkage curves of a linear SRM. 32
3.2 Flux linkage in a real saturated SRM. 33
3.3 Linear torque and nonlinear torque at a certain position of the SRM. 34
3.4 Theoretical torque mapping boundary for SRM. 35
3.5 Flux linkage characteristics for (a) 8/6 5.1 kW SRM and (b)12/8 2.3 kW SRM. 36
3.6 Inductance profile of the 8/6 SRM. 36
3.7 Typical mapping lines for the studied 8/6 SRM. 37
3.8 Typical mapping lines for the studied 12/8 SRM. 38
3.9 Block diagram to verify the torque mapping. 39
3.10 Original reference current and reconstructed linear current (a) when σ is 4.5 and (b) when σ is 22.3 at 3000 r/min. 39
3.11 Position dependent current limitation if using the equivalent linear torque model. 42
3.12 Current reference generation process for a given value σ. 43
3.13 Flow chart of the GA bi-objective optimization algorithm for the (a) proposed method and (b) method in (Li *et al.*, 2019). 45
3.14 Current and torque waveform for refence current evaluation. 47
3.15 Time calculation process for T_2 and T_3. 47
3.16 Current reference generated (a) if using the equivalent linear torque model and (b) converted to nonlinear torque model at 1000 r/min and 8 N·m for the proposed method. 49

3.17 Time comparison at 1000 r/min and 8 N·m torque command.(Note: Literature [22] refers to (Li *et al.*, 2019)) 51
3.18 Time comparison at 1000 r/min and 8 N·m torque command.(Note: Literature [22] refers to (Li *et al.*, 2019)) 52
3.19 Pareto front comparison at 1000 r/min and 8 N·m torque command.(Note: Literature [22] refers to (Li *et al.*, 2019)) 54
3.20 Pareto front comparison at 3000 r/min and 8 N·m torque command.(Note: Literature [22] refers to (Li *et al.*, 2019)) 54
3.21 Current and torque waveform for the proposed method at 1000 r/min and 8 N·m torque command when σ is 11.09. 55
3.22 Current and torque waveform for the method in (Li *et al.*, 2019) at 1000 r/min and 8 N·m torque command when σ is 9.46. 55
3.23 Four-phase 8/6 SRM experimental setup. 56
3.24 Current and torque waveforms at 1000 r/min and 6 N·m torque command (a) for the proposed method when σ is 0.92 and (b) for the method in (Li *et al.*, 2019) when σ is 0.47. 56
3.25 Current and torque waveforms at 3000 r/min and 6 N·m torque command (a) for the proposed method when σ is 2.52 and (b) for the method in (Li *et al.*, 2019) when σ is 0.71. 57
4.1 Flow-chart for LUT-based MPTC method. 62
4.2 Region illustration for the improved switching table. 65
4.3 Flux-linkage for a linear and nonlinear SRM at a certain position. . . 68
4.4 (a) Flux-linkage transforming at two certain positions when $I_{Nl,f}$ value reaches the maximum and (b) Simplified mapping lines at two positions. 69

4.5 The $1/L_{Li}(\theta)$ curve for the studied 8/6 SRM. 70
4.6 Flux-linkage mapping lines from linear SRM to nonlinear SRM. . . . 71
4.7 (a) Flux-linkage transformation from nonlinear SRM to linear SRM and (b) Flux-linkage transformation from nonlinear SRM to linear SRM. 72
4.8 Torque for a linear and nonlinear SRM at a certain position. 72
4.9 (a) Torque transformation from linear SRM to nonlinear SRM and (b) Torque transformation from nonlinear SRM to linear SRM. 73
4.10 Flow chart of the proposed linear-space-based MPTC method. 75
4.11 Torque and current waveforms for (a) conventional LUT-based method, (b) improved LUT-based method, and (c) proposed linear-model-based method at 100 r/min and 8 N·m operating conditions. 82
4.12 Torque and current waveforms for (a) conventional LUT-based method, (b) improved LUT-based method, and (c) proposed linear-model-based method at 1000 r/min and 8 N·m operating conditions. 85
4.13 Torque and current waveforms for (a) conventional LUT-based method, (b) improved LUT-based method, and (c) proposed linear-model-based method at 5000 r/min and 4 N·m operating conditions. 87
4.14 Total torque, speed, and current waveforms of the proposed linear-model-based method during the speed rising period. 89
4.15 Torque, speed, and current waveforms during motor starting period of the proposed linear-model-based method. 89
5.1 Block diagrams for the FCS MPTC method and CCS MPTC method. 93
5.2 Linear torque model (blue curve) and nonlinear torque model (red curve) at a certain position of the SRM. 96

5.3 Process from nonlinear SRM model to equivalent linear SRM model. . 96
5.4 Feasible region for the optimization problem in the CCS MPTC method. 100
5.5 Contour plot for the cost function J_{Li} when the third constraint is active. 101
5.6 Flow chart of obtaining the optimum torque references for the proposed CCS MPTC method. 104
5.7 Switching feature illustration of the proposed CCS MPTC method. . 106
5.8 Simulation results of (a) the FCS MPTC method in (Peyrl *et al.*, 2009), (b) the FCS MPTC method in (Fang *et al.*, 2021a), and (c) the proposed CCS MPTC method when θ_1 is 8° at 500 r/min and 8 N·m operation conditions. 109
5.9 Simulation results of (a) the FCS MPTC method in (Peyrl *et al.*, 2009), (b) the FCS MPTC method in (Fang *et al.*, 2021a), and (c) the proposed CCS MPTC method when θ_1 is 8° at 1000 r/min and 4 N·m operation conditions. 111
5.10 Simulation results of (a) the FCS MPTC method in (Peyrl *et al.*, 2009), (b) the FCS MPTC method in (Fang *et al.*, 2021a), and (c) the proposed CCS MPTC method when θ_1 is 8° at 1000 r/min and 8 N·m operation conditions. 112
5.11 Simulation results of (a) the FCS MPTC method in (Peyrl *et al.*, 2009), (b) the FCS MPTC method in (Fang *et al.*, 2021a), and (c) the proposed CCS MPTC method when θ_1 is 5° at 3000 r/min and 4 N·m operation conditions. 113

5.12 Simulation results of (a) the FCS MPTC method in (Peyrl *et al.*, 2009), (b) the FCS MPTC method in (Fang *et al.*, 2021a), and (c) the proposed CCS MPTC method when θ_1 is 5° at 3000 r/min and 8 N·m operation conditions. 114
5.13 Simulation results of (a) the FCS MPTC method in (Peyrl *et al.*, 2009), (b) the FCS MPTC method in (Fang *et al.*, 2021a), and (c) the proposed CCS MPTC method when θ_1 is 4° at 6000 r/min and 4 N·m operation conditions. 115
5.14 Experimental results of (a) the FCS MPTC method in (Peyrl *et al.*, 2009), (b) the FCS MPTC method in (Fang *et al.*, 2021a), and (c) the proposed CCS MPTC method when θ_1 is 8° at 500 r/min and 8 N·m operation conditions. 120
5.15 Experimental results of (a) the FCS MPTC method in (Peyrl *et al.*, 2009), (b) the FCS MPTC method in (Fang *et al.*, 2021a), and (c) the proposed CCS MPTC method when θ_1 is 8° at 1000 r/min and 4 N·m operation conditions. 121
5.16 Experimental results of (a) the FCS MPTC method in (Peyrl *et al.*, 2009), (b) the FCS MPTC method in (Fang *et al.*, 2021a), and (c) the proposed CCS MPTC method when θ_1 is 8° at 1000 r/min and 8 N·m operation conditions. 122
5.17 Experimental results of (a) the FCS MPTC method in (Peyrl *et al.*, 2009), (b) the FCS MPTC method in (Fang *et al.*, 2021a), and (c) the proposed CCS MPTC method when θ_1 is 5° at 3000 r/min and 4 N·m operation conditions. 123

5.18 Experimental results of (a) the FCS MPTC method in (Peyrl *et al.*, 2009), (b) the FCS MPTC method in (Fang *et al.*, 2021a), and (c) the proposed CCS MPTC method when θ_1 is 5° at 3000 r/min and 8 N·m operation conditions. 124
5.19 Experimental results of (a) the FCS MPTC method in (Peyrl *et al.*, 2009), (b) the FCS MPTC method in (Fang *et al.*, 2021a), and (c) the proposed CCS MPTC method when θ_1 is 4° at 5000 r/min and 4 N·m operation conditions. 126
5.20 Experimental results for the FCS MPTC method in (Fang *et al.*, 2021a) at speed transient from 1000 r/min to 2000 r/min. 128
5.21 Experimental results for the proposed CCS MPTC method at speed transient from 1000 r/min to 2000 r/min when θ_1 is fixed at 8°. . . . 128
5.22 Experimental results for the FCS MPTC method in (Fang *et al.*, 2021a) when the torque command stepped from 4 N·m to 8 N·m. 130
5.23 Experimental results for the proposed CCS MPTC method when the torque command stepped from 4 N·m to 8 N·m (Note: θ_1 is fixed at 8°.).130
6.1 Relationship between phase current, switching modes, control period, and sampling rate in HCC mode. (Note: MCU indicates microcontroller unit and ADC represents analog-to-digital converter.) 134
6.2 Block diagram for the proposed current controller. 136
6.3 Execution sequence for the proposed duty cycle prediction method. . 137
6.4 The current, position, and flux-linkage information when (a) i_{ref}^{k+2} is larger than i_{pre}^{k+1} and (b) i_{ref}^{k+2} is smaller than i_{pre}^{k+1}. 139

6.5 The current is rising from i_{pre}^{k+1} to i_{ref}^{k+2} under (a) asymmetric PWM scheme and (b) symmetric PWM scheme. 140
6.6 The current is decreasing from i_{pre}^{k+1} to i_{ref}^{k+2} under (a) asymmetric PWM scheme and (b) symmetric PWM scheme. 141
6.7 Model mismatch calibration flow diagram. 145
6.8 Normal switching scheme. 146
6.9 Proposed balanced switching scheme. 146
6.10 Flux-linkage characteristics of the studied 8/6 SRM. 147
6.11 (a) Converging process of $\hat{\alpha}$, (b) current at the stating instant during the converging process, and (c) current after $\hat{\alpha}$ converges for nominal $\hat{H}$. 150
6.12 (a) Converging process of $\hat{\alpha}$, (b) current at the stating instant during the converging process, and (c) current after $\hat{\alpha}$ converges for 0.75 times nominal $\hat{H}$. 151
6.13 (a) Converging process of $\hat{\alpha}$, (b) current at the stating instant during the converging process, and (c) current after $\hat{\alpha}$ converges for 1.25 times nominal $\hat{H}$. 152
6.14 (a) Phase current and reference current I and (b) phase current and reference current II at 1000 r/min for HCC method when the control frequency is 60 kHz. 154
6.15 (a) Phase current and reference current I and (b) phase current and reference current II at 1000 r/min for the proposed method when the control frequency is 20 kHz. 154

6.16 (a) Phase current and reference current I and (b) phase current and reference current II at 3000 r/min for HCC method when the control frequency is 60 kHz. 156
6.17 Explanation for the delay in the CCC method. 156
6.18 (a) Phase current and reference current I and (b) phase current and reference current II at 3000 r/min for the proposed method when the control frequency is 20 kHz. 156
6.19 Phase current and reference current I at (a) nominal ψ_m, (b) 0.75 times nominal ψ_m, and (c) 1.25 times nominal ψ_m for the deadbeat controller in Mikail *et al.* (2014) when the SRM operates at 1000 r/min. 158
6.20 Phase current and reference current III at (a) 500 r/min, (b) 1000 r/min, (c) 2000 r/min, (d) 3000 r/min, (e) 4000 r/min, and (f) 5500 r/min for the proposed method. 159
6.21 Gate signals for the normal mode PWM operation. 161
6.22 Gate signals for the balanced PWM operation. 161
7.1 Description of the integral line. 167
7.2 (a) Contour plot and flux lines at 20 A current excitation and (b) Radial flux density B_r at the aligned position θ_{al} for the studied 8/6 SRM. 168
7.3 Root of radial force and scaled flux-linkage profiles at aligned position θ_{al} for the (a) four phase 8/6 SRM and (b) three phase 12/8 SRM. . 169
7.4 (a) Contour plot and flux lines at 20 A current excitation and (b) Radial flux density B_r at the aligned position θ_{al} for the studied 8/6 SRM. 170

7.5 Root of radial force and scaled flux-linkage profiles at (a) 15° for the four phase 8/6 SRM and (b) 15° for the three phase 12/8 SRM. . . . 171
7.6 Flow chart of the proposed radial force characteristic estimation method. 172
7.7 Flux linkage characteristics for the 8/6 SRM (a) when the airgap length is decreased to 0.15 mm and (b) when the airgap length is increased to 0.55 mm. (Note: the results represented by solid lines imitate ψ_{ExpM}.) 174
7.8 Radial force characteristics for the 8/6 SRM (a) when the simulated profiles at the nominal airgap length are used (conventional method) and (b) when the proposed method is used at the reduced airgap length situation. (Note: the results represented by dash lines are the real values of radial force.) 175
7.9 Radial force characteristics for the 8/6 SRM (a) when the simulated profiles at the nominal airgap length are used (conventional method) and (b) when the proposed method is used at the increased airgap length situation. (Note: the results represented by dash lines are the real values of radial force.) 176
7.10 Radial force characteristics for the 12/8 SRM (a) when the simulated profiles at the nominal airgap length are used (conventional method) and (b) when the proposed method is used at the reduced airgap length situation. (Note: the results represented by dash lines are the real values of radial force.) 177

7.11 Radial force characteristics for the 12/8 SRM (a) when the simulated profiles at the nominal airgap length are used (conventional method) and (b) when the proposed method is used at the increased airgap length situation. (Note: the results represented by dash lines are the real values of radial force.) 177

List of Tables

2.1 Summary and comparison of the SRM torque control strategies. (Note: MCU represents the microcontroller unit, and the switching angles are the turn-on and turn-off angles) 28

3.1 Elapsed Time T_2 for the Proposed Method and the Method in (Li *et al.*, 2019). 48

3.2 Detailed Parameters for the Studied 12/8 SRM. 49

3.3 Time Comparison Between the Proposed Method and Method in (Li *et al.*, 2019) at 1000 r/min and 8 N·m. 51

3.4 Time Comparison Between the Proposed Method and Method in (Li *et al.*, 2019) at 3000 r/min and 8 N·m. 52

3.5 T_{r_rms} Comparison Between the Proposed Method and Method in (Li *et al.*, 2019) with Different Angle Steps. 53

3.6 T_{r_perc} Comparison Between the Proposed Method and Method in (Li *et al.*, 2019) with Different Angle Steps. 53

3.7 Performance Comparison Between the Proposed Method and the method in (Li *et al.*, 2019) at 1000 r/min 6 N·m Torque Command. 57

3.8 Performance Comparison Between the Proposed Method and the method in (Li *et al.*, 2019) at 3000 r/min 6 N·m Torque Command. 57

4.1 Conventional switching table derived from (Peyrl *et al.*, 2009) for 8/6 SRM 63
4.2 Proposed improved switching table for 8/6 SRM 66
4.3 The employed switching table and SRM model for the three methods 78
4.4 MPTC Time Consumption Comparison 79
4.5 Storage Space Consumption Comparison 81
4.6 Control performance comparison at 100 r/min and 8 N·m operating condition 83
4.7 Control performance comparison at 1000 r/min and 8 N·m operating condition 86
4.8 Iron losses comparison between conventional method and proposed linear-model-based method 86
4.9 Control performance comparison at 5000 r/min and 4 N·m operating condition 87
5.1 Improved Switching Table for Obtaining Torque Reference Boundary Values of the Studied 8/6 SRM 98
5.2 Lagrange Multiplier and Optimum Torque References at Different Cases When One Constraint Is Active 102
5.3 Simulated Performance Comparison at 500 r/min and 8 N·m T_{ref} . . 110
5.4 Simulated Performance Comparison at 1000 r/min and 4 N·m T_{ref} . . 111
5.5 Simulated Performance Comparison at 1000 r/min and 8 N·m T_{ref} . . 112
5.6 Simulated Performance Comparison at 3000 r/min and 4 N·m T_{ref} . . 113
5.7 Simulated Performance Comparison at 3000 r/min and 8 N·m T_{ref} . . 114
5.8 Simulated Performance Comparison at 6000 r/min and 4 N·m T_{ref} . . 115

5.9 Computational Burden Comparison among Different MPTC Methods 118
5.10 Experimental Performance Comparison at 500 r/min and 8 N·m T_{ref} 120
5.11 Experimental Performance Comparison at 1000 r/min and 4 N·m T_{ref} 121
5.12 Experimental Performance Comparison at 1000 r/min and 8 N·m T_{ref} 122
5.13 Experimental Performance Comparison at 3000 r/min and 4 N·m T_{ref} 125
5.14 Experimental Performance Comparison at 3000 r/min and 8 N·m T_{ref} 125
5.15 Experimental Performance Comparison at 5000 r/min and 4 N·m T_{ref} 127
6.1 Balanced switching scheme 146
6.2 Current References Employed in the Experimental Tests 149
6.3 I_{error}^{RMSE} Comparison Between HCC and the Proposed Method at 1000 r/min 155
6.4 I_{error}^{RMSE} Comparison Between HCC and the Proposed Method at 3000 r/min 157
6.5 I_{error}^{RMSE} Comparison Between Deadbeat Method in Mikail *et al.* (2014) and the Proposed Method at 1000 r/min 158
6.6 I_{error}^{RMSE} for the Proposed Method at Different Speed 160
6.7 Average Frequency Comparison Between Normal and Balanced PWM Operation 161

Chapter 1

Introduction

1.1 Motivation

With the increasing depletion of non-renewable fossil fuels, people are increasingly interested in researching renewable energy and developing the applications of these alternative energy sources. Among them, the electrified transportation using different types of electric machines is trending to replace the conventional internal-combustion-engine-based transportation vehicles. Switched reluctance machines (SRMs) are emerging as a promising candidate in this electrification trend due to their low manufacturing cost, simple and robust structure, excellent fault-tolerant capability, wide constant-power region, and reliable operation in high-temperature conditions (Bilgin *et al.*, 2019). Applications in electrical vehicles (Bilgin *et al.*, 2020), aviation starter/generator (Valdivia *et al.*, 2014; Wiegand, 2018), and home appliance (Kim and Krishnan, 2009) were reported recently in the literature. Nevertheless, the inherent pulsative torque and the unique double salient structure lead to the well-known torque ripple and acoustic noise issues for SRMs. Through geometry design, the

torque ripple and acoustic noise can be reduced to a certain extent (Gan *et al.*, 2018), but these methods cannot be applied to the SRMs that are already in service. On the other hand, the advanced control methods, which directly manipulate the switching signals or shape the phase current, have been studied intensively to address the above issues.

It is well known that the linear model is easier to carry out analysis and develop control methods, such as the voltage and torque equations in the permanent magnet synchronous machines adopting the linear magnetic circuit. Unfortunately, the SRMs show high nonlinearity in normal operation due to the double salient structure. Therefore, it would be beneficial to develop an algorithm to make the most of the linear SRM model but also consider the high nonlinearity phenomenon in the actual SRM.

In addition, there are considerable methods in the literature shaping the phase current into a certain profile to reduce the torque ripple and/or acoustic noise. Obviously, to achieve the expected performance of these methods, a current controller with accurate tracking capability and robust performance is necessary.

As for the vibration reduction and acoustic noise suppression methods, the radial force information is vital for such control methods. Since the radial force is barely possible to measure directly, such information is normally obtained from the finite element analysis (FEA) software. However, during the SRM manufacturing process, the air gap length possibly varies (Ge *et al.*, 2020), which leads that the actual radial force differs from the one obtained from the FEA. Such deviation inevitably degrades the performance of the vibration reduction and acoustic noise suppression methods. Hence, developing methods to estimate the radial force characteristics with good

accuracy is essential.

1.2 Contributions

The author has contributed to a number of original developments in the equivalent-linear-model-based torque control and performance improvements for SRMs. These contributions are briefly described below.

(1) The concept and features of torque mapping from the linear SRM model to the nonlinear SRM model are developed. Based on this mapping, a time-efficient torque sharing function (TSF) method is presented.

(2) The flux-linkage mapping concept and features between the linear SRM model and the nonlinear SRM model are developed. Based on the above torque and flux-linkage mappings, an equivalent linear SRM model is presented. With this equivalent linear SRM model and the proposed improved switching table, a linear-model-based finite control set (FCS) model predictive torque control (MPTC) method is proposed.

(3) The high nonlinearity of the SMRs makes it barely possible to analytically solve the optimization problem in the continuous control set (CCS) MPTC method for SRM drives. To address this issue, the adoption of the equivalent linear SRM model and proper modification on the cost function in this thesis turn the optimization problem in the CCS MPTC algorithm to be simple and to be solved analytically. The torque control performance is further enhanced for the SRM drives in a wide speed range.

(4) An intersection-method-based current controller is proposed to accurately predict the required duty cycle for the next control period under a certain reference current. And an adaptive flux-linage model is presented to enhance the robustness of the presented current controller.

(5) The relationship between the square root of the lumped radial force and the flux-linkage curve at a certain position is studied in detail with the aid of the FEA simulation. Then, based on this relationship and the measured flux-linkage characteristics, the radial force characteristics is estimated with good accuracy regardless of the possible air gap length variation.

1.3 Outline of the Thesis

This thesis mainly focuses on advanced torque control methods for the SRM drive system based on the developed equivalent linear SRM model. Other performances such as phase current tracking capability and lumped radial force estimation accuracy are also enhanced. The four-phase 8/6 SRM experimental setup and simulation softwares are employed to validate the proposed methods.

Chapter 2 presents a thorough review on the advanced torque control methods. The SRM drive system is introduced briefly at first. Then, the torque control methods are reviewed in detail from two perspectives, namely the indirect method and the direct method. Emphasis on the TSF methods is presented. Finally, these methods are compared regarding the implementation complexity, torque-ripple-free speed, computational burden, consumed storage space, if need current loop, and if require switching angles.

Chapter 3 introduces a time-efficient torque shaping technique for the SRM. The torque mapping concept between the linear SRM model and the nonlinear model is introduced first. Then, the feasible regions and properties of this torque mapping are studied in detail. Based on this torque mapping, the current reference is first generated from the linear SRM model and later converted to the current reference

suitable for the actual SRM considering the nonlinearity of the SRM. Finally, the genetic algorithm (GA) is adopted to find the optimum current reference from the Pareto-front when considering the torque ripple and copper losses. Comparisons on the time consumption and the torque ripple reduction between the conventional and proposed methods are presented.

Chapter 4 presents a finite control set linear-model-based MPTC method for the SRM drive system. Firstly, an improved switching table with only 6 switching states is developed based on the inductance characteristics. The adoption of this improved switching table not only reduces the computational burden by 25% but also improves the torque control performance and system efficiency at a high-speed region. However, the look-up-table (LUT) based MPTC methods suffer from occupying numerous storage spaces. To address this issue, the simple linear SRM model is utilized. The flux-linkage and torque mappings are introduced to address the difference between the linear and nonlinear SRM models. With these mappings, the MPTC based on the linear SRM model is proposed. Comparisons between the conventional LUT-based MPTC method and the proposed linear-model-based MPTC method on the execution time, storage space requirement, torque ripple, and efficiency are presented.

Chapter 5 describes a continuous control set MPTC method for SRM. With proper modifications on the cost function and the adoption of the equivalent linear SRM model, the problem to obtain the torque references applied on the next control period for different phases under this cost function is converted to a constrained optimization problem. The Lagrange multiplier method is then utilized to obtain the optimum solution for this cost function. With the optimum torque reference for each phase, the duty cycles are calculated from the torque variation rates. Comparisons between the

FCS MPTC method and the proposed CCS MPTC method reveal that the proposed CCS MPTC method reduces the torque ripples and current ripples.

Chapter 6 describes a robust predictive current controller. Firstly, the required duty cycle for the next control period under specific reference current is estimated through the intersection method. A Lyapunov-based adaptive flux-linkage observer is utilized to address the heavy dependence on the accurate flux-linkage model for the current controller. With the above techniques, robust reference current tracking is achieved in a simple form and only one observer gain. Moreover, a balanced switching scheme is presented to reduce the switching frequency requirement of the power transistors and evenly distribute the switching losses.

Chapter 7 presents a lumped radial force estimation technique to address the inaccuracy of the radial force obtained from FEA when the air gap length varies during the manufacturing process. Firstly, the relationship between the radial force and the flux-linkage is explained in detail. The above relationship can be easily obtained from the FEA simulation at the nominal air gap length. With this relationship and the measured flux-linkage profiles, the actual radial force characteristics can be reconstructed with good accuracy regardless of the possible air gap length variations. Simulation results on two different type SRMs verify the effectiveness of the proposed method.

Chapter 8 draws the conclusion of this thesis and presents some possible further research topics.

Chapter 2

Switched Reluctance Motor (SRM) Drives and Advanced Torque Control Methods

2.1 SRM Drive System

2.1.1 SRM model

The switched reluctance machine is a type of machine with a unique double salient structure and the concentrated windings only attached to the stator core. Fig. 2.1 shows the cross sections of the typical four-phase 8/6 SRM and three-phase 12/8 SRM. During the operation of SRMs, the electromagnetic torque is generated from the tendency that the rotor poles seek alignment with the corresponding stator poles once the excitation current is applied. Due to this special torque generation mechanism, each phase of SRMs is conducting sequentially to produce a continuous shaft torque.

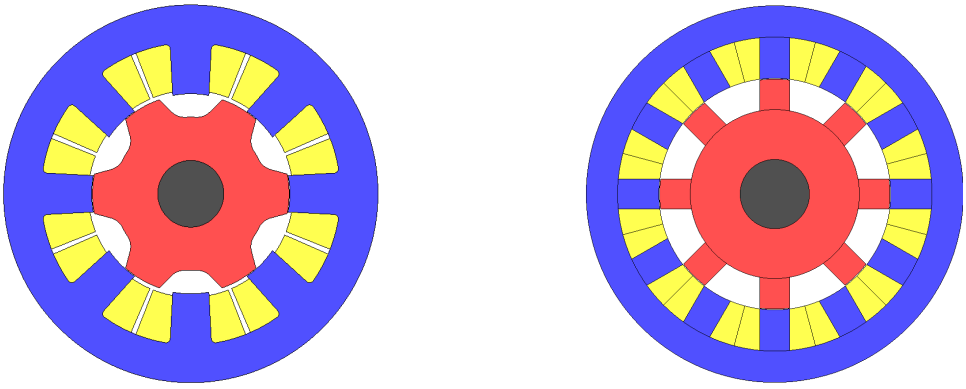

(a) (b)

Figure 2.1: Cross section of the typical (a) four phase 8/6 SRM and (b) three-phase 12/8 SRM.

The voltage equation and torque equation can be used to analyze and predict the behaviour of SRMs.

Based on the Faraday's law, the phase voltage equation can be expressed as (2.1):

$$v = Ri + \frac{d\psi(\theta, i)}{dt} \tag{2.1}$$

where v is the terminal voltage, R is the phase resistance, i is the phase current, and $\psi(\theta, i)$ is the flux-linkage. When neglecting the mutual inductance of SRMs, the flux-linkage $\psi(\theta, i)$ can be expressed as the product of the nonlinear self-inductance $L_{Nl}(\theta, i)$ and phase current:

$$\psi(\theta, i) = L_{Nl}(\theta, i)i \tag{2.2}$$

the phase voltage can be finally expressed as:

$$v = Ri + l_{inc}(\theta, i)\frac{di}{dt} + e_b \tag{2.3}$$

where

$$l_{inc}(\theta, i) = L_{Nl}(\theta, i) + i\frac{\partial L_{Nl}(\theta, i)}{\partial i} \tag{2.4}$$

$$e_b = i\omega_r \frac{\partial L_{Nl}(\theta, i)}{\partial \theta} \tag{2.5}$$

The term $l_{inc}(\theta, i)$ shown in (2.4) is the incremental inductance. It is observed that this term is related to both the rotor position θ and phase current i, which indicates that the magnitude of this term is affected by the saturation of the SRM. The term e_b in (2.5) is the back electromotive force (emf), which also depends on the position θ and current i. Besides, e_b is proportional to the rotor speed ω_r. Since both $l_{inc}(\theta, i)$ and e_b terms are correlated with θ and i, the current regulation for SRM is expected to be challenging according to (2.3).

The expression of the electromagnetic torque T_e can be derived from the co-energy W', which is shown as (2.6):

$$T_e = \left.\frac{\partial W'}{\partial \theta}\right|_{i=constant} = \left.\frac{\partial \int_0^i \psi(\theta, i) di}{\partial \theta}\right|_{i=constant} \tag{2.6}$$

Since the flux-linkage $\psi(\theta, i)$ is highly nonlinear, it is difficult to express this term analytically. Therefore, the electromagnetic torque T_e either cannot be expressed as an analytical function of phase current and inductance. For an unsaturated SRM, the torque can be simplified as (2.7). The term $L_{Li}(\theta)$ is the linear self-inductance and it only depends on the rotor position.

$$T_e = \frac{1}{2} i^2 \frac{dL_{Li}(\theta)}{d\theta} \tag{2.7}$$

If the radial and tangential flux-density information is known, such as by using the

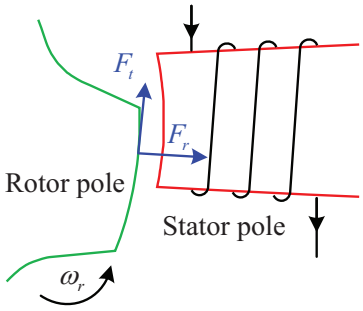

Figure 2.2: Tangential and radial forces generated in a SRM.

finite element software (FEA), the torque and even the radial force can be calculated via the Maxwell stress tensor. Specifically, the radial force, F_r, and tangential force (related with torque), F_t, as shown in Fig. 2.2, can be calculated as:

$$F_r = \frac{1}{2\mu_0} \int_s (B_r^2 - B_t^2) ds \tag{2.8}$$

$$F_t = \frac{1}{\mu_0} \int_s B_r B_t ds \tag{2.9}$$

where B_r, B_t, μ_0, and ds represent the radial flux density, tangential flux density, vacuum permeability, and infinitesimal increment of the integral surface area. The tangential force acting on the rotor poles generates electromagnetic torque, while the radial force acting on the stator poles deforms the stator core and finally leads to acoustic noise.

2.1.2 Asymmetrical Half-Bridge inverter

Because the phases of the SRMs are sequentially conducted, a suitable inverter is requited to drive the SRMs. A typical drive system for the studied four-phase 8/6 SRM is shown in Fig. 2.3, where the commonly applied asymmetrical half bridge

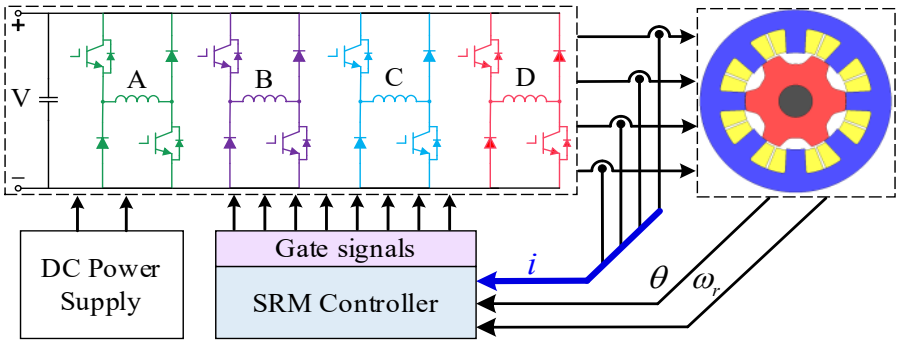

Figure 2.3: Block diagram of the typical drive system for the four-phase 8/6 SRM.

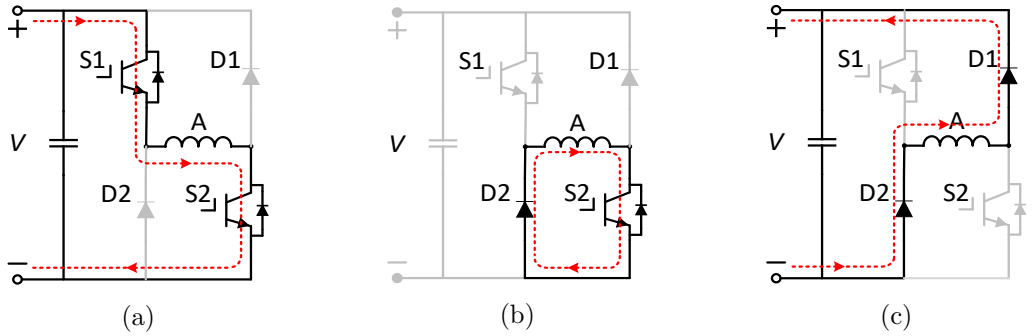

Figure 2.4: Three operation modes of an AHB inverter: (a) magnetization mode, (b) freewheeling mode and (c) demagnetization mode.

(AHB) inverter is used here to regulate the phase current.

And this AHB inverter normally can be operated in three modes: magnetization mode ("1"), freewheeling mode ("0"), and demagnetization mode ("-1"), which are described in Fig. 2.4.

In magnetization mode, switch S1 and switch S2 are closed simultaneously, where the conduction phase is directly fed with the positive power supply to allow immediate current rise. As for freewheeling mode, one switch remains closed while the other switch is open, in which the phase current would decrease slowly under 0-volt voltage across the phase terminal. Switch S1 and switch S2 would both be open status in demagnetization mode, where the negative supply voltage is applied to reduce the

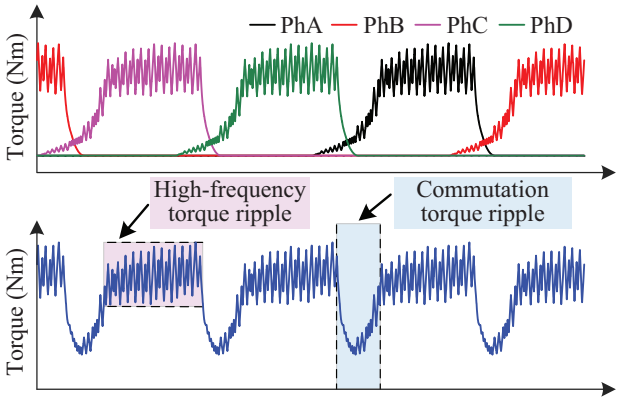

Figure 2.5: Torque ripple illustration for SRMs.

phase current as fast as possible.

To control the shaft torque or phase current, the adopted controller generates corresponding gate signals for the AHB inverter.

2.2 Advanced Torque Control Methods

Although the double salient structure brings merits to SRMs, such as low manufacturing cost and ruggedness, it also brings some drawbacks.

Firstly, the sequential conduction mechanism makes the phase current and the resultant phase torque inherently pulsed. This inherently-pulsed feature inevitably brings the challenge when controlling the total instantaneous output torque, especially on the torque ripples. The typical phase torque and total torque waveforms for an 8/6 SRM are shown in Fig. 2.5. From this figure, two kinds of torque ripples can be observed, namely commutation torque ripple and high-frequency torque ripple. The commutation torque ripple results from the inherently-pulsed toque waveforms, and normally it is the majority of the torque ripple. The high-frequency torque ripple is caused by switching actions during the current or torque regulation process and it is

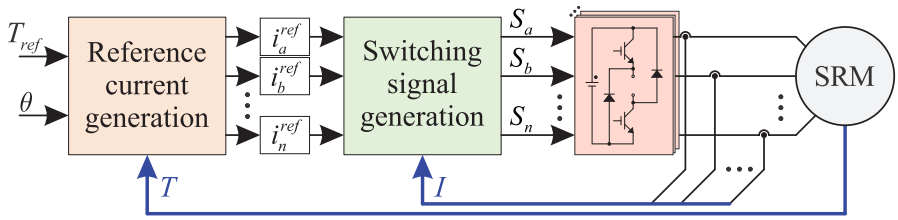

Figure 2.6: General block diagram for indirect torque control.

related to both the setup hardware and the machine parameters.

Secondly, there is no reference transformation to eliminate the position from its voltage and torque expression (Ilić-Spong *et al.*, 1985). Hence, the well-known vector control method, used in alternative current (AC) machines, cannot be directly transferred to the SRMs. This poses difficulties with regards to the torque control for SRMs. For decades, researchers have been focusing on this field and numerous methods are proposed to regulate the output torque. These methods can be categorized as indirect and direct methods, based on the control objectives observed in the control loop.

2.2.1 Indirect Method

Since current is related with electromagnetic torque in SRMs, indirect control methods regulate the output torque by controlling phase current. Fig. 2.6 describes the general block diagram for an indirect torque control structure. The reference current for each phase is firstly generated according to the torque command, T_{ref}, position information, θ, and reference current generation algorithm. The feedback instantaneous torque might also be used in this process. Then, the corresponding switching signals are generated with the aid of the actual phase current and later applied to the inverter

so the phase current attempts to track its reference value. The torque control performance relies on the reference current generation algorithm and the switching signal generation method. Among the existing literature, the indirect control methods can be roughly divided in torque sharing functions (TSF), current profiling techniques, harmonic current injection and vector control strategies.

Torque sharing functions

Due to the pulsed nature of the output phase torque in SRMs, the total torque to be produced needs to be shared between the active phases in the commutation region. The use of TSFs works in a rather straightforward way, where appropriate torque references are generated for each phase. Then, an important nonlinear function $i(T, \theta)$ is utilized to convert the torque reference to the corresponding current reference. As torque is a highly nonlinear function of current and position, the torque control performance is significantly affected by the TSF used (Bilgin *et al.*, 2019).

TSF method can be traced back to (Ilić-Spong *et al.*, 1985), where the total torque is distributed to each phase in a pattern of a mathematical function, with an exponential TSF being presented in order to deliver the constant total torque. A more general expression for the TSF method can be described as (2.10) and (2.11),

$$T_{total} = T_{ref} \times f_T(\theta) \tag{2.10}$$

$$f_T(\theta) = \sum_{1}^{n} f_k(\theta) = 1 \tag{2.11}$$

where T_{total}, T_{ref}, $f_T(\theta)$, and $f_k(\theta)$ are total shaft torque, reference torque, sum of the distribution function and phase distribution function, respectively. Numerous kinds of the $f_k(\theta)$ can be found in the literature.

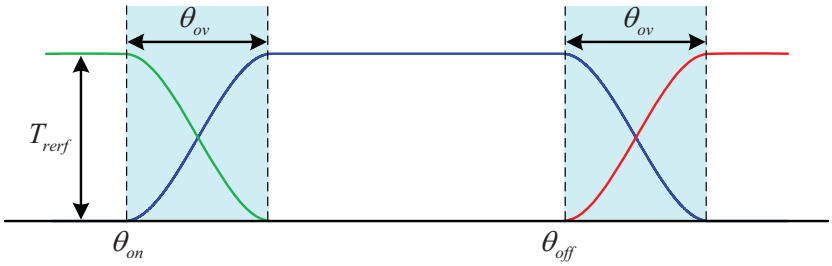

Figure 2.7: Example waveforms of a torque sharing function based strategy.

According to the torque distribution scheme, TSFs can be categorized as analytical TSFs, dynamic allocation TSFs and numerically optimized TSFs. The analytical-expression-based reference torque distribution function is the most straightforward allocation scheme, which uses a simple analytical expressions to represent the phase reference torque. The linear (Schramm *et al.*, 1992), sinusoidal (Husain and Ehsani, 1996), cubic (Sahoo *et al.*, 1999) and exponential (Ilić-Spong *et al.*, 1985) TSF functions are most commonly employed in literature. A cubic TSF function is shown in Fig. 2.7, where the θ_{on}, θ_{ov}, and θ_{off} indicate turn-on angle, overlap angle, and turn-off angle, respectively. These parameters have great effects on the torque control performance for the TSF method. In (Xue *et al.*, 2009), a genetic algorithm (GA) is used to optimize the turn-on angle and overlap angle for the four previously mentioned functions. Moreover, the rate-of-change of the flux-linkage and root mean square (rms) value of the phase current were also compared. In (Vujičić, 2012) a family of reference current waveforms is analytically derived, with minimized p-norm, based on an inverse torque model. The linear SRM model was used to derive the current reference in (Rana and Raviteja, 2021), and the nonlinear torque features were included based on a nonlinear modulation factor.

Due to the limited current changing rate of the drive system, the reference current

derived from the above analytical reference torque might not be tracked, especially at high speed and heavy load conditions (Bilgin *et al.*, 2019). In this case, the torque control performance is degraded due to the actual phase current deviating from the reference one. To address this issue, the dynamic allocation scheme distributes the phase reference torque in a way that considers the output torque capability of the incoming and outgoing phases. In (Tseng and Shuyu Cao, 2001), the pre-assigned linear torque reference is readjusted based on the maximum output torque capability of the machine. The special position in which the incoming phase is able to provide the reference torque divides the commutation region into two subregions. In different subregions, the phase with higher torque per ampere ratio was reassigned a higher reference torque (Sun *et al.*, 2016). In (Lee *et al.*, 2011; Dowlatshahi *et al.*, 2013; Gan *et al.*, 2020), the torque tracking error is estimated with the instantaneous torque feedback. The error is compensated with the phase with the higher torque output capability during the commutation period, while (Ro *et al.*, 2015) utilizes a fuzzy-logic controller to adjust the torque reference. In (Lee *et al.*, 2009), the reference torque is adjusted in such a way to demagnetize the outgoing phase as soon as possible, aiming to smooth out the output torque. The commutation region is divided into two subregions considering the absolute rate of change of the flux-linkage for the incoming and outgoing phase in (Ye *et al.*, 2015a). The developed feed forward proportional-integral (PI) compensator helps to improve the torque control performance at high speed operating conditions. In (Sahoo *et al.*, 2001, 2005; Lin *et al.*, 2006), intelligent control strategies, such as iterative learning control (ILC) and neural networks, are adopted to correct the initial reference current derived from the simple analytical TSF with the instantaneous torque feedback.

Apart from torque ripple reduction, other metrics such as average torque, copper losses, and torque-ripple-free speed are also vital criteria when evaluating the performance of a drive. This problem is suitable for a standard numerical optimization procedure, where the copper losses might be the objective function, the constant torque requirement is the equality constraint, and other conditions such as the current limitation form the inequality constraints, for example. Taking advantages of global numerical optimization algorithms, such as GA, the reference current which meets the requirements at different operating conditions can be obtained. In (Lovatt and Stephenson, 1997) the optimal reference current is determined aiming to minimize current rms value while considering bus voltage limitations. In (Changhwan Choi *et al.*, 2002), optimized TSFs are extended to negative torque production, giving enough time to increase current, allowing for good performance at high speed operation. The current profiles are given by a series of B-spline functions, significantly reducing memory requirements. Moreover, copper losses and voltage limitations are also considered as secondary objectives in the optimization procedure. A new offline optimized torque sharing function is presented in (Ye *et al.*, 2015b), where the squared current and its derivative were optimized through the method of Lagrange multipliers. A multi-objective GA algorithm is employed to find a suitable parameter that balances the compromise between copper losses and torque ripple reduction performance, while also considering current tracking capability (Li *et al.*, 2019). A new torque sharing function is proposed in (Xia *et al.*, 2020), aiming not only to improve torque control performance at high speed and heavy load operating conditions but also reduce the current tracking error.

The three categories of TSF, described previously, are summarized in Fig. 2.8,

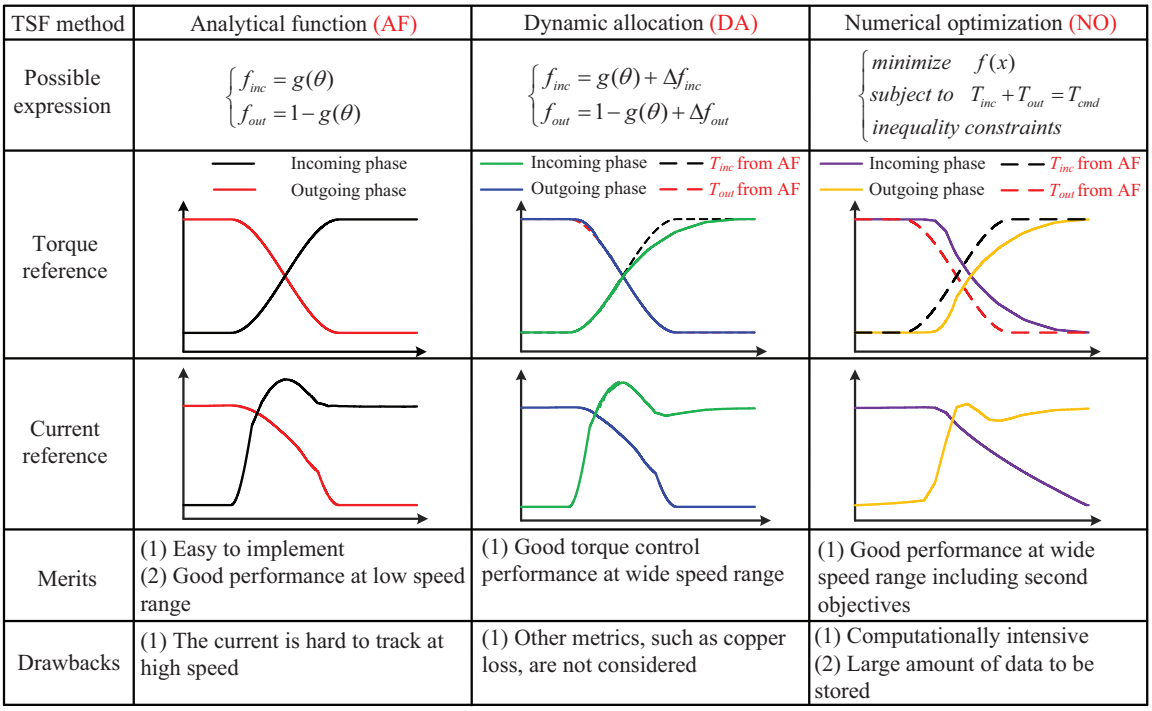

Figure 2.8: Illustration of the TSF method. (Note 1: f_{inc}, f_{out}, T_{inc}, and T_{out} represent the incoming phase torque distribution function, outgoing phase torque distribution function, incoming phase reference torque, and outgoing phase reference torque. Note 2: The dashed black and red lines in the last two columns represent the torque reference from the analytical TSF)

where the expression, references, merits and drawbacks of each approach are presented.

Current profiling technique

Unlike the TSF method, which distributes the reference torque first, the current profiling technique is another effective indirect approach which directly determines the reference current, without making use of the $i(T, \theta)$ lookup table. Normally, the current profiling method starts from a simple reference current and requires fine-tuning to reach the final reference current with good torque control performance. The

phase current was arranged to rise and fall linearly during the commutation region in (Wallace and Taylor, 1992). An initial reference current with trapezoidal shape was utilized and then tuned twice with instantaneous torque feedback to obtain the final reference current profile in (Mikail *et al.*, 2013). The work was extended in (Mikail *et al.*, 2015) to a four quadrant operation, and further enhanced in (Mehta *et al.*, 2018) by considering the rate of current variation, and improving high-speed performance. The work of (Kusumi *et al.*, 2020) analytically derived the reference current based on the unsaturated SRM to not only reduce the torque ripple but also suppress the bus current ripple. The rotor shape design is also optimized with the intent of helping to minimize copper losses. It should be noted, however, that this method only works for unsaturated SRMs. In (Chapman and Sudhoff, 2002), the reference current is expressed by means of a Fourier series and a numerical optimization is used in order to determine the optimal coefficient. A common rectangular reference current is shaped with the aid of the negative part of the bus current and commutation shifting scheme in (Chai and Liaw, 2010), with the intent of reducing torque ripple. Additional current profiling techniques which employ intelligent control can be found in (Mir *et al.*, 1999; Shang *et al.*, 1999; Henriques *et al.*, 2002).

Harmonic current injection

Since the current and inductance profiles are periodical in steady state, it is beneficial to analyze the effects of each current harmonic component on the torque ripple and average torque. As reported in (Zhu *et al.*, 2017) and (Liu *et al.*, 2012), the average torque is mainly contributed by the DC, first order and seconder harmonics, while the fourth and fifth harmonics have a more significant affect on torque ripple. In this

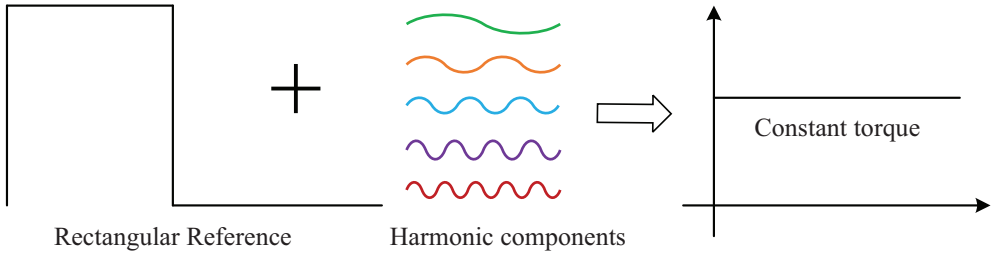

Figure 2.9: General block diagram for the harmonic current injection method.

case, it is possible to improve the output torque quality by actively and selectively injecting current harmonics, as shown in Fig. 2.9.

The injected current I_{inj} can be described as (2.12) (Stephenson *et al.*, 2001),

$$I_{inj} = \sum_{1}^{n} I_n cos(nN_r\theta + \varphi_n) \tag{2.12}$$

where I_n and φ_n indicate the magnitude and phase for the n-th order injected current, N_r represents the rotor pole numbers. In (Stephenson *et al.*, 2001), the first five current harmonics with optimized amplitude and phase are superimposed on the rectangular current reference to improve the torque control performance in the low speed region. The method is extended to the high speed range in (Stephenson *et al.*, 2002), where optimized current harmonics are determined online though the use of the simplex method. Five kinds of current references based on the half-sine waveforms are presented in (Shaked and Rabinovici, 2005), seeking to suppress torque ripple. Proper current harmonics are determined though numerical optimization in order to reduce the torque ripple and radial force ripple simultaneously in (Ma *et al.*, 2016) and (Gundogmus *et al.*, 2019). A segmented harmonic currents was optimized online through fuzzy logic to suppress torque ripple in (Ma *et al.*, 2019).

Vector control

With the advent of the Park's transformation and the wide spread use of vector control strategies, the torque control performance of AC machines was greatly enhanced. Unfortunately, in the early development of SRM control strategies, (Ilić-Spong *et al.*, 1985) and (Liu *et al.*, 1989) proved that there is no such transformation to decouple the position from the flux-linkage and torque for SRMs even in the linear case. Nevertheless, for decades, researchers sought approaches to control SRMs using vector control strategies, with the intent to improve torque control performance.

According to the torque expression for the unsaturated SRM, (Nagel and Lorenz, 2000, 1999) constructed two rotating complex vectors, namely complex derivative of inductance vector $\overline{dL(\theta)}/d\theta$ and complex squared current vector $\overline{I(\theta)^2}$, as expressed in (2.13) and (2.14):

$$\overline{\frac{dL(\theta)}{d\theta}} = \sum_{N} \frac{dL(\theta)}{d\theta} e^{j(k-1)\frac{2\pi}{N}} \tag{2.13}$$

$$\overline{I(\theta)^2} = \sum_{N} I(\theta)^2 e^{j(k-1)\frac{2\pi}{N}} \tag{2.14}$$

where N indicate the number of phases for the employed SRM. A closed form of the torque-ripple-free phase current is derived for the unsaturated SRM. However, iterative calculation is required in the reference current generation for the saturated SRM. In (Husain *et al.*, 2015; Ding *et al.*, 2019), the authors directly map a synchronous reluctance machine to the SRM, by maintaining equal torque. From the perspective of control variables, the SRM is controlled in a manner as the vector torque control method. However, please note that phase current is not sinusoidal for both of the above mentioned methods.

In (Liu *et al.*, 2011) is presented that the bipolar sinusoidal current excitation reduces the torque ripple but delivers lower average torque compared to the unipolar rectangular current excitation. Since the majority of the torque is generated by the DC and first two harmonics (Zhu *et al.*, 2017; Liu *et al.*, 2012), the DC plus first harmonic current excitation, as shown in (2.15), for the vector control method are intensively studied.

$$i_N = I_0 + I_1 cos(N_r\theta + (N-1)\frac{2}{3}\pi + \varphi_1) \tag{2.15}$$

It is detailed in (Nakao and Akatsu, 2014b) that in SRM drives with unipolar current excitation, the DC component virtually generates the rotor flux and that the AC component generates the rotating stator field. A vector controller was developed based on the average value of the first order inductance and the relationship between the q-axis current and torque was derived, but only for the unsaturated SRM. An improved current controller for this vector control strategy is presented in (Nakao and Akatsu, 2014a). The vector controller was further studied in (Kuai *et al.*, 2018) and (Kuai *et al.*, 2020), from the perspective of space vector modulation and variable q-axis current control. In (Yu *et al.*, 2020), an alternative explanation of the DC plus first order current excitation is presented, based on the flux modulation principle. Although the speed of the SRM can be controller in the *dq* frame, the exact torque expression is not derived.

2.2.2 Direct Method

Directly regulating torque with the torque feedback and manipulating the power transistors is a more straightforward way to control the output torque compared to

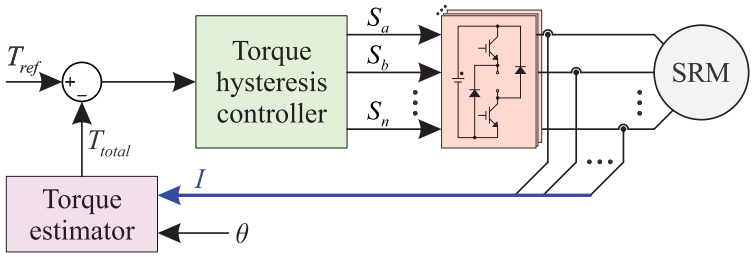

Figure 2.10: General block diagram for DITC.

doing it indirectly. According to the existing literature, the direct method can be categorized as: direct instantaneous torque control (DITC), direct torque control (DTC) and model predictive torque control (MPTC).

Direct Instantaneous Torque Control

Direct instantaneous torque control method was first presented in (Inderka and De Doncker, 2002, 2003), with Fig. 2.10 describing the general block diagram of this method. The key components in the DITC method are the toque estimator and torque hysteresis controller. With the instantaneous total torque calculated from the toque estimator and knowing the reference torque, the torque tracking error can be easily obtained. Then, the torque hysteresis controller generates the appropriate switching signals based on the estimated torque error and position information.

In (Inderka and De Doncker, 2002, 2003) it is validated that the DITC method could deliver smooth torque up to the rated speed with the appropriate conduction angles in the motoring mode. The work is extended in (Fuengwarodsakul *et al.*, 2005), developing the method to four quadrant operation and further reducing the torque ripple through the adoption of a predictive step and the use of PWM control in (Neuhaus *et al.*, 2006). The turn-on and turn-off angles are optimized online in

(d. Paula and Dos Santos Barros, 2021) to achieve better torque ripple reduction. Other performance enhancements, such as minimum torque ripple point tracking (d. Paula and Dos Santos Barros, 2021; de Paula *et al.*, 2020), efficiency improvements (Wang *et al.*, 2014; Sun *et al.*, 2020; Yao and Zhang, 2017; Song *et al.*, 2020b; Brauer *et al.*, 2011), lower torque ripple through the use of multi-level inverters (Liang *et al.*, 2009; Song *et al.*, 2019), torque-ripple-free speed range extension (Zeng *et al.*, 2015; Husain *et al.*, 2018), and lower cost algorithms (Gan *et al.*, 2016) were developed in recent years.

Direct Torque Control

It is well-known that good torque control performance can be achieved by adopting the DTC method, as it was first presented for induction machines (IM). Thus, researchers tried to apply this control strategy to SRMs, with the intent to reduce torque ripple. Similar to the DTC method in IMs, the torque expression is firstly derived in (Cheok and Fukuda, 2002) as a means to build the link between the instantaneous torque and the flux-linkage variation, as shown in (2.16):

$$T_e \approx i \frac{\partial \psi}{\partial \theta}\bigg|_{i=constant} \tag{2.16}$$

This approximate formula indicates that the instantaneous torque can be regulated by accelerating and decelerating the spatial combined flux-linkage vector under the constant current assumption. Based on this concept, the general block diagram for the DTC method for SRMs can be depicted in Fig. 2.11.

The toque error, flux-linkage error, and flux-linkage vector sector information are responsible for deciding the appropriate voltage vector which could keep the torque

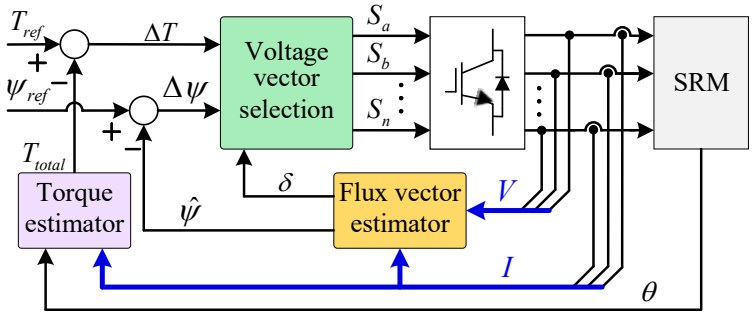

Figure 2.11: General block diagram for DTC.

and flux-linkage within a hysteresis band. The work of (Guo, 2006) points out several key concepts when implementing the DTC method, including the flux-linkage reference value in different operating conditions and the difference between the flux-linkage vector position and actual rotor position. Improved voltage vectors are used to enhance the torque control performance in (Ai-De *et al.*, 2018; Deng *et al.*, 2017; Xu *et al.*, 2019; Reddy *et al.*, 2019). The speed-dependent flux-linkage reference was presented in (Zhao *et al.*, 2017) to reduce the phase current rms value. A dead-beat DTC is developed in (Zhang *et al.*, 2019) to further reduce the torque ripple. The function of the flux-linkage loop was explained in (Yan *et al.*, 2018) in detail, and the authors suggested to remove this loop since the constant flux-linkage does not mean constant torque in SRMs. The torque per ampere ratio is significantly enhanced by eliminating the negative torque. In (Sun *et al.*, 2020), the speed loop PI regulator is replaced by a sliding mode controller along with a disturbance observer in order to improve the dynamic performance of the DTC method.

Model Predictive Torque Control

The MPTC method regulates the electromagnetic torque by considering the possible future states for all available voltage values. A typical control block diagram for the

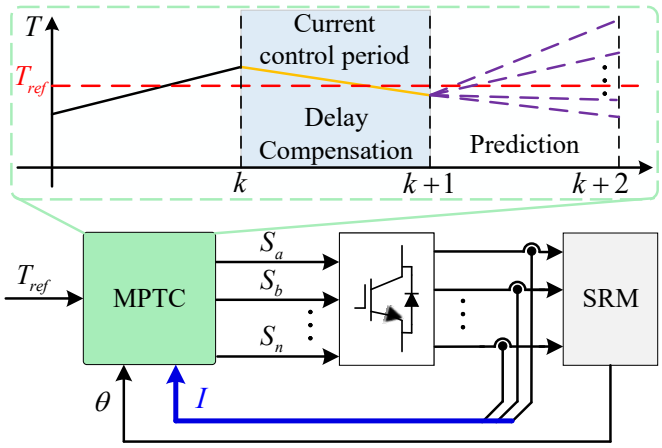

Figure 2.12: General block diagram for MPTC.

finite control set (FCS) MPTC method with one control period delay compensation and one sample prediction horizon is shown in Fig. 2.12.

According to the applied voltage vector calculated at the previous control period, the sampled phase current, and the sampled position, the phase current and total toque at future sampling instants can be estimated based on the employed SRM model. Then, a scalar cost function is adopted to evaluate the control performance under different candidate voltage vectors and the one that presents minimal cost function value is selected to be applied to the SRM in the next control period. An example of one commonly utilized cost function is expressed as (2.17) and (2.18):

$$J = (T_{ref} - T_{total,kp2})^2 + \omega_1 \sum (i_{kp2})^2 + \omega_2 \sum (S_{kp1} - S_k)^2 + g(i_{kp2}) \tag{2.17}$$

$$g(i(k)) = \begin{cases} \infty, & \text{if } i_k \geq i_{MAX} \\ 0, & \text{if } i_k < i_{MAX} \end{cases} \tag{2.18}$$

where ω_1 and ω_2 are the weighting factors (Peyrl *et al.*, 2009), S_{kp1} and S_k are the voltage vectors, and $T_{total,kp2}$ is the sum of the phase torque. It is observed that the

total torque error, copper losses, switching losses and maximum current limitations, for example, can all be included in the cost function. By carefully tuning ω_1 and ω_2, the control performance regarding torque ripples, copper losses and average switching frequency can all be improved, which is one of the merits of MPTC method.

The MPTC method was first applied to SRMs in (Peyrl *et al.*, 2009), based on a versatile analytical SRM model. It was later extended in the work of (Villegas *et al.*, 2010) with virtual discrete voltage vectors to further reduce torque ripples. In (Hu *et al.*, 2019) and (Song *et al.*, 2020a) model predictive control is employed as an inner current loop, allowing the phase torque to track the pre-assigned reference with minimal error. The Fourier expansion and exponential function based analytical SRM model along with improved switching tables are used in (Li *et al.*, 2017). Large torque ripples and low torque per ampere ratio issues related to the significant negative torque in high-speed operating conditions was explained in (Tarvirdilu-Asl *et al.*, 2019) and improved by using an adaptive turn-off angle.

2.2.3 Comparison of the torque control methods

All the torque control methods presented above can significantly reduce the torque ripples to a certain extent but might differs in other perspectives. In order to comprehensively show the difference of the presented strategies, a list of some key aspects of each method is presented in Table 2.1.

In general, the analytical TSF method possesses simplicity and delivers smooth torque in the low speed region. However, its torque control performance at the medium and high-speed regions is degraded due to the bad reference current trackability. The dynamic allocation TSFs improve their torque control performance at

Table 2.1: Summary and comparison of the SRM torque control strategies. (Note: MCU represents the microcontroller unit, and the switching angles are the turn-on and turn-off angles)

Method	**Implementation complexity**	**Torque-ripple-free speed**	**Consumed storage space**
Analytical TSF	Simple	Low	Low
Dynamic allocation TSF	Simple	High	Low
Numerical optimization TSF	Complex	High	High
Current profiling	Complex	High	High
Harmonic injection	Medium	Medium	Low
Vector control	Medium	Low/Medium	Low
DITC	Simple	High	Low
DTC	Medium	Low/Medium	Low
MPTC	Simple	Medium	Medium

Method	**Computational burden on MCU**	**Current loop**	**Switching angles**
Analytical TSF	Low	Yes	Yes
Dynamic allocation TSF	Low/Medium	Yes	Yes
Numerical optimization TSF	Low	Yes	No
Current profiling	Low	Yes	No
Harmonic injection	Medium	Yes	Yes
Vector control	Medium	Yes	Yes
DITC	Low	No	Yes
DTC	Low/Medium	No	No
MPTC	High	No	No

medium and high-speed regions but might sacrifice other performance aspects, such as copper losses and overall efficiency. To simultaneously enhance the performance on the torque control and other aspects, like copper losses, the turn-on and overlap angles need to be optimized, either online or off-line, increasing complexity. As for the numerically optimized TSFs, although it may take substantial computational efforts to obtain the reference current waveforms and require large amounts of memory on implementation, this method not only can generate smooth torque at high speeds but also exhibits the highest flexibility level when considering the second objective of the optimization, which can be copper losses and average torque, for example. Current profiling and harmonic injection can deliver smooth torque to a certain speed region,

but show limited performance when it comes to a secondary objective, since the reference current for both methods has to meet a specific shape. The vector control method normally shows good torque control performance at light load conditions, but suffers at heavy load conditions due to the severe saturation in the SRM. The above methods are all indirect, thus requiring the use of a current control loop and making the torque control performance dependant on the current controller's tracking capability.

On the other hand, the DITC, DTC and MPTC are direct methods, where the torque control performance is directly related with the control method itself. With proper choice of the switching angles, the DITC method can deliver smooth torque up to rated speed and the copper losses can be reduced by optimizing the commutation interval. Due to the extra flux-linkage loop in the DTC method, the torque-ripple-free speed and efficiency of the technique are limited. The MPTC method possesses the advantage of optimizing different objectives through a simple scalar cost function and does not require the switching angles to be varied at different operating conditions. However, the heavy computational burden and significant negative torque at the high speed region are the main drawbacks for this method.

Chapter 3

Time-Efficient Torque Sharing Method for SRMs Based on Equivalent Linear Torque Model

3.1 Introduction

As introduced in 2.2.1, the torque sharing function method is an effective method to not only reduce the torque ripple but also optimize the secondary objective, such as copper losses and average output torque. To achieve this target in a wide speed range and varied load operation conditions, bi-objective optimization is normally adopted to balance different objectives and reveal the correlations between objectives and variables. However, solving bi-objective optimization takes a significant amount of time, which is the main limitation that must be resolved.

In this chapter, a time-efficient torque shaping technique for the SRMs is proposed

to reduce the torque ripples while optimizing the copper losses. To reduce the computational time for solving the time-consuming bi-objective optimization problem, an efficient and desirable equivalent linear torque model for the SRM is utilized through the torque mapping between the linear torque model and nonlinear torque model. The feasible regions and properties of this torque mapping for SRMs are studied in detail first. Then, based on this torque mapping, the reference current is generated by solving an optimization problem by using the equivalent linear torque model and later converted to the reference current suitable for the saturated SRMs. Compared to the traditional method that only adopts nonlinear SRM model, the proposed current reference generation method requires less than 10% of the time. Furthermore, the proposed method saves more than 70% time consumed by the traditional method for the bi-objective optimization problem but possesses the similar torque ripple reduction performance.

3.2 Torque Mapping for SRMs

3.2.1 Torque Features and Torque Mapping Concept for SRMs

It is well-known that the adoption of the linear model, such as the linear torque model, is more time-efficient to solve the optimization problem for SRMs than the case by employing nonlinear model. To take this advantage and utilize this efficient linear model, it becomes necessary to build the map between the linear torque model (SRM with no saturation) and the nonlinear torque model (saturated SRM). The aim of this torque mapping is to equalize the output torque between the linear torque model and nonlinear torque model for SRMs. To build such torque mapping, the features

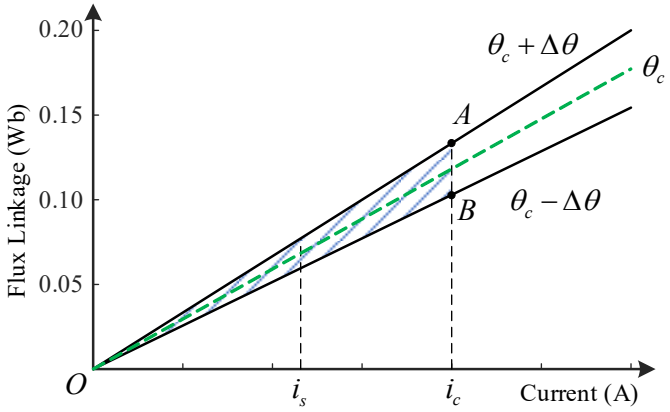

Figure 3.1: Flux linkage curves of a linear SRM.

of the linear and nonlinear toque expressions are expected to be analyzed first.

From the perspective of the energy flow in an ideal coupling magnetic field, the electromagnetic torque T_e for the SRM can be expressed as (2.6), which is repeated below for convenience. The current is supposed to be held constant in this process.

$$T_e = \left.\frac{\partial W'}{\partial \theta}\right|_{i=constant} = \left.\frac{\partial \int_0^i \psi(\theta, i) di}{\partial \theta}\right|_{i=constant}$$

Fig. 3.1 shows the flux-linkage curves for the linear SRM model at a certain rotor position θ_c. Please note that the overlapping between the rotor and stator poles exists at this position θ_c. The i_s shown in the picture represents the saturation point and the detailed definition of i_s can be found in (Song *et al.*, 2018). From the above developed torque expression, the torque T_{e_Li} generated by this linear SRM at current i_c is derived as (3.1):

$$T_{e\_Li} = \frac{\overline{AB}}{2 \times 2\Delta\theta} i_c = \frac{(L_{Li}(\theta_c + \Delta\theta) - L_{Li}(\theta_c - \Delta\theta))i_c}{4\Delta\theta} i_c \tag{3.1}$$

where $\overline{AB}$ represents the length from point A to B, $L_{Li}(\theta_c + \Delta\theta)$ and $L_{Li}(\theta_c - \Delta\theta)$

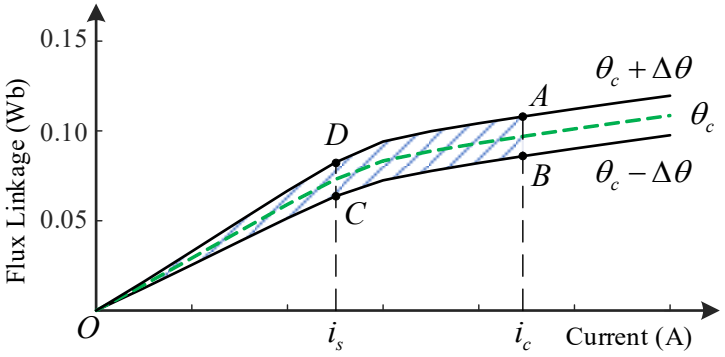

Figure 3.2: Flux linkage in a real saturated SRM.

are the unsaturated inductance at position $\theta_c + \Delta\theta$ and $\theta_c - \Delta\theta$. By observing this equation, the linear torque formula (3.1) exhibits the following two features:

(a) The length of $\overline{AB}$ is linearly proportional to the current magnitude i_c.

(b) Linear torque T_{e_Li} at a certain position is proportional to the squared current.

On the other hand, Fig. 3.2 shows the flux-linkage curves at the same rotor position θ_c for a saturated SRM. From this figure, it is observed that the torque expression is expected to be identical with the above linear SRM when the phase current is smaller than the saturated point i_s. For current values higher than i_s, the length $\overline{AB}$ almost keeps the same due to the saturation effect. Particularly, $\overline{AB}$ even sees reduction at positions close to the aligned position owing to the bulk saturation. It is noted that the position at maximum self-inductance value is referred to as the aligned position and the position at minimum self-inductance value is referred to as the unaligned position.

The torque expression for the nonlinear SRM is derived as (3.2) with the assumption that the co-energy area enclosed by ABCD is estimated by the parallelogram.

$$T_{e\_Nl} = \frac{(L_{Li}(\theta_c + \Delta\theta) - L_{Li}(\theta_c - \Delta\theta))i_s}{4\Delta\theta} i_s + (i_c - i_s)\frac{(L_{Li}(\theta_c + \Delta\theta) - L_{Li}(\theta_c - \Delta\theta))i_s}{2\Delta\theta} \tag{3.2}$$

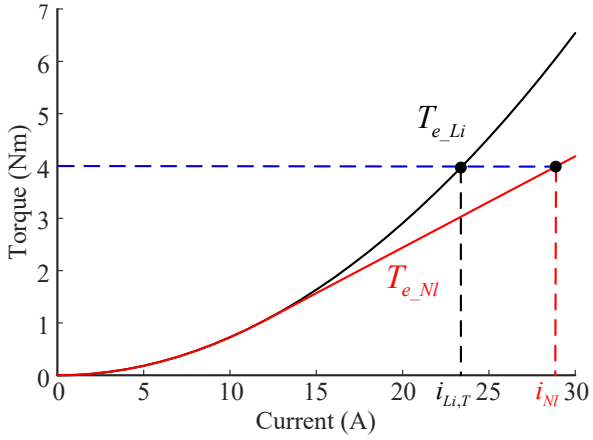

Figure 3.3: Linear torque and nonlinear torque at a certain position of the SRM.

Differing from the torque expression of linear SRM, the torque of the saturated SRM is linearly proportional to the current instead of the squared current once it enters the saturation region, which implies that T_{e_Nl} has a lower value than T_{e_Li} if the phase current is higher than i_s. Fig. 3.3 shows the torque curves for the linear and saturated SRM at a certain position. The current $i_{Li,T}$ and $i_{Nl,T}$ are the values that have the same torque in the linear and saturated SRM at the same rotor position. Owing to the difference between T_{e_Nl} and T_{e_Li} when the current is higher than i_s, $i_{Li,T}$ and i_{Nl} become different as well. The key idea of the torque mapping is to find the relationship between $i_{Li,T}$ and $i_{Nl,T}$ for the studied SRM.

3.2.2 Torque Mapping Properties for SRM

Before studying the mapping curves at every position, it is beneficial to first study their features at some typical positions. At the vicinity of the unaligned position, saturation is ignored due to the large air gap length, so there is no difference between T_{e_Nl} and T_{e_Li}. In this case, a straight line with slope 1 represents the mapping line between $i_{Li,T}$ and $i_{Nl,T}$. Moreover, this line forms the lower boundary for the toque

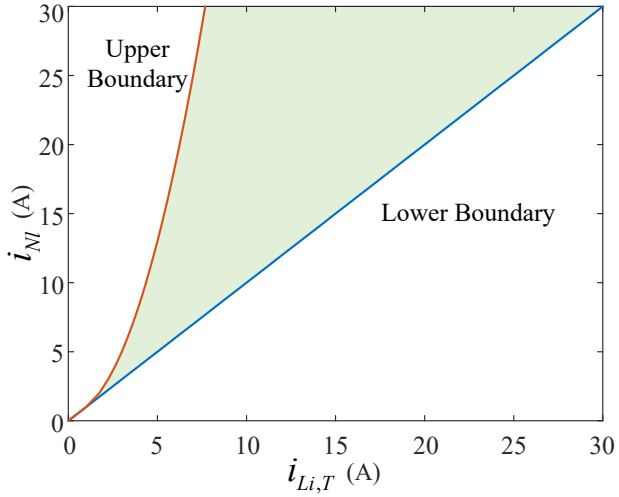

Figure 3.4: Theoretical torque mapping boundary for SRM.

mapping since T_{e_Nl} will never exceed T_{e_Li}. On the contrary, the situation where the saturation is assumed to begin at a very low current level is considered. Under this condition, the mapping line is supposed to have a large slope because of the enormous deviation between T_{e_Nl} and T_{e_Li} after the assumed low saturation point. And this mapping line is regarded as the upper mapping boundary.

Fig. 3.4 shows these two mapping boundary lines by assuming that the machine is saturated at 1 A for the upper mapping boundary. The area between these two boundary lines is regarded as the mapping feasible region for the torque mapping curves. To explain the detailed mapping curve features, a three-phase 2.3 kW 12/8 SRM and a four-phase 5.1 kW 8/6 SRM are adopted. The simulated flux-linkage curves for these two SRM are shown in the Fig. 3.5.

Considering the torque mapping concept and the torque expression (3.1) and (3.2), the mapping curve will move from the lower boundary to the upper boundary under the condition that i_s or length of $\overline{AB}$ will reduce along this movement. The inductance profile of the 8/6 SRM is utilized to analyze this phenomenon, which is

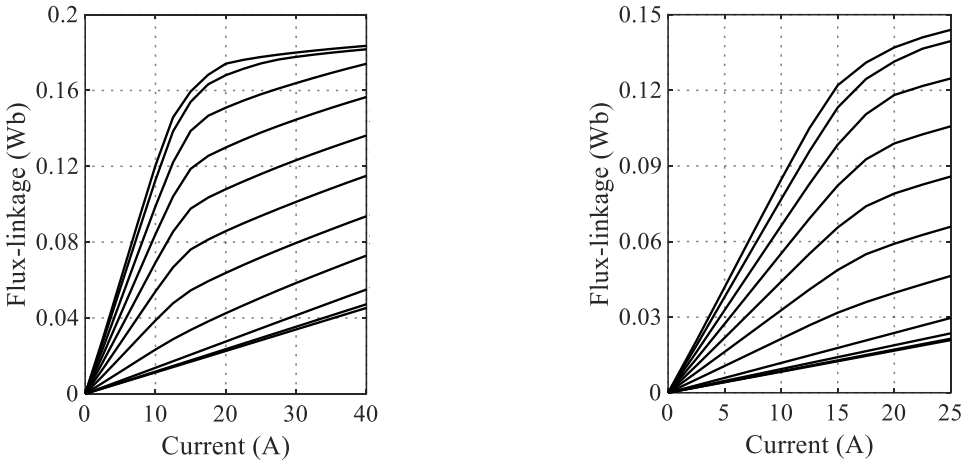

Figure 3.5: Flux linkage characteristics for (a) 8/6 5.1 kW SRM and (b)12/8 2.3 kW SRM.

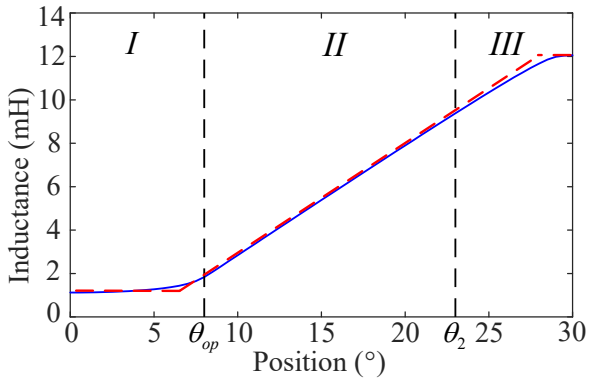

Figure 3.6: Inductance profile of the 8/6 SRM.

drawn in Fig. 3.6. According to the theory in (Miller and McGilp, 1990), three regions can be divided for the inductance curve, where θ_{op} is the angle when the rotor pole starts to overlap with the stator pole and θ_2 is the angle where the linear inductance region ends. In region I, as the rotor moving from the unaligned position to θ_{op}, the i_s equivalently varies from infinity to a normal saturated current while the mapping line moves from the lower boundary to the black curve as shown in Fig. 3.7. The black line is obtained by mapping the T_{e_Li} to T_{e_Nl} at position θ_{op}.

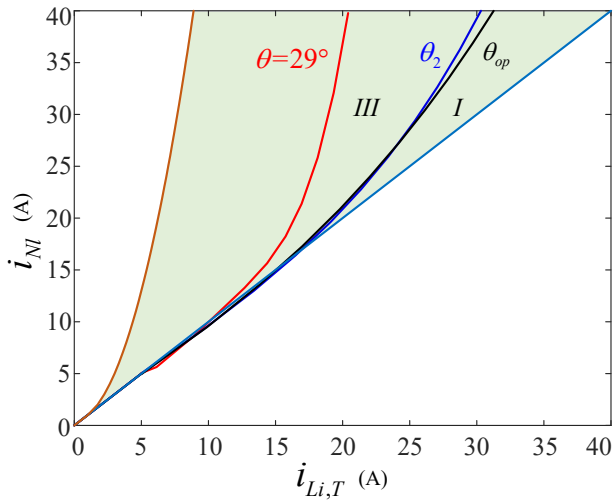

Figure 3.7: Typical mapping lines for the studied 8/6 SRM.

The inductance rises linearly in region II, but the i_s almost keeps the same as explained below. The magnetomotive force for one phase of the SRM can be expressed as (3.3) when the magnetic circuit just starts to saturate, where B_s represents the magnetic flux density, l is the stack length, r_1 denotes the bore radius, β is the overlapping angle, and N_t is the number of turns per phase.

$$N_t i_s = \frac{B_s l r_1 \beta(\theta) N_t^2}{L_{Li}(\theta)} \tag{3.3}$$

It can be observed from (3.3) that the only varying quantities during the movement from θ_{op} to θ_2 in region II are $\beta(\theta)$ and inductance $L_{Li}(\theta)$. However, both these quantities rise in a linear manner, thus the saturation point i_s will not change. As seen in Fig. 3.7, the mapping curves for positions θ_{op} and θ_2 just slightly differ at the high current region, which might be caused by the reduction of length of $\overline{AB}$. In region III, since $\beta(\theta)$ still rise linearly before the fully overlapping position but the inductance $L_{Li}(\theta)$ increases in a nonlinear manner, a smaller i_s is required to

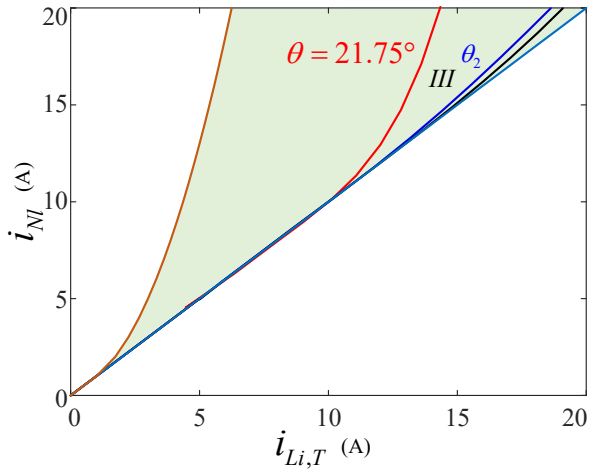

Figure 3.8: Typical mapping lines for the studied 12/8 SRM.

saturate the magnetic circuit. Besides, because bulk saturation exists in this region, the length of $\overline{AB}$ is reduced at a high current level. These two factors together make the mapping line move from the blue line to the red line in Fig. 3.7. To verify the generality of the above mapping curve features, these key mapping lines for the 12/8 SRM is shown in Fig. 3.8. It is clearly observed that the same mapping line moving trend and region division exists. This is because the typical SRMs exhibit the same inductance characteristics shown in Fig. 3.6 and these features are reflected at the torque mapping curves. In the following section, these key mapping lines and some extra mapping lines are utilized to convert the reference current generated from the equivalent linear torque model to be applicable for the saturated SRMs.

To further verify the correctness of the torque mapping, the method shown in Fig. 3.9 is employed. The reference current is first generated based on the linear model, which will be addressed in detail in the following section. Then, this linear reference current is converted back to nonlinear current by the torque mapping. Afterwards, this nonlinear current is converted back to the linear current, which is

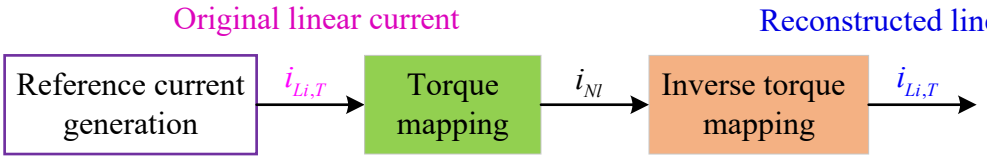

Figure 3.9: Block diagram to verify the torque mapping.

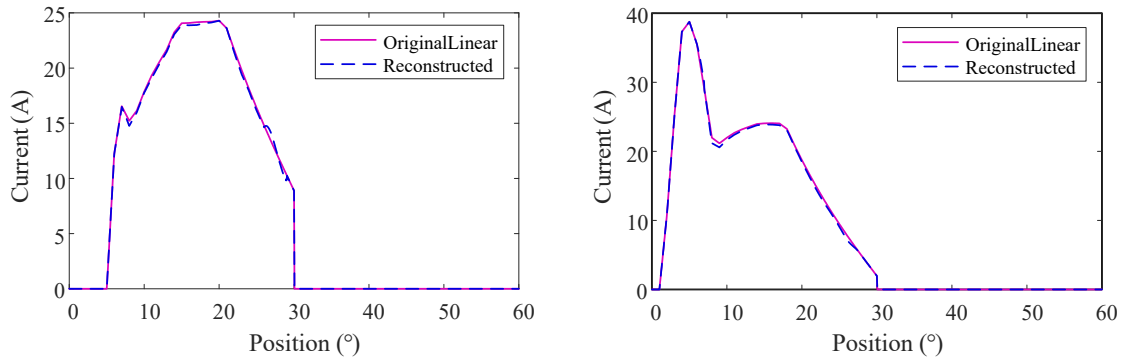

Figure 3.10: Original reference current and reconstructed linear current (a) when σ is 4.5 and (b) when σ is 22.3 at 3000 r/min.

labeled as reconstructed linear current. Fig. 3.10 shows the original linear current and reconstructed linear current for two different parameters. It can be observed these two current waveforms are almost identical, which proves the correctness of the torque mapping. Since the mapping curves are fitted by fourth-order polynomials, there is small deviation resulted from the above fitting error.

3.3 Proposed Time-Efficient TSF Method

The off-line optimization-based TSF method was recently proposed to regulate the output torque owing to its superior performance on the torque ripple reduction. Meanwhile, other performance such as copper losses, average torque could also be optimized by introducing the multi-objective optimization algorithm. The method proposed in

(Li *et al.*, 2019) employed just one parameter σ to compromise the copper losses and torque ripples. In this chapter, with the aid of the developed torque mapping technique, which can convert the reference current generated from the equivalent linear torque model to that is suitable for the saturated SRMs, the reference current generation part in (Li *et al.*, 2019) is replaced by the proposed technique to reduce its time-consumption significantly.

3.3.1 TSF based on the equivalent linear torque model

The objective function of the copper losses optimized TSF, with the reference current generated based on the equivalent linear torque model, could be described as (3.4):

$$f = min((i_{Li,T}^{inc})^2 + \sigma(i_{Li,T}^{out})^2) \tag{3.4}$$

where the superscript "*inc*" indicates the incoming phase, the superscript "*out*" indicates the outgoing phase, and σ is the weight parameter. It is noted that parameter σ is a definite number in this subsection. By selecting the weight parameter σ, the copper losses vary correspondingly. Hence, the parameter σ is necessary to be optimized to provide the best trade-off between the copper losses and torque ripples, which is addressed in the next subsection.

The primary task of the TSF is to keep the total torque closely tracking the command torque T_{ref} and reduce the torque ripples. Hence, the equality constraint for this optimization problem is (3.5):

$$T = T(i_{Li,T}^{inc}, \theta^{inc}) + T(i_{Li,T}^{out}, \theta^{out}) \tag{3.5}$$

The torque $T(i_{Li,T}^{inc}, \theta^{inc})$ or $T(i_{Li,T}^{out}, \theta^{out})$ provided by different phases could be directly calculated through the simple linear torque equation written in (3.1). And the unsaturated inductance information is obtained either by the FEA software or via experimental measurement. Considering the current limitation imposed by the machine thermal constraint, the phase current should be limited to a certain value. Normally, this value is a constant if using the nonlinear torque expression as described in (Li *et al.*, 2019). However, after the torque mapping, this constant value is changed to a position-dependent variable. By setting $i_{Nl,T}$ to the constant limitation value which is adopted in the nonlinear torque model, the corresponding current constraint for the equivalent linear SRM torque model could be easily read from the developed mapping curves. Hence, the current constraint for the equivalent linear SRM torque model is expressed as (3.6):

$$\begin{cases} i_{Li,T}^{inc} & < i_{max,Li}(\theta^{inc}) \\ i_{Li,T}^{out} & < i_{max,Li}(\theta^{out}) \end{cases} \tag{3.6}$$

where $i_{max,Li}$ is the maximum safety operation current for the equivalent linear torque model and is drawn in Fig. 3.11 under the condition that phase current is limited at 40 A for the nonlinear torque model.

The other inequality constraints imposed by the voltage equation is to limit the current variation rate so that the generated reference current is trackable, as shown in (3.7), where ψ_{Li}^{inc} and ψ_{Li}^{out} represent the incoming and outgoing phase flux-linkage

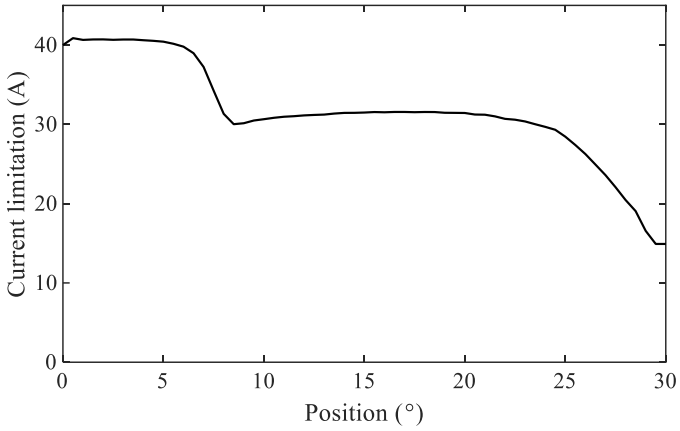

Figure 3.11: Position dependent current limitation if using the equivalent linear torque model.

by using the equivalent linear SRM model.

$$\begin{cases} \Delta\psi_{Li}^{inc}(i_{Li,T},\theta^{inc})/\Delta t \le V - i_{Li,T}^{inc}R \\ \Delta\psi_{Li}^{inc}(i_{Li,T},\theta^{inc})/\Delta t \ge -V + i_{Li,T}^{inc}R \\ \Delta\psi_{Li}^{out}(i_{Li,T},\theta^{out})/\Delta t \le V - i_{Li,T}^{out}R \\ \Delta\psi_{Li}^{out}(i_{Li,T},\theta^{out})/\Delta t \ge -V + i_{Li,T}^{out}R \end{cases} \tag{3.7}$$

The trackability of the generated reference current can be justified as below:

(a) The current variation rate between two consecutive points by using the equivalent linear torque model could be derived as:

$$\frac{di_{Li,T}}{dt} = \frac{v - i_{Li,T}R - i_{Li,T}\omega_r dL_{Li}(\theta)/d\theta}{L_{Li}(\theta)} \tag{3.8}$$

Compared to current variation rate if using the nonlinear torque equation, the term $\omega_r dL_{Li}(\theta)/d\theta$ and the denominator quantity $L_{Li}(\theta)$ are larger if using the equivalent linear torque model, so the current variation rate is probably smaller in this case.

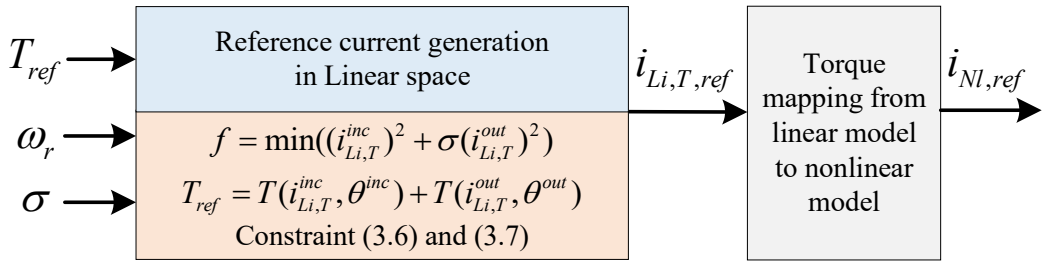

Figure 3.12: Current reference generation process for a given value σ.

This property makes the generated reference current after mapping at least not hard to follow.

(b) The bi-objective optimization algorithm adopted in the next subsection will automatically eliminate the current reference which is hard to follow due to its resultant high torque ripple.

By solving the above optimization problem for a certainly weight parameter σ, the reference current $i_{Li,T,ref}$ is obtained first. Then, converting $i_{Li,T,ref}$ to $i_{Nl,ref}$ through the above developed torque mapping, the final reference current $i_{Nl,ref}$ can be used for the saturated SRMs. The above reference current generation process could be described in Fig. 3.12. Please note the mapping lines at the following positions are utilized for the studied 8/6 SRM: 6°, 7°, 8°, 9°, 10°, 11°, 23°, 26°, and 29°. And the above mapping lines are selected mainly base on the torque mapping feature, which is that region I and III in Fig. 3.7 occupies a large area and the mapping lines in region II show slight deviation. The mapping coefficient at other positions is estimated by the interpolation algorithm.

3.3.2 Time-Efficient Parameter Selection

The GA bi-objective optimization algorithm is employed to select the suitable weight parameter σ (Li *et al.*, 2019) owing to the fact that not only the relationship between the copper losses and torque ripples is visualized but also the trade-off decision is easy to make. However, the heavy time consumption poses the main issue for this optimization process.

Fig. 3.13 (a) shows the flow chart of this optimization process for the proposed time-efficient parameter selection method and Fig. 3.13 (b) shows this optimization process for the method in (Li *et al.*, 2019). Both methods contain three parts, namely GA algorithm, current reference generation, and dynamic model operation. It is noticed that the reference current generation part for the proposed method incorporates two functions, namely the reference generation by using the equivalent linear torque model and reference current mapping from equivalent linear torque model to nonlinear torque model. The GA algorithm is mainly responsible for σ selection and decision making, which is represented by the block filled with a light orange color in Fig. 3.13. And the current reference generation part provides the current reference under a certain σ while the evaluation of this reference is conducted on the dynamic model operation. It is observed that the difference between the proposed method and the method in (Li *et al.*, 2019) lies in the reference generation part. The method in (Li *et al.*, 2019) generates the reference current directly by using the time-consuming nonlinear torque model, while the proposed method generates reference current by using the efficient linear torque model first and then transfer to the nonlinear torque model through simple polynomials. The time consumed by each part is labeled as T_1, T_2, and T_3. And the total time consumption for this bi-objective optimization is the

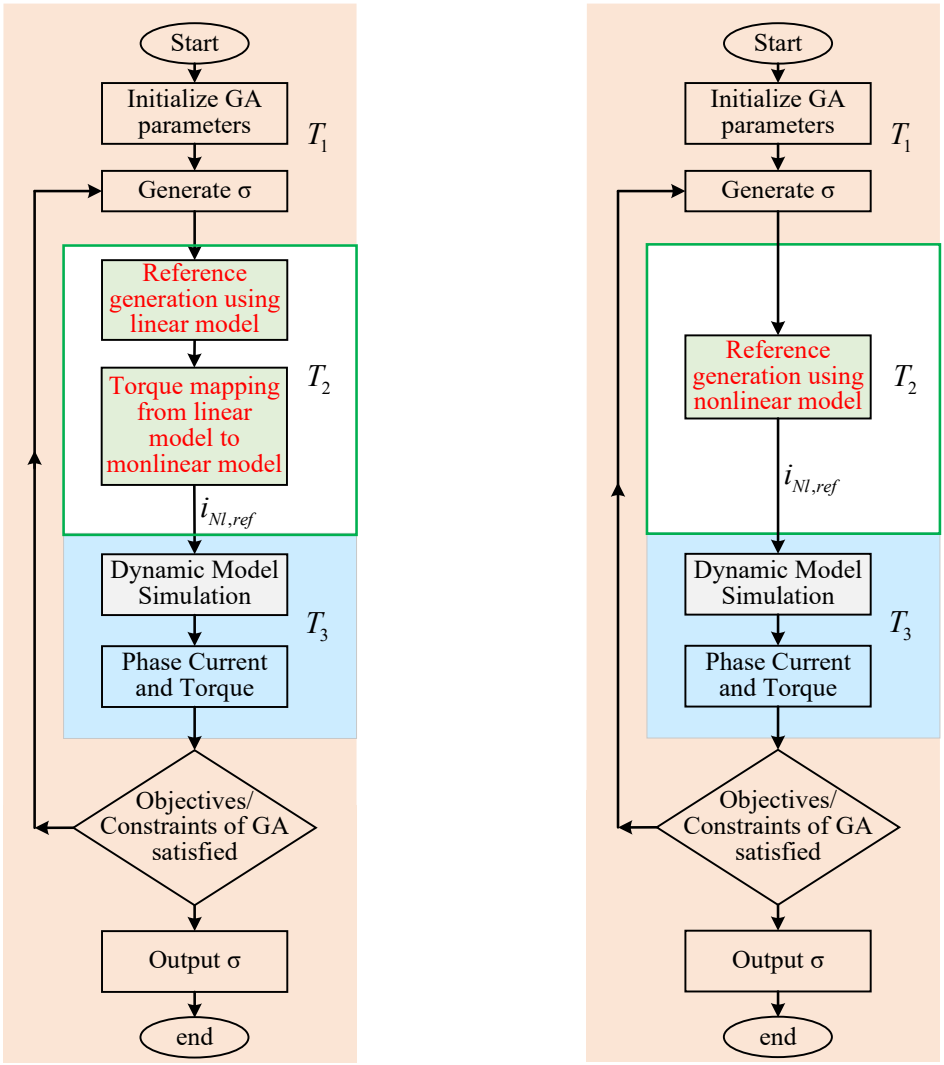

Figure 3.13: Flow chart of the GA bi-objective optimization algorithm for the (a) proposed method and (b) method in (Li *et al.*, 2019).

product of iteration number and $(T_1 + T_2 + T_3)$.

The time T_1 and T_3 can be easily reduced by proper configuration setting but the convergency and accuracy of the optimization algorithm should be guaranteed, and this is identical for both the proposed method and method in (Li *et al.*, 2019). Nevertheless, by using the equivalent linear torque model to generate the reference current,

the time T_2 is effectively reduced for the proposed method so that the parameter selection process is much more efficient. The reasons for the time T_2 reduction in the proposed method lies in the following facts: (a) The equality constraint in (3.5) is constructed just by simple quadratic polynomials and (b) The inequality constraints in (3.7) are constructed by four linear inequalities. On the other hand, ten 2-dimensional (2D) LUTs along with the 2D interpolation method are required to construct these constraints if using the nonlinear torque model as described in (Li *et al.*, 2019). This implies the reference current generation requires a heavy computational burden to solve this optimization problem in (Li *et al.*, 2019).

To gain some insight to the time consumption, it is beneficial to quantify the time T_2 and T_3. For T_1, it is ignored in this chapter due to the following two reasons: (a) it is hard to measure this amount of time directly, and (b) this part is supposed to be not time-consuming since it only focuses on σ generation and ranking. Because time T_2 is related with the simulation duration time and step size, the following conditions are set for all the simulation tests to evaluate the consumed time in this bi-objective optimization process: (a) The simulation step is configured at 1/360k and the switching/control frequency is 60 kHz; (b) The simulation duration is set for running two strokes at constant speed for the studied 8/6 SRM, as shown in Fig. 3.14.

The reason for setting the switching frequency at 60 kHz is to keep the simulation switching frequency consistent with that on the experimental tests. The current and torque information is collected in the latter half of the simulation results. And all the elapsed time is recorded based on a desktop computer equipped with an i7-8700 CPU and 32GB RAM. It is noticed that the Matlab function “tic” and “toc” are placed at the beginning and end of the testing program to accurately measure the

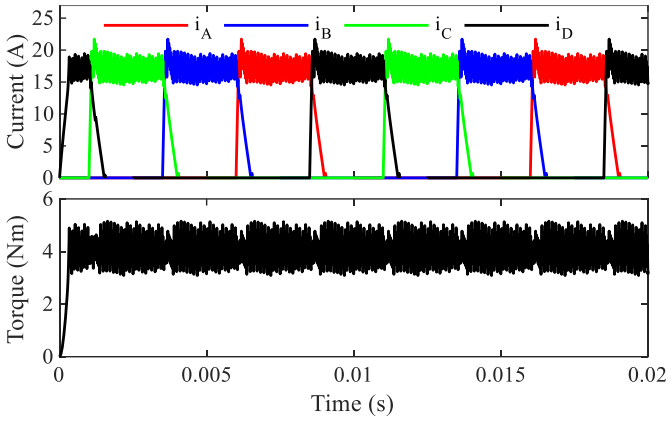

Figure 3.14: Current and torque waveform for refence current evaluation.

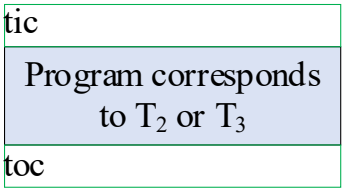

Figure 3.15: Time calculation process for T_2 and T_3.

consumed time T_2 and T_3, as shown in Fig. 3.15. Under the above setting conditions, the calculated elapsed time T_3 is 0.2912 seconds.

Then, the elapsed time T_2 of the proposed method and that of the method in (Li *et al.*, 2019) are supposed to be evaluated and compared. Because the reference current is normally stored in a series of points with equal angle step, the time consumption T_2 is highly related to the angle step. For example, if the angle step is set to 0.5 mechanical degrees, the number of the current reference points that need to be evaluated and stored is 60 in the positive torque region for an 8/6 SRM. Obviously, the bigger angle step implies a smaller number of reference points to be calculated in the reference current generation part, hence consumes less time. Under the same setting conditions described above, Table 3.1 lists the elapsed time T_2 for the proposed method and the method in (Li *et al.*, 2019) under different angle steps. It is noticed

Table 3.1: Elapsed Time T_2 for the Proposed Method and the Method in (Li *et al.*, 2019).

Angle Step (Mechnical)	Proposed Method	Method in (Li *et al.*, 2019)	$\frac{Proposed}{(Li\ et\ al.,2019)} \times 100\%$
0.50°	0.1885 s	2.3027 s	8.2 %
0.75°	0.1442 s	1.6086 s	9.0 %
1.00°	0.1041 s	1.1932 s	8.7 %
1.25°	0.0989 s	1.0357 s	9.6 %
1.50°	0.0743 s	0.8715 s	8.5 %
2.50°	0.0461 s	0.7070 s	6.5 %
5.00°	0.0248 s	0.4489 s	5.5 %

that the nonlinear solver "fmincon" integrated in the Matlab optimization tool-box is employed to solve the optimization problem to generate the reference current for the above two methods. From the listed results, the proposed method shows superior performance over the method in (Li *et al.*, 2019) regarding the elapsed time. Moreover, in all the testing results, the time consumed by the proposed method is less than 10% of the time consumed by the method in (Li *et al.*, 2019), as shown in the fourth column of Table 3.1. During the GA bi-objective optimization, thousands of cases need to be evaluated for one operation point. Therefore, substantial time could be saved by the proposed method, which will be verified in the next section.

3.4 Simulation Verification

To verify the effectiveness of the proposed method, the dynamic model and bi-objective optimization algorithm were built in the Matlab/Simulink environment. All the simulation tests are carried out on a four-phase 5.1 kW SRM. Fig. 2.1 (a) shows the 2D structure of the studied four-phase SRM and Table 3.2 lists some of the related parameters. It is noted that all the phase current in the simulation and experimental tests are controlled through a widely employed asymmetrical half-bridge

Table 3.2: Detailed Parameters for the Studied 12/8 SRM.

Parameter	Value
Number of stator poles	8
Number of rotor poles	6
Rated power	5.1 kW
Rated torque	8 N·m
Rated mechanical speed	6000 r/min
Rated voltage	300 V
Rated current (root mean square value of phase current)	14.35 A

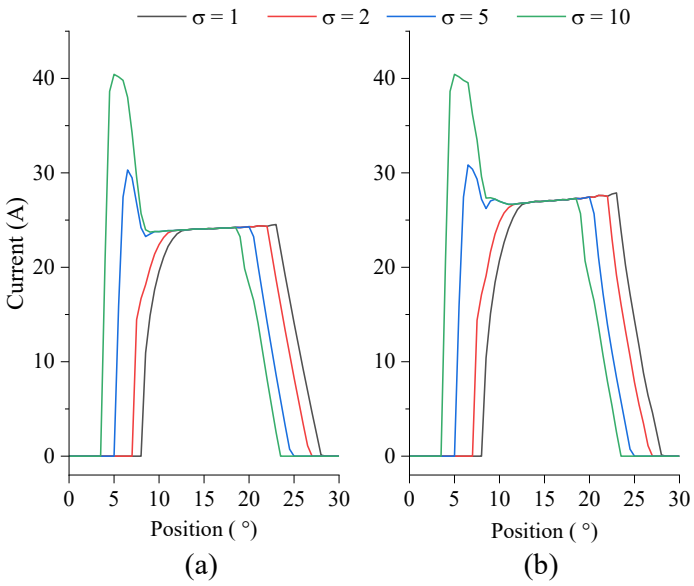

Figure 3.16: Current reference generated (a) if using the equivalent linear torque model and (b) converted to nonlinear torque model at 1000 r/min and 8 N·m for the proposed method.

converter, which is shown in Fig. 2.3. Because the proposed method generates the reference current directly, the turn-on and turn-off angles are not required. Owing to the fact that soft current chopping (SCC) method has low current decreasing rate, the current tracking performance might be poor if the reference current decrease fast. Therefore, the hard current chopping (HCC) method is adopted, and the switching signal is generated automatically once the current hysteresis band is set.

Fig. 3.16 shows the current reference waveform generated by the proposed method

before and after torque mapping at 1000 r/min and 8 N·m torque command condition. It is clearly observed that (a) the weight parameter σ effectively shapes the reference current with different copper losses, (b) higher σ value implies a higher copper loss, and (c) the current reference after torque mapping obviously differs from the original one. Please note that the conclusion that higher σ value indicates higher copper losses is applied to the SRM which has the same torque and flux-linkage characteristics. If these two essential characteristics are different, the σ value under the same operating condition might be different and a higher σ value does not necessarily indicate higher copper losses. The converted reference current then is integrated into the bi-objective optimization algorithm as described in Fig. 3.13.

The time consumption and other performance indicators, like rms value of the torque ripples T_{r_rms} and peak to peak torque ripple percentage T_{r_perc} were evaluated and compared between the proposed method and the method in (Li *et al.*, 2019). The T_{r_rms} and T_{r_perc} are evaluated through (3.9) and (3.10), where θ_{on}, θ_{off}, T_{avg}, T_{total_max}, and T_{total_min} represent turn-on angle, turn-off angle, average torque, maximum torque, and minimum torque.

$$T_{r\_rms} = \sqrt{\frac{1}{\theta_{off} - \theta_{on}} \int_{\theta_{on}}^{\theta_{off}} (T_e - T_{avg})^2 d\theta} \tag{3.9}$$

$$T_{r\_perc} = (T_{total\_max} - T_{total\_min})/T_{avg} \tag{3.10}$$

Regarding the time consumption evaluation, it is noticed that the GA bi-objective algorithm is set with the following parameters for all the simulation tests: population size is 20, termination tolerance is 1e-2, and σ ranges from 0 to 100. The bar plot in Fig. 3.17 shows the time comparison between the proposed method and the method in

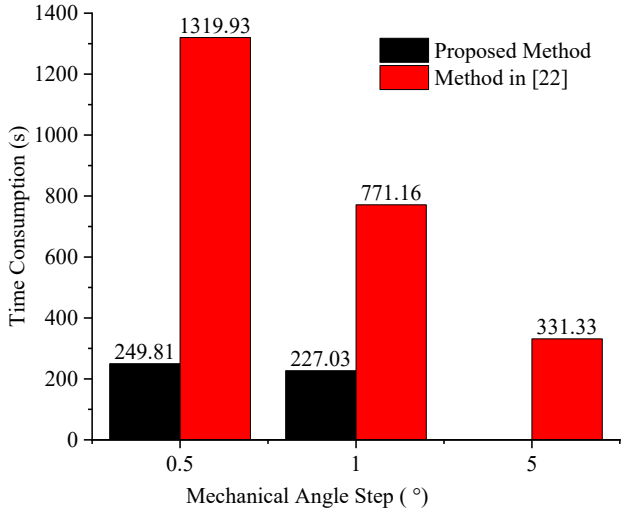

Figure 3.17: Time comparison at 1000 r/min and 8 N·m torque command.(Note: Literature [22] refers to (Li *et al.*, 2019))

Table 3.3: Time Comparison Between the Proposed Method and Method in (Li *et al.*, 2019) at 1000 r/min and 8 N·m.

Angle Step (Mechnical)	Proposed Method	Method in (Li *et al.*, 2019)	$\frac{Proposed}{(Li\ et\ al.,2019)} \times 100\%$
0.50°	249.81 s	1319.93 s	19.93 %
1.00°	227.03 s	771.16 s	29.44 %
5.00°	\	331.33 s	\

(Li *et al.*, 2019) for this bi-objective optimization at 1000 r/min and 8 N·m operating condition. It is observed that the total elapsed time is significantly saved by employing the proposed method. Although the consumed time is reduced with a bigger angle step, the time consumption at 5° for the method in (Li *et al.*, 2019) is still longer than that of the propose method at 0.5°. Table 3.3 summarizes this time consumption information and reveals that the time saved by the proposed method is more than 70%.

Fig. 3.18 provides the time comparison at 3000 r/min and 8 N·m operating condition. Similar to the situation in Fig. 3.17, the consumed time for the proposed method

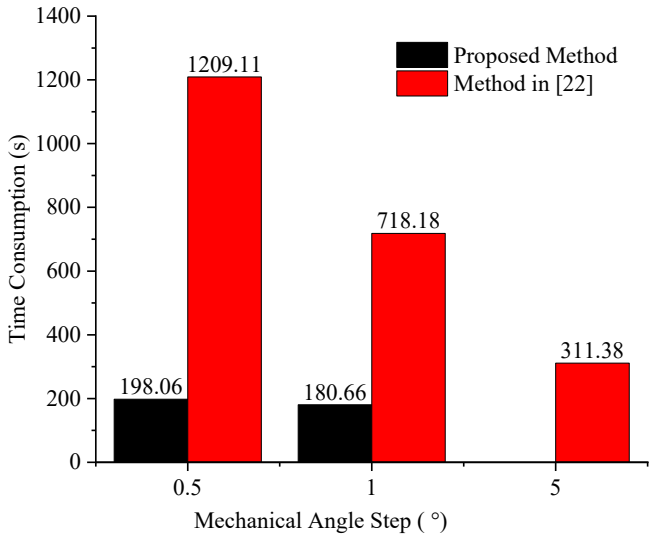

Figure 3.18: Time comparison at 1000 r/min and 8 N·m torque command.(Note: Literature [22] refers to (Li *et al.*, 2019))

Table 3.4: Time Comparison Between the Proposed Method and Method in (Li *et al.*, 2019) at 3000 r/min and 8 N·m.

Angle Step (Mechnical)	Proposed Method	Method in (Li *et al.*, 2019)	$\frac{Proposed}{(Li\ et\ al.,2019)} \times 100\%$
0.50°	198.06 s	1209.11 s	16.38 %
1.00°	180.66 s	718.18 s	25.16 %
5.00°	\	311.38 s	\

is much less than that of the method in (Li *et al.*, 2019). Table 3.4 summarizes this information and indicates that the time saved by the proposed method is more than 74%.

Table 3.5 and Table 3.6 show the T_{r_rms} and T_{r_perc} comparison between the proposed method and the method in (Li *et al.*, 2019) at different angle steps. When the angle step is the same at 0.5° or 1.0°, the method in (Li *et al.*, 2019) shows slightly better performance. However, as compared in the above, the time consumed by the proposed method is less than 30%. When the angle step is intentionally increased to 5.0° to reduce the time for the method in (Li *et al.*, 2019), the T_{r_rms} and T_{r_perc} are

Table 3.5: T_{r_rms} Comparison Between the Proposed Method and Method in (Li *et al.*, 2019) with Different Angle Steps.

Angle Step	1000 r/min 8 N·m		3000 r/min 8 N·m	
	Proposed method	Method in (Li *et al.*, 2019)	Proposed method	Method in (Li *et al.*, 2019)
0.50°	0.5258	0.5096	0.5600	0.5601
1.00°	0.5291	0.5152	0.5648	0.5640
5.00°	\	0.6185	\	0.6987

Table 3.6: T_{r_perc} Comparison Between the Proposed Method and Method in (Li *et al.*, 2019) with Different Angle Steps.

Angle Step	1000 r/min 8 N·m		3000 r/min 8 N·m	
	Proposed method	Method in (Li *et al.*, 2019)	Proposed method	Method in (Li *et al.*, 2019)
0.50°	0.3388	0.3400	0.3280	0.3202
1.00°	0.3440	0.3461	0.3493	0.3298
5.00°	\	0.3964	\	0.4757

much higher than that of the proposed method.

Fig. 3.19 and Fig. 3.20 show the Pareto front plot for the proposed method and method in (Li *et al.*, 2019) at 1000 r/min and 3000 r/min when the torque command is 8 N·m. It is observed that the copper losses is inversely proportional to the rms value of torque ripples in these two methods, and higher σ normally implies high copper losses but low T_{r_rms} value. The trade-off can be made by selecting the proper weight parameter. Although the rms value of torque ripples for the proposed method is slightly higher, the time it consumes is 70% less than the method in (Li *et al.*, 2019). Moreover, regarding the peak to peak torque ripple, these two methods show almost the same performance, as shown in Fig. 3.19 and Fig. 3.20. The T_{r_perc} value in this case is 0.3388 for the proposed method and 0.3400 for the method in (Li *et al.*, 2019), respectively.

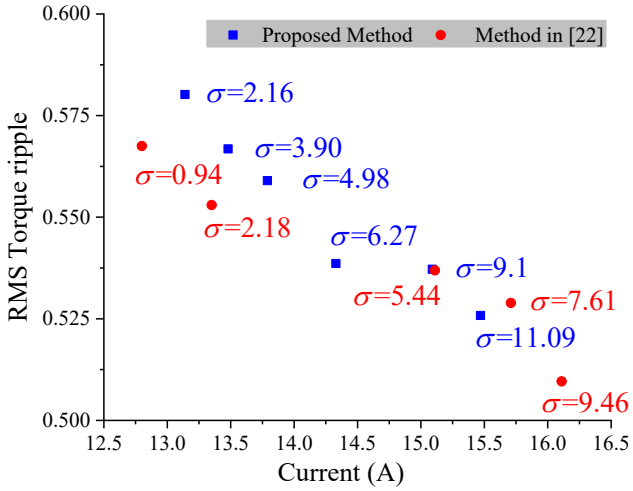

Figure 3.19: Pareto front comparison at 1000 r/min and 8 N·m torque command.(Note: Literature [22] refers to (Li *et al.*, 2019))

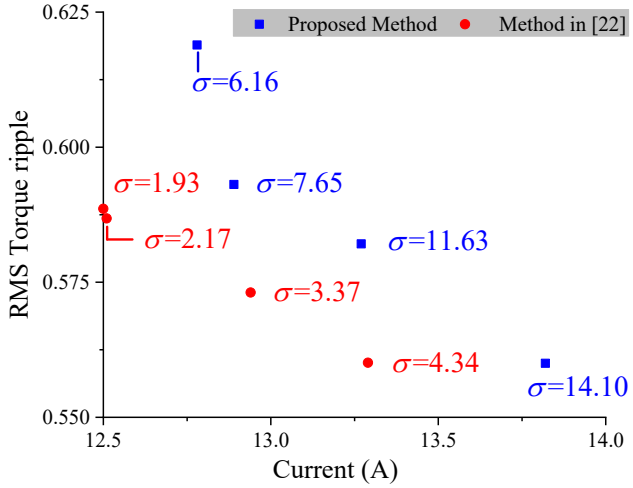

Figure 3.20: Pareto front comparison at 3000 r/min and 8 N·m torque command.(Note: Literature [22] refers to (Li *et al.*, 2019))

3.5 Experimental Verification

Experimental tests were carried out to further verify the effectiveness of the proposed time-efficient torque shaping method. Fig. 3.23 describes the test setup, which is

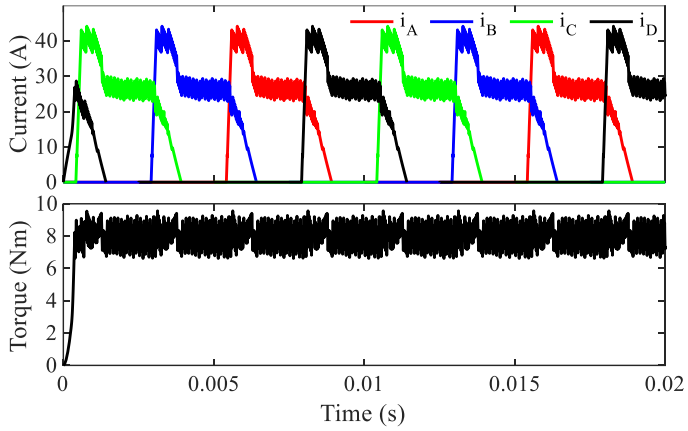

Figure 3.21: Current and torque waveform for the proposed method at 1000 r/min and 8 N·m torque command when σ is 11.09.

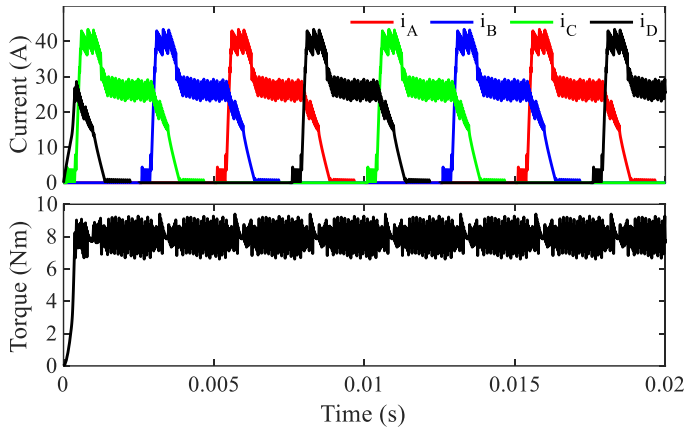

Figure 3.22: Current and torque waveform for the method in (Li *et al.*, 2019) at 1000 r/min and 8 N·m torque command when σ is 9.46.

mainly composed of SRM, SRM controller, induction machine (IM), and IM controller. During the test, the SRM and the IM share the bus voltage 300 V for all the experimental tests, which is the rated voltage for the studied SRM. It is noted that the shaft speed is controlled by the IM. When the SRM is operated with specific current reference, the IM will be served as a generator.

In the SRM controller, the digital signal processor (DSP) TMS320F28335 is used to realize the whole control algorithm. Due to the limited performance of this DSP,

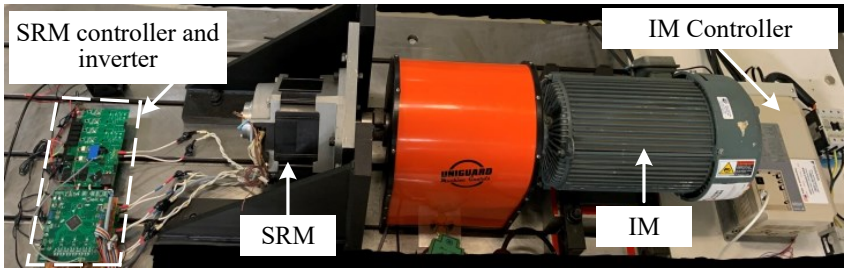

Figure 3.23: Four-phase 8/6 SRM experimental setup.

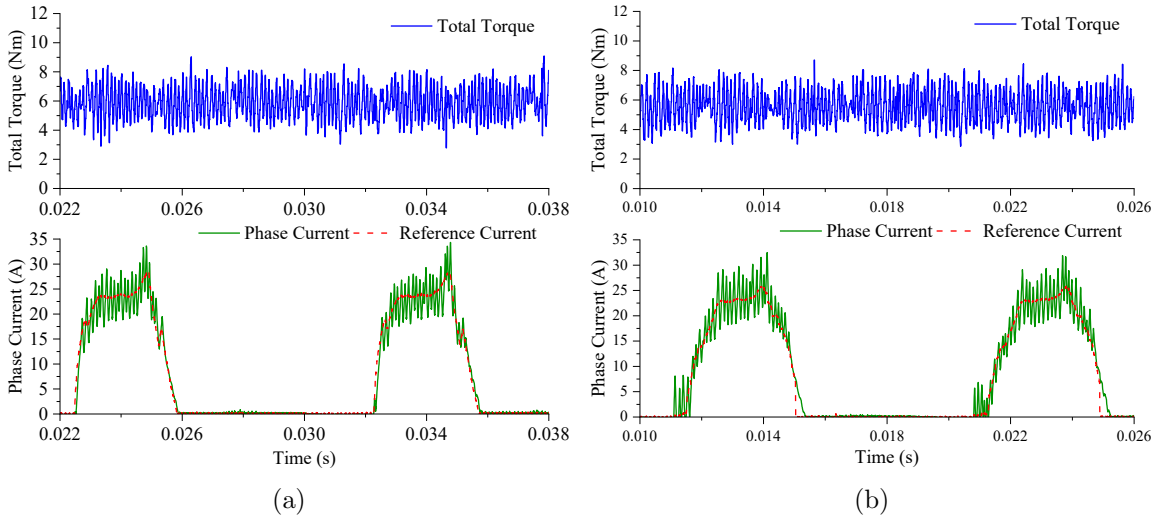

Figure 3.24: Current and torque waveforms at 1000 r/min and 6 N·m torque command (a) for the proposed method when σ is 0.92 and (b) for the method in (Li *et al.*, 2019) when σ is 0.47.

the achievable highest control frequency is 60 kHz, which is set for all the experimental tests.

Fig. 3.24 show the torque and current results at 1000 r/min when the torque command is set at 6 N·m. The instantaneous torque waveform is obtained through the measured SRM characteristics and a 12-bit digital to analog converter. Smooth torque is observed for both methods, and the $T_{r,rms}$ values for the proposed method and the method in (Li *et al.*, 2019) are 1.1431 and 1.1193, respectively. Other performance indicators are listed in Table 3.7. Although the reference current is different, similar

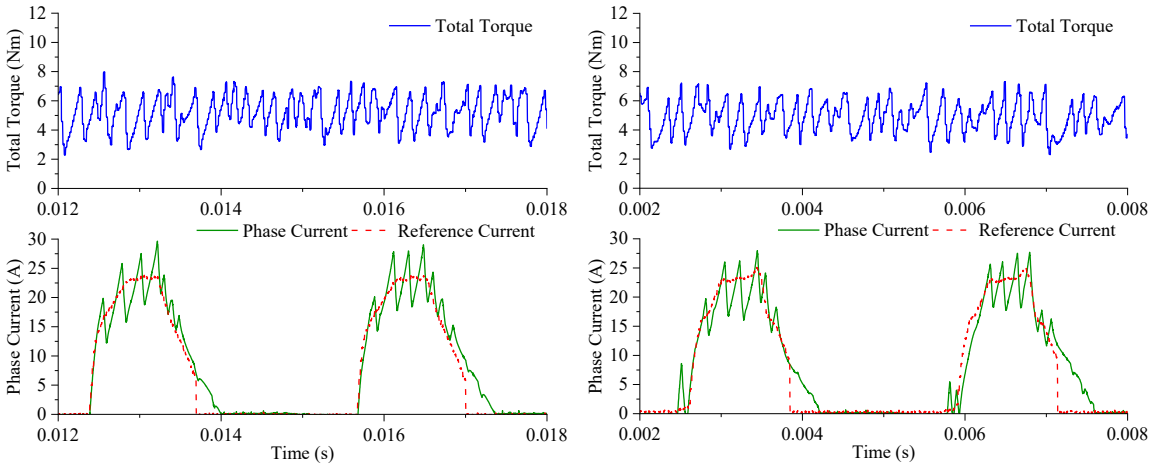

Figure 3.25: Current and torque waveforms at 3000 r/min and 6 N·m torque command (a) for the proposed method when σ is 2.52 and (b) for the method in (Li *et al.*, 2019) when σ is 0.71.

Table 3.7: Performance Comparison Between the Proposed Method and the method in (Li *et al.*, 2019) at 1000 r/min 6 N·m Torque Command.

Method	T_{r_rms}	I_{rms}	T_{avg}
Proposed method	1.1431	12.02	5.89
Method in (Li *et al.*, 2019)	1.1193	12.25	5.57

Table 3.8: Performance Comparison Between the Proposed Method and the method in (Li *et al.*, 2019) at 3000 r/min 6 N·m Torque Command.

Method	T_{r_rms}	I_{rms}	T_{avg}
Proposed method	1.1156	11.11	5.20
Method in (Li *et al.*, 2019)	1.0627	11.44	5.09

performance is achieved. It is noticed again that only 30% time is required for the proposed method.

Fig. 3.25 show the testing results at 3000 r/min, and the related performance is listed in Table 3.8. Not surprisingly, similar performance is achieved in both methods, which proves the generality and effectiveness of the proposed method.

3.6 Conclusion

The torque ripple is one of the main issues preventing the widespread application of SRMs. Normally, an off-line optimization torque shaping technique is adopted to smooth the output torque. Bi-objective optimization is always used to get the proper weight parameter to balance the copper losses and torque ripples. However, enormous time consumption is required caused by the high nonlinearity of the constructed optimization problem if using the nonlinear flux-linkage torque models. To address this problem, the torque mapping which bridges the equivalent linear torque model and nonlinear torque model is studied first in this chapter. Then, the current reference generation part is realized by using the simple linear torque model. After integrated into the bi-objective optimization process, the total consumed time is significantly reduced for the proposed method. Specifically, the proposed method only consumes 30% of the time that the method in (Li *et al.*, 2019) needed. Moreover, the torque quality is kept almost the same with the method in (Li *et al.*, 2019). Extensive simulation and experimental results have verified the effectiveness of the proposed time-efficient TSF method.

Chapter 4

Computational-Efficient Model Predictive Torque Control for SRMs Based on Equivalent Linear SRM Model

4.1 Introduction

The time-efficient TSF method developed in the previous chapter indeed could effectively reduce the torque ripple and optimize the copper losses, but it shows the following drawbacks. Firstly, the derived reference currents at varied operation conditions need to be stored as LUTs in the microcontroller and require a significant amount of storage space. Secondly, the performance of torque ripple reduction, especially the high-frequency torque ripples, heavily depends on the utilized current

controller, which adds complexity to the control system. The MPTC method, which takes advantage of the SRM model, uses a simple scalar function to optimize the command torque tracking error, copper losses, and switching losses. The best voltage vector is calculated online and requires no off-line optimization. Due to these features, the MPTC method becomes attractive for SRM drives.

However, for the existed MPTC methods, due to the inherent high nonlinearity of the SMRs, modeling of SRMs faces issues. The most straightforward way to build such high nonlinear model is by using several LUTs. However, such technique requires a huge number of storage units. Alternatively, analytical expressions such as Fourier series and polynomials can be used, but the computational burden and accuracy might be the problem. Besides, the torque control performance at high-speed range is still challenging for the existed MPTC methods. To ease the above issues, a novel MPTC method is presented in this chapter based on the equivalent linear SRM model and the improved switching table. Firstly, an improved switching table with only 6 switching states is developed based on the inductance characteristics. The adoption of this improved switching table not only reduces the computational burden by 25% but also improves the torque control performance and system efficiency at high-speed region. Secondly, to reduce the requirement on the storage space, the simple linear SRM model is utilized. The flux-linkage and torque transformations are introduced to address the difference between the equivalent linear and nonlinear SRM models. With these transformations, the MPTC method based on the equivalent linear SRM model is realized.

4.2 LUT-Based MPTC with Improved Switching Table

4.2.1 Conventional LUT-Based MPTC

Model accuracy and the applied switching table are two important aspects that affect the performance of the MPTC in the SRM drive system. Since the 2-D flux-linkage $\psi(\theta, i)$, current $i(\psi, \theta)$, and torque $T(\theta, i)$ LUTs not only preserve the accuracy of the SRM model but also possess a low computational burden, the conventional LUT-based MPTC method is studied and investigated first in this chapter.

The flow-chart of the LUT-based MPTC method is shown in Fig. 4.1, along with the illustration for the present and future control period.

From Fig. 4.1, the execution process of the LUT-based MPTC methods can be described as below:

a) The command torque T_{ref} and weight coefficients are sent to the MPTC algorithm. It is noticed that T_{ref} is either set manually or generated from the outer speed loop.

b) The phase current i_k and rotor position information is sampled at the starting instant k of the corresponding control period. With this information, the flux-linkage ψ_k is immediately obtained from the flux-linkage LUT.

c) The flux-linkage ψ_{kp1} which is expected to reach at the end of this control period, namely control instant $k+1$, is predicted based on the previously calculated optimized voltage vector $S_{j,min,k}$ and expression (4.1), where V_{bus}, ΔT and R represent the bus voltage, the control period, and the phase resistance. Then, the current of each phase at the control instant $k+1$ is estimated from the

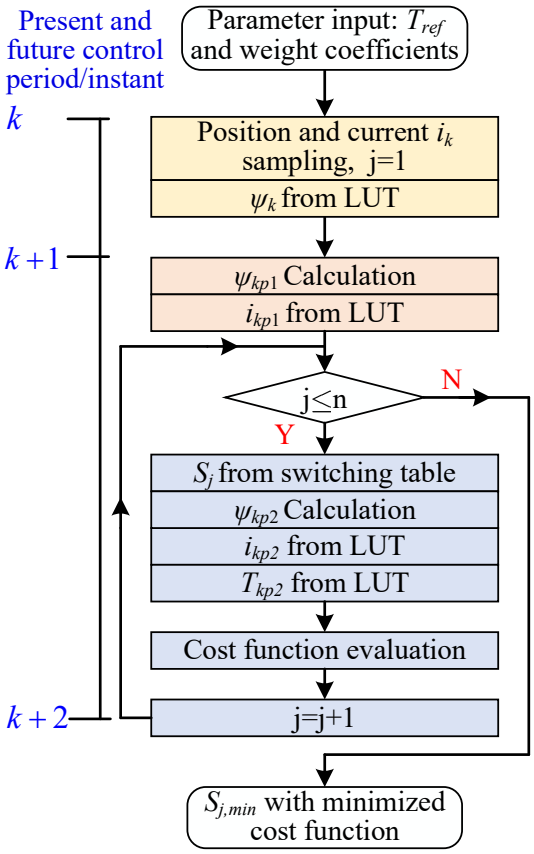

Figure 4.1: Flow-chart for LUT-based MPTC method.

current LUT $i(\psi, \theta)$ based on the predicted ψ_{kp1}.

$$\psi_{kp1} = S_{i,min,k} \times V_{bus} \times \Delta T - Ri_k + \psi_k \tag{4.1}$$

d) Search for the optimum voltage vector through the exhaustive execution of the voltage vectors in the switching table based on the predicted ψ_{kp1}, i_{kp1}, i_{kp2}, and T_{kp2}. It is noticed that the phase current i_{kp2} and torque T_{kp2} are estimated with the aid of the voltage vector and LUTs. The cost function is constructed as (4.2), where ω_1 represents the weight factor for the sum of the squared phase current and the function $g(i_{kp2})$ is employed to ensure the phase current below the maximum value i_{MAX}. The trade-off between torque ripple performance

Table 4.1: Conventional switching table derived from (Peyrl *et al.*, 2009) for 8/6 SRM

Switching State	Position θ_A	Phase A	Phase B	Phase C	Phase D
Region 1	$[0°, 15°]$	1, 0, -1	-1	-1	1, 0, -1
Region 2	$[15°, 30°]$	1, 0, -1	1, 0, -1	-1	-1
Region 3	$[30°, 45°]$	-1	1, 0, -1	1, 0, -1	-1
Region 4	$[45°, 60°]$	-1	-1	1, 0, -1	1, 0, -1

and copper losses can be realized by adjusting the weigh factor ω_1.

$$J = (T_{ref} - \sum T_{kp2})^2 + \omega_1 \sum (i_{kp2})^2 + g(i_{kp2})$$
$$g(i(k)) = \begin{cases} \infty, & \text{if } i_k \geq i_{MAX} \\ 0, & \text{if } i_k < i_{MAX} \end{cases} \tag{4.2}$$

From the above execution process description, it is observed that for an m-phase SRM with n voltage vectors, the total number of times for calling the LUT is $N_{LUT} = m \times (2n+2)$ and the total number of times for flux-linkage calculation is $N_{\psi,ca} = m \times (n+1)$. Apparently, the execution time of the MPTC method in the microcontroller is proportional to the number of the voltage vectors. For the studied four-phase 8/6 SRM, the number of the total voltage vectors is $n = 3^4 = 81$ given the prediction horizon is 1. Obviously, the execution time of the MPTC method would be extremely long if the total number of voltage vectors is not reduced appropriately.

The total number of the voltage vectors can be significantly reduced if follow the switching restrictions presented in (Peyrl *et al.*, 2009). Table 4.1 shows the voltage vectors of the studied four-phase 8/6 SRM by applying rules shown in (Peyrl *et al.*, 2009). The switching state "1", "0", and "-1" represent the magnetization mode, freewheeling mode, and demagnetization mode of the widely employed asymmetrical half bridge inverter. It is found that there are 9 voltage vectors in Table 4.1. In this

thesis, the MPTC algorithm that adopts the switching table shown in Table 4.1 and corresponding LUTs is referred to as the conventional LUT-based MPTC.

4.2.2 Improved LUT-Based MPTC

Although the total number of the voltage vectors is significantly reduced in the above conventional LUT-based MPTC, there is still potential to further reduce it so the execution time could be further reduced. Besides, as reported in Tarvirdilu-Asl *et al.* (2019), the negative torque at high-speed operation conditions is an issue for the conventional LUT-based MPTC. This negative torque is mainly caused from the following two reasons: (a) Each phase can conduct in the whole positive torque region, so a significant amount of current will probably be held near the aligned position; (b) The absolute value of the current decreasing rate after the aligned position is lower at the high-speed range compared to that at the low-speed range. The generated negative torque not only increases the torque ripple but also reduces the system efficiency. To address these two issues, an improved switching table is proposed in this chapter according to the characteristics of the SRM inductance profile.

Fig. 4.2 shows the ideal inductance profile of the studied 8/6 SRM, where θ_u indicates the unaligned position, θ_a represents the aligned position, and θ_{op} is the position where the rotor pole just overlaps with the stator pole. In an electric period, 8 regions can be divided based on these angles. And the voltage vectors in each region can be developed according to the characteristics of the inductance profile.

Taking region 1 as an example, the phase A position θ_A lies between θ_u and θ_{op}. To avoid negative torque generation, phase B and C are demagnetized ("-1"). Because phase A is close to the unaligned position, the derivative of inductance is low. Hence,

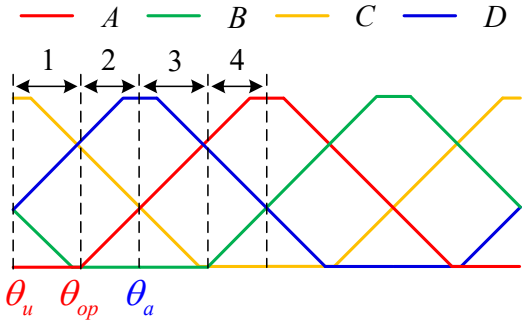

Figure 4.2: Region illustration for the improved switching table.

it is reasonable to set its switching states as "1" and "0" to build the current. As for phase D, the derivative of its inductance is in the high-value region, so the majority of total torque is generated by this phase, and the switching states are set as "1", "0", and "-1".

In region 2, the phase-A position θ_A is between θ_{op} and 15°. It is noted the 15° is the stroke angle for the 8/6 SRM. At this region, although phase D is near the aligned position, the inductance derivative is still large around the first half of this region. In this case, to fully utilize this phase, the switching state is set to "0" and "-1" at the low-speed region. When the rotor speed ω_r is high, its switching state is only set to "-1" to demagnetize as soon as possible to avoid generating the negative torque. The switching speed ω_t can be determined at the speed when there is negative torque generation for "0" and "-1" switching states. The switching states for phase A are set to "-1","0", and "1" owing to its derivative of inductance is relatively high in this region.

The switching states of phase A and phase B in regions 3 and 4 are repeated in a similar pattern as phase D and phase A in regions 1 and 2. It is noted that regions 5 to 8 are not shown in Fig. 4.2 but the switching states are repeated in the similar manner as that in regions 1 to 4. The detailed switching states at each

Table 4.2: Proposed improved switching table for 8/6 SRM

Switching State	Position θ_A	Phase A	Phase B	Phase C	Phase D
Region 1	$[0°, \theta_{op}]$	1, 0	-1	-1	1, 0, -1
Region 2 ($\omega_r < \omega_t$)	$[\theta_{op}, 15°]$	1, 0, -1	-1	-1	-1, 0
Region 2 ($\omega_r \geq \omega_t$)	$[\theta_{op}, 15°]$	1, 0, -1	-1	-1	-1
Region 3	$[15°, 15° + \theta_{op}]$	1, 0, -1	1, 0	-1	-1
Region 4 ($\omega_r < \omega_t$)	$[15° + \theta_{op}, 30°]$	-1, 0	1, 0, -1	-1	-1
Region 4 ($\omega_r \geq \omega_t$)	$[15° + \theta_{op}, 30°]$	-1	1, 0, -1	-1	-1
Region 5	$[30°, 30° + \theta_{op}]$	-1	1, 0, -1	1, 0	-1
Region 6 ($\omega_r < \omega_t$)	$[30° + \theta_{op}, 45°]$	-1	-1, 0	1, 0, -1	-1
Region 6 ($\omega_r \geq \omega_t$)	$[30° + \theta_{op}, 45°]$	-1	-1	1, 0, -1	-1
Region 7	$[45°, 45° + \theta_{op}]$	-1	-1	1, 0, -1	1, 0
Region 8 ($\omega_r < \omega_t$)	$[45° + \theta_{op}, 60°]$	-1	-1	-1, 0	1, 0, -1
Region 8 ($\omega_r \geq \omega_t$)	$[45° + \theta_{op}, 60°]$	-1	-1	-1	1, 0, -1

region are listed in Table 4.2. It is observed that there are only up to 6 voltage vectors in this improved switching table. Obviously, the computational burden on the microcontroller is reduced compared to 9 voltage vectors in (Peyrl *et al.*, 2009) and (Li *et al.*, 2017). Besides, since the phase is forced to turn-off at $15° + \theta_1$ when the speed is high, the negative torque is eliminated.

The LUT-based MPTC, which adopts the above-proposed switching table, is referred to as the improved LUT-based MPTC. Although the execution time is reduced

and the negative torque is eliminated by this improved MPTC, the enormous consumption of the storage space poses the main issue since it employs three 2-D LUTs. And this is a common issue for the LUT-based MPTC methods. To ease this problem, the MPTC implemented on equivalent linear SRM model is proposed in the following section.

4.3 Proposed Linear-Model Based MPTC

The simple linear SRM model is an ideal model to implement control algorithms such as MPTC, but the issue raised by the inherent high nonlinearity of the SRM has to be well addressed. In this section, an equivalent linear SRM model with transformations is developed first. Then, the MPTC algorithm based on the equivalent linear SRM model is introduced.

4.3.1 Equivalent Linear SRM Model with Transformations

Flux-linkage and torque characteristics are the two most important features for SRM, which basically determine the voltage input and torque output for SRM. If the relationship of flux-linkage and torque between linear and nonlinear SRM models is developed, the linear SRM model and these transformations can be viewed as the equivalent linear model for the nonlinear SRM model.

Fig. 4.3 shows the flux-linkage at a certain position for a nonlinear SRM (the red curve) and its corresponding linear SRM (the blue curve). It is observed that the flux-linkage for the linear SRM and nonlinear SRM have the same value when the current is smaller than the saturation point I_s, but the flux-linkage of the linear SRM

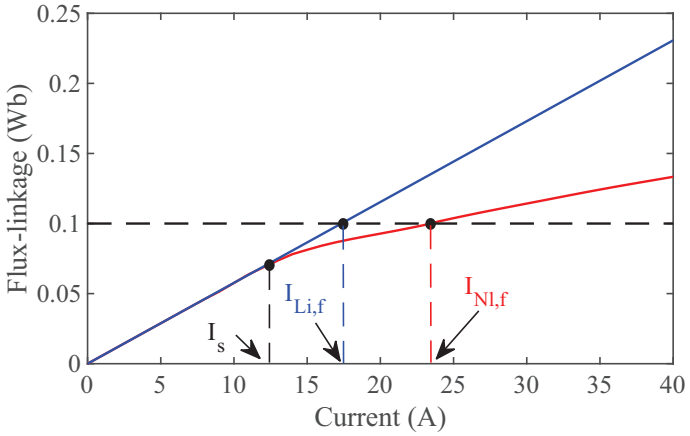

Figure 4.3: Flux-linkage for a linear and nonlinear SRM at a certain position.

shows a higher value compared to that of the nonlinear SRM when the current is higher than I_s. Apparently, such a difference is resulted from the saturation in the nonlinear SRM. The target of the flux-linkage transformation is to find the current $I_{Li,f}$ for linear SRM and the current $I_{Nl,f}$ for nonlinear SRM, which have the same flux-linkage value. The complete transformation can be easily obtained from the flux-linkage curves of the linear and nonlinear SRM, but it might be possible to represent this transformation only with a limited number of mapping lines so the storage space will be saved. To achieve this goal, it is beneficial to study the features of these mapping lines.

The features of the flux-linkage transformation mapping lines can simply be checked by the mapped linear current value $I^{\theta}_{Li,f}$ at the maximum nonlinear current value $I^{max}_{Nl,f}$. Fig. 4.4 (a) shows the flux-linkage curves at two certain positions θ_{m1} and θ_{m2} for a nonlinear SRM and its corresponding linear SRM. When the nonlinear current $I_{Nl,f}$ is larger than I_s, the flux-linkage curves at all the positions for the nonlinear SRM are approximated by straight lines with slope L_s (Ahmad and Narayanan, 2016). In this case, the mapped linear current $I_{Li,f}$ can be calculated as (4.3), where the $L_{Li}(\theta)$

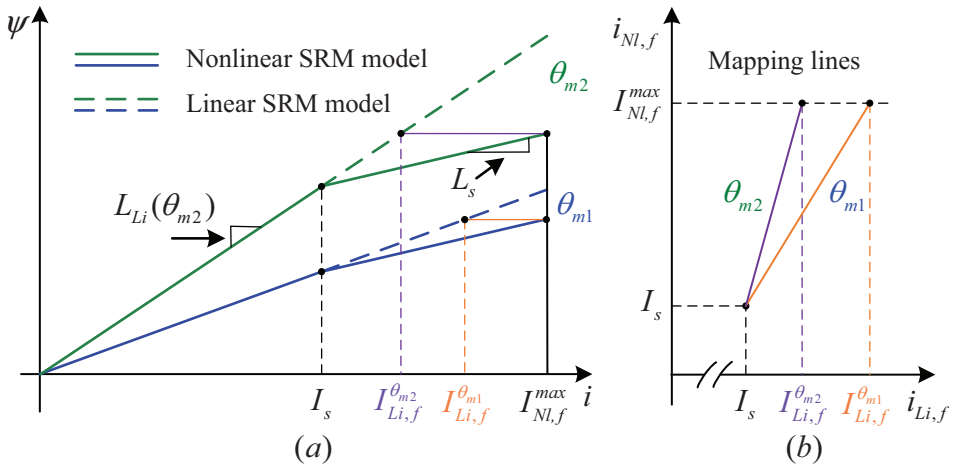

Figure 4.4: (a) Flux-linkage transforming at two certain positions when $I_{Nl,f}$ value reaches the maximum and (b) Simplified mapping lines at two positions.

represents the linear inductance.

$$I_{Li,f} = I_s + \frac{(I_{Nl,f} - I_s)L_s}{L_{Li}(\theta)} \qquad (I_{Nl,f} > I_s) \tag{4.3}$$

Apparently, when the nonlinear current reaches the maximum value $I^{max}_{Nl,f}$, the mapped linear current is:

$$I^{\theta}_{Li,f} = I_s + \frac{(I^{max}_{Nl,f} - I_s)L_s}{L_{Li}(\theta)} \tag{4.4}$$

Fig. 4.4 (a) shows the $I^{\theta}_{Li,f}$ for two positions θ_{m1} and θ_{m2}. Since each mapping line is a monotonous continuous curve and the $I_{Li,f}$ equals $I_{Nl,f}$ at I_s, the mapping lines can roughly be estimated as the straight line between the point (I_s, I_s) and point ($I^{\theta}_{Li,f}$, $I^{max}_{Nl,f}$), as shown in Fig. 4.4 (b). It is observed that the larger difference between $I^{\theta_{m1}}_{Li,f}$ and $I^{\theta_{m2}}_{Li,f}$ shown in Fig. 4.4 (b) indicates the mapping lines need to be stored in a smaller angle interval to accurately store the flux-linkage transformation. Hence, with this observation and the fact that the $I^{\theta}_{Li,f}$ value only varies with $1/L_{Li}(\theta)$ (from (4.4)), the $1/L_{Li}(\theta)$ curve can be used to provide some guidance on the angle interval

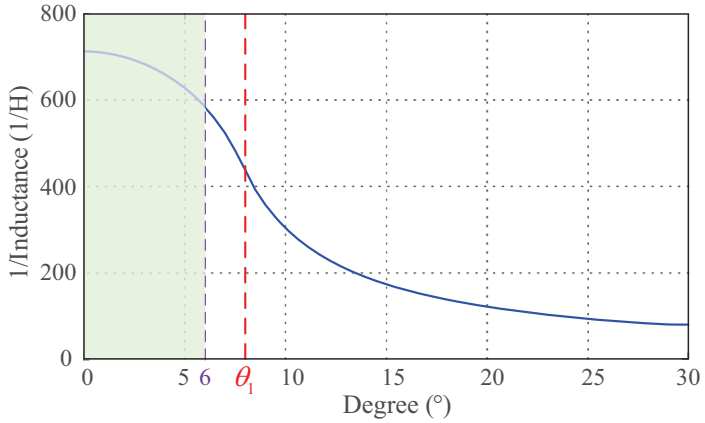

Figure 4.5: The $1/L_{Li}(\theta)$ curve for the studied 8/6 SRM.

of the mapping lines to store the flux-linkage transformation.

Fig. 4.5 shows the $1/L_{Li}(\theta)$ profile for the studied 8/6 SRM. In the region where the rotor position is smaller than 6°, considering the fact that θ_{op} is 8°, the mapping lines can be regarded as straight lines with slope 1 due to the unsaturated magnetic circuit. Therefore, the $1/L_{Li}(\theta)$ curve at that region is covered with green colour. At around θ_{op}, it is clearly observed that there is a steep variation, which means the $I^{\theta}_{Li,f}$ value significantly varies with the angle. Besides, the mapping lines will undergo a transition from the straight line with slope 1 to the straight line with a larger slope. Based on the above two reasons, the mapping lines around θ_1 need to be stored in a small angle interval. Starting around the middle of 10° and 15°, the $1/L_{Li}(\theta)$ curve drops close to a linear manner, so the mapping lines at this region can be stored in a relatively larger angle interval. It is noted that the above features are universal for SRM since these features are derived from the most basic linear inductance curve $L_{Li}(\theta)$.

Fig. 4.6 shows the mapping lines from linear SRM to the nonlinear SRM. It is noted that these mapping lines start from 6° and end at 29° with 1° interval. The

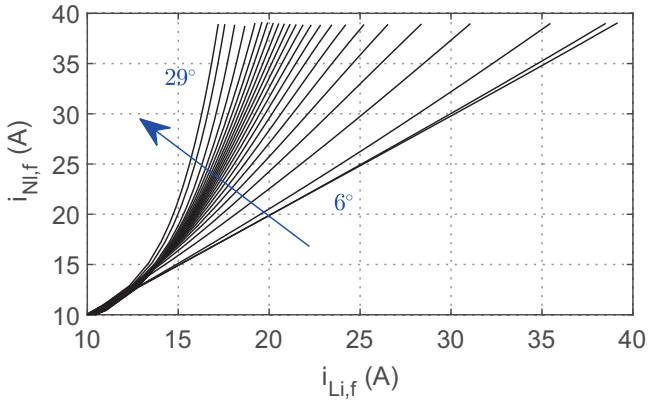

Figure 4.6: Flux-linkage mapping lines from linear SRM to nonlinear SRM.

features that described above can be clearly seen in this plot, which verifies the above analysis. Based on the features of the flux-linkage mapping lines, the mapping lines of the flux-linkage between linear and nonlinear SRM at 7°, 8°, 9°, 10°, 11°, 12°, 15°, 18°, 21°, 24°, 27°, 29° constitutes the flux-linkage transformation for the studied SRM. Notably, when the sampled current is smaller than I_s or the rotor position is smaller than 6°, the linear current is the same with the nonlinear current since the magnetic circuit is not saturated. If the rotor angle is larger than 6° and the mapping coefficients are not provided, linear interpolation method is used to estimate the mapping coefficients. To store this information in the microprocessor, these mapping lines can be expressed as fourth-order polynomials.

Fig. 4.7 shows the actual mapping lines and its polynomial representations at θ_u, θ_{op}, θ_{hr}, and 29° for the studied SRM, where θ_{hr} is half way between θ_a and θ_{op}. The left figure shows the transformation from linear SRM to nonlinear SRM while the right figure shows the transformation from nonlinear SRM to linear SRM. Notably, the transformations indicated by the black solid mapping lines are obtained directly from the measured data and the transformations represented by the red circles are

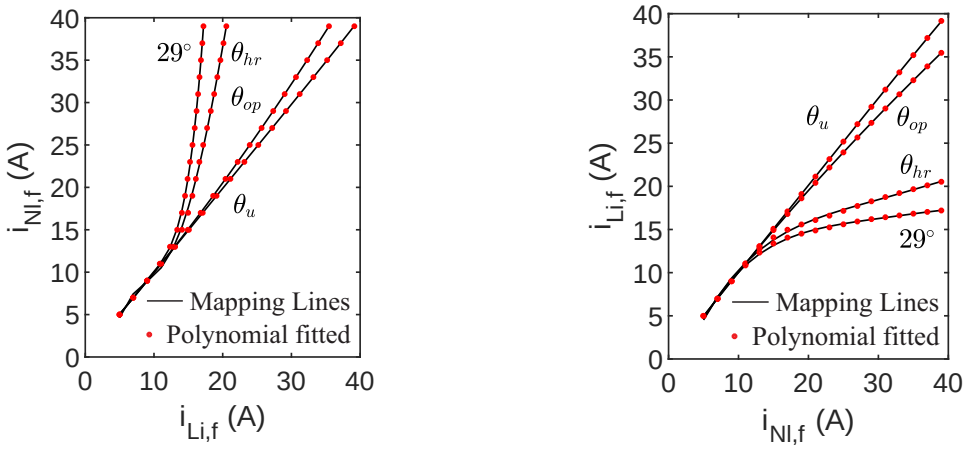

Figure 4.7: (a) Flux-linkage transformation from nonlinear SRM to linear SRM and (b) Flux-linkage transformation from nonlinear SRM to linear SRM.

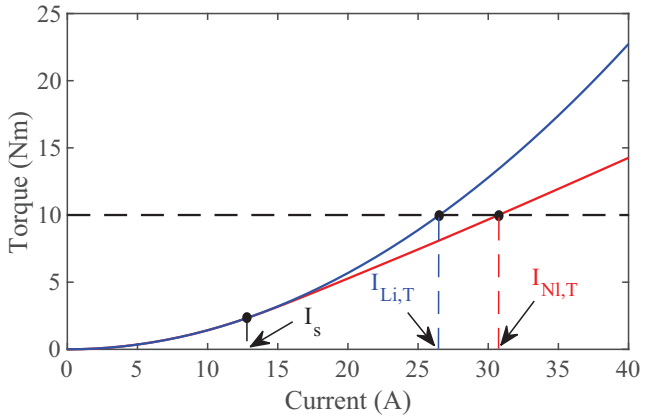

Figure 4.8: Torque for a linear and nonlinear SRM at a certain position.

the approximated transformations by the fourth-order polynomials. Good matches between the actual mapping relationship and fitted ones can be found. The torque mapping between the linear SRM and nonlinear SRM can be obtained in the similar approach.

Fig. 4.8 shows the torque for a nonlinear SRM (red curve) and the corresponding linear SRM (blue curve) at a certain position. For the linear SRM, the torque is

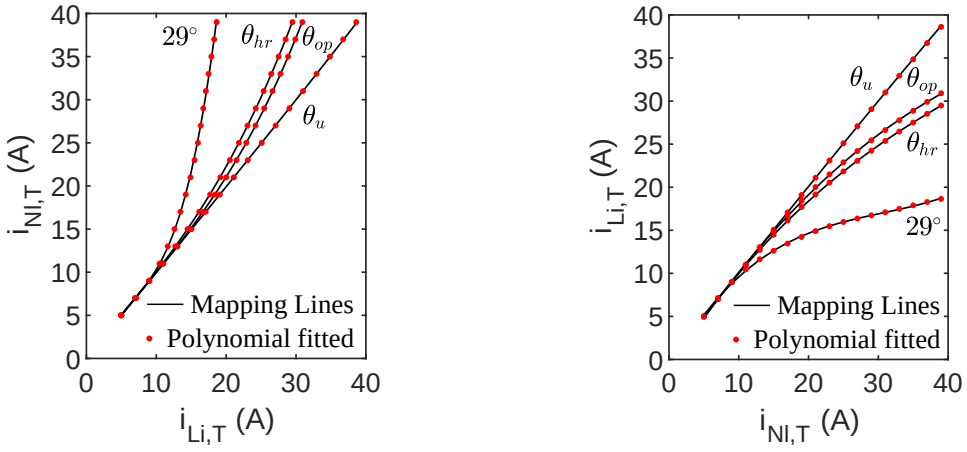

Figure 4.9: (a) Torque transformation from linear SRM to nonlinear SRM and (b) Torque transformation from nonlinear SRM to linear SRM.

proportional to the square of its current. However, for the nonlinear SRM, the torque is proportional to the square of its current when the current is smaller than I_s but only approximately proportional to the current when the current is higher than I_s (Fang *et al.*, 2021b). Therefore, the torque difference is obvious after I_s. The target of the torque mapping is to find the relationship between the current $I_{Li,T}$ for linear SRM and $I_{Nl,T}$ for nonlinear SRM which have the same torque value.

Apparently, the complete torque mapping can be obtained from the torque characteristics of linear and nonlinear SRM. The torque mapping lines at the same angles as that used in the flux-linkage transformation are employed to construct the torque transformation. Fig. 4.9 shows the typical torque mapping curves at θ_u, θ_{op}, θ_{hr}, and 29° for the studied SRM. The figure on the left shows the torque transformation from linear SRM to nonlinear SRM while the figure on the right shows the transformation from nonlinear SRM to linear SRM. It is noticed that the solid black curves represent the actual transformation from measured torque LUT while the red circles indicate

the transformation from the third-order polynomials. Good matches can be observed between the actual and fitted transformations.

Once the flux-linkage and torque transformation between the nonlinear and linear SRM are developed, the equivalent linear model for the nonlinear SRM can be expressed as the following set of equations:

$$i_{Li,f} = f^{f}_{Nl2Li}(i_{Nl}, \theta) \tag{4.5}$$

$$v = Ri_{Nl,f} + L_{Li}\frac{di_{Li,f}}{dt} + i_{Li,f}\omega_r\frac{dL_{Li}}{d\theta} \tag{4.6}$$

$$i_{Li,T} = f^{T}_{Nl2Li}(i_{Nl}, \theta) \tag{4.7}$$

$$T_e = \frac{1}{2}\frac{dL_{Li}}{d\theta}i^2_{Li,T} \tag{4.8}$$

where f^{f}_{Nl2Li} is the transformation from nonlinear SRM to the linear SRM with equal flux-linkage, i_{Nl} is the actual sampled current, L_{Li} is the unsaturated inductance, ω_r is the rotor speed, θ is the rotor position, f^{T}_{Nl2Li} is the transformation from nonlinear SRM to the linear SRM with equal torque, and T_e is the electromagnetic torque. Regarding (4.6), in the real application, if the nonlinear current $i_{Nl,f}$ is not available, the linear current $i_{Li,f}$ is used for the resistance drop term since this voltage error caused by the current difference between $i_{Nl,f}$ and $i_{Li,f}$ is acceptable. The constructed equivalent linear SRM model is utilized to implement MPTC method.

4.3.2 Linear-Model-Based MPTC

With the above developed equivalent linear SRM model, the MPTC method based on this linear model is proposed. Fig. 4.10 shows the flow-chart of the proposed MPTC method. In order to clearly identify the proposed method in the following section,

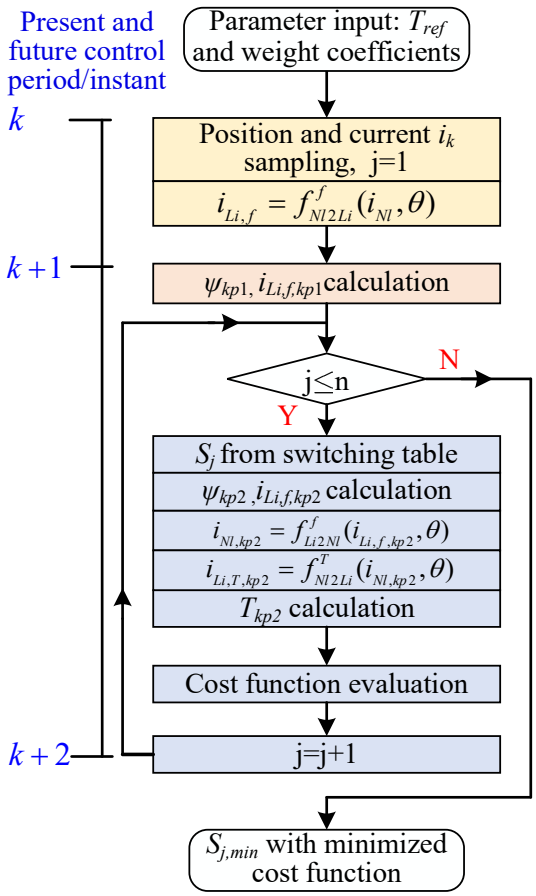

Figure 4.10: Flow chart of the proposed linear-space-based MPTC method.

the method shown in Fig. 4.10 refers to linear-model-based MPTC. The execution process of this method can be described below:

a) The command torque T_{ref} and weight coefficients are sent to the algorithm.

b) The instantaneous position and current $i_{Nl,k}$ are collected at the beginning instant k of the control period. Then, the sampled current $i_{Nl,k}$ is converted to $i_{Li,f,k}$ with the flux-linkage transformation from nonlinear SRM to linear SRM. The flux-linkage at k instant can be immediately obtained with the information of unsaturated inductance $L_{Li,k}$. Since the unsaturated inductance value only relies on the rotor position, this information is only required once for each phase

during one control period and it is obtained via the prestored 1-dimension (1-D) LUT.

c) The flux-linkage which is expected to reach at the instant $k+1$ is estimated from (4.9). Apparently, the linear current $i_{Li,f,kp1}$ can be easily calculated with the linear inductance information.

$$\psi_{kp1} = S_{min,k} \times V_{bus} \times \Delta T - Ri_{Li,f,k} + \psi_k \tag{4.9}$$

d) Search for the best voltage vector S_{min} with minimized cost function by exhaustive execution of all the voltage vectors in the proposed improved switching table. Firstly, the flux-linkage excited by different switching states at $k+2$ instant are estimated in a similar manner as (4.9). And the current $i_{Li,f,kp2}$ is directly calculated from the flux-linkage and linear inductance. Secondly, the linear current $i_{Li,f,kp2}$ is converted back to the nonlinear current through the flux-linkage transformation from linear SRM to the nonlinear SRM. Then, the predicted nonlinear current $i_{Nl,f,kp2}$ is converted to the linear current through the torque transformation from nonlinear SRM to linear SRM, so the torque can be calculated by the simple equation (4.8). The cost function for this method is the same as (4.2).

Comparing the conventional LUT-based method, improved LUT-based method, and proposed linear-model-based MPTC method, the main differences are summarized as below:

a) The LUT-based method requires three 2-D LUTs, which are flux-linkage LUT $\psi(\theta, i)$, torque LUT $T(\theta, i)$, and current LUT $i(\psi, \theta)$. During the exhaustive searching step between $k+1$ and $k+2$ instant, each phase needs to call torque and current LUT for each voltage vector.

b) The conventional LUT-based MPTC method needs to evaluate 9 voltage vectors at every control period while the improved LUT-based MPTC method and linear-model-based MPTC method only evaluate 6 voltage vectors at each control period.

c) The improved LUT-based method and linear-model-based MPTC method could reduce the negative torque and improve system efficiency at high speed operation conditions.

d) The proposed linear-model-based MPTC requires three transformations, but these transformations can be represented as several simple polynomials. In this case, the storage space will be saved since the coefficients for these polynomials only occupies a limited number of storage space. In the searching step between $k+1$ and $k+2$ instant, two transformations are needed for each phase on each switching state. And these transformations are represented as third- and fourth- order polynomials.

The torque control performance, efficiency, execution time, and required storage space for the above three methods will be further studied in the experimental section.

4.4 Experimental Validation

To verify the effectiveness of the proposed linear-model-based MPTC, experimental tests are conducted at different operation conditions on the four-phase 8/6 SRM setup. To clearly identify the above mentioned three methods, Table 4.3 shows the utilized switching table and SRM model for these methods. For concise expression, the following text may use the convention method, improved method, and linear method to represent the conventional LUT-base method, improved LUT-based method, and

Table 4.3: The employed switching table and SRM model for the three methods

Method	Switching table	SRM model
Conventional LUT-based Method	Conventional	Nonlinear
Improved LUT-based Method	Improved	Nonlinear
Linear-model-based MPTC	Improved	Linear

linear-model-based method, respectively. Fig. 3.23 shows the employed setup, which is mainly composed of the induction machine (IM), IM controller, SRM and SRM controller. During the experimental tests, IM serves as a load generator and the torque on the shaft is provided by the SRM. The rated power, rated torque, and rated speed for the studied SRM are 5.1 kW, 8 N·m, and 6000 r/min, respectively. For all the testing results shown below, the applied voltage is 300 volts, which is the rated value for the studied SRM. It is noted all the MPTC algorithm is implemented on the TSM320F28335 digital signal processor (DSP).

4.4.1 Execution Time and Storage Space Comparison

Because the torque control performance is related to the control frequency, the execution time for the three methods are measured and compared first. Table 4.4 shows the measured execution time for each MPTC method. It is noticed that this amount of time only considers the MPTC algorithm. The basic functions such as position and current sampling are not taken into account here.

From Table 4.4, it is found the improved method and linear method consume less time compared with the conventional method. Specifically, the improved method consumes 39.2 μs, the proposed linear method requires 37.76 μs, and the conventional method consumes 52.64 μs. Hence, the time saved by the proposed method is more

Table 4.4: MPTC Time Consumption Comparison

Method	Execution time
Conventional LUT-based Method	52.64 μs
Improved LUT-based Method	39.20 μs
Linear-space-based MTPC	37.76 μs

than 25% compared with the conventional method. Because the maximum control frequency for the conventional method is around 15 kHz, for fair comparison, all the experimental results for the three methods shown below are carried out at 15 kHz control frequency.

The storage space is another important aspect when implementing the control algorithm in the microcontroller. For the proposed linear method, it requires three transformations, which are flux-linkage transformations from linear model to nonlinear model f^f_{Li2Nl}, flux-linkage transformations from nonlinear model to linear model f^f_{Nl2Li}, and torque transformations from nonlinear model to linear model f^T_{Nl2Li}.

Regarding the storage space, the transformation f^f_{Li2Nl} and f^f_{Nl2Li} are represented by fourth-order polynomials, so these two transformations require two 5×12 LUTs. And the transformation f^T_{Nl2Li} is represented by the third-order polynomials, so it requires one 4×12 LUT. It is observed that these transformations are all represented by small-size 2-D LUTs. The other two utilized 1-D LUTs are the linear inductance derivative respect to position LUT $dL_{Li}/d\theta$ and linear inductance LUT $L_{Li}(\theta)$, which are both stored in 1×30 form with 1° step. The above five small-size LUTs consume 228 storage units in total and could be used to accurately represent the nonlinear behavior of SRM and perform torque control such as MPTC.

On the other hand, if the MPTC adopts the nonlinear SRM model, three 2-D LUTs

are required. These three 2-D LUTs are torque characteristics $T(i,\theta)$, flux-linkage characteristics $\lambda(i,\theta)$, and inverse flux-linkage characteristics $i(\lambda,\theta)$. Normally, these 2-D LUTs are stored in an equal position and current step interval. If the 2-D LUTs with unequal position and current steps are utilized, the consumed storage space indeed will be reduced. However, the time to call these LUTs inevitably increases due to more complex index calculation method so the total time of the toque control method becomes longer. Therefore, equal position and current steps are adopted for the conventional method and improved method.

To accurately store the 2-D LUTs for the studied 8/6 SRM, the position step is set 1°, and the current step is set 2.5 A. The reasons for selecting these two steps are: (a) The inductance changes steeply near θ_{op}, so the flux-linkage will also change steeply in this region. Therefore, 1° position interval is used to accurately store these information; (b) The flux-linkage normally varies in a highly nonlinear way near the saturation point I_s. To accurately capture these variations, the 2.5 A step is employed. Based on the above reasons, the 2-D LUT has a dimension of 17×30 under 40 A phase current limit. Hence, the total storage units consumed for the conventional method and improved method are 1530.

Based on the above discussion, it is observed the proposed linear-model-based method consumes much less storage units to store the full nonlinear behaviour compared with the nonlinear-model-based method. And Table 4.5 summarized the detailed consumed storage space for the three mentioned methods.

Table 4.5: Storage Space Consumption Comparison

Method	Storage space consumption
Conventional LUT-based Method	2-D $T(i,\theta)$ LUT: 17×30
	2-D $i(\lambda,\theta)$ LUT: 17×30
	2-D $\lambda(i,\theta)$ LUT: 17×30
Improved LUT-based Method	2-D $T(i,\theta)$ LUT: 17×30
	2-D $i(\lambda,\theta)$ LUT: 17×30
	2-D $\lambda(i,\theta)$ LUT: 17×30
Linear-model-based MPTC	1-D $dL_{Li}/d\theta$ LUT: 1×30
	1-D $L_{Li}(\theta)$ LUT: 1×30
	f^f_{Nl2Li} coefficients: 5×12
	f^f_{Li2Nl} coefficients: 5×12
	f^T_{Nl2Li} coefficients: 4×12

4.4.2 Torque Control Performance Comparison

Fig. 4.11 shows the total instantaneous torque, one-phase instantaneous torque and two-phase current waveforms for the conventional method, improved method, and proposed linear-model-based method at 100 r/min and 8 N·m operating conditions. It is noted that the switching speed ω_t is around 3000 r/min for the studied 8/6 SRM. Because the employed oscilloscope only has four channels, only two phase currents are captured. It is noted that the weight factor ω_1 is set at 0.003 for all the three methods and this value is tuned manually according to the method in (Rodriguez and Cortes, 2012).

From the presented torque waveform, it is observed that all the methods effectively eliminate the commutation torque ripple and this commutation torque ripple is one of the main drawbacks for SRM. As for the current waveforms, the improved method and the linear-model-based method show higher peak value but fewer chopping actions compared to the conventional method.

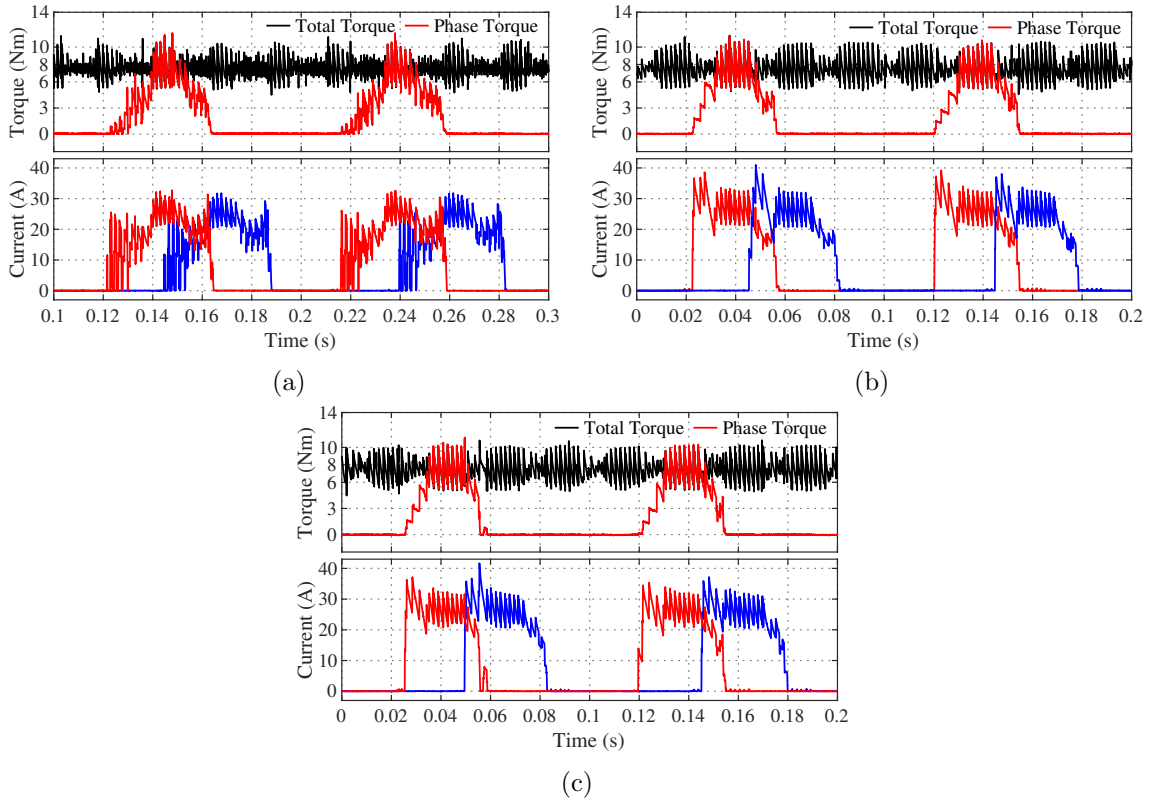

Figure 4.11: Torque and current waveforms for (a) conventional LUT-based method, (b) improved LUT-based method, and (c) proposed linear-model-based method at 100 r/min and 8 N·m operating conditions.

In order to better compare the torque control performance of the three methods, the rms value of the torque ripple $T_{r,rms}$, rms value of the phase current I_{rms}, peak to peak torque ripple $T_{r,p}$, and system efficiency η are evaluated. The definition of $T_{r,p}$, $T_{r,rms}$, and I_{rms} are shown as (4.10), (4.11), and (4.12), where T_{ave}, T_{max}, and T_{min} are the average torque, maximum instantaneous total torque, and minimum instantaneous total torque. Due to the switching instant is automatically defined by the MPTC algorithm, it is hard to obtain the exact turn-on and turn-off angles for these three methods. In this case, the $T_{r,rms}$ and I_{rms} values are quantified during a testing period between t_1 and t_2. For example, the t_1 is 0.1 and t_2 is 0.3 for the result

Table 4.6: Control performance comparison at 100 r/min and 8 N·m operating condition

Method	Conventional	Improved	Linear
$T_{r,p}$	0.9301	0.9017	0.8774
$T_{r,RMS}$	0.9514	1.1794	1.1749
T_{ave}(Nm)	7.5376	7.3972	7.4954
I_{RMS}(A)	13.1688	14.0821	14.1600
f_{sw}(kHz)	2.2265	1.7042	1.6441
η(%)	24.27	23.91	23.92

shown in Fig. 4.11 (a). For fair comparison, the I_{rms} value is the average rms value of the captured two phase current.

$$T_{r,p} = \frac{T_{max} - T_{min}}{T_{ave}} \tag{4.10}$$

$$T_{r,rms} = \sqrt{\int_{t_1}^{t_2} \frac{1}{t_2 - t_1}(T_{total} - T_{ave})^2 dt} \tag{4.11}$$

$$I_{rms} = \sqrt{\int_{t_1}^{t_2} \frac{1}{t_2 - t_1} i^2 dt} \tag{4.12}$$

Table 4.6 lists the $T_{r,p}$, $T_{r,rms}$, T_{ave}, I_{rms}, average switching frequency f_{sw}, and η for the three methods. It is observed that the $T_{r,p}$ values of the three methods are close, which verifies the same effectiveness on the commutation torque ripple reduction for the three methods. As for the performance index $T_{r,rms}$, it is found that the $T_{r,rms}$ value of the conventional method is lower compared to that of the improved method and the linear-model-based method due to the employment of 9 voltage vectors. From the above two observations, the $T_{r,rms}$ difference among the three methods is mainly incurred from the high-frequency torque ripple.

Regarding the conventional method, the adoption of the 9 voltage vectors leads to a higher f_{sw}, as seen in Table 4.6. This higher f_{sw} value of the conventional

method indicates higher switching losses and affects the driving system efficiency. From the efficiency data shown in Table 4.6, the η of this method is just slightly higher than that of the other two methods due to the effect of the switching losses, although the conventional method shows lower I_{rms} values. From the above comparison, the proposed improved LUT-based method and linear-model-based method show close control performance with the conventional LUT-based method at very low-speed operating conditions. Notably, the proposed two methods significantly reduce the computational burden. Moreover, the linear-model-based method also saves storage space.

Fig. 4.12 shows the measured torque and current waveforms for the mentioned three methods at 1000 r/min and 8 N·m operation conditions. Similar to the results shown in 100 r/min, the total instantaneous torque chops around the command torque and is bounded in a certain region. The low-frequency commutation torque ripple is significantly reduced, and the high-frequency torque ripple results from the current chopping controlled by the MPTC algorithm.

Table 4.7 compares the $T_{r,p}$, $T_{r,rms}$, T_{ave}, I_{rms}, f_{sw}, and η for the three methods at 1000 r/min and 8 N·m operating conditions. Not surprisingly, the $T_{r,p}$ values of the three methods are close since all the methods effectively reduce the commutation torque ripple. And the $T_{r,rms}$ value for the conventional method is slightly lower compared to the other two methods owing to the 9 voltage vectors adoption in the conventional method. Again, the $T_{r,rms}$ difference is mainly from the high frequency torque ripple. The average torque T_{ave} for the three methods are close. As for the system efficiency, it is surprisingly found the conventional method shows lower efficiency although it has lowest I_{rms} among the three methods. This phenomenon

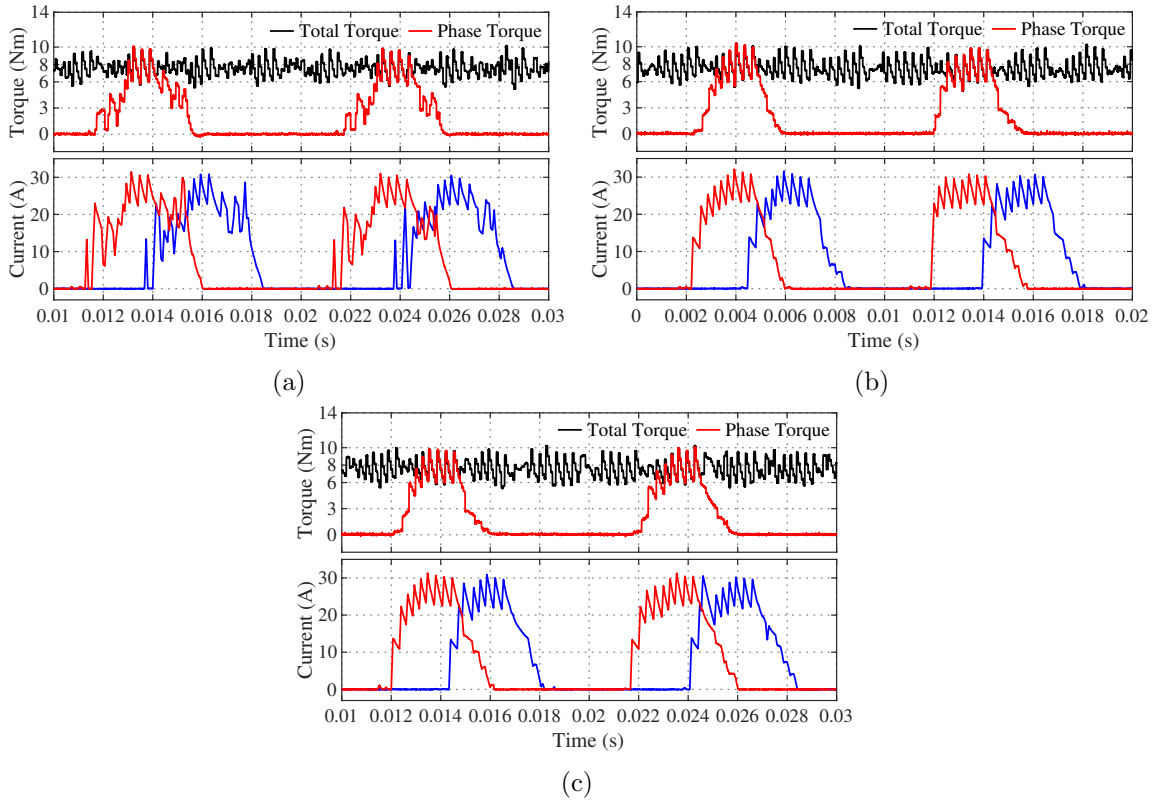

Figure 4.12: Torque and current waveforms for (a) conventional LUT-based method, (b) improved LUT-based method, and (c) proposed linear-model-based method at 1000 r/min and 8 N·m operating conditions.

can be mainly explained by the following tow reasons: (a) Higher f_{sw}, as shown in Table 4.7, in the conventional method affects the driving system efficiency; (b) Higher iron losses lead to efficiency decreasing. Since the iron losses are hard to measure in the experimental tests, the FEA software is used to estimate the iron losses based on the measured current waveforms and position information. Table 4.8 compares the iron losses for the conventional method and linear-model-based method. It is found the total iron losses for the conventional method is higher than the linear-model-based method. Since the improved method employs the same switching table with the linear-model-based method and shows similar current waveforms, it is reasonable

Table 4.7: Control performance comparison at 1000 r/min and 8 N·m operating condition

Method	Conventional	Improved	Linear
$T_{r,p}$	0.6620	0.7076	0.6511
$T_{r,rms}$	1.0667	1.2224	1.2337
T_{ave} (N·m)	7.6711	7.6540	7.6961
I_{rms} (A)	12.9322	13.4061	13.4116
f_{sw} (kHz)	3.1187	2.5279	2.4571
η (%)	66.27	68.38	68.54

Table 4.8: Iron losses comparison between conventional method and proposed linear-model-based method

Method	Conventional	Linear
Stator iron losses (W)	39.2243	28.2839
Rotor iron losses (W)	13.0504	9.6559
Total iron losses (W)	52.2747	37.9398

to assume these two methods have similar iron losses.

Fig. 4.13 shows the torque and current waveforms for the three methods at 5000 r/min and 4 N·m operating conditions. The weight factor ω_1 is also set at 0.003 for all the methods as in the case above. In Fig. 4.13 (a), the negative torque is clearly observed because the conducted phase still holds a significant amount of current near the aligned position. Regarding the phase current, the conventional method shows higher peak current and wider conducted region. Besides, the current waveforms vary significantly, which is mainly caused by the sampled position difference in each inductance period and the generated negative torque. Due to the adoption of the improved switching table, the negative torque is eliminated for the improved method and proposed linear-model-based method, as shown in Fig. 4.13 (b) and Fig. 4.13 (c).

Table 4.9 lists the related performance indices for the experimental results shown

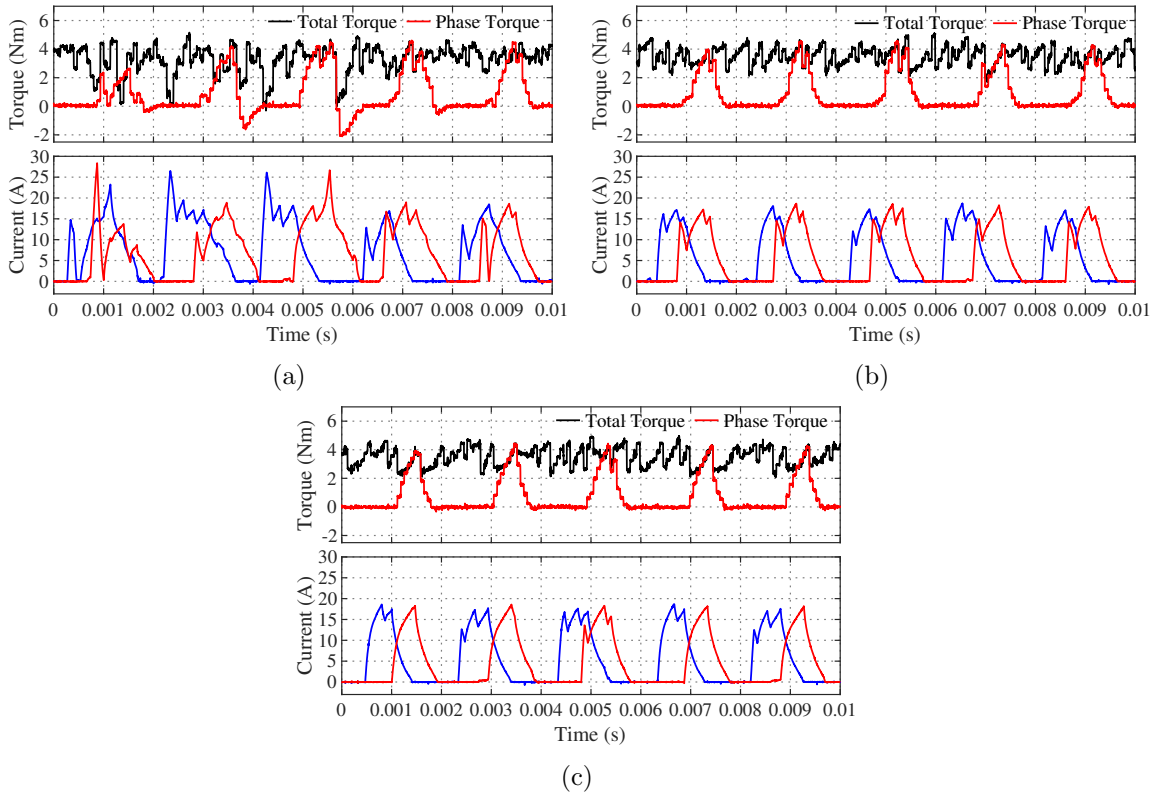

Figure 4.13: Torque and current waveforms for (a) conventional LUT-based method, (b) improved LUT-based method, and (c) proposed linear-model-based method at 5000 r/min and 4 N·m operating conditions.

Table 4.9: Control performance comparison at 5000 r/min and 4 N·m operating condition

Method	Conventional	Improved	Linear
$T_{r,p}$	1.6691	0.9732	0.8325
$T_{r,rms}$	0.9889	0.6259	0.6552
T_{ave} (N·m)	3.3508	3.6126	3.5743
I_{rms} (A)	10.4290	8.5921	8.4538
η (%)	74.91	79.61	78.83

in Table 4.9. Not surprisingly, the improved method and proposed linear-model-based method show much lower $T_{r,rms}$ values and $T_{r,p}$ values. Due to the generated negative torque, the average torque and efficiency of the conventional method are also lower

compared to that of the other two methods.

In summary, the presented three methods effectively eliminate the commutation torque ripple at low speed range but the improved method and the proposed method have higher high-frequency torque ripple. At high-speed conditions, the improved method and the proposed method show much better torque control performance due to the elimination of the negative torque. As for the system efficiency, the improved method and linear-model-based method have higher efficiency except at very low speed range. The detailed comparison of the losses and efficiency for the three methods will be studied in the future.

4.4.3 Dynamic Performance Evaluation of the Linear-Model-Based MPTC

To verify the applicability of the proposed method in a variable speed situation, a test rising the speed from 500 r/min to 1000 r/min at 8 N·m torque reference was carried out. Fig. 4.14 shows the total torque, shaft speed, one phase current waveforms in this situation. It can be found that the total torque is well controlled and there is no commutation torque ripple during the shaft speed rising period. Because the limitation of the setup, the IM cannot accurately control the torque in the transient period. In this case, the torque is controlled by the SRM and the speed is controlled by the IM for this test.

The performance of the proposed linear-model-based method is also checked in starting the motor. Under this situation, the torque reference is generated by the speed proportional-integral (PI) controller. Furthermore, the speed is controlled by the SRM, while the IM works in torque control mode. Fig. 4.15 shows the torque,

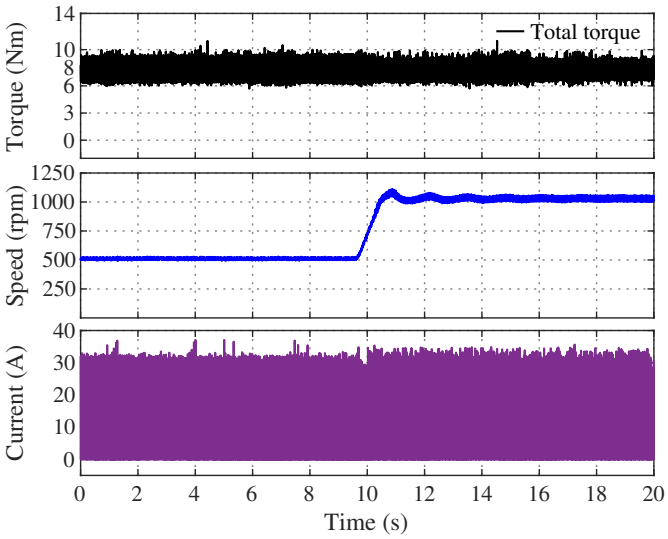

Figure 4.14: Total torque, speed, and current waveforms of the proposed linear-model-based method during the speed rising period.

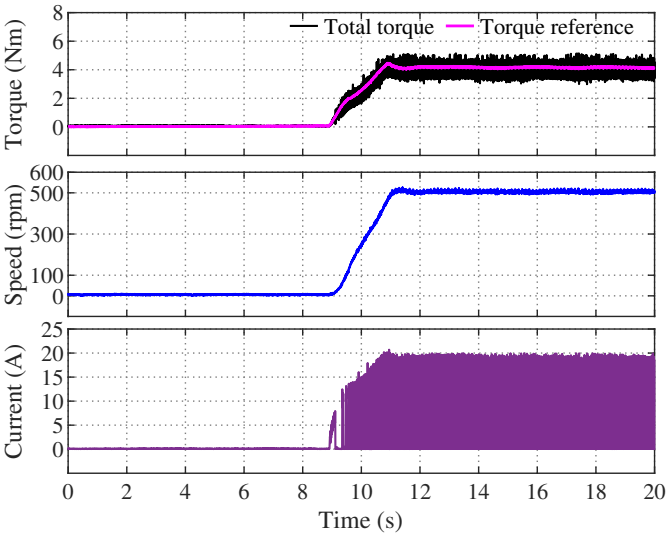

Figure 4.15: Torque, speed, and current waveforms during motor starting period of the proposed linear-model-based method.

torque reference, speed and one phase current waveforms in starting the motor from 0 r/min to 500 r/min. Due to the setup limitation, the torque of the IM cannot be accurately controlled during the transient period at torque control mode. The

final load applied by the IM reaches around 4 N·m at 500 r/min. It is observed that the SRM shaft torque follows the torque reference well with no commutation torque ripple, and the shaft speed reaches the setting value within 2 s.

4.5 Conclusion

Torque ripple is known as one of the main drawbacks for the SRM. The MPTC is regarded as an effective direct torque control method, which not only possesses high torque control performance but also optimizes the copper losses at the same time. Heavy computation burden and degraded high-speed torque control performance are the main issues for the conventional LUT-based MPTC method. To ease these issues, the proposed improved switching table reduces the computational time by 25% compared to the conventional method and enhance the high-speed torque control performance. To further reduce the storage space of the LUT-based MPTC method, the linear-model-based MPTC method is proposed based on the developed flux-linkage and torque transformation. This proposed method requires only 228 storage units compared to 1530 storage units consumption of the LUT-based methods. Experimental results reveal that the proposed method effectively eliminates the commutation torque ripple as the conventional LUT-based method at the low-speed region and enhances the control performance at the high-speed region.

Chapter 5

Low-Ripple Continuous Control Set Model Predictive Torque Control for SRMs Based on Equivalent Linear SRM Model

5.1 Introduction

The finite control set (FCS) MPTC methods developed in the previous chapter indeed effectively reduce the commutation torque ripple. However, the limited voltage vectors in the FCS MPTC methods lead to large high-frequency torque ripples. Besides, the switching frequency in the existed FCS MPTC methods is not fixed, which may increase the complexity in designing the electromagnetic interface filter.

In this chapter, a low-ripple continuous control set (CCS) MPTC method for

SRMs is presented. The inherent high nonlinearity of the SRMs makes it difficult to analytically solve the optimization problem in the CCS MPTC algorithm. To address this issue, an equivalent linear SRM model is adopted, and the cost function is also properly modified. Then, with the torque boundary values provided by executing the voltage vectors of an improved switching table, the optimization problem in the CCS MPTC method becomes simple and analytically solvable. The Lagrange multiplier method is employed to solve this optimization problem analytically and generate the optimum torque reference values for the active phases. Based on the estimated torque variation rates, the duty cycles for each phase are calculated. Extensive simulation and experimental tests reveal that the proposed CCS MPTC method shows much lower torque ripples and current ripples in a wide speed range than the existing methods.

5.2 Merit and Challenge to Develop CCS MPTC

The conventional FCS MPTC method normally finds the best voltage vector for the next control period through the exhaustive execution of the voltage vectors in the switching table. The optimal voltage vector will be selected to minimize the cost function. Generally, the cost function employed during this optimization process can be expressed as (5.1):

$$J = (T_{ref} - \sum T_{kp2})^2 + \omega_1 \sum (i_{kp2})^2 + g(i_{kp2})$$
$$g(i_{kp2}) = \begin{cases} \infty, & \text{if } i_{kp2} \geq i_{MAX} \\ 0, & \text{if } i_{kp2} < i_{MAX} \end{cases} \tag{5.1}$$

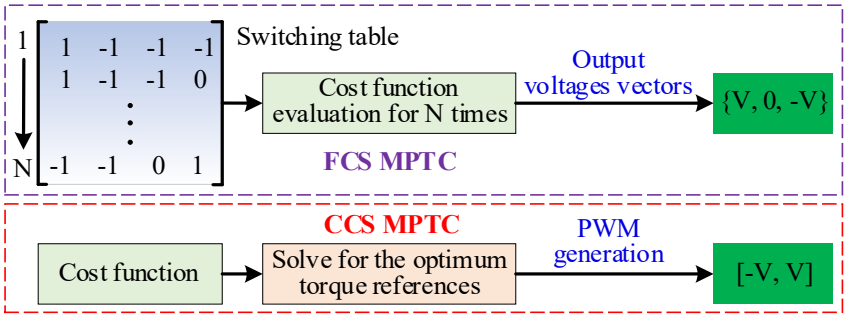

Figure 5.1: Block diagrams for the FCS MPTC method and CCS MPTC method.

where T_{ref} is the input command torque, T_{kp2} is the estimated phase torque at the sampling instant $k+2$, i_{kp2} is the estimated phase current at the sampling instant $k+2$, ω_1 is the weight factor, and i_{MAX} is the maximum current allowed by the drive system. It is noted that the beginning of the present control period is labeled as the sampling instant k. The output of the FCS MPTC method is the voltage vector combined among "1", "0", and "-1", which indicates the phase voltage can only be selected from positive bus voltage, zero, and negative bus voltage. The limited voltage vector adoption inevitably leads to large torque ripples and current ripples.

On the other hand, the CCS MPTC method analytically solves the cost function. As for the torque control for SRMs, the CCS MPTC method is supposed to generate the optimum torque references, which have a minimum cost function. Then, the duty cycle for each phase is calculated. Due to the PWM adoption, the CCS MPTC method can equivalently utilize any voltage between negative bus voltage and positive bus voltage. Therefore, the torque control performance can be significantly enhanced. Fig. 5.1 summarizes the above-mentioned general process for the FCS MPTC method and CCS MPTC method.

The main challenges to developing the CCS MPTC method for SRM drives are the inherent high nonlinearity and the present form of the cost function (5.1). The reasons

can be explained below. Considering the commutation period that two phases share the total command torque T_{ref}, the cost function (5.1), in this case, is equivalently reduced to (5.2):

$$J = (T_{ref} - T^{inc}_{ref,kp2} - T^{out}_{ref,kp2})^2 + \omega_1((i^{inc}_{kp2})^2 + (i^{out}_{kp2})^2) \tag{5.2}$$

where $T^{inc}_{ref,kp2}$, $T^{out}_{ref,kp2}$, i^{inc}_{kp2}, and i^{out}_{kp2} represent the incoming phase reference torque, outgoing phase reference torque, incoming phase current and outgoing phase current. Please note these four quantities are all estimated values at the sampling instant $k+2$ and the term $g(i_{kp2})$ is ignored here for simplicity. To analytically solve the cost function, the gradient information of the cost function, which is $[\partial J/\partial T^{inc}_{ref,kp2}, \partial J/\partial T^{out}_{ref,kp2}]^T$, is normally required. As mentioned previously, the phase torque of SRMs cannot be analytically expressed due to the severe saturation. If using the nonlinear torque expression (2.6) or some Fourier series related torque models, the current i^{inc}_{kp2} and i^{out}_{kp2} cannot be derived as the function of $T^{inc}_{ref,kp2}$ and $T^{out}_{ref,kp2}$. Hence, the gradient information of J is barely possible to obtain. The adoption of the LUT $i(\theta, T_e)$ also cannot find the gradient information since the premise of using the numerical differentiation methods, such as the central difference method, is the knowledge at the sampling instant $k+2$, which is unknown and needs to be solved. Besides, with such LUT, there is no analytical relation between current and torque to make the optimization problem analytically solvable. Even if directly modeling the inverted torque characteristics $i(\theta, T_e)$, the expression of such model is complex and the constructed optimization problem is difficult to solve analytically to obtain the optimum torque references. However, these optimum torque references are necessary for the CCS MPTC method. Therefore, with (5.2), the impossibility of analytically finding the optimum torque references results in failure to develop the CCS MPTC method

for SRM drives.

5.3 Proposed CCS MPTC Method

The nonlinear toque expression poses the issue when attempts are made to solve the cost function to develop the CCS MPTC method. To address this issue, the equivalent linear SRM model is used, and the cost function shown in (5.2) is modified properly. With such improvement, the CCS MPTC method is developed.

5.3.1 Equivalent Linear SRM Model

Although the phase instantaneous torque cannot be expressed analytically in normal operation conditions, it actually can be expressed as the simple form (5.3) under unsaturated operation conditions, where $L_{Li}(\theta)$ is the phase unsaturated inductance.

$$T_e = \frac{1}{2} i^2 \frac{dL_{Li}(\theta)}{d\theta} \tag{5.3}$$

To take advantage of this simple torque expression, the torque mapping between the nonlinear SRM model and linear SRM model is required. Such concept was first developed in chapter 3. Fig. 5.2 shows nonlinear torque model (red curve) and linear torque model (blue curve) at a certain position. The toque mapping is to find the relationships between the linear current $i_{Li,T}$ and actual current i_{Nl} which have the same torque value. With the actual torque data and unsaturated inductance value, it is easy to find the complete mapping. The flux-linkage mapping can be developed in a similar way. The target of this mapping is to find the relationship between the linear current $i_{Li,f}$ and nonlinear current i_{Nl} which have the same flux-linkage value.

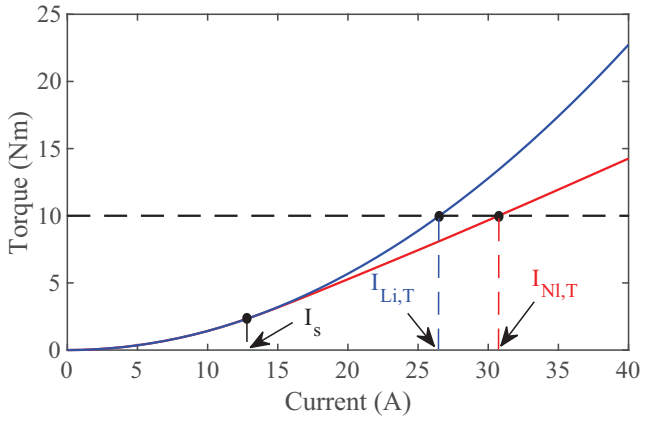

Figure 5.2: Linear torque model (blue curve) and nonlinear torque model (red curve) at a certain position of the SRM.

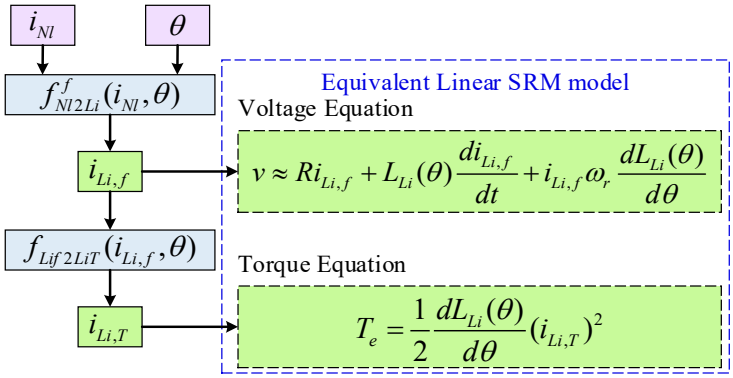

Figure 5.3: Process from nonlinear SRM model to equivalent linear SRM model.

Based on the above two mappings, the nonlinear SRM model can be converted to the equivalent linear SRM model, as shown in Fig. 5.3, where ω_r is measured shaft speed, $f^{f}_{Nl2Li}(i_{Nl},\theta)$ is the transformation from nonlinear SRM model to linear SRM model with equal flux-linkage, $i_{Li,f}$ is the linear current with equal flux-linkage, $f_{Lif2LiT}(i_{Li,f},\theta)$ is the transformation from linear current with equal flux-linkage to the linear current with equal torque, and $i_{Li,T}$ is the linear current with equal torque. It is noted that the transformation $f_{Lif2LiT}(i_{Li,f},\theta)$ is synthesized from the transformation $f^{f}_{Li2Nl}(i_{Li,f},\theta)$ and transformation $f^{T}_{Nl2Li}(i_{Nl},\theta)$, where $f^{f}_{Li2Nl}(i_{Li,f},\theta)$ is the

transformation from linear SRM model to nonlinear SRM model with equal flux-linkage and $f^{T}_{Nl2Li}(i_{Nl},\theta)$ is the transformation from nonlinear SRM model to linear SRM model with equal torque.

Once converted to the equivalent linear SRM model, the voltage equation is used to estimate the phase current for the MPTC method, and the simple torque equation can not only be used to estimate the phase torque but also be used to simplify the cost function, which is a vital step toward the CCS MPTC.

With the converted linear variables, the cost function of the MPTC method is modified to (5.4), where $i_{Li,T,kp2}$ is the estimated linear current with equal torque at sampling instant $k+2$, and $i_{Li,T,MAX}(\theta_{kp2})$ is the maximum linear current $i_{Li,T}$ allowed by the drive system.

$$\begin{aligned} J_{Li} &= (T_{ref} - \sum T_{ref,kp2})^2 + \omega_1 \sum (i_{Li,T,kp2})^2 + g(i_{Li,T,kp2}) \\ g(i_{Li,T,kp2}) &= \begin{cases} \infty, & \text{if } i_{Li,T,kp2} \geq i_{Li,T,MAX}(\theta_{kp2}) \\ 0, & \text{if } i_{Li,T,kp2} < i_{Li,T,MAX}(\theta_{kp2}) \end{cases} \end{aligned} \tag{5.4}$$

Substituting the linear torque equation into equation (5.4), the cost function is simplified to (5.5). And it can be observed that the only variable quantities are torque references.

$$J_{Li} = (T_{ref} - \sum T_{ref,kp2})^2 + \omega_1 \sum \frac{2T_{ref,kp2}}{dL_{Li}(\theta_{kp2})/d\theta} + g(i_{Li,T,kp2}) \tag{5.5}$$

To effectively solve the cost function (5.5) in a reasonable region, the boundaries for the phase torque reference T_{kp2} are required. Considering one control period duration, the extreme torque values that one phase can reach are the torque values under magnetization and demagnetization excitation. Hence, the extreme torque

Table 5.1: Improved Switching Table for Obtaining Torque Reference Boundary Values of the Studied 8/6 SRM

Switching State	Position θ_A	Phase A	Phase B	Phase C	Phase D
Region 1	$[0°, \theta_1]$	1, 0	-1	-1	1, -1
Region 2	$[\theta_1, 15°]$	1, -1	-1	-1	-1, 0
Region 3	$[15°, 15° + \theta_1]$	1, -1	1, 0	-1	-1
Region 4	$[15° + \theta_1, 30°]$	-1, 0	1, -1	-1	-1
Region 5	$[30°, 30° + \theta_1]$	-1	1, -1	1, 0	-1
Region 6	$[30° + \theta_1, 45°]$	-1	-1, 0	1, -1	-1
Region 7	$[45°, 45° + \theta_1]$	-1	-1	1, -1	1, 0
Region 8	$[45° + \theta_1, 60°]$	-1	-1	-1, 0	1, -1

values for each phase during the exhaustive execution of the switching table employed in the FCS MPTC method can be used as the boundary values. In order to suppress the negative torque and possess a good torque control performance in a wide speed range, the improved switching table is used to obtain the boundary torque references. Table 5.1 shows this switching table for obtaining the torque reference boundary values, where θ_1 is an auxiliary angle to separate different regions in one electronic period. Normally, at low speed range, θ_1 is set at the angle where the rotor pole just overlaps with the stator pole. Please note that if magnetization or demagnetization excitation is not allowed in the switching table, the toque value under freewheeling mode is regarded as the extreme value.

5.3.2 Proposed CCS MPTC Method

For the generally employed three- or four-phase SRMs, the situation that there are at most two phases conducting at the same time is more common. Hence, the modified cost function (5.5) can be simplified as (5.6):

$$J_{Li} = (T_{ref} - T^{inc}_{ref,kp2} - T^{out}_{ref,kp2})^2 + \omega_1(\frac{2T^{inc}_{ref,kp2}}{dL_{Li}(\theta^{inc}_{kp2})/d\theta} + \frac{2T^{out}_{ref,kp2}}{dL_{Li}(\theta^{out}_{kp2})/d\theta}) \tag{5.6}$$

where θ^{inc}_{kp2} and θ^{out}_{kp2} indicate the estimated position for the incoming phase and outgoing phase at sampling instant $k+2$. Please note the term $g(i_{Li,T,kp2})$ is ignored here for simplicity and this simplified form (5.6) is only used during the calculation process to get the optimum torque reference values. Observing the simplified form (5.6) and considering the torque reference boundary values, it is apparent that minimizing J_{Li} becomes an optimization problem with inequality constraints, as shown below:

$$\begin{cases} \boldsymbol{T_{ref,kp2}} = arg \min\limits_{\boldsymbol{T_{ref,kp2}}} J_{Li}(\boldsymbol{T_{ref,kp2}}) \\ T^{inc}_{ref,kp2} - T^{inc}_{max} \leq 0 \\ -T^{inc}_{ref,kp2} + T^{inc}_{min} \leq 0 \\ T^{out}_{ref,kp2} - T^{out}_{max} \leq 0 \\ -T^{out}_{ref,kp2} + T^{out}_{min} \leq 0 \end{cases} \tag{5.7}$$

where $T_{ref,kp2} = [T^{inc}_{ref,kp2}\ T^{out}_{ref,kp2}]^T$, T^{inc}_{max}, T^{inc}_{min}, T^{out}_{max}, and T^{out}_{min} are torque boundary values for the incoming and outgoing phases. It is noted that these four torque reference boundary values are obtained in the exhaustive execution process of the voltage vectors shown in Table 5.1. Because the gradient information of (5.5) is easy to calculate, the Lagrange multiplier method can be used to analytically solve the above problem (Bakr, 2013). According to the Karush-Kuhn-Tucker (KKT) conditions (Bakr, 2013), theoretically, there are 16 possibilities for the solution of the optimization problem in (5.7). Observing these constraints, it can be found that all the constraints are the expression of straight lines, and there are two pairs of parallel

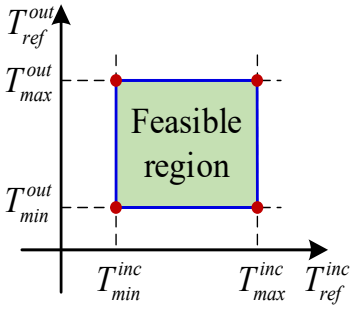

Figure 5.4: Feasible region for the optimization problem in the CCS MPTC method.

lines, as shown in Fig. 5.4. In this case, the 16 possibilities are reduced to 9 possibilities, including 4 possibilities that two constraints are active, 4 possibilities that only one constraint is active, and 1 possibility that none of the constraints is active.

If two constraints are active, the solution for (5.7) is the intersection point of the two straight lines, as shown by the red solid circles in Fig. 5.4. These points correspond to the estimated torque values calculated by the voltage vectors in Table 5.1.

If only one constrain is active, the solution for (5.7) is on the boundary lines, as shown by the blue solid lines in Fig. 5.4. In this case, the Lagrange multiplier has to be solved. Taking the case that the third inequality constraint is active as an example, the necessary optimality conditions in this case are expressed as (5.8), where the λ is the Lagrange multiplier. Solving the above equations, the λ is calculated as (5.9). The KKT conditions require λ to be positive if the solution is indeed in this boundary line, which indicates $dL_{Li}(\theta_{kp2}^{inc})/d\theta$ should be smaller than $dL_{Li}(\theta_{kp2}^{out})/d\theta$. This condition is reasonable since the higher inductance variation rate means a higher torque per ampere ratio. And in this case, the outgoing phase delivers the maximum torque within its capability.

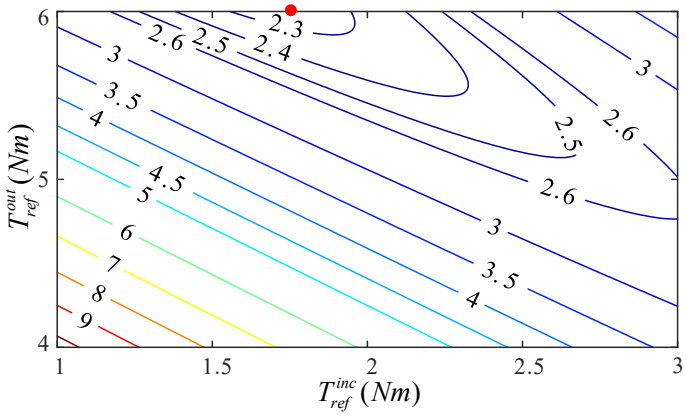

Figure 5.5: Contour plot for the cost function J_{Li} when the third constraint is active.

$$\begin{bmatrix} -2(T_{ref} - T_{ref,kp2}^{inc} - T_{ref,kp2}^{out}) + \dfrac{2\omega_1}{dL_{Li}(\theta_{kp2}^{inc})/d\theta} \\ -2(T_{ref} - T_{ref,kp2}^{inc} - T_{ref,kp2}^{out}) + \dfrac{2\omega_1}{dL_{Li}(\theta_{kp2}^{out})/d\theta} \end{bmatrix} + \lambda \begin{bmatrix} 0 \\ 1 \end{bmatrix} = \begin{bmatrix} 0 \\ 0 \end{bmatrix} \tag{5.8}$$

$$\lambda = \frac{2\omega_1}{dL_{Li}(\theta^{inc})/d\theta} - \frac{2\omega_1}{dL_{Li}(\theta^{out})/d\theta} \tag{5.9}$$

The optimum torque references for the incoming phase and outgoing phase in this case are calculated as (5.10).

$$\begin{cases} T_{ref,kp2}^{inc} = T_{ref} - T_{max}^{out} - \dfrac{\omega_1}{dL_{Li}(\theta_{kp2}^{out})/d\theta} - \dfrac{\lambda}{2} \\ T_{ref,kp2}^{out} = T_{max}^{out} \end{cases} \tag{5.10}$$

An example contour plot for the case that the third constraint is active is also provided, as shown in Fig. 5.5. It is observed that the minimum cost function value, marked by red solid circle, is obtained on the T_{max}^{out} boundary line.

Table 5.2 summarizes the Lagrange multiplier λ and the optimum torque reference values for different cases when only one constant is active. It can be observed from the table that the sign of the value $(dL_{Li}(\theta_{kp2}^{inc})/d\theta - dL_{Li}(\theta_{kp2}^{out})/d\theta)$ can first be

Table 5.2: Lagrange Multiplier and Optimum Torque References at Different Cases When One Constraint Is Active

Active constraint	Lagrange multiplier and optimum torque references
First constraint is active $T^{inc}_{ref,kp2} - T^{inc}_{max} = 0$	$\lambda = \frac{2\omega_1}{dL_{Li}(\theta^{out}_{kp2})/d\theta} - \frac{2\omega_1}{dL_{Li}(\theta^{inc}_{kp2})/d\theta}$ $T^{inc}_{ref,kp2} = T^{inc}_{max}$ $T^{out}_{ref,kp2} = T_{ref} - T^{inc}_{max} - \frac{\omega_1}{dL_{Li}(\theta^{inc}_{kp2})/d\theta} - \frac{\lambda}{2}$
Second constraint is active $-T^{inc}_{ref,kp2} + T^{inc}_{min} = 0$	$\lambda = \frac{2\omega_1}{dL_{Li}(\theta^{inc}_{kp2})/d\theta} - \frac{2\omega_1}{dL_{Li}(\theta^{out}_{kp2})/d\theta}$ $T^{inc}_{ref,kp2} = T^{inc}_{min}$ $T^{out}_{ref,kp2} = T_{ref} - T^{inc}_{min} - \frac{\omega_1}{dL_{Li}(\theta^{inc}_{kp2})/d\theta} + \frac{\lambda}{2}$
Third constraint is active $T^{out}_{ref,kp2} - T^{out}_{max} = 0$	$\lambda = \frac{2\omega_1}{dL_{Li}(\theta^{inc}_{kp2})/d\theta} - \frac{2\omega_1}{dL_{Li}(\theta^{out}_{kp2})/d\theta}$ $T^{inc}_{ref,kp2} = T_{ref} - T^{out}_{max} - \frac{\omega_1}{dL_{Li}(\theta^{out}_{kp2})/d\theta} - \frac{\lambda}{2}$ $T^{out}_{ref,kp2} = T^{out}_{max}$
Fourth constraint is active $-T^{out}_{ref,kp2} + T^{out}_{min} = 0$	$\lambda = \frac{2\omega_1}{dL_{Li}(\theta^{out}_{kp2})/d\theta} - \frac{2\omega_1}{dL_{Li}(\theta^{inc}_{kp2})/d\theta}$ $T^{inc}_{ref,kp2} = T_{ref} - T^{out}_{min} - \frac{\omega_1}{dL_{Li}(\theta^{out}_{kp2})/d\theta} + \frac{\lambda}{2}$ $T^{out}_{ref,kp2} = T^{out}_{min}$

used to select which two cases might be the possible solutions for this optimization problem. Then, whether the calculated optimum torque reference values are within the boundary values can finally decide which constraint is active. Please note the above required derivative information $dL_{Li}(\theta)/d\theta$ is obtained from a pre-stored 1-D LUT.

The remaining one possibility is that none of the constraints is active. In this

case, the optimum solution is expected to be in the interior of the feasible region. By constructing the necessary optimality conditions and solving them, the value of $dL_{Li}(\theta_{kp2}^{inc})/d\theta$ should equal to $dL_{Li}(\theta_{kp2}^{out})/d\theta$ value for the case that no constraint is active. This equal condition rarely happens for the linear self-inductance of the SRMs. Besides, the cost function in this case is reduced to (5.11). From this expression, it is found that the value of J_{Li} only depends on the addition of the $T_{ref,kp2}^{inc}$ and $T_{ref,kp2}^{out}$. Based on the above two reasons, the optimum torque references for the incoming and outgoing phases can be simply set at half of T_{ref} in this situation.

$$J_{Li} = (T_{ref} - T_{ref,kp2}^{inc} - T_{ref,kp2}^{out})^2 + \frac{2\omega_1(T_{ref,kp2}^{inc} + T_{ref,kp2}^{out})}{dL_{Li}(\theta_{kp2})/d\theta} \tag{5.11}$$

The complete process for obtaining the optimum torque reference values for the proposed CCS MPTC method is described in Fig. 5.6. Assuming the beginning of the current control period is labeled as sampling instant k. Firstly, the actual current i_{Nl} and position information is measured. Later, this measured current i_{Nl} is converted to $i_{Li,f}$. Then, based on the equivalent linear voltage equation and the applied PWM duty cycle between k and k+1 sampling instant, the flux-linkage and the linear current $i_{Li,f}$ at k+1 sampling instant are estimated. With this information, the SRM behavior at $k+2$ sampling instant can be predicted. Firstly, the case that two constraints are active is evaluated. For each voltage vector shown in Table 5.1, the torque and current are predicted. Since all the intersection points shown in Fig. 5.4 exactly correspond to the voltage vectors in the improved switching table, exhaustive execution of these voltage vectors will give the voltage vector with minimized cost function value in the case that two constraints are active. Because there are four voltage vectors, the loop of two constraints are active will be iterated four times. Then, the best voltage

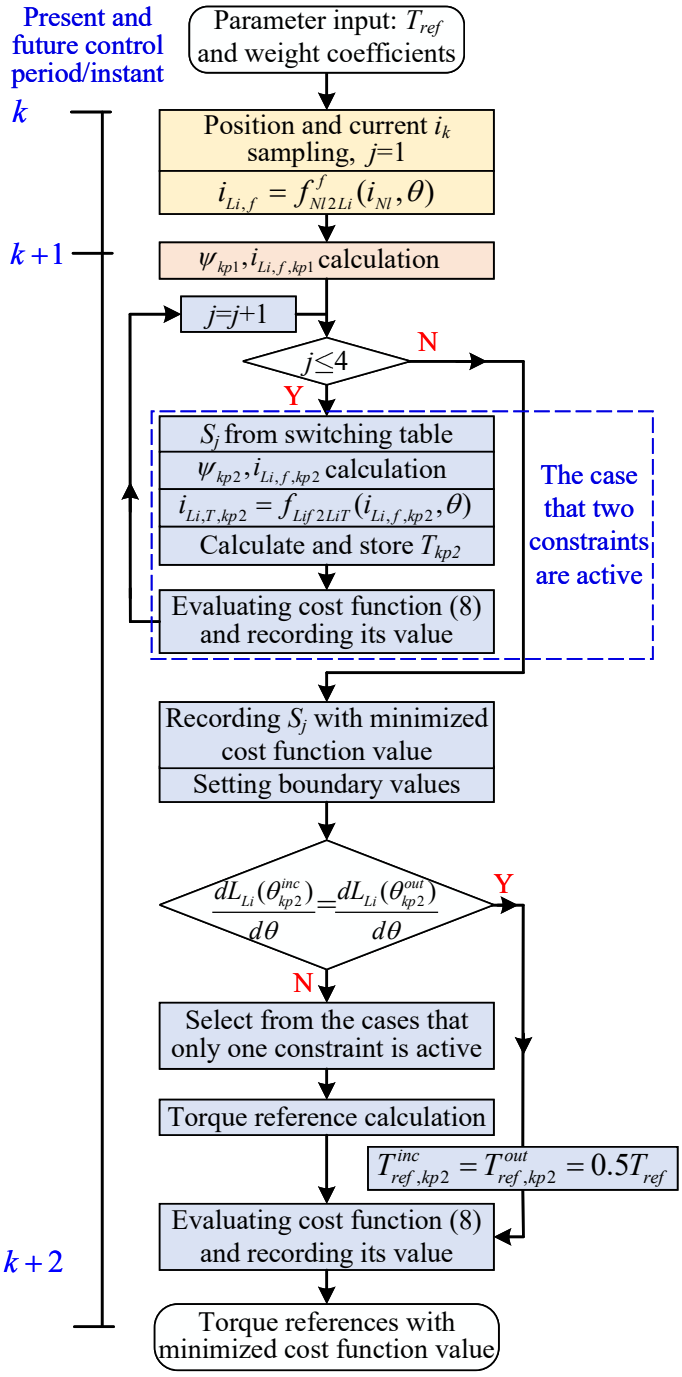

Figure 5.6: Flow chart of obtaining the optimum torque references for the proposed CCS MPTC method.

vector and its cost function value will be recorded. Please note that the torque information is stored during this exhaustive execution process. Afterward, according to the linear inductance information, the optimum torque references for either the case that one constraint is active or the case that no constraint is active are obtained. Finally, compare all the cost function values and select the one with the minimum value. Please note that the cost function value is evaluated based on the (5.5) in the proposed method to ensure the transient phase current below the maximum value.

Once the optimum torque references are available, the PWM duty cycles are calculated based on the torque decreasing and increasing rate. These torque variation rates are calculated from the estimated torque information at sampling instant $k+2$ and the estimated torque information at sampling instant $k+1$.

5.3.3 Wide Speed Operation of the Proposed CCS MPTC Method

Although torque ripples affect more on the low-speed range for SRM drives, good torque control performance over a wide speed range is also important. To ensure good torque control performance in a wide-speed operation, it is beneficial to study the switching features of the proposed CCS MPTC method. The switching features here refer to at which position the phase turns on and at which position the phase turns off. And these switching features can be studied from Fig. 5.7, which shows the idealized linear inductance, rotor position, and voltage vectors linked with the torque reference boundary values. For the simplicity of illustration, the toque reference boundary values that one phase can achieve within one control period under excitation "1", "0", "-1" are labeled as T_{max}, T_{zero}, and T_{min}, correspondingly. Apparently, these

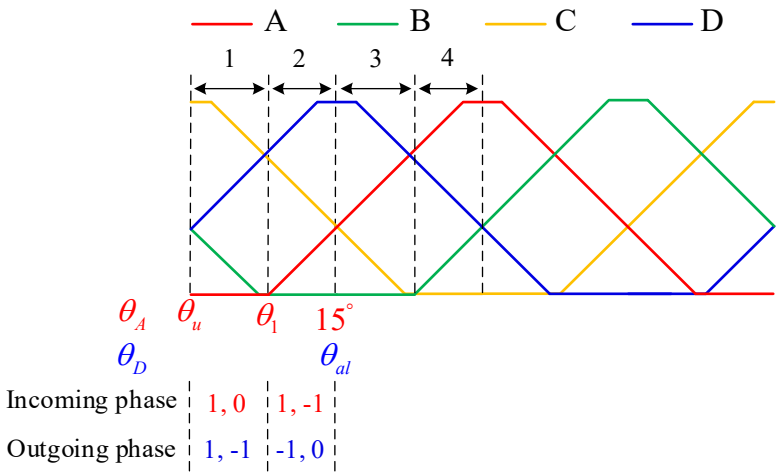

Figure 5.7: Switching feature illustration of the proposed CCS MPTC method.

torque reference boundary values have the following relationship for one specific phase within one specific control period: $T_{max} > T_{zero} > T_{min}$.

In region 1, where phase A position θ_A is between unaligned position θ_u and auxiliary angle θ_1, the incoming phase (phase A) torque reference is allowed to select any value between $T_{zero,A}$ and $T_{max,A}$, and the outgoing phase (phase D) toque reference is allowed to select any value between $T_{min,D}$ and $T_{max,D}$. It is noted that only phase A and phase D are active phases in region 1. Besides, at the point that θ_A equals θ_u, there is no current for phase A but a significant amount of current for phase D. Observing the inductance waveform in this region, it is found that the derivative of inductance is small for phase A but that is quite big for phase D. This indicates that the torque per ampere ratio for phase D at region 1 is much higher than that of phase A. Since the second objective of the CCS MPTC algorithm aims to minimize the copper losses, in region 1, the algorithm will assign all the torque references to phase D due to the higher torque per ampere ratio of this phase. And the torque reference for phase A will always be zero in region 1.

In region 2, where position θ_A is between θ_1 and 15°, the incoming phase (phase A) torque reference is allowed to select any value between $T_{min,A}$ and $T_{max,A}$, and the outgoing phase (phase D) toque reference is allowed to select any value between $T_{min,D}$ and $T_{zero,D}$. It is observed that phase D is forced to reduce the current from the beginning of region 2 since the phase D is close to its aligned position in region 2. In this case, the turn-off instant of the phase D can be regarded at phase A position θ_1. On the other hand, it is noted that the derivative of inductance for phase A is close to that of phase D in this region, which means the two phases have close torque per ampere ratio value. Considering the torque reference boundary values and the demagnetization of phase D, the turn-on instant of phase A is regarded at phase A position θ_1.

From the above description, it is observed that θ_1 is a crucial angle and it affects the switching features of the proposed CCS MPTC algorithm. Considering the current variation rate around the turn-on instant, the auxiliary angle θ_1 should be advanced at high speed operation conditions to build up the phase current. Please note that the angle θ_1 ranges from 0° to the angle θ_{op}, and θ_{op} is where the rotor pole just overlaps with the stator pole. For the studied four phase SRM, θ_1 is between 0° and 8°.

The value of the crucial angle θ_1 can be obtained from the following three rules. Firstly, if the rotor speed is low, the angle θ_1 can be directly set at θ_{op}. For higher speed operation, θ_1 can be tuned as below. Firstly, the angle θ_1 is tuned at rated torque condition since this condition requires the highest phase current. In this case, θ_1 is gradually reduced with the increment of the speed. Then, a simple offline 1-D LUT can be used to store these angles. Normally, with this 1-D LUT, the proposed

method can achieve a good control performance over a wide speed range and varied load condition. The following simulation and experimental results will verify this point. For better control performance, this angle should be tuned at different load conditions. Based on the above 1-D LUT obtained at the rated torque condition, the angle θ_1 gradually increases with the decreasing of the load when the speed is unchanged since lower load implies lower current requirement. With the above three rules, the angle θ_1 can be simply obtained. Alternatively, simple online technique can also be used to tune this angle to ensure wide-speed and varied load operation.

5.4 Simulation Validation

To verify the effectiveness of the proposed CCS MPTC method, simulation tests are carried out in the Matlab/Simulink environment. The simulation results of the existed FCS MPTC methods, which was proposed in (Peyrl *et al.*, 2009) and (Fang *et al.*, 2021a), are also presented for comparison. Please note that the complete torque and flux-linkage characteristics are utilized in this chapter instead of the simple analytical model in (Peyrl *et al.*, 2009) for the MPTC method in (Peyrl *et al.*, 2009). To make the simulation results consistent with the experimental results, the control frequency and the sampling frequency are set at 15 kHz. It is noted that the ω_1 is manually tuned to 0.003 for all the MPTC methods according to the method shown in (Rodriguez and Cortes, 2012). The studied four-phase 8/6 SRM has the rated parameters shown in Table 3.2.

Fig. 5.8 show the simulation results at 500 r/min and 8 N·m operation conditions for the three MPTC methods. From the presented torque waveforms, it is observed that the torque of the FCS MPTC methods chops within around 6 N·m and 10

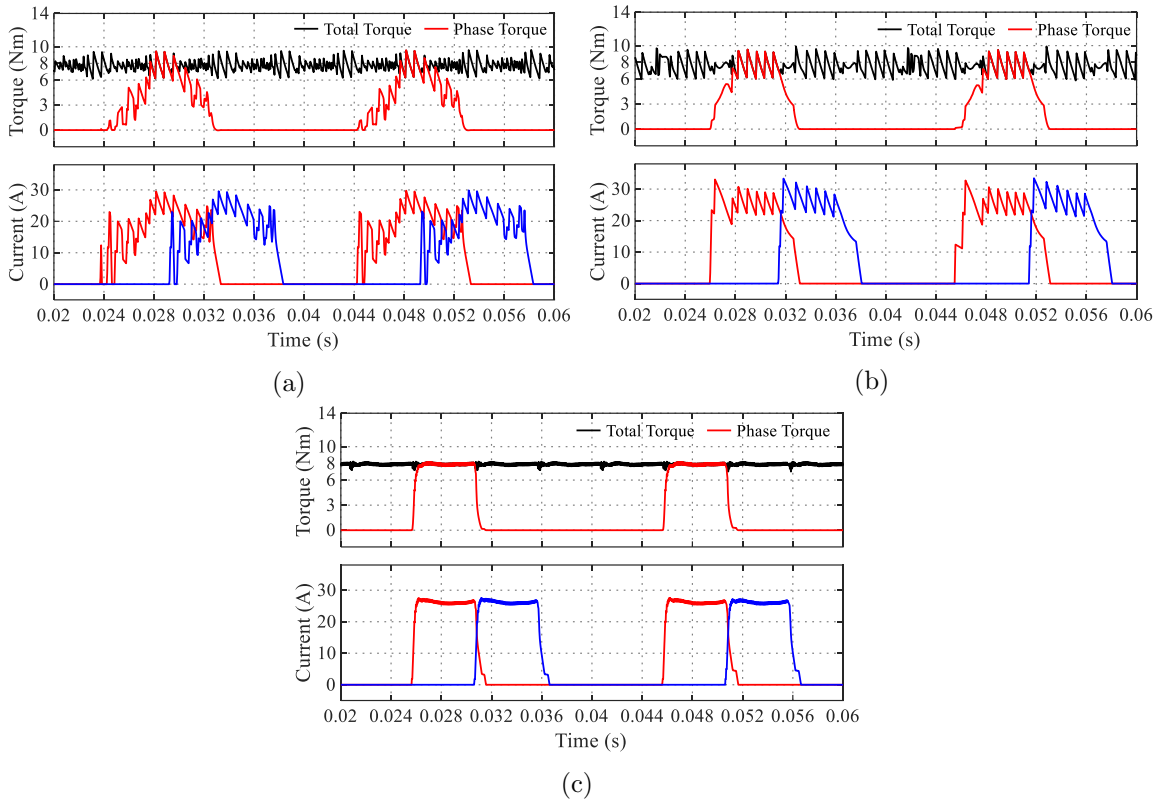

Figure 5.8: Simulation results of (a) the FCS MPTC method in (Peyrl *et al.*, 2009), (b) the FCS MPTC method in (Fang *et al.*, 2021a), and (c) the proposed CCS MPTC method when θ_1 is 8° at 500 r/min and 8 N·m operation conditions.

N·m. This high frequency and large amplitude chopping phenomenon results from the limited voltage vectors in the FCS MPTC methods. On the contrary, the torque of the CCS MPTC method holds closely around the command torque value, which is due to the adoption of the continuous terminal voltage. As for the current waveforms, it is found that current of FCS MPTC methods shows much larger current ripples compared to that of the proposed CCS MPTC method. Please note angle θ_1 is set at 8° in this case since the speed is low.

To quantitatively present the control performance difference between the FCS MPTC methods and the proposed CCS MPTC method, the performance indices,

Table 5.3: Simulated Performance Comparison at 500 r/min and 8 N·m T_{ref}

Performance index	MPTC in (Peyrl *et al.*, 2009)	MPTC in (Fang *et al.*, 2021a)	CCS MPTC
$T_{r,rms}$	0.68	0.95	0.15
T_{ave} (N·m)	7.75	7.60	7.88
I_{rms} (A)	13.22	14.00	13.10
T_{ave}/I_{rms}	0.59	0.54	0.60

namely rms value of the torque triple $T_{r,rms}$, the average torque T_{ave} and the rms value of the phase current I_{rms}, are calculated. The definitions of the $T_{r,rms}$ and I_{rms} are shown in (4.11) and (4.12), where the T_{total} is the total instantaneous torque. For more precise calculation, the I_{rms} value is the average value of the rms values of the four-phase currents.

Table 5.3 compares the above performance indices among the three MPTC methods at 500 r/min and 8 N·m conditions. It is observed that the $T_{r,rms}$ value is reduced from 0.69 of the FCS MPTC method in (Peyrl *et al.*, 2009) and 0.95 of the MPTC method in (Fang *et al.*, 2021a) to 0.15 of the proposed CCS MPTC method. And the proposed method has a slightly lower I_{rms} value.

Fig. 5.9 and Fig. 5.10 show the simulation results at 1000 r/min and different T_{ref} value conditions. Similar to the case at 500 r/min, the proposed CCS MPTC method shows a smoother instantaneous total torque. And the phase current of the proposed method also has smaller current ripples. These comparisons show the superiority of the proposed method.

The $T_{r,rms}$, T_{ave}, and I_{rms} are also compared for the 1000 r/min operation conditions among the three MPTC methods, as shown in Table 5.4 and Table 5.5. Not surprisingly, the proposed method shows smaller $T_{r,rms}$ value both in 8 N·m and 4 N·m cases.

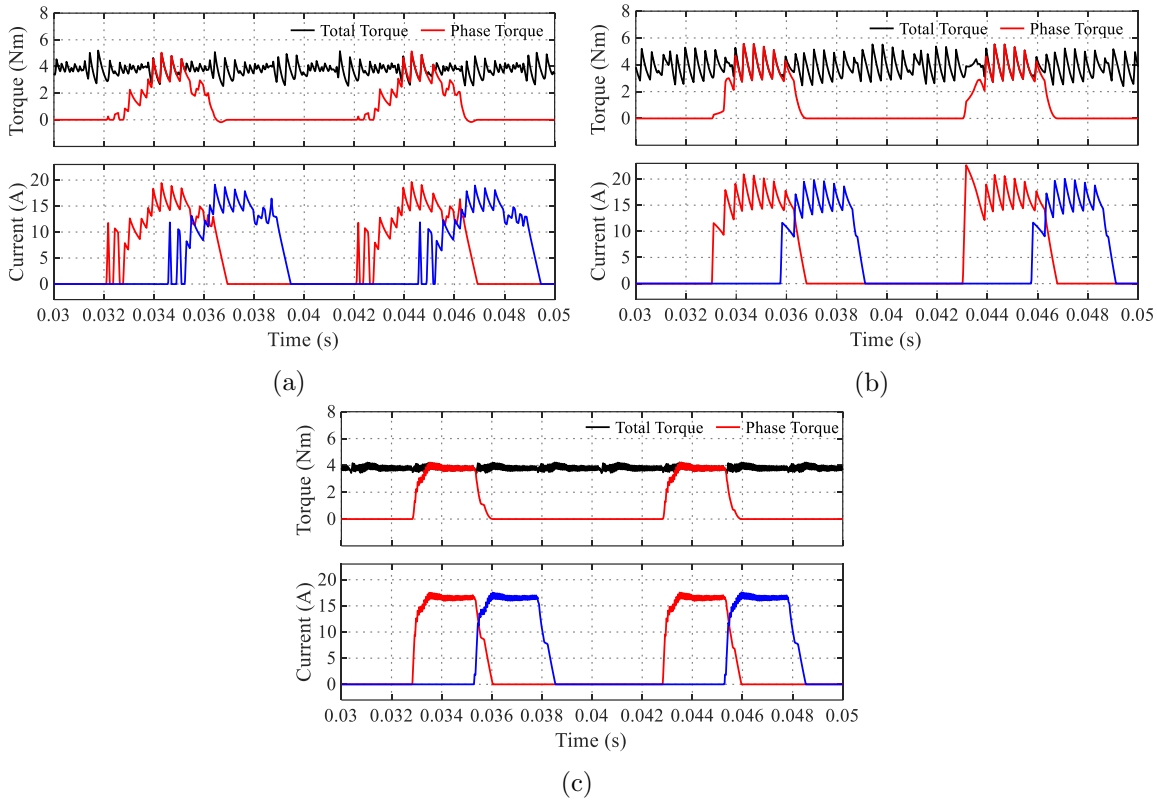

Figure 5.9: Simulation results of (a) the FCS MPTC method in (Peyrl *et al.*, 2009), (b) the FCS MPTC method in (Fang *et al.*, 2021a), and (c) the proposed CCS MPTC method when θ_1 is 8° at 1000 r/min and 4 N·m operation conditions.

Table 5.4: Simulated Performance Comparison at 1000 r/min and 4 N·m T_{ref}

Performance index	MPTC in (Peyrl *et al.*, 2009)	MPTC in (Fang *et al.*, 2021a)	CCS MPTC
$T_{r,rms}$	0.49	0.74	0.16
T_{ave} (N·m)	3.75	3.85	3.81
I_{rms} (A)	8.59	8.88	8.27
T_{ave}/I_{rms}	0.44	0.43	0.46

To further verify the torque control performance of the proposed method in a wide speed range, the high speed tests are carried out. Fig. 5.11 and Fig. 5.12 show the simulation results of the three MPTC methods at 3000 r/min and different torque

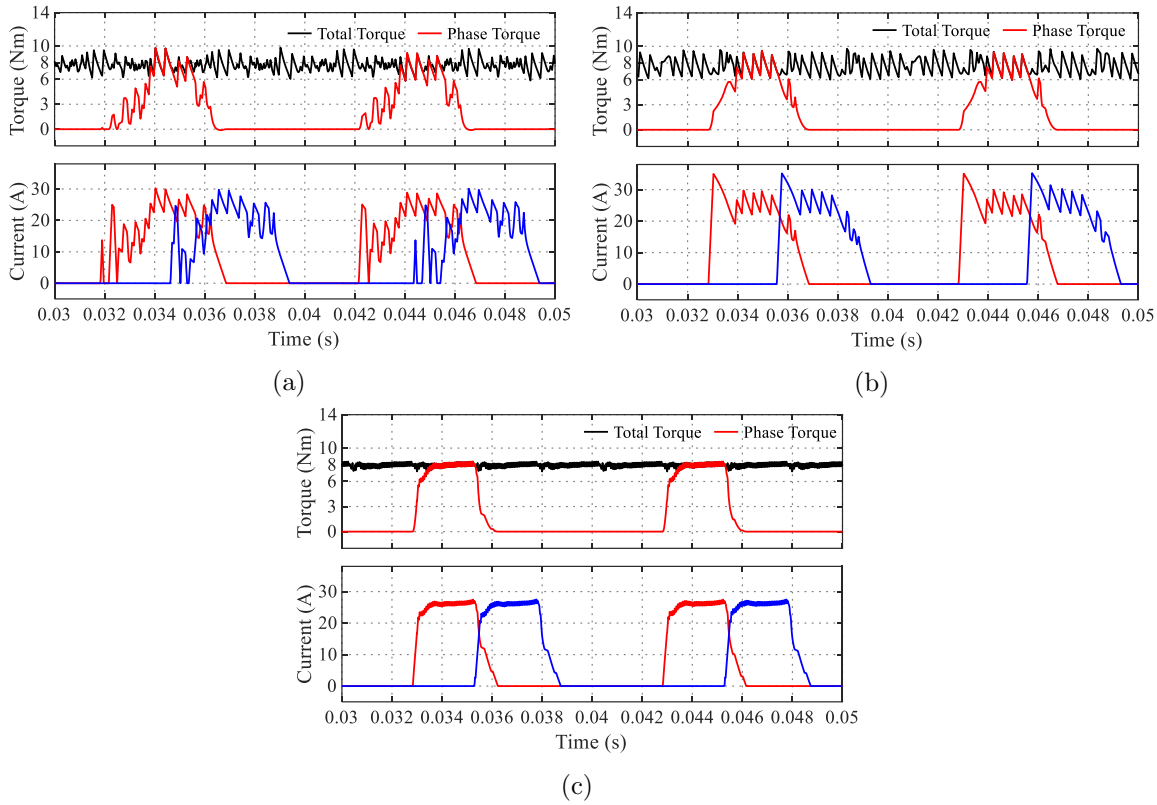

Figure 5.10: Simulation results of (a) the FCS MPTC method in (Peyrl *et al.*, 2009), (b) the FCS MPTC method in (Fang *et al.*, 2021a), and (c) the proposed CCS MPTC method when θ_1 is 8° at 1000 r/min and 8 N·m operation conditions.

Table 5.5: Simulated Performance Comparison at 1000 r/min and 8 N·m T_{ref}

Performance index	MPTC in (Peyrl *et al.*, 2009)	MPTC in (Fang *et al.*, 2021a)	CCS MPTC
$T_{r,rms}$	0.65	0.96	0.23
T_{ave} (N·m)	7.77	7.69	7.95
I_{rms} (A)	13.23	14.53	13.02
T_{ave}/I_{rms}	0.59	0.53	0.59

reference operation conditions. Please note that the auxiliary angle θ_1 is set at 5° for the proposed method for both 4 N·m load and 8 N·m load. From the results of the FCS MPTC methods shown in Fig. 5.11 and Fig. 5.12, it is observed that the

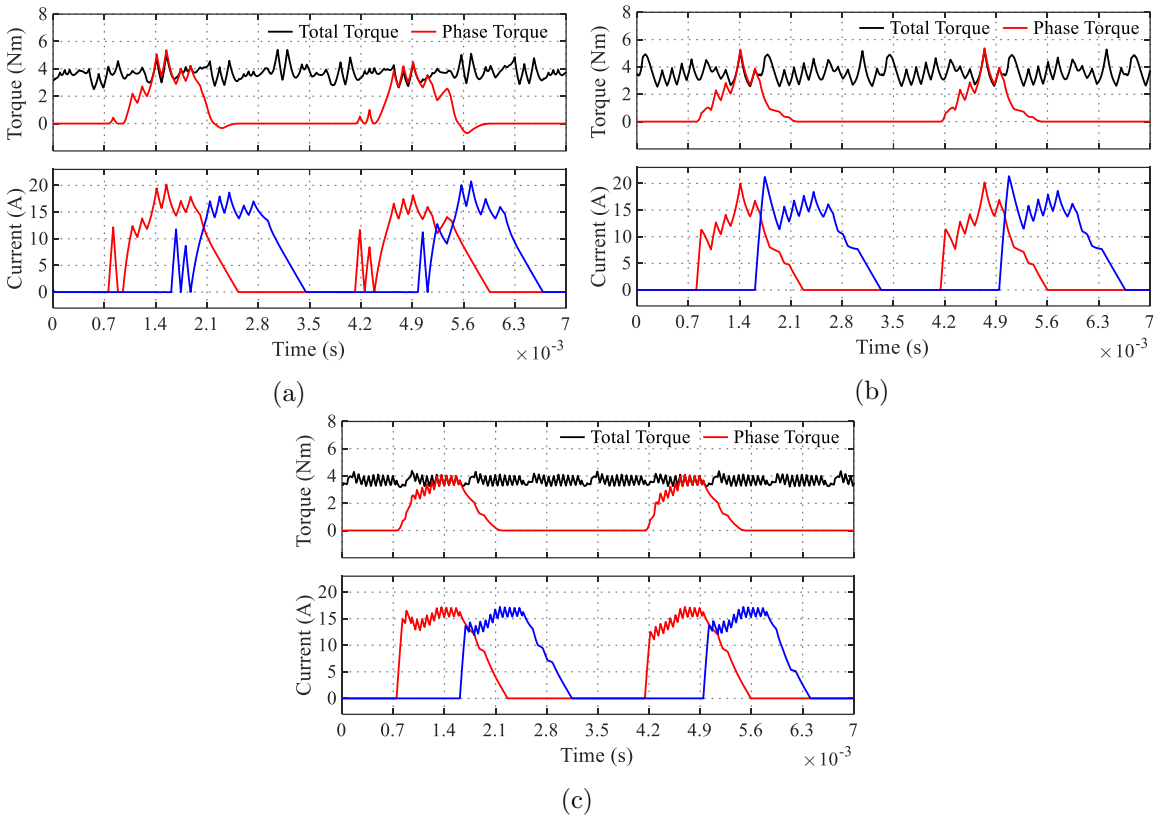

Figure 5.11: Simulation results of (a) the FCS MPTC method in (Peyrl *et al.*, 2009), (b) the FCS MPTC method in (Fang *et al.*, 2021a), and (c) the proposed CCS MPTC method when θ_1 is 5° at 3000 r/min and 4 N·m operation conditions.

Table 5.6: Simulated Performance Comparison at 3000 r/min and 4 N·m T_{ref}

Performance index	MPTC in (Peyrl *et al.*, 2009)	MPTC in (Fang *et al.*, 2021a)	CCS MPTC
$T_{r,rms}$	0.44	0.58	0.24
T_{ave} (N·m)	3.69	3.60	3.66
I_{rms} (A)	8.63	8.37	8.33
T_{ave}/I_{rms}	0.43	0.43	0.44

output torque fluctuates around the setting reference value with significant ripples for both FCS MPTC methods. The torque waveforms of the proposed method shown in Fig. 5.11(c) and Fig. 5.12(c) exhibit smoother output torque with lower ripples.

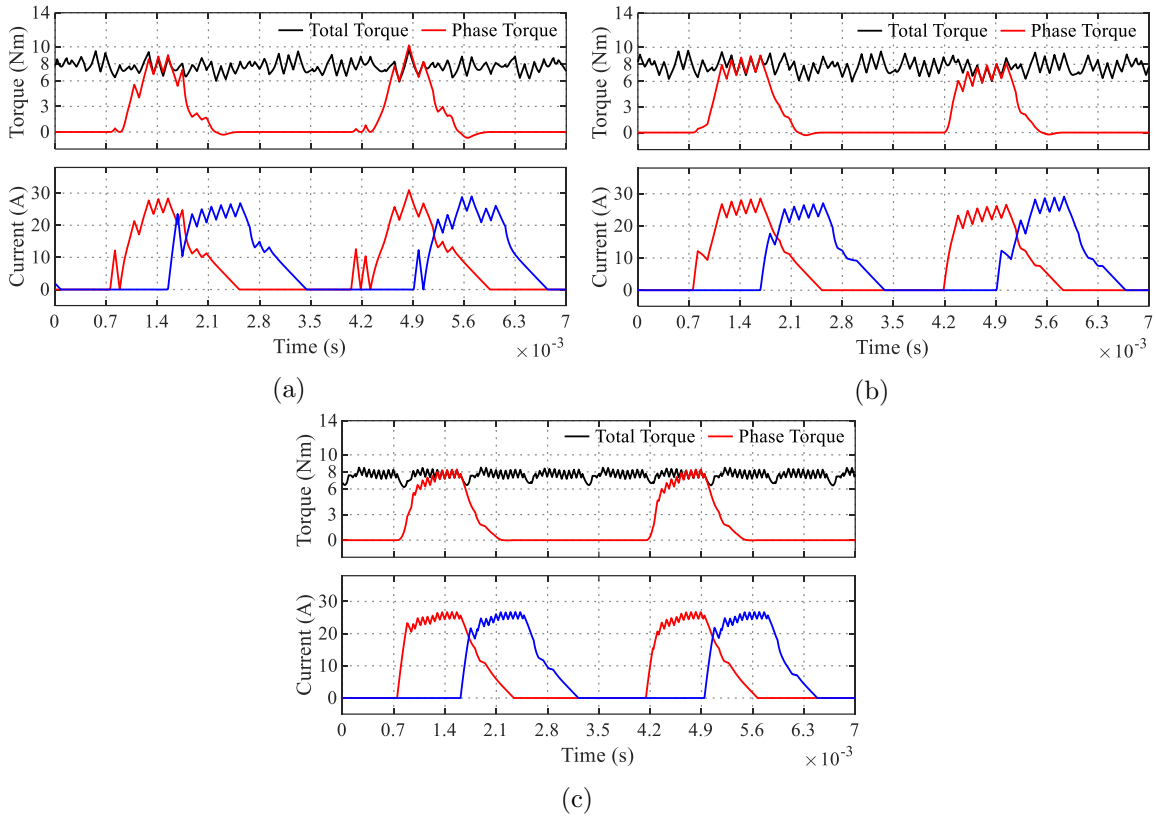

Figure 5.12: Simulation results of (a) the FCS MPTC method in (Peyrl *et al.*, 2009), (b) the FCS MPTC method in (Fang *et al.*, 2021a), and (c) the proposed CCS MPTC method when θ_1 is 5° at 3000 r/min and 8 N·m operation conditions.

Table 5.7: Simulated Performance Comparison at 3000 r/min and 8 N·m T_{ref}

Performance index	MPTC in (Peyrl *et al.*, 2009)	MPTC in (Fang *et al.*, 2021a)	CCS MPTC
$T_{r,rms}$	0.62	0.71	0.45
T_{ave} (N·m)	7.71	7.78	7.62
I_{rms} (A)	13.03	12.90	12.81
T_{ave}/I_{rms}	0.59	0.60	0.59

To quantitatively compare the control performance of the three mentioned methods at 3000 r/min, Table 5.6 and Table 5.7 list the performance indices. It can be seen that the $T_{r,rms}$ value of the proposed CCS MPTC method is lower compared to

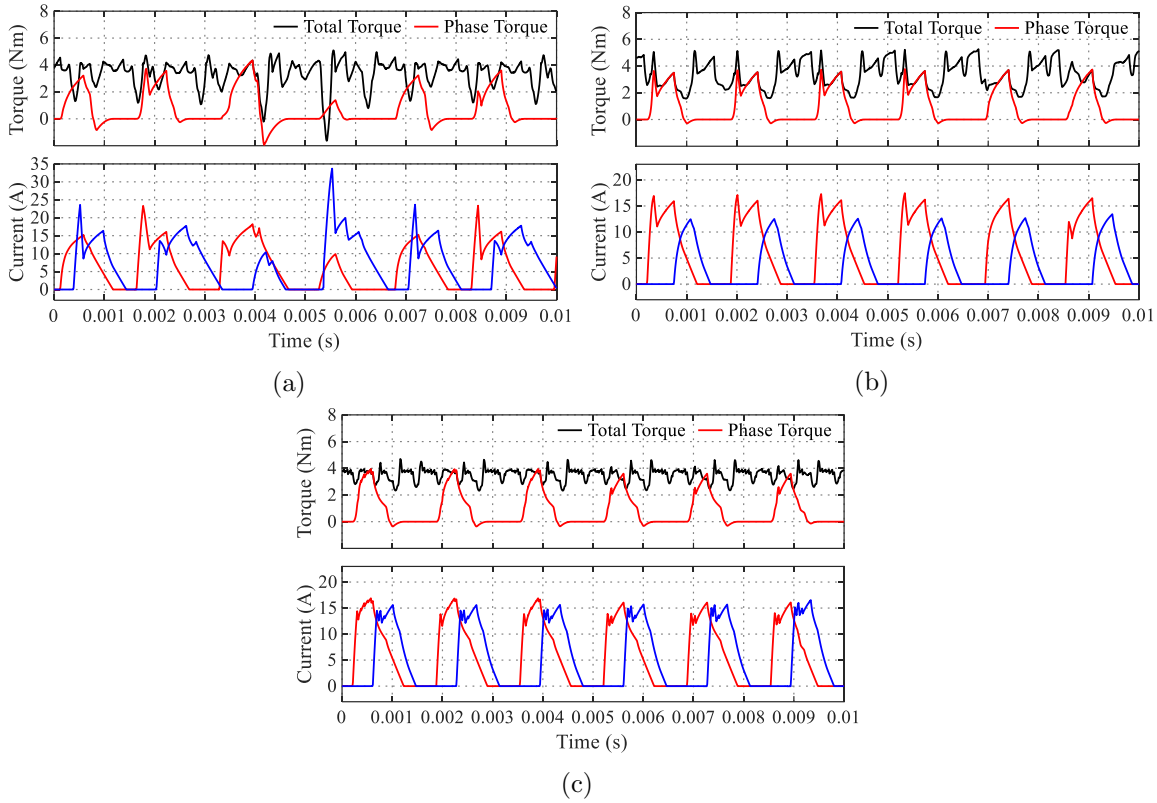

Figure 5.13: Simulation results of (a) the FCS MPTC method in (Peyrl *et al.*, 2009), (b) the FCS MPTC method in (Fang *et al.*, 2021a), and (c) the proposed CCS MPTC method when θ_1 is 4° at 6000 r/min and 4 N·m operation conditions.

Table 5.8: Simulated Performance Comparison at 6000 r/min and 4 N·m T_{ref}

Performance index	MPTC in (Peyrl *et al.*, 2009)	MPTC in (Fang *et al.*, 2021a)	CCS MPTC
$T_{r,rms}$	1.00	0.99	0.47
T_{ave} (N·m)	3.33	3.35	3.49
I_{rms} (A)	9.53	8.01	8.42
T_{ave}/I_{rms}	0.35	0.42	0.42

that of the other two methods. The other performance indices, such as T_{ave}, I_{rms}, and torque per ampere ratio T_{ave}/I_{rms} of the three methods show close values.

Fig. 5.13 shows the simulated waveforms of the three methods at 6000 r/min

and 4 N·m operation conditions. Since the method in (Peyrl *et al.*, 2009) probably keeps a significant current around the aligned position, the generated negative torque degrades the torque control performance, as explained in (Fang *et al.*, 2021a). Due to the above reason, the torque waveform in Fig. 5.13(a) shows large torque ripples and significant negative torque at some regions. Besides, the current waveforms of different phases also become different. Fig. 5.13(b) shows the torque and current waveforms for the FCS MPTC method in (Fang *et al.*, 2021a). Although significant torque ripples are observed, it shows better performance regarding the peak to peal torque ripple compared to the results shown in Fig. 5.13(a). Fig. 5.13(c) shows the torque and current waveforms of the proposed CCS MPTC method. Please note the auxiliary angle θ_1 is set at 4° in this case. Although the torque ripple increases at the rated speed, the proposed method still has much better torque control performance compared to the results shown in Fig. 5.13(a) and Fig. 5.13(b), which proves the superiority of the proposed method in a wide speed range.

Table 5.8 shows the comparison of the performance indices among the three methods at 6000 r/min and 4 N·m torque reference conditions. At this case, the $T_{r,rms}$ value of the proposed method is 0.47, which proves the low torque ripple feature of the proposed method compared to the value 1.00 and 0.99 of the other two FCS MPTC methods. Due to the generated negative torque, the method in (Peyrl *et al.*, 2009) has lower average torque and lower torque per ampere ratio. The method in (Fang *et al.*, 2021a) and the proposed method have close values regarding the rest of the performance indicators.

5.5 Experimental Validation

To test the control performance of the proposed CCS MPTC method in the real environment, experimental tests are carried out on a four-phase 8/6 SRM setup. The experimental rig is shown in Fig. 3.23, which consists of SRM, SRM controller and inverter, induction machine (IM), and IM controller. During the testing, the IM controls the shaft speed. Once the torque reference is applied and the SRM runs as a motor, the IM serves as a generator automatically. The digital signal processor TSM320F28335 is used to implement the mentioned three MPTC methods and the control frequency is set at 15 kHz for all the MPTC methods. For all the experimental tests, the weight factor ω_1 and the auxiliary angle θ_1 are set to the same values used in the simulation.

To evaluate the complexity of the proposed method, the computational burden of the mentioned three MPTC methods is discussed. The computational burden of the three MPTC methods can be mainly divided into three parts, which are the data preparation period, iteration period, and processing period after iteration. The detailed calculation burden for each part of the three MPTC methods is summarized in Table 5.9.

It can be observed that the computational burden in the data preparation period for the three methods is probably close. This is because all the methods need to sample the rotor position, phase current and estimate the flux-linkage and the current at $k+1$ sampling instant. Moreover, all the above quantities in the data preparation period only need to be calculated once in one control period. Please note the transformation $f^{f}_{Nl2Li}(i_{Nl}, \theta)$ is represented by the simple fourth-order polynomial.

Comparing the computational burden between the FCS MPTC methods in (Peyrl

Table 5.9: Computational Burden Comparison among Different MPTC Methods

Method	FCS MPTC in (Peyrl *et al.*, 2009)	FCS MPTC in (Fang *et al.*, 2021a)	Proposed CCS MPTC
Data preparation	θ_k, i_k sampling ψ_k from 2D LUT ψ_{kp1} calculation i_{kp1} from 2D LUT	θ_k, i_k sampling $i_{Li,f} = f^f_{Nl2Li}(i_{Nl}, \theta)$ ψ_{kp1}, $i_{Li,f,kp1}$ calculation	θ_k, i_k sampling $i_{Li,f} = f^f_{Nl2Li}(i_{Nl}, \theta)$ ψ_{kp1}, $i_{Li,f,kp1}$ calculation
Iteration	ψ_{kp2} calculation i_{kp2}, T_{kp2} from 2D LUTs	ψ_{kp2}, $i_{Li,f,kp2}$ calculation $i_{Nl,kp2} = f^f_{Li2Nl}(i_{Li,f,kp2}, \theta)$ $i_{Li,T,kp2} = f^T_{Nl2li}(i_{Nl,kp2}, \theta)$ T_{kp2} calculation	ψ_{kp2}, $i_{Li,f,kp2}$ calculation $i_{Li,T,kp2} =$ $f_{Lif2liT}(i_{Li,f,kp2}, \theta)$ T_{kp2} calculation
	9 iterations	6 iterations	(4+1) iterations
Processing after iteration	\	\	Calculating λ and $T_{ref,kp2}$ for one active constrain PWM duty calculation
Execution time in DSP	63.72 μs	49.68 μs	47.48 μs

et al., 2009) and (Fang *et al.*, 2021a) in the iteration period, it seems that the latter method shows slightly heavy computational burden in one iteration. However, it is noted the transformation $f^f_{Li2Nl}(i_{Li,f,kp2}, \theta)$ is represented by the simple fourth-order polynomial, and the transformation $f^T_{Nl2Li}(i_{Nl,kp2}, \theta)$ is represented by the simple third-order polynomial. The quantities $i_{Li,f,kp2}$ and T_{kp2} are calculated by the simple formulas derived under unsaturated case for SRMs. Moreover, the iteration number of the FCS MPTC method in (Fang *et al.*, 2021a) is only 2/3 of that for the conventional FCS MPTC method in (Peyrl *et al.*, 2009). The experimental measurement shows the execution time for the MPTC algorithm in (Peyrl *et al.*, 2009) is 63.72 μs in total, and that for the MPTC algorithm in (Fang *et al.*, 2021a) is 49.68 μs in total. This difference is reasonable since the iteration number is significantly reduced for the MPTC method in (Fang *et al.*, 2021a) and the calculation for the MPTC method

in (Fang *et al.*, 2021a) is simple.

Comparing with the FCS MPTC method in (Fang *et al.*, 2021a), the proposed method requires only one transformation in the iteration period. Please note that this transformation $f_{LifLiT}(i_{Li,f,kp2}, \theta)$ is represented by the simple fourth-order polynomial. Moreover, the number of iterations is also reduced to 4+1. The extra one iteration for the proposed method is used to obtain the torque information at the freewheeling state, which is used to calculate the torque variation rate later. Therefore, the computational burden is less for the proposed method in the iteration period. As for the processing after iteration, it is true that the proposed method needs to calculate the Lagrange multiplier, the torque references, and the PWM duty for each phase. However, these calculations are simple and needed once for one control period. Finally, the experimental measurement shows the proposed CCS MPTC method consumes 47.48 μs in total for the whole algorithm, which is the least among the three methods. Please note the switching signals assignment and digital to analog conversion are not shown in Table 5.9 since these are the same for the three methods.

5.5.1 Steady-State Performance Comparison

Fig. 5.14 show the experimental results for the two FCS MPTC methods and the proposed CCS MPTC method at 500 r/min and 8 N·m T_{ref} operation conditions. It is observed that all three MPTC methods effectively eliminate the commutation torque ripple. However, there are large high-frequency torque ripples for the FCS MPTC methods, which mainly result from the limited voltage vectors. On the other hand, the proposed CCS MPTC method significantly reduces this high frequency torque ripple and well controls the shaft torque closely around the torque command

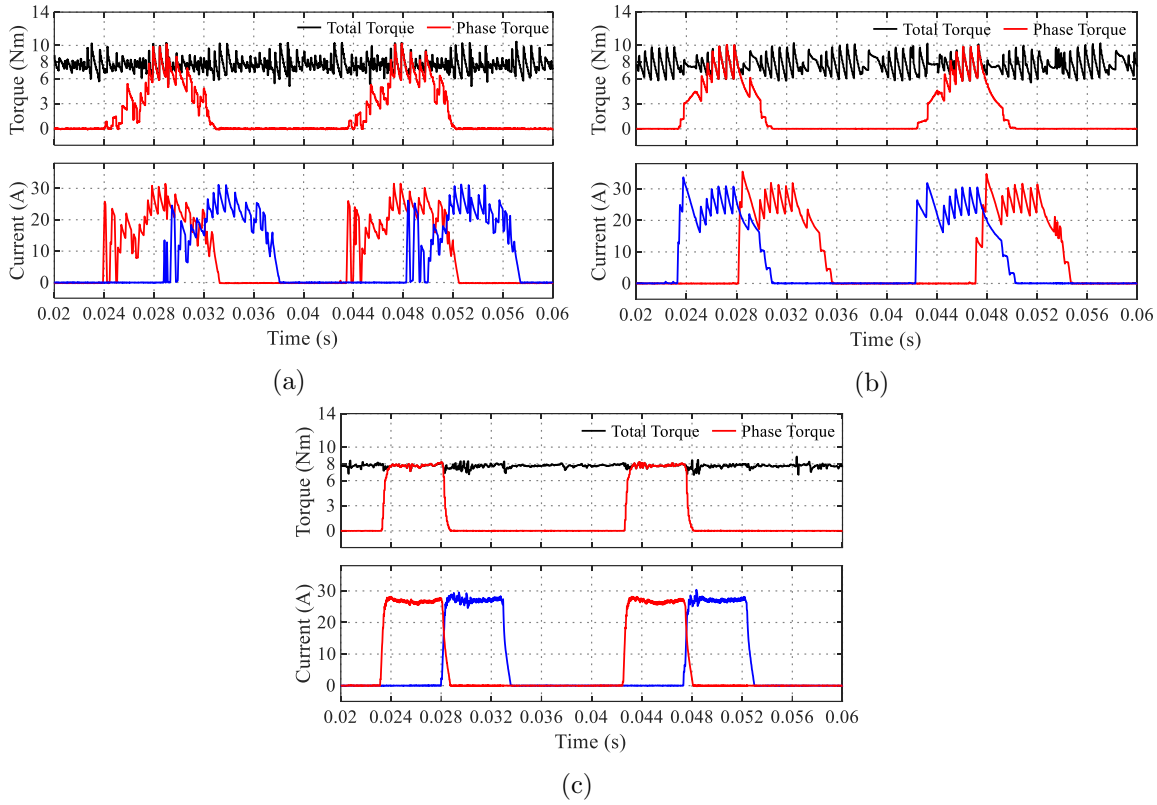

Figure 5.14: Experimental results of (a) the FCS MPTC method in (Peyrl *et al.*, 2009), (b) the FCS MPTC method in (Fang *et al.*, 2021a), and (c) the proposed CCS MPTC method when θ_1 is 8° at 500 r/min and 8 N·m operation conditions.

Table 5.10: Experimental Performance Comparison at 500 r/min and 8 N·m T_{ref}

Performance index	MPTC in (Peyrl *et al.*, 2009)	MPTC in (Fang *et al.*, 2021a)	CCS MPTC
$T_{r,rms}$	0.95	1.12	0.25
T_{ave} (N·m)	7.70	7.67	7.75
I_{rms} (A)	13.30	13.90	13.28
T_{ave}/I_{rms}	0.58	0.55	0.58

value. As for the phase current, it is found the current ripples of the FCS MPTC method are much higher. The above comparisons show the superiority of the proposed CCS MPTC method on torque control.

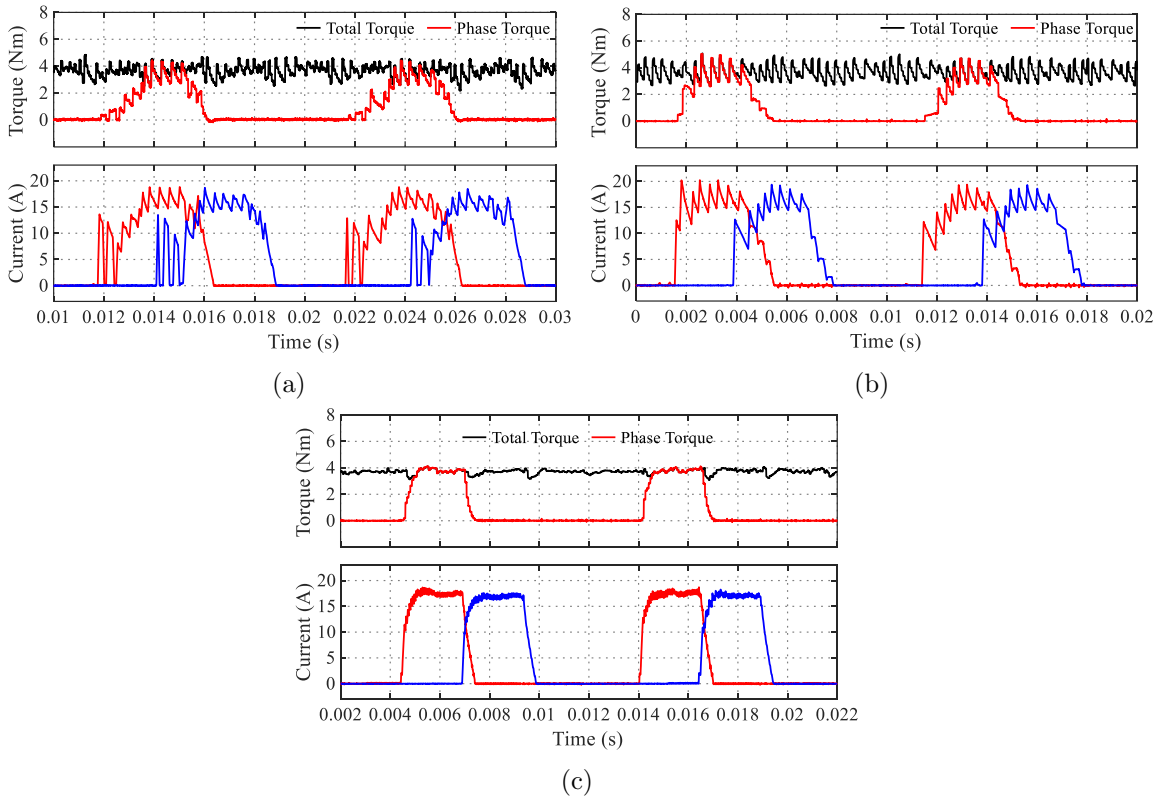

Figure 5.15: Experimental results of (a) the FCS MPTC method in (Peyrl *et al.*, 2009), (b) the FCS MPTC method in (Fang *et al.*, 2021a), and (c) the proposed CCS MPTC method when θ_1 is 8° at 1000 r/min and 4 N·m operation conditions.

Table 5.11: Experimental Performance Comparison at 1000 r/min and 4 N·m T_{ref}

Performance index	MPTC in (Peyrl *et al.*, 2009)	MPTC in (Fang *et al.*, 2021a)	CCS MPTC
$T_{r,rms}$	0.55	0.62	0.19
T_{ave} (N·m)	3.66	3.68	3.71
I_{rms} (A)	8.68	8.45	8.39
T_{ave}/I_{rms}	0.42	0.44	0.44

Table 5.10 shows the $T_{r,rms}$, T_{ave}, and I_{rms} comparison for the mentioned three MPTC methods. The performance index $T_{r,rms}$ is found reduced to 0.25 of the CCS MPTC method from 0.95 of the FCS MPTC method in (Peyrl *et al.*, 2009) and 1.12 of the MPTC method in (Fang *et al.*, 2021a). The I_{rms} value of the CCS MPTC

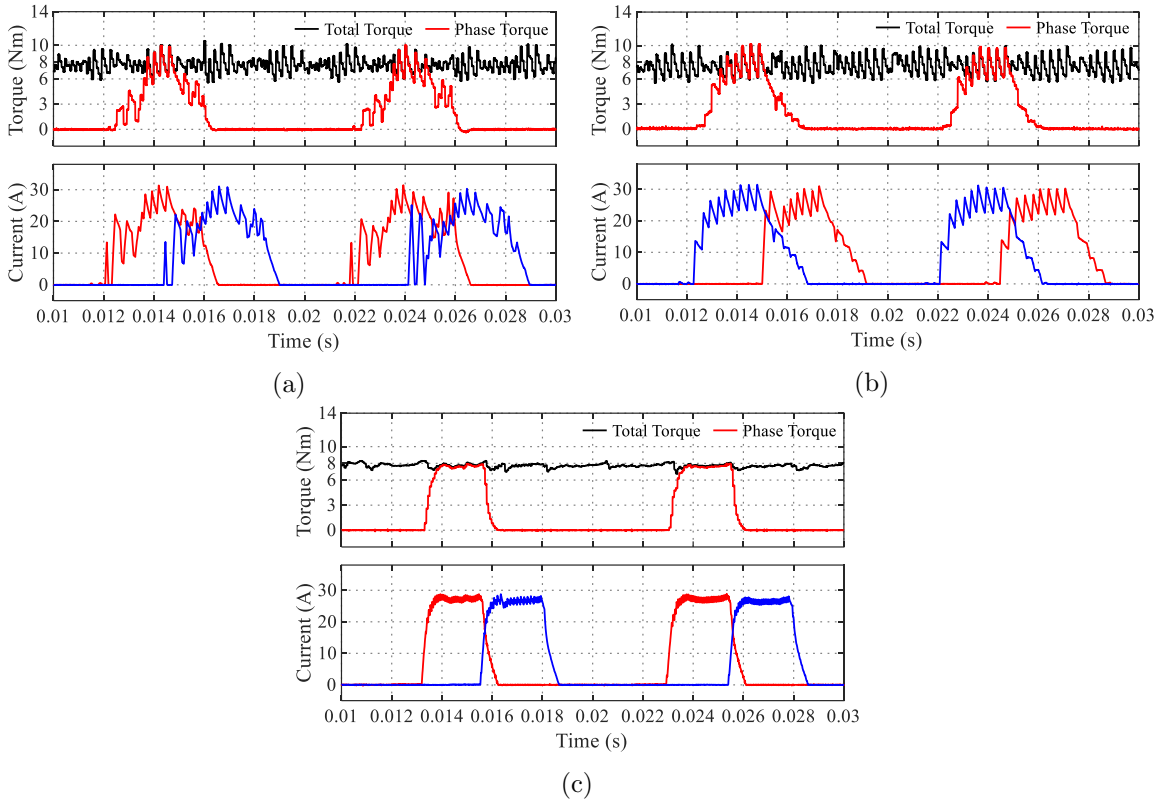

Figure 5.16: Experimental results of (a) the FCS MPTC method in (Peyrl *et al.*, 2009), (b) the FCS MPTC method in (Fang *et al.*, 2021a), and (c) the proposed CCS MPTC method when θ_1 is 8° at 1000 r/min and 8 N·m operation conditions.

Table 5.12: Experimental Performance Comparison at 1000 r/min and 8 N·m T_{ref}

Performance index	MPTC in (Peyrl *et al.*, 2009)	MPTC in (Fang *et al.*, 2021a)	CCS MPTC
$T_{r,rms}$	1.04	1.21	0.26
T_{ave} (N·m)	7.70	7.58	7.73
I_{rms} (A)	12.98	13.44	13.12
T_{ave}/I_{rms}	0.59	0.56	0.59

method is slightly lower compared to that of the FCS MPTC methods.

Fig. 5.15 and Fig. 5.16 present the experimental results at 1000 r/min and different T_{ref} operation conditions for the three MPTC methods. These results further prove

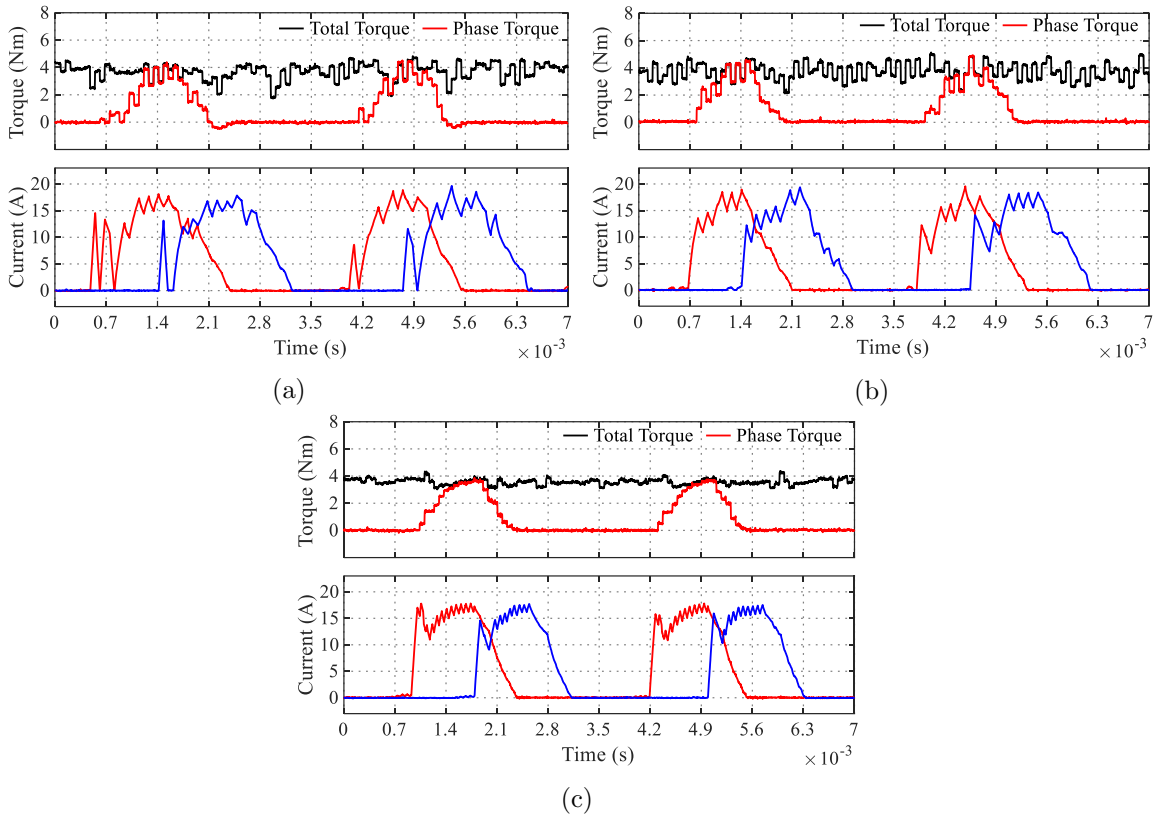

Figure 5.17: Experimental results of (a) the FCS MPTC method in (Peyrl *et al.*, 2009), (b) the FCS MPTC method in (Fang *et al.*, 2021a), and (c) the proposed CCS MPTC method when θ_1 is 5° at 3000 r/min and 4 N·m operation conditions.

the large high-frequency torque ripple issue of the FCS MPTC methods and excellent torque control performance of the proposed CCS MPTC method. Table 5.11 and Table 5.12 also compare the $T_{r,rms}$, T_{ave}, and I_{rms} for 1000 r/min operation conditions. Not surprisingly, the $T_{r,rms}$ value is significantly reduced for the proposed method.

The experimental results of the three MPTC methods at 3000 r/min and 4 N·m operation conditions are described in Fig. 5.17. Please note the auxiliary angle θ_1 is set at the same value as the simulation results in Fig. 5.11(c), namely 5° in this operating condition. Due to the hold feature of the digital to analog converter (DAC) and the limited control frequency, the captured torque waveforms is not continuous

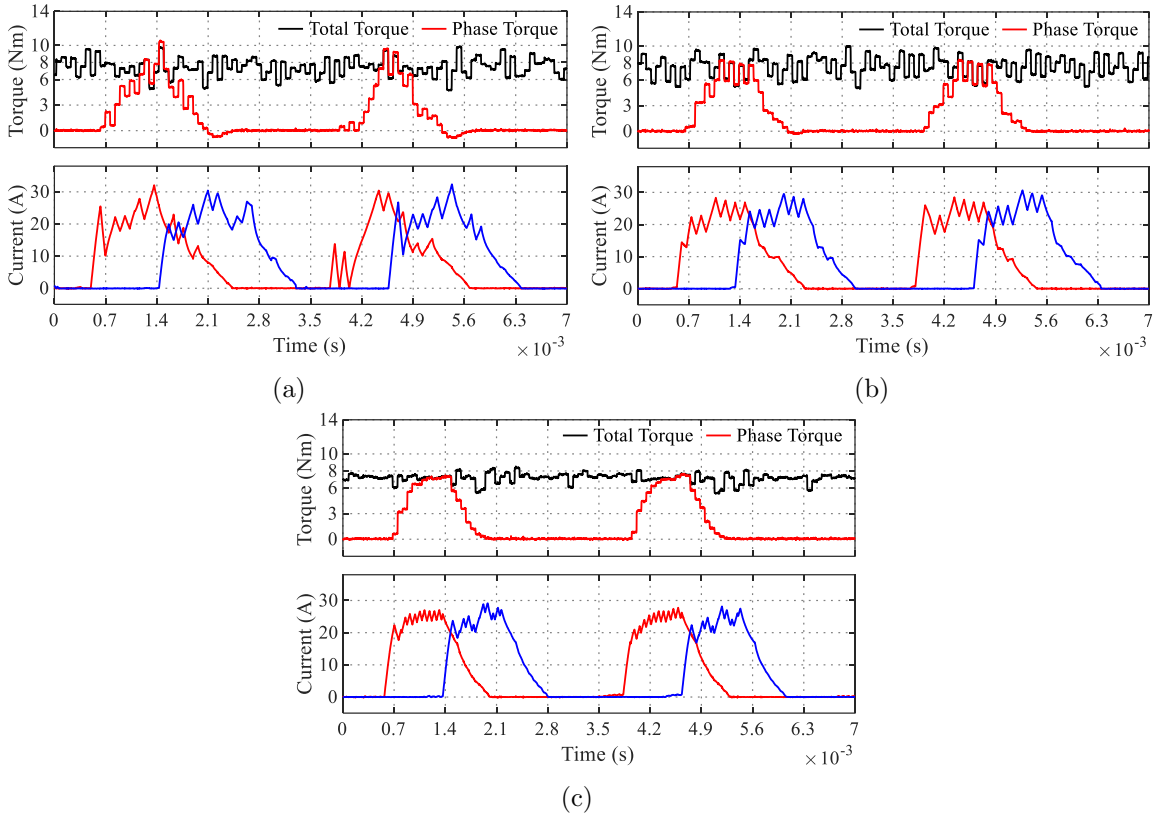

Figure 5.18: Experimental results of (a) the FCS MPTC method in (Peyrl *et al.*, 2009), (b) the FCS MPTC method in (Fang *et al.*, 2021a), and (c) the proposed CCS MPTC method when θ_1 is 5° at 3000 r/min and 8 N·m operation conditions.

and the stairs between two adjacent control periods are obvious. From the presented torque and current waveforms in Fig. 5.17, it can be observed that the proposed CCS MPTC method has smoother output torque and lower current ripples, as expected. Fig. 5.18 shows the experimental results of the three mentioned methods at 3000 r/min and 8 N·m operation conditions. The auxiliary angle θ_1 is also set at the same value 5° for the proposed method. Similarly, it is found that the proposed method keeps the lower torque ripples feature. These two experimental results prove that the proposed method also has outstanding torque control performance at the high speed range compared to the other two FCS MPTC methods.

Table 5.13: Experimental Performance Comparison at 3000 r/min and 4 N·m T_{ref}

Performance index	MPTC in (Peyrl *et al.*, 2009)	MPTC in (Fang *et al.*, 2021a)	CCS MPTC
$T_{r,rms}$	0.60	0.63	0.22
T_{ave} (N·m)	3.70	3.74	3.57
I_{rms} (A)	8.55	8.26	8.15
T_{ave}/I_{rms}	0.43	0.45	0.44

Table 5.14: Experimental Performance Comparison at 3000 r/min and 8 N·m T_{ref}

Performance index	MPTC in (Peyrl *et al.*, 2009)	MPTC in (Fang *et al.*, 2021a)	CCS MPTC
$T_{r,rms}$	1.05	1.22	0.55
T_{ave} (N·m)	7.43	7.56	7.17
I_{rms} (A)	13.11	12.97	12.21
T_{ave}/I_{rms}	0.57	0.58	0.59

Table 5.13 and Table 5.14 summarize the performance indices of the three mentioned methods at 3000 r/min operation condition. At 4 N·m T_{ref} condition, the proposed method reduced the $T_{r,rms}$ value from 0.60 of the MPTC method in (Peyrl *et al.*, 2009), 0.63 of the MPTC method in (Fang *et al.*, 2021a) to 0.22. The other performance, including the average torque, rms value of the phase current, and the torque per ampere ratio is close for the three methods at this condition. When the T_{ref} value is 8 N·m, the proposed method still has much lower $T_{r,rms}$ value compared to the other two methods. Although the proposed method shows slightly lower average torque, in this case, it will not be an issue since there normally is a speed loop except for the torque loop, and this speed loop will take care of the torque reference value. Besides, the torque per ampere ratio of the proposed method is the highest in this case.

Fig. 5.19 shows experimental results of the three methods at 5000 r/min and 4 N·m

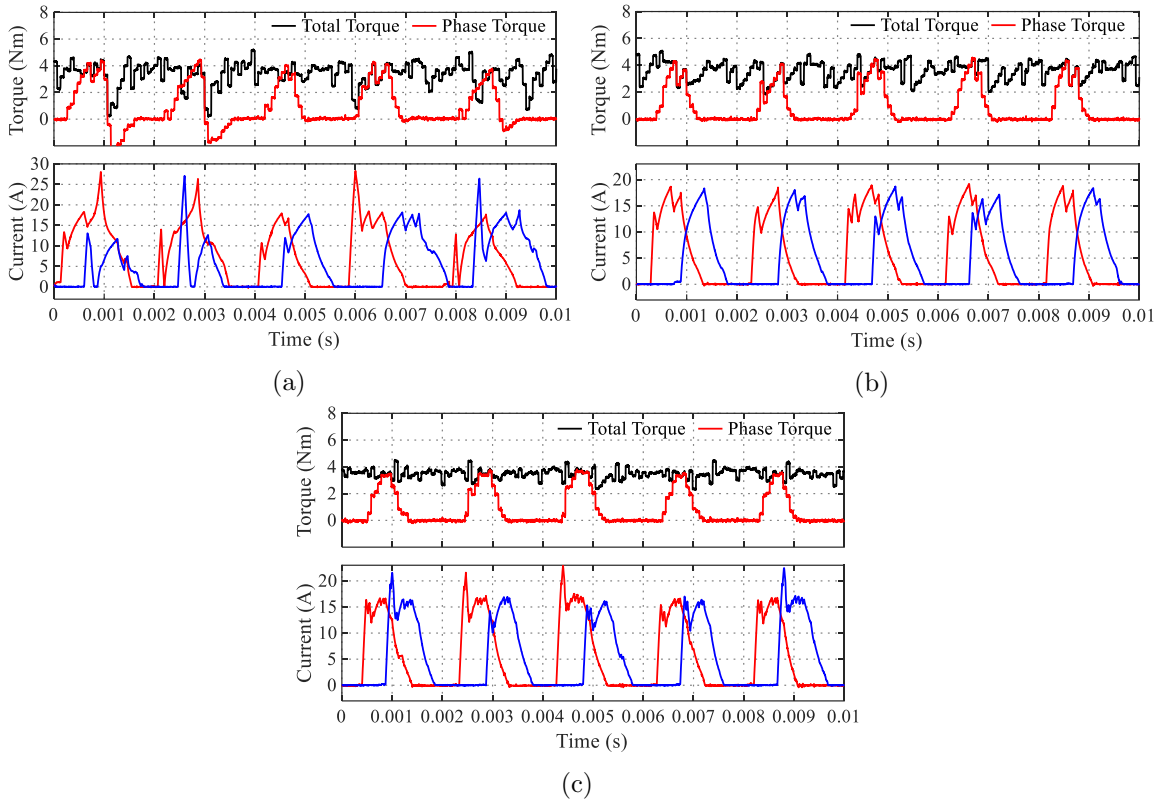

Figure 5.19: Experimental results of (a) the FCS MPTC method in (Peyrl *et al.*, 2009), (b) the FCS MPTC method in (Fang *et al.*, 2021a), and (c) the proposed CCS MPTC method when θ_1 is 4° at 5000 r/min and 4 N·m operation conditions.

operating conditions. As explained previously, the generated negative torque in (Peyrl *et al.*, 2009) degrades its high-speed torque control performance. Not surprisingly, in Fig. 5.19 (a), the negative toque and significant torque ripples are clearly found for the FCS MPTC method in (Peyrl *et al.*, 2009). Fig. 5.19 (b) shows results for the MPTC method in (Fang *et al.*, 2021a), the negative torque issue is addressed and the torque control performance is improved compared to that of the method in (Peyrl *et al.*, 2009). The torque and current waveforms of the proposed method are shown in Fig. 5.19 (c). From the presented waveforms, it is clearly observed that the proposed method has smoother output torque and lower torque ripples, which proves

Table 5.15: Experimental Performance Comparison at 5000 r/min and 4 N·m T_{ref}

Performance index	MPTC in (Peyrl *et al.*, 2009)	MPTC in (Fang *et al.*, 2021a)	CCS MPTC
$T_{r,rms}$	0.93	0.70	0.37
T_{ave} (N·m)	3.36	3.57	3.47
I_{rms} (A)	9.51	8.45	8.49
T_{ave}/I_{rms}	0.35	0.42	0.41

the superiority of the proposed method at high speed range.

Table 5.15 summarizes the performance indices for the 5000 r/min and 4 N·m operation conditions. It can be found the $T_{r,rms}$ value is reduced to 0.37 of the proposed method from the 0.93 of the method in (Peyrl *et al.*, 2009) and 0.70 of the method in (Fang *et al.*, 2021a). As for the rest of the performance indices, the proposed method shows the close values with that of the method in (Fang *et al.*, 2021a). Due to the negative torque, the method in (Peyrl *et al.*, 2009) has the lowest torque per ampere ratio value. These numbers quantitatively shows the good torque performance of the proposed method at high speed range.

5.5.2 Dynamic-State Performance Comparison

To further verify the performance of the proposed method, the torque waveforms at the dynamic operation conditions are captured and compared. Fig 5.20 and Fig 5.21 show the total torque, speed, and phase current waveforms for the FCS MPTC method in (Fang *et al.*, 2021a) and proposed CCS MPTC method when the shaft speed rises from 1000 r/min to 2000 r/min. The torque command is set at 4 N·m. Please note the shaft speed is controlled by the IM and the auxiliary angle is fixed at 8° for the proposed method. It can be observed from the torque waveforms that the proposed

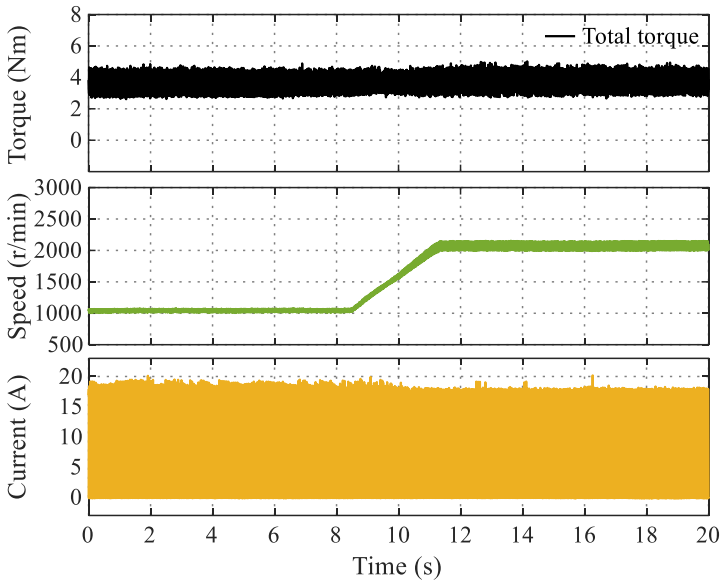

Figure 5.20: Experimental results for the FCS MPTC method in (Fang *et al.*, 2021a) at speed transient from 1000 r/min to 2000 r/min.

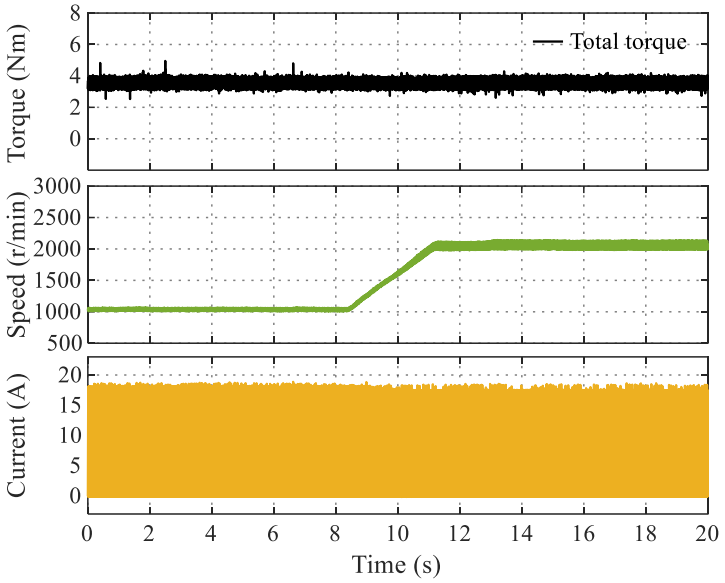

Figure 5.21: Experimental results for the proposed CCS MPTC method at speed transient from 1000 r/min to 2000 r/min when θ_1 is fixed at 8°.

method delivers the shaft torque with lower torque ripples in the whole period. And the $T_{r,rms}$ performance index is reduced from 0.35 of the FCS MPTC method to 0.17

of the proposed CCS MPTC method, which is as expected. Please note the $T_{r,rms}$ values of both methods are evaluated based on the whole captured period. Since the sample interval is increased in this long recording period, the calculated $T_{r,rms}$ values in this case are both smaller than that shown in Table 5.11.

Fig 5.22 and Fig 5.23 show the measured total torque, speed, and phase current waveforms for the FCS MPTC method in (Fang *et al.*, 2021a) and the proposed CCS MPTC method when the command torque stepped from 4 N·m to 8 N·m. The shaft speed is controlled at 1000 r/min. Please note the auxiliary angle is also fixed at 8° for the proposed method. It can be visually observed that the torque waveform of the proposed method shows lower torque ripples compared to that of the FCS MPTC method during the whole period. Due to the speed being controlled by the IM and the IM being operated as a generator, the shaft speed shows some transient change at the command torque step instant. Since the FCS MPTC method turns on the phase automatically and does not necessarily turn on the phase at exactly the same angle, its current waveforms might show some peaks, as shown in Fig 5.22.

5.6 Conclusion

The high torque ripple is one of the main drawbacks for the SRM drives. Although the FCS MPTC methods in the literature can effectively eliminate the commutation torque ripple, the limited voltage vectors lead to large high frequency torque ripples. To address this issue and enhance the torque control performance, a CCS MPTC method with low torque ripples is proposed in this chapter. The proposed CCS MPTC method is implemented based on the optimum torque references. And these optimum torque references are analytically obtained via the Lagrange multiplier

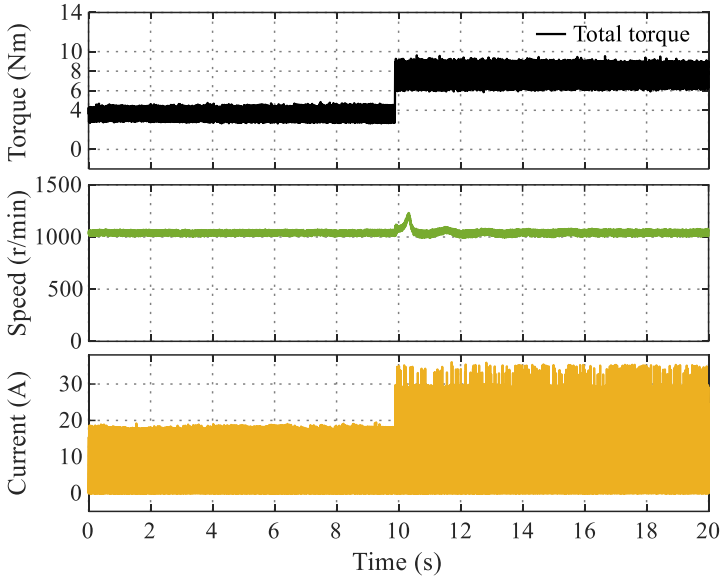

Figure 5.22: Experimental results for the FCS MPTC method in (Fang *et al.*, 2021a) when the torque command stepped from 4 N·m to 8 N·m.

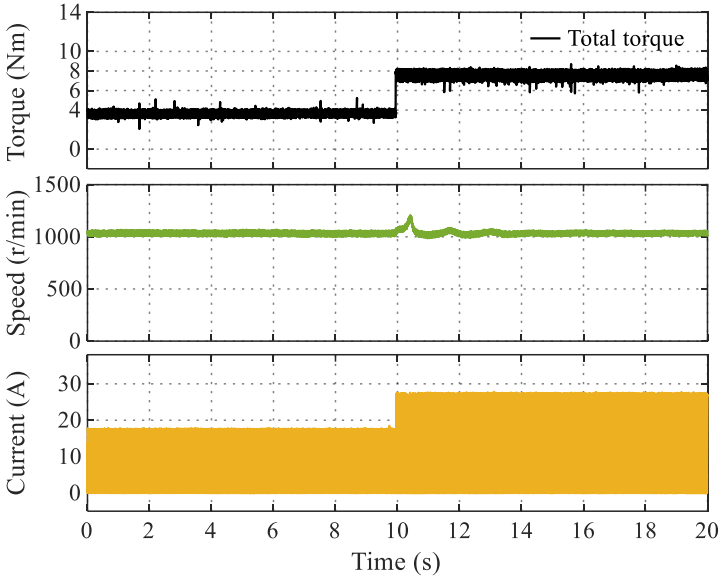

Figure 5.23: Experimental results for the proposed CCS MPTC method when the torque command stepped from 4 N·m to 8 N·m (Note: θ_1 is fixed at 8°.).

method after introducing the equivalent linear SRM model and modifying the cost function properly. Then, the PWM technique is employed to implement the above

optimum torque references. Several simple guidelines are given to tune the auxiliary angle to ensure good torque control performance in a wide speed range. Extensive simulation and experimental results reveal that the proposed CCS MPTC method significantly reduce the high frequency torque ripple compared to the conventional FCS MPTC methods in a wide speed range. Moreover, the current waveform of the proposed method has fixed frequency and shows much lower current ripples. The computational burden is also discussed and reveals that the proposed method shows the least execution time among the three MPTC methods.

Chapter 6

A Predictive Current Controller for SRMs with Robust Tracking Performance

6.1 Introduction

The previous chapters present several methods, especially the MPTC methods, to improve the torque control performance for SRM drives. Since there are still a significant amount of current profiling methods to reduce the torque ripple or/and acoustic noise, it is important to develop a robust current tracking controller.

An intersection-method-based current controller for the SRM with robust tracking performance is presented in this chapter. Firstly, with the aid of the predicted current at the next sampling instant, the pre-stored reference current, and the flux-linkage information, the required duty cycle for the next control period under specific reference current is estimated through the intersection method. To compensate for

the difference between the adopted flux-linkage model and the real ones inside the machine, a Lyapunov-based adaptive flux-linkage observer is presented. Hence, the heavy dependence issue on the accurate flux-linkage model for the current controller is resolved. With the above techniques, robust reference current tracking is achieved in a simple form and only one observer gain. Besides, a balanced switching scheme is presented to reduce the switching frequency requirement of the power transistors and evenly distribute the switching losses.

6.2 Drawbacks of the CCC Methods

The SRM is a type of electrical machine which only has the excitation winding on the stator. By neglecting the mutual coupling between phases, the terminal voltage for each phase can be expressed as (6.1).

$$v = Ri + \frac{d\psi}{dt} = Ri + \frac{\partial\psi}{\partial i}\frac{di}{dt} + \frac{\partial\psi}{\partial\theta}\frac{d\theta}{dt} \tag{6.1}$$

For the SRM driving system, the current chopping control (CCC) method is widely used as the current controller due to its compact structure and fast dynamic performance. According to the switching modes, the CCC method is classified into the soft current chopping (SCC) method and hard current chopping (HCC) method. The SCC method adopts magnetization mode ("1") and freewheeling mode ("0") excitation, while the HCC method utilizes magnetization mode and demagnetization mode ("-1"). The magnetization mode, freewheeling mode, and demagnetization mode for the applied asymmetrical half bridge inverter are shown in Fig. 2.4. Theoretically, the CCC method could track the reference current accurately if the control frequency

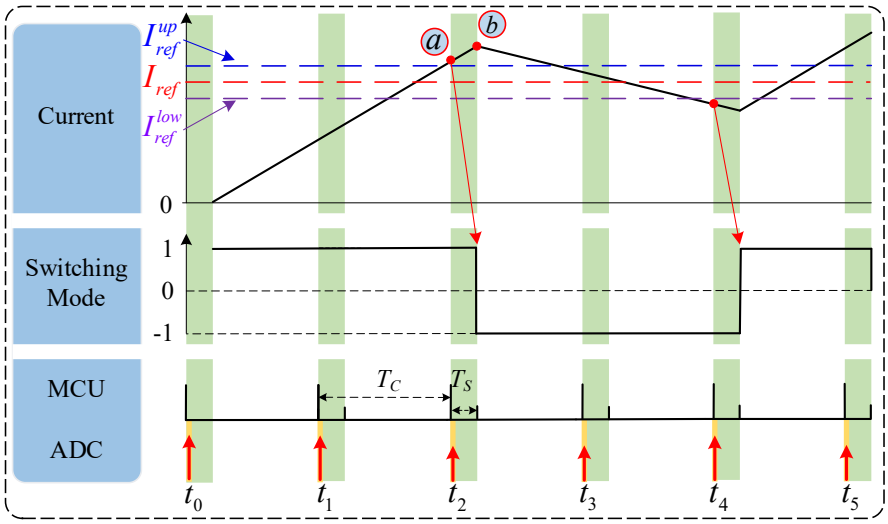

Figure 6.1: Relationship between phase current, switching modes, control period, and sampling rate in HCC mode. (Note: MCU indicates microcontroller unit and ADC represents analog-to-digital converter.)

and sampling rate are sufficiently high. However, the limited control frequency and sampling rate in practical applications degrade its tracking performance.

To clearly illustrate the effects of the control frequency and sampling rate on the tracking performance of the CCC method, the relationship between phase current, switching modes, control periods, and sampling rate in the HCC method is described in Fig. 6.1. The fixed current reference I_{ref} is assumed while the upper and lower bounds are I_{ref}^{up} and I_{ref}^{low}. Taking the second control period T_c as an example, the phase current is sampled at the starting instant t_1. Then, this value will be converted to the digital number after the ADC conversion time. Apparently, the conversion time is the duration from the sampling instant to the instant that the digital results are available. After the delay time T_s, the switching mode will be changed according to the relationship between the sampled current, upper, and lower bounds. It is noted that this amount of delay time includes the current sampling, position sampling, and

controller decision time. Since this sampled current is smaller than the upper bound in this instant, the magnetization mode is applied to this phase and the current keeps rising to the starting instant t_2 of the following control period. Due to the delay between the sampling instant and the switching mode changing instant, the current will keep rising to instant b of the third control period. The above sampling and switching mode variation process will be repeated for every control period. From this operation process, it is observed that the 100% duty cycle excitation and the delay time T_s are the two influential elements on its tracking performance for the HCC method.

The effects of 100% duty cycle excitation are summarized in the following two aspects: (a) The phase current responds in its maximum variation rate; (b) The value of the phase current possibly exceeds the upper bound at the end of the control period when the rotor speed is not high. Similar effects can be deduced from the negative bus voltage excitation, and the phase current descends at the largest current variation rate. It is straightforward to conclude that the fast response and large current ripples of the CCC method at medium and low speed range stem from the 100% duty cycle excitation. Hence, increasing the control frequency could effectively reduce the current ripples.

On the other hand, the delay time T_s affects the following aspects: (a) The current keeps ascending from point a to point b, but this effect will be eliminated after point b since the control period is kept the same after point b, as shown in Fig. 6.1; (b) This delay time limits the control frequency from further improvement.

From the analysis above, the control frequency and sampling rate are supposed to be increased simultaneously for the CCC method to reduce the current ripples.

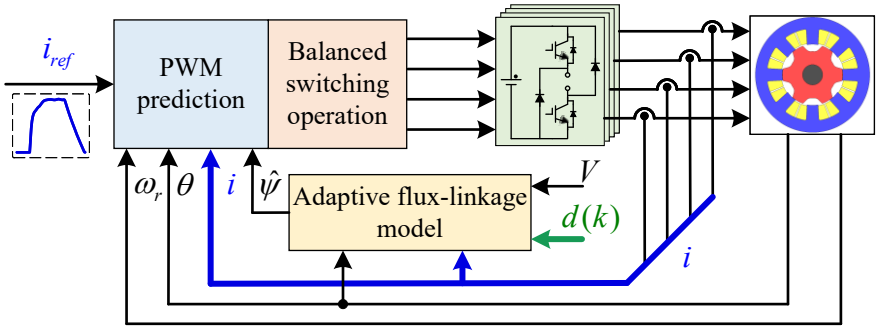

Figure 6.2: Block diagram for the proposed current controller.

However, this limitation is imposed by hardware, and it is normally costly to upgrade it. In this case, improving the current tracking performance by properly adjusting the excitation duty cycle becomes more effective and practical.

6.3 Proposed Current Controller

In this section, the proposed robust current controller is introduced, which mainly incorporates three parts: PWM duty cycle prediction module, adaptive flux-linkage model, and balanced switching operation, as shown in Fig. 6.2. The PWM duty prediction module generates the accurate duty cycle for the coming control period. Considering the possible model mismatch, an adaptive flux-linkage model is adopted to enhance the reference current tracking capability. Finally, the balanced switching strategy is presented to reduce the switching frequency.

6.3.1 PWM Duty Prediction Scheme

The prediction of the duty cycle applied to the coming control period is calculated based on the predicted current at the coming sampling instant and the intersection method.

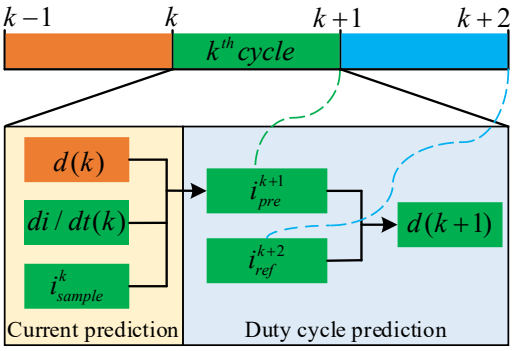

Figure 6.3: Execution sequence for the proposed duty cycle prediction method.

Fig. 6.3 explains the execution sequence of the proposed duty cycle estimation method. During the operation of k^{th} control cycle, which is bounded by the sampling instant k and $(k+1)$, the current i_{pre}^{k+1} that is expected to approach at the end of the k^{th} control cycle under the excitation of the calculated duty cycle $d(k)$ is firstly predicted as:

$$i_{pre}^{k+1} = i_{sample}^{k} + \frac{di}{dt} \times T_c = i_{sample}^{k} + \frac{V \times d(k) - i_{sample}^{k} R - \omega_r \times \partial\psi/\partial\theta}{\partial\psi/\partial\theta} \times T_c \quad (6.2)$$

where i_{sample}^{k} is the sampled current at the beginning of the k^{th} control cycle, T_c is the control period, and V is the bus voltage.

It is noted that the current variation rate is estimated based on the average voltage applied on the k^{th} control cycle. The partial derivative $\partial\psi/\partial\theta$ employed in (6.2) and the following equations can be obtained as (6.3). When the phase current is smaller than the saturation current I_s, $\partial\psi/\partial\theta$ can be calculated from the derivative of the unsaturated inductance L_{Li}. It is noted that the derivative of the unsaturated inductance L_{Li} is obtained from the prestored 1-D LUT. If the phase current is higher than the I_s, the central difference method is employed to obtain this partial derivative

while holding the phase current as a constant. The definition of the saturation current can be found in (Song *et al.*, 2020a). Similarly, the partial derivative $\partial\psi/\partial i$ can be estimated from (6.4).

$$\frac{\partial\psi}{\partial\theta} = \begin{cases} i \times (dL_{Li}/d\theta), & i \leq I_s \\ \psi(\theta + \Delta\theta, i) - \psi(\theta - \Delta\theta, i)/2\Delta\theta, & i > I_s \end{cases} \tag{6.3}$$

$$\frac{\partial\psi}{\partial i} = \begin{cases} L_{Li}, & i \leq I_s \\ \psi(\theta, i + \Delta i) - \psi(\theta, i - \Delta i)/2\Delta i, & i > I_s \end{cases} \tag{6.4}$$

The predicted current i_{pre}^{k+1} is easily obtained with the above information. Besides, the value of the reference current i_{ref}^{k+2} that is supposed to reach at the sampling instant $(k+2)$ is indispensable for estimating the duty cycle $d(k+1)$. It is noticed that i_{ref}^{k+2} is obtained from the prestored LUT with the estimated position θ_{k+2}. Since the mechanical time constant of the electric machine is much larger than the electrical time constant, it is reasonable to assume the rotor speed keeps constant for the consecutive two control cycles. Hence, the position θ_{k+1} and θ_{k+2} can be estimated from (6.5) based on the measured position θ_k and speed ω_r.

$$\begin{cases} \theta_{k+1} & = \theta_k + \omega_r \times T_c \\ \theta_{k+2} & = \theta_k + \omega_r \times 2T_c \end{cases} \tag{6.5}$$

The duty cycle is estimated according to the relationship between i_{ref}^{k+2} and i_{pre}^{k+1}. Typically, the current value i_{ref}^{k+2} either increases or decreases regarding the current value i_{pre}^{k+1}. If the value at these two points keeps unchanged, the phase current is assumed to rise first then go back to its original value or vice versa. Therefore, only

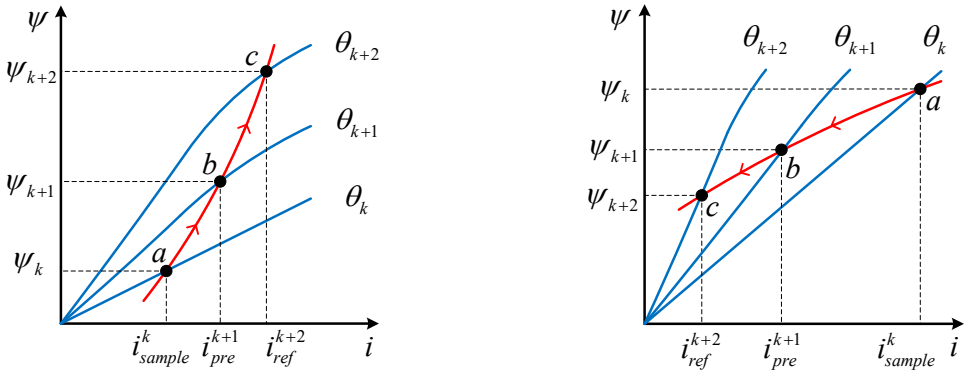

Figure 6.4: The current, position, and flux-linkage information when (a) i_{ref}^{k+2} is larger than i_{pre}^{k+1} and (b) i_{ref}^{k+2} is smaller than i_{pre}^{k+1}.

current rising and decreasing scenarios are considered in this chapter, as shown in Fig. 6.4. Specifically, Fig. 6.4 (a) describes the current, position, and flux-linkage in two consecutive control cycles when the phase current is going up. And Fig. 6.4 (b) shows these variables when the current is decreasing. It is noted that the sampled current i_{sample}^{k} and duty cycle $d(k)$ is known on the k^{th} control cycle, so only the relationship between i_{pre}^{k+1} and i_{ref}^{k+2} is considered.

When the current is arranged to increase from point b to point c, as shown in Fig. 6.5 (a), two steps are assumed. In the beginning, the current goes up from point b to point d under magnetization mode for a period T_1. Then, it goes down from point d to point c under freewheeling mode for a period T_2. From the voltage equation of SRM shown in (6.1), the current rising rate S_b^r in point b and decreasing rate S_c^r in point c can be derived as (6.6) and (6.7).

$$S_b^r = \frac{d\psi/dt}{di/dt} = \frac{(V - Ri) \times \partial\psi/\partial i}{V - Ri - \omega_r \times \partial\psi/\partial\theta} \tag{6.6}$$

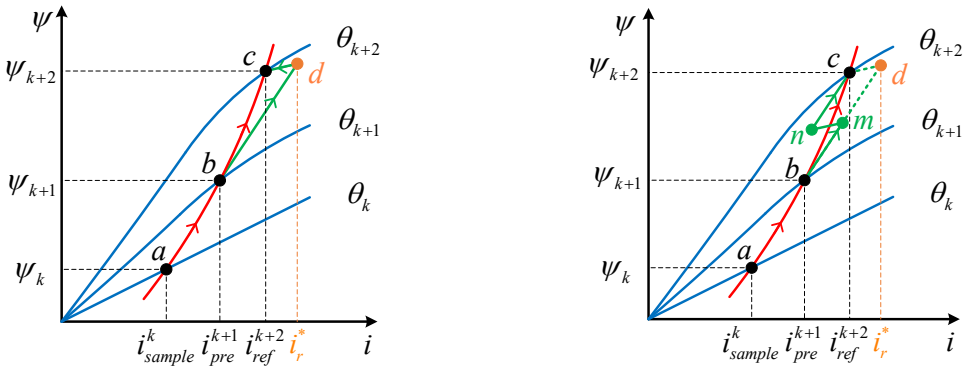

(a) (b)

Figure 6.5: The current is rising from i_{pre}^{k+1} to i_{ref}^{k+2} under (a) asymmetric PWM scheme and (b) symmetric PWM scheme.

$$S_c^r = \frac{d\psi/dt}{di/dt} = \frac{(0 - Ri) \times \partial\psi/\partial i}{0 - Ri - \omega_r \times \partial\psi/\partial\theta} \tag{6.7}$$

Based on the current i_{pre}^{k+1}, i_{ref}^{k+2}, and the above slope information, the expression of straight lines L_{bd}^r and L_{cd}^r can be derived as:

$$L_{bd}^r = S_b^r \times i + (\psi_{k+1} - S_b^r \times i_{pre}^{k+1}) \tag{6.8}$$

$$L_{cd}^r = S_c^r \times i + (\psi_{k+2} - S_c^r \times i_{ref}^{k+2}) \tag{6.9}$$

Then, the current value at the intersection point d of lines L_{bd}^r and L_{cd}^r is calculated as:

$$i_r^* = \frac{(\psi_{k+2} - \psi_{k+1}) - (S_c^r \times i_{ref}^{k+2} - S_b^r \times i_{pre}^{k+1})}{S_b^r - S_c^r} \tag{6.10}$$

If i_r^* is larger than i_{ref}^{k+2}, this reference current at point c can be reached by applying proper duty cycle excitation. Otherwise, the reference current i_{ref}^{k+2} is beyond the current trackability of this driving system. Once i_r^* is calculated, the duty cycle d_1

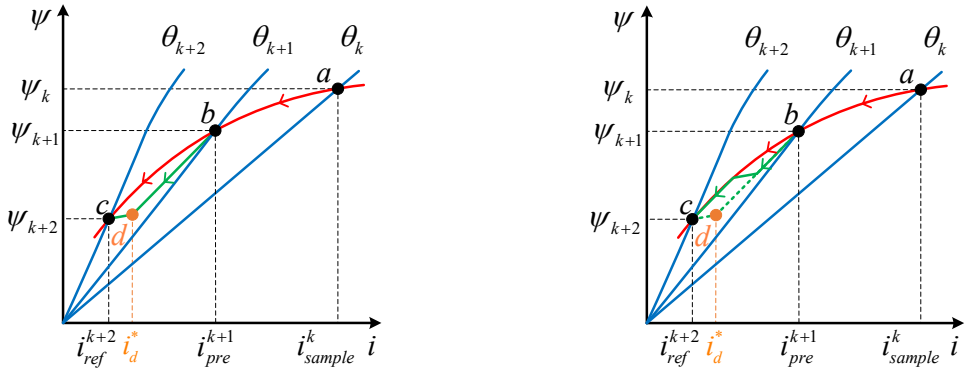

Figure 6.6: The current is decreasing from i_{pre}^{k+1} to i_{ref}^{k+2} under (a) asymmetric PWM scheme and (b) symmetric PWM scheme.

for applying the positive bus voltage excitation is quantified as:

$$d_1 = \frac{i_r^* - i_{pre}^{k+1}}{di/dt} = \frac{(i_r^* - i_{pre}^{k+1}) \times \partial\psi/\partial i}{V - iR - \omega_r \times \partial\psi/\partial\theta} \tag{6.11}$$

To further reduce the current ripple, a symmetric PWM scheme shown in Fig. 6.5 (b) is adopted. In this case, the phase current rises from point b to point m first, then drops from point m to point n under the freewheeling mode, and finally rises from point n to point c.

On the other hand, when the current is set to drop from point b to point c, as shown in Fig. 6.6, the current decreasing rate S_b^d in point b and S_c^d in point c can be expressed as:

$$S_b^d = \frac{(-V - Ri) \times \partial\psi/\partial i}{-V - Ri - \omega_r \times \partial\psi/\partial\theta} \tag{6.12}$$

$$S_c^d = \frac{(0 - Ri) \times \partial\psi/\partial i}{0 - Ri - \omega_r \times \partial\psi/\partial\theta} \tag{6.13}$$

Similar to the case when the current is rising from i_{pre}^{k+1} to the i_{ref}^{k+2}, the current

value i_d^* at the intersection point d can be calculated as (6.14). And the duty cycle d_2 for applying the negative bus voltage excitation is quantified as (6.15).

$$i_d^* = \frac{(\psi_{k+2} - \psi_{k+1}) - (S_c^d \times i_{ref}^{k+2} - S_b^d \times i_{pre}^{k+1})}{S_b^d - S_c^d} \tag{6.14}$$

$$d_2 = \frac{i_d^* - i_{pre}^{k+1}}{di/dt} = \frac{(i_d^* - i_{pre}^{k+1}) \times \partial\psi/\partial i}{-V - iR - \omega_r \times \partial\psi/\partial\theta} \tag{6.15}$$

6.3.2 Adaptive Flux-linkage Model

The accuracy of the flux-linkage model plays a vital role in the tracking performance of the proposed method. However, this flux-linkage model obtained from the FEA software or experimental measurement might not be accurate due to the model mismatch. It is pointed out in (Ge *et al.*, 2020) that the model obtained from the FEA differs from the real ones. And the main reason for this difference is the variation of the airgap length that happened in the manufacturing process.

Assuming the real model inside the motor is expressed as (6.16), where $\dot{\psi}$ is the time derivative of the actual flux-linkage, $\hat{H}$ is the product of current and reciprocal of the adopted flux-linkage model ψ_m, and α is the real calibrated coefficient for the adopted flux-linkage model.

$$\begin{cases} \dot{\psi} = v - iR \\ i = \alpha \hat{H} \psi \\ \hat{H} = i/\psi_m \end{cases} \tag{6.16}$$

In order to calibrate this modeling error, an adaptive flux-linkage observer is

constructed as:

$$\begin{cases} \dot{\hat{\psi}} = v - \hat{i}R + K_1(i - \hat{i}) \\ \hat{i} = \hat{\alpha}\hat{H}\hat{\psi} \end{cases} \tag{6.17}$$

where $\dot{\hat{\psi}}$, $\hat{\alpha}$, $\hat{i}$ and K_1 are the time derivative of the estimated flux-linkage model $\hat{\psi}$, the estimated calibrate coefficient, the estimated phase current, and the gain of the observer.

If a Lyapunov candidate is selected as:

$$W = \frac{1}{2}\tilde{\psi}^2 + \frac{1}{2}\tilde{\alpha}^2 \tag{6.18}$$

where $\tilde{\psi}$ is the flux-linkage error and $\tilde{\alpha}$ is the calibrated coefficient error, which can be defined as:

$$\begin{cases} \tilde{\psi} = \psi - \hat{\psi} \\ \tilde{\alpha} = \alpha - \hat{\alpha} \end{cases} \tag{6.19}$$

The derivative of the selected Lyapunov candidate is:

$$\begin{aligned} \dot{W} &= \tilde{\psi}\dot{\tilde{\psi}} + \tilde{\alpha}\dot{\tilde{\alpha}} \\ &= -\tilde{\psi}(K_1 + R)(\alpha\hat{H}\psi - \hat{\alpha}\hat{H}\hat{\psi}) + \tilde{\alpha}\dot{\tilde{\alpha}} \\ &= -\alpha\hat{H}\tilde{\psi}^2(K_1 + R) - (K_1 + R)\tilde{\psi}\tilde{\alpha}\hat{H}\hat{\psi} + \tilde{\alpha}(\dot{\alpha} - \dot{\hat{\alpha}}) \\ &\approx -\alpha\hat{H}\tilde{\psi}^2(K_1 + R) - (K_1 + R)\tilde{\psi}\tilde{\alpha}\hat{H}\hat{\psi} - \tilde{\alpha}\dot{\hat{\alpha}} \end{aligned} \tag{6.20}$$

According to the stability criteria of the Lyapunov direct method, the flux-linkage observer is robust only if $\dot{W}$ is small than 0. Because the real model inside the motor varies slowly, $\dot{\alpha}$ is close to 0 thus could be ignored. Under the above conditions, the

following relationship is obtained:

$$\begin{cases} -\alpha\hat{H}\tilde{\psi}^2(K_1+R) & <0 \\ -(K_1+R)\tilde{\psi}\tilde{\alpha}\hat{H}\hat{\psi}-\tilde{\alpha}\dot{\hat{\alpha}} & =0 \end{cases} \tag{6.21}$$

To satisfy equation (6.21), the following relationship is obtained based on the fact that α and $\hat{H}$ are positive numbers:

$$\begin{cases} K_1+R>0 \\ \dot{\hat{\alpha}}=-(K_1+R)\tilde{\psi}\hat{H}\hat{\psi} \end{cases} \tag{6.22}$$

With a proper gain K_1, the estimated calibrated coefficient $\hat{\alpha}$ and estimated flux-linkage $\hat{\psi}$ converge to their actual values. In this case, the adopted flux-linkage model ψ_m could approach the real flux-linkage model ψ adaptively through the method indicated by (6.23).

$$\frac{\hat{i}}{\hat{\alpha}\hat{H}}=\hat{\psi}=\frac{\psi_m}{\hat{\alpha}}=\psi \tag{6.23}$$

The above calibration process can be summarized as the flow diagram described in Fig. 6.7. Firstly, the adopted flux-linkage model ψ_m is stored in the MCU as a two-dimensional LUT. Then, the converged calibrated coefficient value $\hat{\alpha}$ can be obtained through the proposed adaptive flux-linkage observer based on the position, voltage, and current information. Finally, the prestored flux-linkage ψ_m is calibrated to the real flux-linkage with the aid of $\hat{\alpha}$.

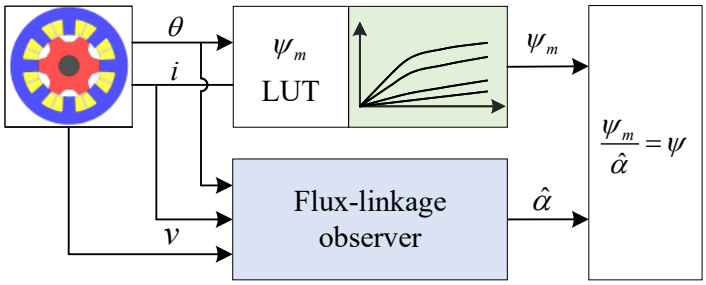

Figure 6.7: Model mismatch calibration flow diagram.

6.3.3 Balanced Switching Operation

As illustrated in section 6.2, the performance of the CCC method highly relies on the control frequency and sampling rate. Notably, the limits of the switching frequency on the power transistors should also be considered because the improvement of the control frequency and the sampling rate is easier than that of the switching frequency. One phase of the applied asymmetrical half-bridge inverter is shown in Fig. 2.4. The upper and lower switches are represented by S1 and S2, respectively. Fig. 6.8 describes the switching mode and corresponding upper and lower switching signals for the normal switching scheme. It is observed that the lower switch keeps closed during the conduction period while the upper switch keeps chopping at the control frequency. Apparently, the switching frequency requirement and switching losses differ between the upper and lower switch. To reduce the switching frequency requirement and evenly distribute the switching losses, a balanced switching scheme is proposed, as shown in Fig. 6.9.

Assuming the sequence of the control cycles is represented by the number $2n$, where n is an integer. When the phase current is arranged to increase, the upper switch keeps close in the $(2k+1)^{th}$ control cycle, and chops in the $(2k+2)^{th}$ control cycle. As for the lower switch, it keeps close in the $(2k+2)^{th}$ control cycle, and chops

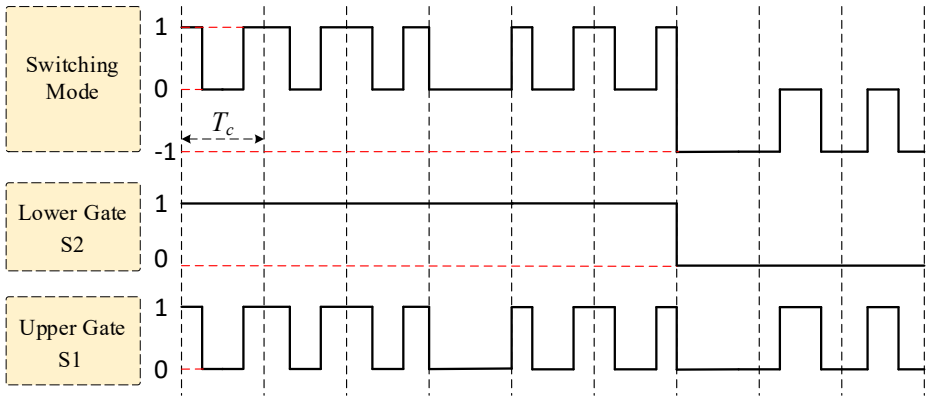

Figure 6.8: Normal switching scheme.

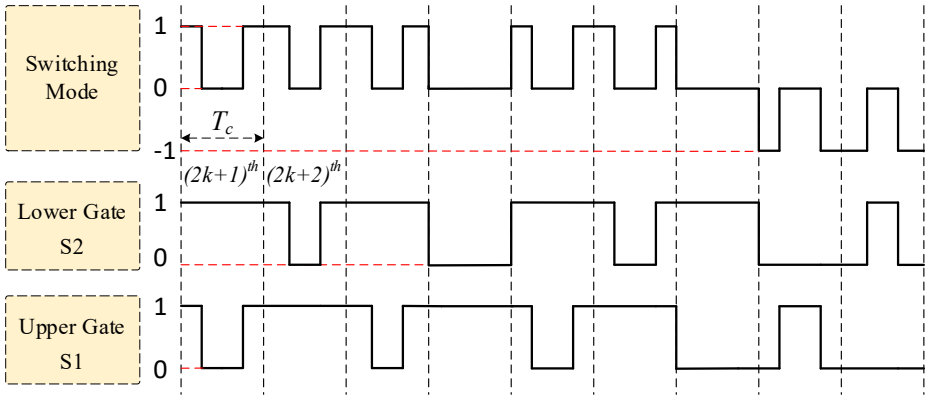

Figure 6.9: Proposed balanced switching scheme.

Table 6.1: Balanced switching scheme

	Current rising		Current decresing	
Control cycle	$(2k+1)^{th}$	$(2k+2)^{th}$	$(2k+1)^{th}$	$(2k+2)^{th}$
Upper switch	1	chopping	0	chopping
Lower switch	chopping	1	chopping	0

in the $(2k+1)^{th}$ control cycle. When the phase current is arranged to decrease, the upper and lower switches operate in a similar manner, and the detailed operation is summarized in Table 6.1. Under such a switching scheme, not only the switching frequency of the upper and lower switch is balanced, but also the switching frequency

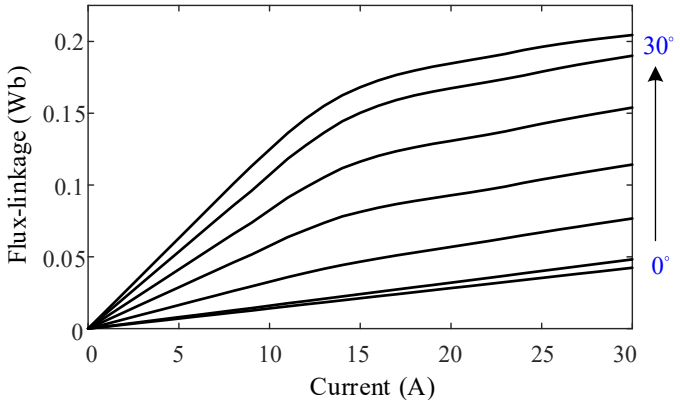

Figure 6.10: Flux-linkage characteristics of the studied 8/6 SRM.

requirement of the transistors is reduced to almost half of the control frequency f_c.

6.4 Experimental Validation

To verify the effectiveness of the proposed current controller, extensive experimental tests have been carried out in a four-phase 5.1 kW 8/6 SRM. The detailed parameters of the studied SRM are listed in Table 3.2. Fig. 6.10 shows the measured flux-linkage characteristics, which is the adopted flux-linkage model ψ_m employed in the proposed current controller. It is noted that the flux-linkage characteristics are obtained by the DC excitation method (Gobbi *et al.*, 2008) with the rotor locked mechanically.

Fig. 3.23 describes the testing setup, which is composed of the induction machine (IM), the IM controller, SRM, and the SRM controller. The experimental testing results for the HCC method, deadbeat controller in (Mikail *et al.*, 2014), and the proposed current controller are all carried out in this setup. During the testing process, the speed is controlled by the IM. If a specific current reference is applied to the SRM, the SRM serves as the prime mover, and the IM operates as a generator. It is noted that the IM and SRM share the same bus voltage during the testing, which

is fixed at 300 volts. The digital signal processor (DSP) TMS320F28335 is adopted to implement the HCC, deadbeat, and the proposed current controller for SRM. To achieve better current tracking performance for the HCC method, the control frequency for the HCC method is set at 60 kHz, which is the maximum achievable control frequency for this experimental setup. The control frequency for the deadbeat current controller and the proposed current controller is set at 20 kHz in the tests.

To test the proposed current controller at different operation conditions, different kinds of reference currents are employed as testing current references. All the current references are obtained by solving an optimization problem as described in (Li *et al.*, 2019). The objective function of this optimization problem is shown as (6.24), where i_{inc} and i_{out} represent the current of the incoming phase and outgoing phase. The parameter σ is to be optimized to compromise between the copper losses and torque ripple performance. To keep a constant torque during normal operation, the equality constraint described in (6.25) should be satisfied. Equation (6.26) ensures the reference current below its rated value i_{rated}. The trackability of the derived current is taken care of by limiting the time derivative of the flux-linkage within the range of the applied bus voltage, as shown in (6.27).

$$J = i_{inc}^2 + \sigma i_{out}^2 \tag{6.24}$$

$$T_{ref} = T(i_{inc}, \theta_{inc}) + \sigma T(i_{out}, \theta_{out}) \tag{6.25}$$

$$\begin{cases} 0 \leq i_{inc} \leq i_{rated} \\ 0 \leq i_{out} \leq i_{rated} \end{cases} \tag{6.26}$$

Table 6.2: Current References Employed in the Experimental Tests

Current reference	Reference I	Reference II	Reference III
Speed (r/min)	3000	3000	6000
Torque (N·m)	3	6	3

$$\begin{cases} \Delta\psi_{inc}(i,\theta)/\Delta t \leq V - i_{inc}R \\ \Delta\psi_{inc}(i,\theta)/\Delta t \geq -V + i_{inc}R \\ \Delta\psi_{out}(i,\theta)/\Delta t \leq V - i_{out}R \\ \Delta\psi_{out}(i,\theta)/\Delta t \geq -V + i_{out}R \end{cases} \tag{6.27}$$

The employed current references are summarized in Table 6.2. It is noted the speed in this table indicates the maximum trackable speed for that reference current (Li *et al.*, 2019).

6.4.1 Model Mismatch Calibration Verification

Because the accuracy of the adopted flux-linkage model ψ_m is not known, the flux-linkage observer is tested first to obtain the calibrated coefficient $\hat{\alpha}$. In the test, the parameter K_1 is tuned manually. A small initial value that meets the convergence condition (6.22) is selected first. Then, K_1 is gradually increased until the calibrated coefficient $\hat{\alpha}$ converges within a limited time and the phase current tracks the reference current well. Fig. 6.11 shows the $\hat{\alpha}$, actual current, and current reference I during the converging process when the $\hat{H}$ is set at its nominal value. It is noted that the nominal value of $\hat{H}$ means the exact adopted flux-linkage model ψ_m is employed to get $\hat{H}$ in (6.16). The converging process in Fig. 6.11 (a) shows that $\hat{\alpha}$ converges at around 2.5 s, and the final value of $\hat{\alpha}$ is around 0.89. The phase current at the

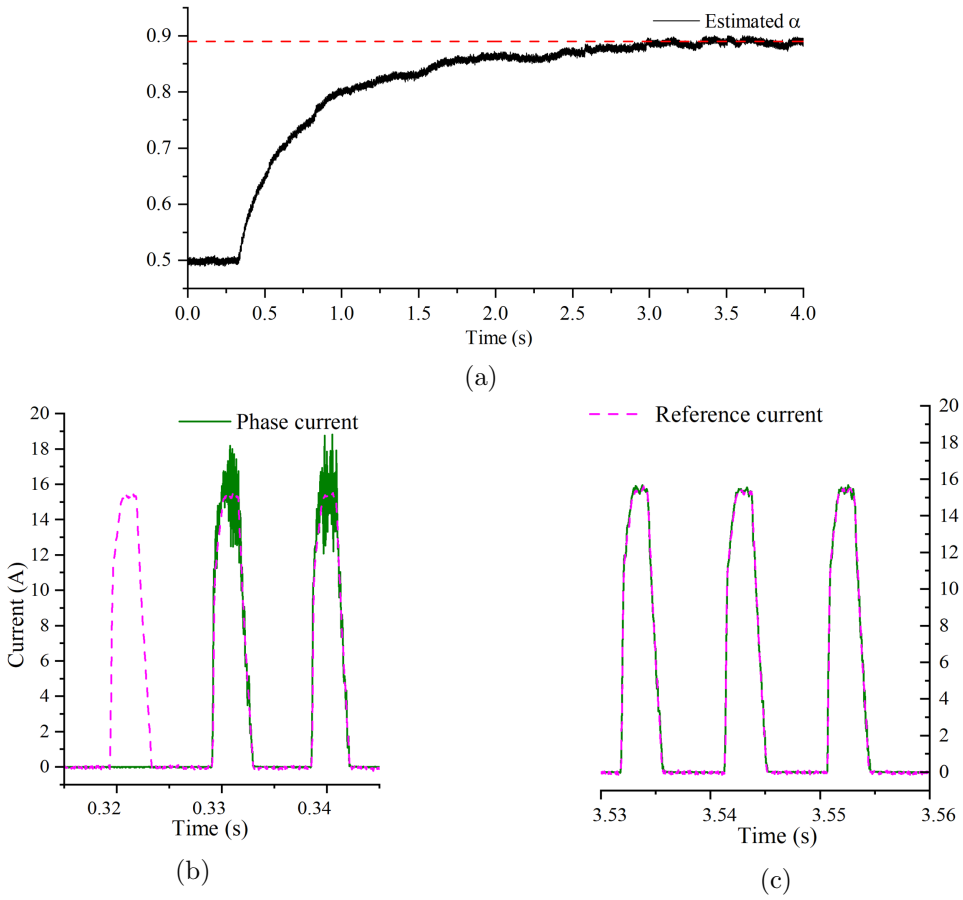

Figure 6.11: (a) Converging process of $\hat{\alpha}$, (b) current at the stating instant during the converging process, and (c) current after $\hat{\alpha}$ converges for nominal $\hat{H}$.

starting instant when $\hat{\alpha}$ equals its initial value 0.5 is depicted in Fig. 6.11 (b). Due to the incorrect calibrated coefficient value, the tracking performance is poor. On the contrary, good reference current tracking performance is observed in Fig. 6.11 (c) after $\hat{\alpha}$ approaches to its real value.

To further verify the effectiveness of the proposed flux-linkage observer, the converging process is carried out under 0.75 times the nominal value of $\hat{H}$. It is noticed that the 0.75 $\hat{H}$ is obtained by deliberately magnifying the ψ_m 1.33 times in (6.16), which aims to test the robustness of the proposed method under a more significant

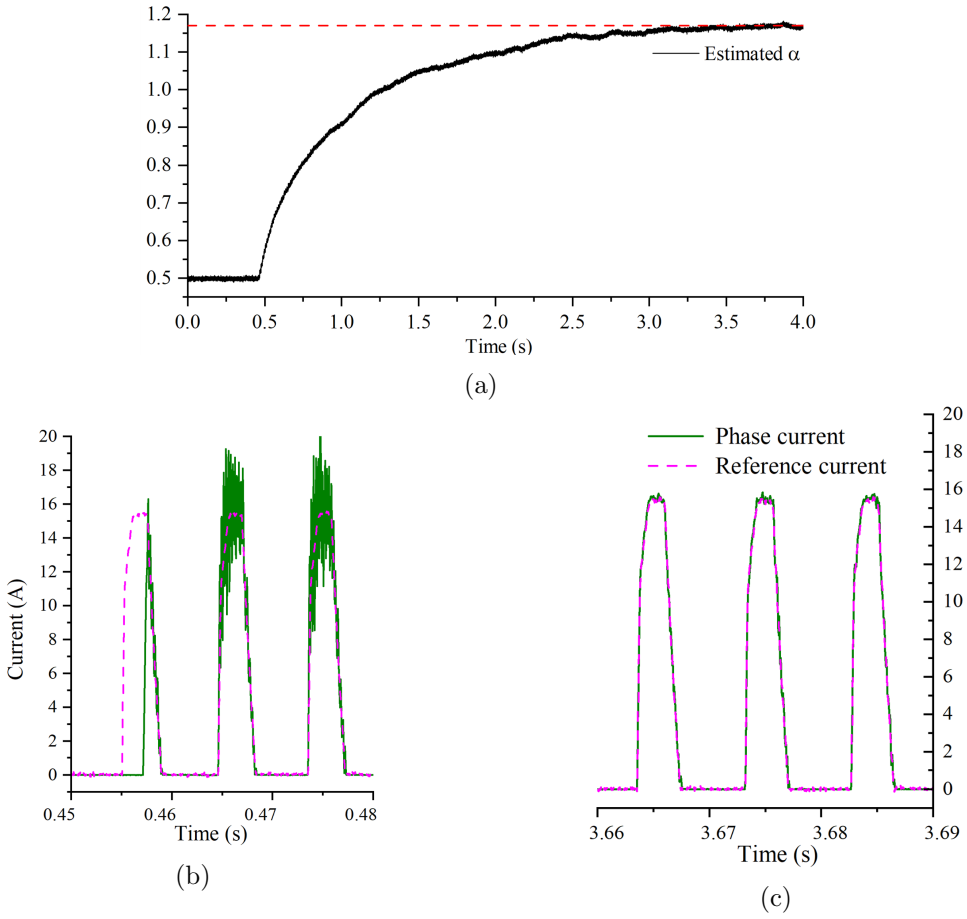

Figure 6.12: (a) Converging process of $\hat{\alpha}$, (b) current at the stating instant during the converging process, and (c) current after $\hat{\alpha}$ converges for 0.75 times nominal $\hat{H}$.

model mismatch case. Fig. 6.12 (a) shows the converging process under this condition. The estimated calibrated coefficient $\hat{\alpha}$ finally approaches 1.17 at around 3.0 s. It is interesting to find that the product of the converged $\hat{\alpha}$ value 1.17 and 0.75 is around 0.88, which is very close to the converged $\hat{\alpha}$ value 0.89 at nominal $\hat{H}$. Fig. 6.12 (b) and Fig. 6.12 (c) describe the current tracking performance at the starting instant and $\hat{\alpha}$ converged region during the converging process of 0.75 $\hat{H}$. Not surprisingly, the proposed method shows good current tracking capability once the calibrate coefficient approaches its actual value.

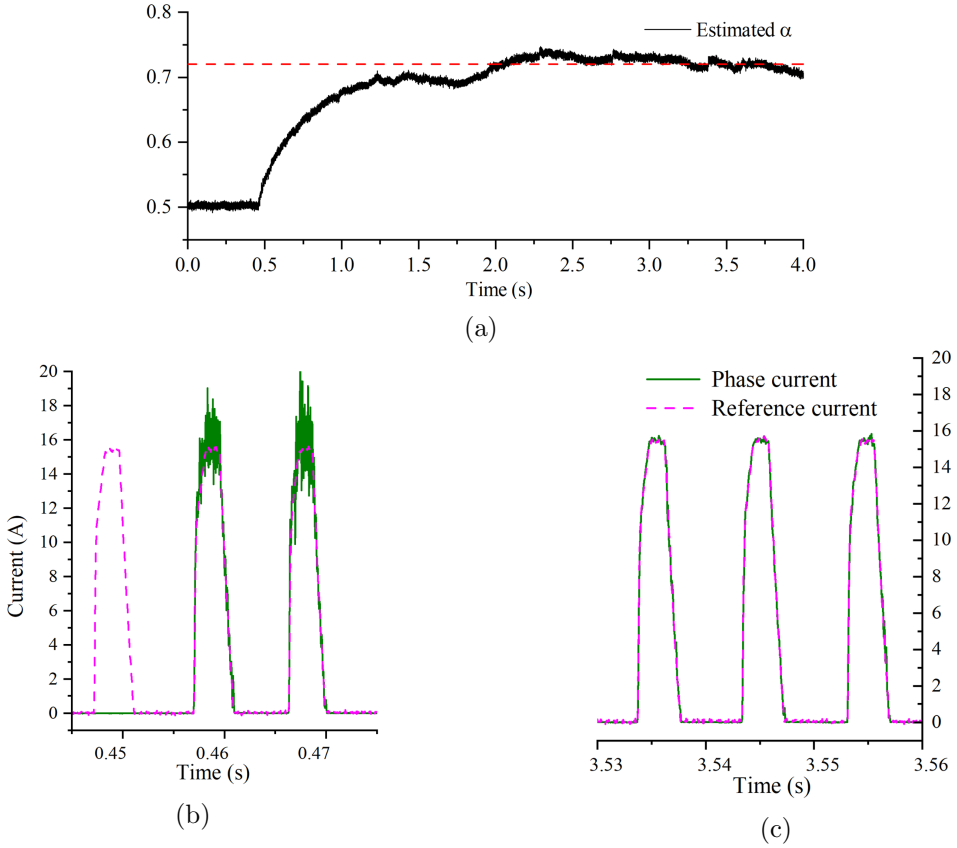

Figure 6.13: (a) Converging process of $\hat{\alpha}$, (b) current at the stating instant during the converging process, and (c) current after $\hat{\alpha}$ converges for 1.25 times nominal $\hat{H}$.

Fig. 6.13 shows the estimated coefficient $\hat{\alpha}$ and the current waveforms during the converging process under 1.25 times nominal value of $\hat{H}$. The final value of $\hat{\alpha}$ reaches around 0.72 in this case at around 2.5 s. Similarly, the product of this $\hat{\alpha}$ value 0.72 and amplifying coefficient 1.25 is very close to the $\hat{\alpha}$ value 0.89 for nominal $\hat{H}$ case, which again verify the effectiveness of the proposed adaptive flux-linkage observer. The current tracking waveform in Fig. 6.13 (b) and (c) show the tracking capability at different stage in the converging process. It is again observed that the phase current follows the reference current well after the $\hat{\alpha}$ converges.

6.4.2 Current Tracking Performance Evaluation

Based on the above converged $\hat{\alpha}$ value in the nominal $\hat{H}$ case, current references I, II, and III are utilized to verify the current tracking performance of the proposed method. The current tracking capability of the HCC method and the deadbeat current controller in (Mikail *et al.*, 2014) are also presented for comparison. The reasons for selecting the HCC method in the current tracking performance comparison are: (a) The SCC method might not be able to track the fast drop part of some specific current reference due to the adoption of the freewheeling mode; (b) The SCC method requires the precise turn-off angle to demagnetize the current; (c) The turn-off angles of the reference currents obtained from the above numerical optimization method typically vary with the operating conditions and these turn-off angles are not given.

Fig. 6.14 show the current tracking performance of the HCC method at 1000 r/min and 60 kHz control/sampling frequency conditions. The current reference in Fig. 6.14 (a) is the current reference I, and the current reference in Fig. 6.14 (b) is the current reference II. From these captured phase current waveforms, it is observed that the phase current shows a significant amount of ripples due to the adoption of the 100% duty cycle and the limited control frequency. Apparently, these large current ripples are not expected from the perspective of current tracking.

Fig. 6.15 (a) shows the current tracking performance of the proposed method under the current reference I, and Fig. 6.15 (b) show the phase current waveform under the current reference II. The shaft speed is 1000 r/min, but the control/sampling frequency is decreased to 20 kHz compared to 60 kHz in the HCC method. In both cases, the phase current is found to follow the reference current closely and shows fewer current ripples, indicating good current tracing capability for the proposed

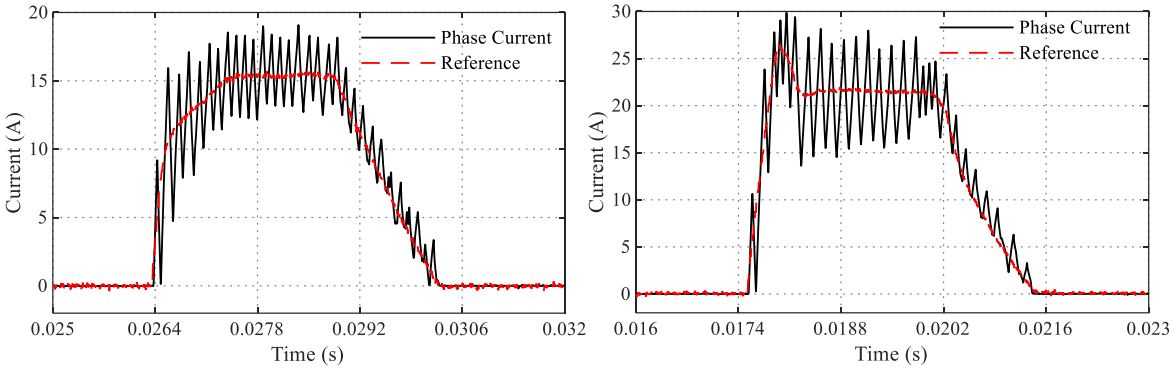

(a) (b)

Figure 6.14: (a) Phase current and reference current I and (b) phase current and reference current II at 1000 r/min for HCC method when the control frequency is 60 kHz.

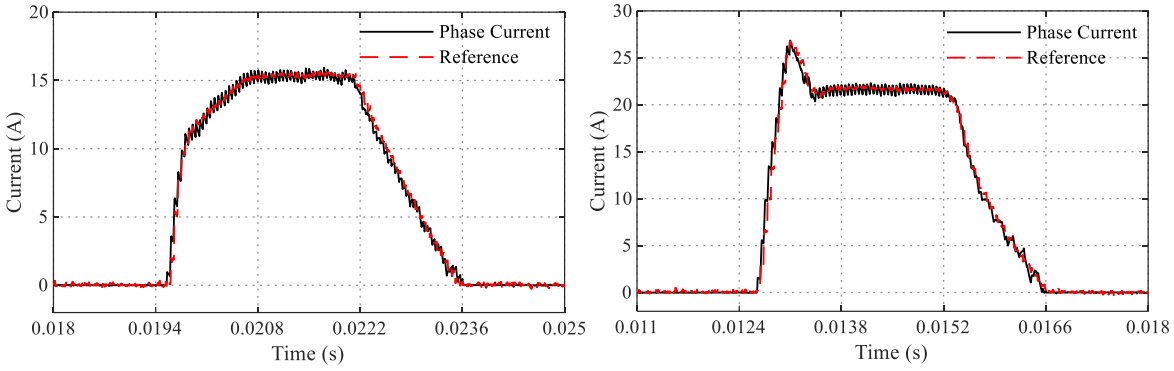

(a) (b)

Figure 6.15: (a) Phase current and reference current I and (b) phase current and reference current II at 1000 r/min for the proposed method when the control frequency is 20 kHz.

method.

To quantify the tracking error and better compare the current tracking performance of different control methods, the root mean square (rms) value of the current tracking error I_{error}^{RMSE} is evaluated. The definition of this performance index is defined in (6.28), where θ_p represents the rotor pole pitch, and i_{phase} is the recorded phase current. The calculated I_{error}^{RMSE} for the HCC method and the proposed method at 1000 r/min are listed in Table 6.3. Not surprisingly, the I_{error}^{RMSE} value of the proposed

Table 6.3: I_{error}^{RMSE} Comparison Between HCC and the Proposed Method at 1000 r/min

Method	Current reference I	Current reference II
HCC	1.18	1.85
Proposed method	0.29	0.52

method is found to be much less than that of the HCC method for the applied current reference I and II, which reveals the superiority of the proposed method.

$$I_{error}^{RMSE} = \sqrt{\frac{1}{\theta_p}\int_0^{\theta_p}(i - i_{phase})^2 d\theta} \tag{6.28}$$

Fig. 6.16 shows the phase current and its reference at 3000 r/min for the HCC method. Compared to the results shown in Fig. 6.14, it is found that the peak current and the number of chopping actions are reduced due to the increased back electromotive force (EMF) in Fig. 6.16. Moreover, the lags between the actual current and the reference current become obvious at higher speed. This is resulted from the delay and can be explained by the following reasons: (a) The reference current might not start at the exact beginning instant of the control cycle, which leads to at most one control cycle delay, as shown in Fig. 6.17; (b) The applied switching signal has one control period delay. With these delays, the current tracking performance of the HCC method remains poor.

Fig. 6.18 show the phase current and corresponding reference current for the proposed method at 3000 r/min. Due to the increment in the angle distance that the rotor moves within one control period, the stairs on the reference current are clearly seen. In terms of the current tracking, the proposed method still exhibits good tracking performance. The rms values of the current tracking error for the HCC method

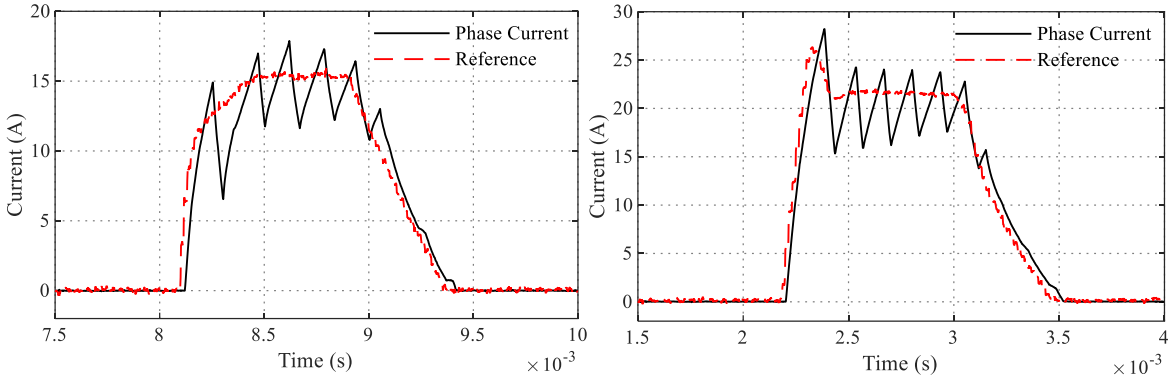

Figure 6.16: (a) Phase current and reference current I and (b) phase current and reference current II at 3000 r/min for HCC method when the control frequency is 60 kHz.

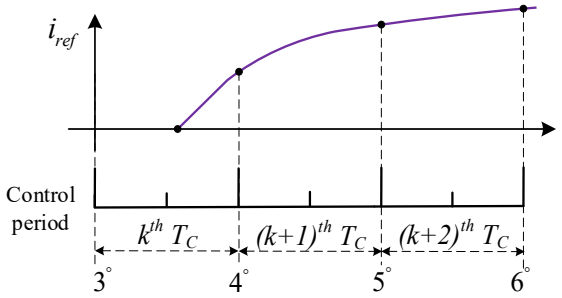

Figure 6.17: Explanation for the delay in the CCC method.

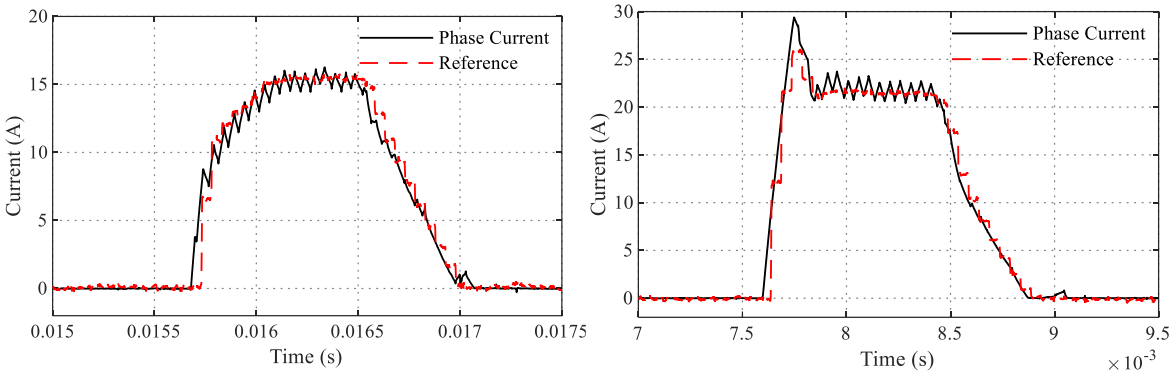

Figure 6.18: (a) Phase current and reference current I and (b) phase current and reference current II at 3000 r/min for the proposed method when the control frequency is 20 kHz.

Table 6.4: I_{error}^{RMSE} Comparison Between HCC and the Proposed Method at 3000 r/min

Method	Current reference I	Current reference II
HCC	1.29	1.60
Proposed method	0.75	1.06

and the proposed method are summarized in Table 6.4. It is observed that this performance index increases for both methods at higher speed, but the proposed method shows lower values as expected.

The deadbeat current controller proposed in Mikail *et al.* (2014) is evaluated experimentally at 1000 r/min to compare with the proposed method. Fig. 6.19 (a) shows the current tracking performance of the deadbeat controller when the nominal flux-linkage model ψ_m is adopted. It is observed that the phase current tracks the current reference I well. However, some oscillations are found between 0.02 s and 0.021 s in Fig. 6.19 (a). These oscillations probably result from the inaccuracy of the adopted flux-linkage model ψ_m. Compared with the results shown in Fig. 6.15 (a), the proposed current controller shows no such oscillations. To further investigate the performance of this deadbeat current controller under model mismatch conditions, Fig. 6.19 (b) and (c) show the current tracking performance when the applied flux-linkage model is deliberately set at 0.75 times nominal ψ_m and 1.25 nominal ψ_m. It is found that the phase current shows a lower value than the current reference when the flux-linkage is less than the nominal value. And the phase current shows a higher value than the current reference when the flux-linkage is higher than the nominal value. The above observations could also be found in (Peng *et al.*, 2016). Since the proposed current controller is equipped with the flux-linkage observer and its convergence has been proved in the above section, the current tracking performance will keep the same under model mismatch conditions. Table 6.5 lists the I_{error}^{RMSE} for the

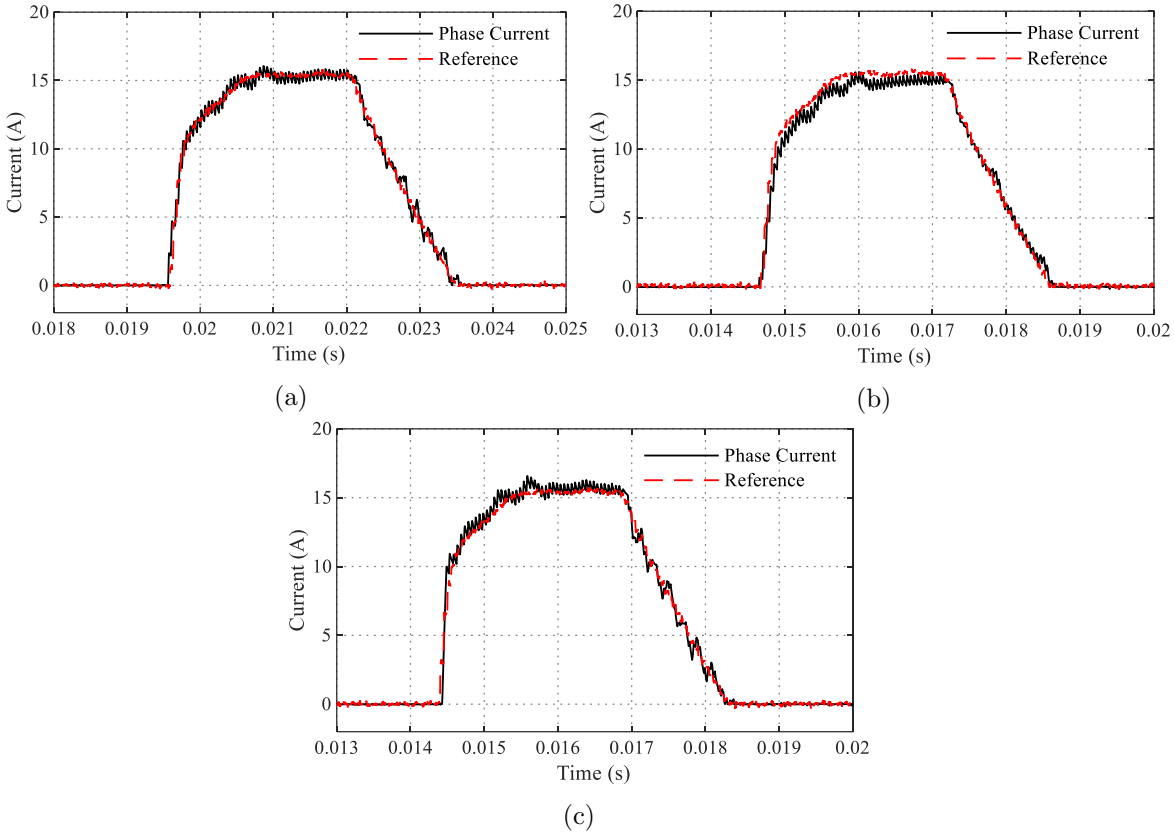

Figure 6.19: Phase current and reference current I at (a) nominal ψ_m, (b) 0.75 times nominal ψ_m, and (c) 1.25 times nominal ψ_m for the deadbeat controller in Mikail *et al.* (2014) when the SRM operates at 1000 r/min.

Table 6.5: I_{error}^{RMSE} Comparison Between Deadbeat Method in Mikail *et al.* (2014) and the Proposed Method at 1000 r/min

Method	Nominal	0.75 times nominal ψ_m	1.25 times nominal ψ_m
Deadbeat in Mikail *et al.* (2014)	0.34	0.46	0.41
Proposed method	0.29	0.29	0.29

deadbeat current controller and the proposed method. Low current tracking errors for the proposed method can be observed, verifying the superiority of the proposed method.

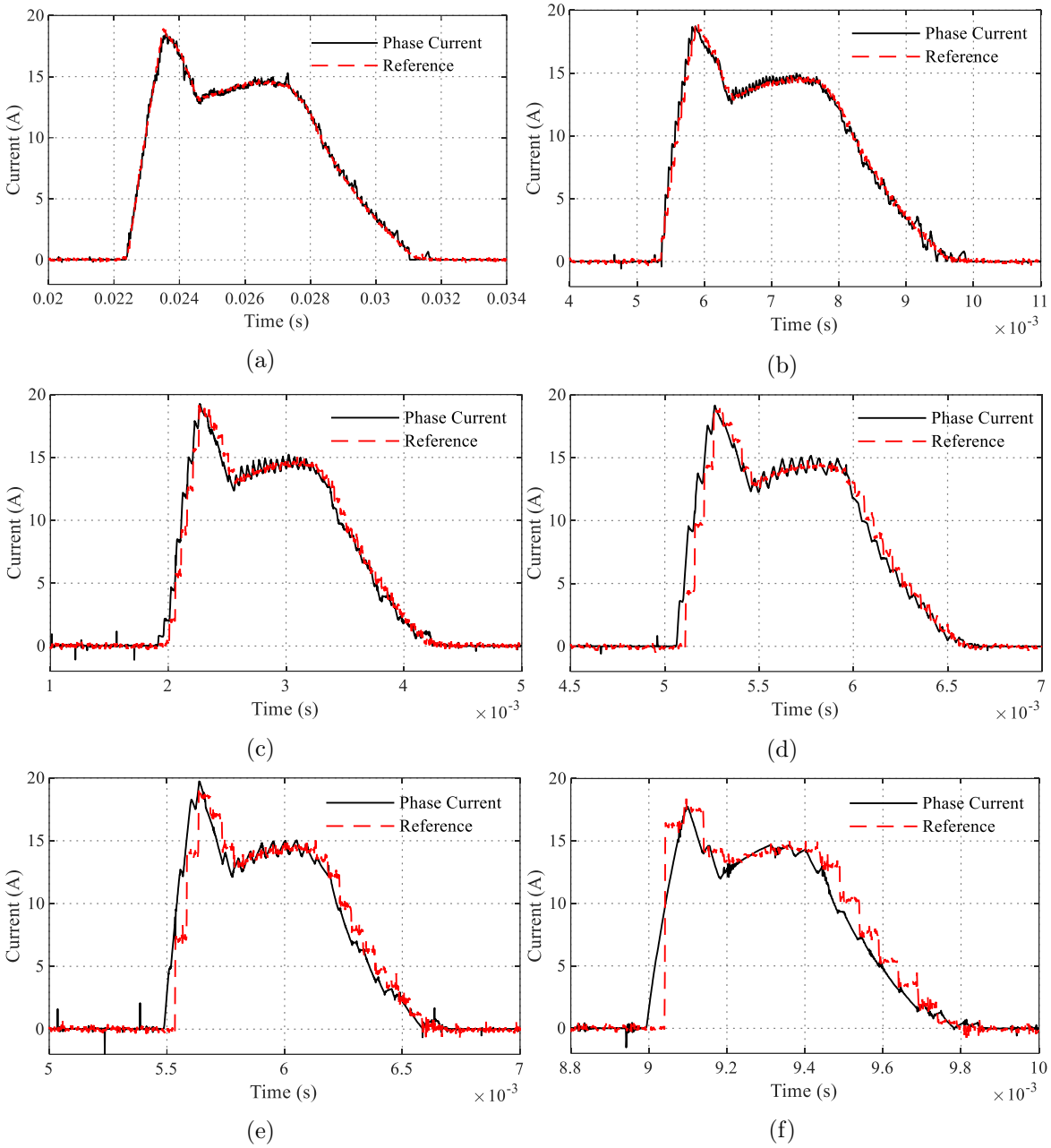

Figure 6.20: Phase current and reference current III at (a) 500 r/min, (b) 1000 r/min, (c) 2000 r/min, (d) 3000 r/min, (e) 4000 r/min, and (f) 5500 r/min for the proposed method.

To validate the current tracking performance of the proposed current controller

Table 6.6: I_{error}^{RMSE} for the Proposed Method at Different Speed

Speed (r/min)	500	1000	2000	3000	4000	5500
I_{error}^{RMSE}	0.23	0.39	0.69	1.03	1.32	1.36

at various operation speeds, experimental tests for the reference current III is carried out. Fig. 6.20 (a)-(f) shows the phase current and its reference at 500 r/min, 1000 r/min, 2000 r/min, 3000 r/min, 4000 r/min, and 5500 r/min operation conditions. Good current tracking performance is observed in all the experimental results, proving that the proposed current controller works well in a wide speed range. The performance index I_{error}^{RMSE} is also calculated for the current tracking tests shown in Fig. 6.20, as shown in Table 6.6. It is found the I_{error}^{RMSE} value increases significantly with the operation speed. This can be explained as the following two reasons: (a) The reference current holds constant between two adjacent sampled positions; and (b) The distance between the two sampled positions increases with the speed when the control frequency keeps the same.

6.4.3 Balanced Switching Operation Verification

Fig. 6.21 and Fig. 6.22 show the transistor switching signal under normal mode and balanced operation mode. Not surprisingly, the high-frequency switching operation concentrates on one transistor for the normal mode. In contrast, the two transistors almost share the same high-frequency operation in the balanced PWM operation. Table 6.7 lists the average switching operation for the above two PWM operation modes. Although the sum of the switching frequency is higher for the balanced operation, the advantages for this operation mode are (a) The heat generated by the switching losses distributes evenly and (b) The switching frequency requirement

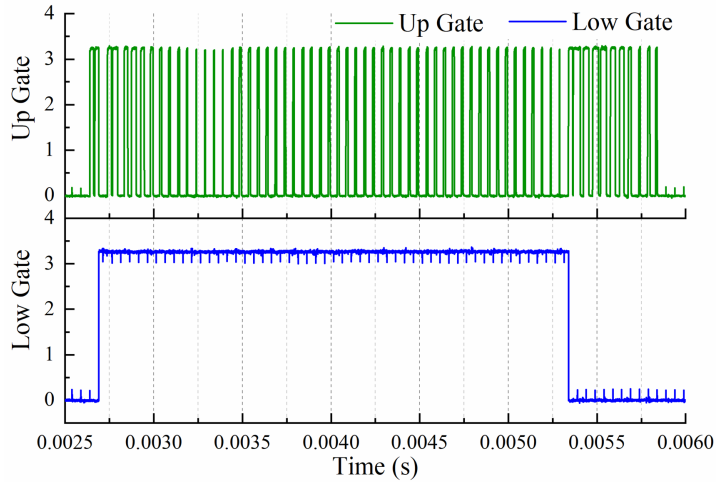

Figure 6.21: Gate signals for the normal mode PWM operation.

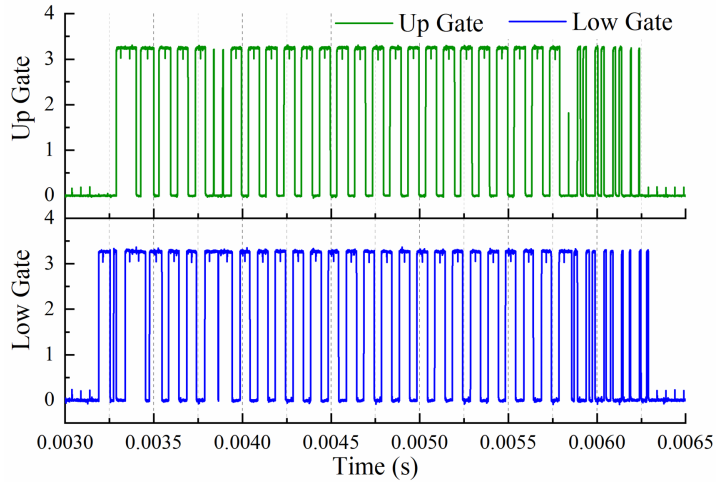

Figure 6.22: Gate signals for the balanced PWM operation.

Table 6.7: Average Frequency Comparison Between Normal and Balanced PWM Operation

Transistor	Normal PWM	Balanced PWM
Upper Gate	21.25 kHz	13.32 kHz
Lower Gate	0.1 kHz	12.98 kHz

is reduced for the transistor, which eases the transistor selection among the existed products.

6.5 Conclusion

High torque ripple and loud acoustic noise are the main problems for SRM. The current profiling techniques provide an effective way to address these issues. In order to achieve the expected performance of these current profiling methods, a high-performance current controller is required. This chapter presented a robust and high-performance current controller, and the contributions of this chapter are as follows:

a) A predictive current controller based on the intersection method with accurate current tracking performance for SRM is introduced.

b) Considering the difference between the actual model and the adopted model in the controller, a robust flux-linkage observer with only one parameter is presented to guarantee the performance of the current controller under large model mismatch conditions.

c) A balanced switching scheme is proposed to evenly distribute the heat generated by the switching loss and ease the selection of the transistor regarding the switching frequency.

d) The simplicity of the proposed method guarantees the stability and real-time performance in the practical application. Extensive experimental results verify the effectiveness and superior performance of the proposed method.

Chapter 7

Lumped Radial Force Characteristics Estimation for SRMs

7.1 Introduction

Another main drawback for SRMs is the acoustic noise issue, which is mainly caused by the generated radial force. To reduce the vibration and acoustic noise, current profiling and direct instantaneous force control methods are effective methods. Obviously, the radial force characteristics are the necessary information for the above methods. Since the radial force characteristics are barely possible to obtain in the experimental tests, these curves are normally obtained from the FEA software. However, it is normal to find that the measured flux-linkage curves differ from the ones obtained from the FEA, which is mainly caused by the airgap length variation during the manufacturing process. This airgap length variation apparently will affect the

accuracy of the radial force characteristics and then degrade the control performance of the acoustic noise reduction method. Therefore, it is crucial to develop a method to accurately estimate the radial force characteristics even when the airgap length has large variation.

This chapter presents a simple and practical method to estimate the lumped radial force characteristics for the SRMs. Firstly, the relationship between the square root of the lumped radial force and the flux-linkage is discussed and analyzed. With the geometry data of the studied SRM, the above relationship under nominal airgap length can be obtained through the FEA software. Since the radial flux density dominates the magnitude of the radial force and it concentrates on the overlapping area, the above relationship is analyzed to be roughly held when the airgap length varies. Based on this relationship obtained from FEA and the actual measured flux-linkage characteristics, the lumped radial force can be easily reconstructed for the actual SRMs regardless of the possible airgap length variation during the manufacturing process. Simulation results on the 8/6 SRM and 12/8 SRM verify that the proposed method provides good radial force estimation results when the airgap length is reduced or increased up to 50%. The accurate radial force estimation proposed in this chapter provides a solid basis for the radial-force-shaping-based advanced control methods to suppress the acoustic noise.

7.2 Proposed Radial Force Estimation Method

7.2.1 Fundamentals of SRMs

The SRMs are a type of machine which features a double salient structure and only has concentrated windings on the stator. And the torque is generated by the tendency that the rotor poles seek alignment to the stator poles. According to the Maxwell stress tensor, the tangential force, which generates torque, and the radial force can be expressed as:

$$F_r = \frac{1}{2\mu_0} \int_s (B_r^2 - B_t^2) ds \tag{7.1}$$

$$F_t = \frac{1}{\mu_0} \int_s B_r B_t ds \tag{7.2}$$

where μ_0 is the vacuum permeability, B_r is the radial flux density, B_t is the tangential flux density, and ds represents the infinitesimal increment of the integral surface area. In the actual situation, the toque characteristics are measured directly by the torque transducer instead of using the above equation since B_r and B_t are barely possible to measure. However, the radial force characteristics are very difficult to measure directly. Therefore, the most possible approach to obtain the radial force characteristics is through the FEA simulation and then use the equation (7.2). It is noted that such simulation can only be carried out at the nominal airgap length. However, as explained in the introduction part, the airgap length possibly varies in the manufacturing process, so this simulated radial force characteristics possibly differ with the real ones. If such inaccurate characteristics are used in the advanced acoustics noise reduction control methods, the performance of these methods will be degraded. To address this issue, this chapter utilizes the easily measured flux-linkage

profiles, which include the effect of the possible airgap length variation, to accurately estimate the radial force characteristics as described below.

7.2.2 Relationship Between Square Root of the Lumped Radial Force and the Flux-linkage

To estimate the lumped radial force from the flux-linkage, the relationship between these two quantities is supposed to be studied first. Assuming the flux density is uniformly distributed on the axial direction, the radial force equation shown in (7.1) can be reduced to the line integration as below:

$$F_r = \frac{L_{stk}}{2\mu_0} \int_l (B_r^2 - B_t^2) dl \tag{7.3}$$

where L_{stk} is the stack length, and dl indicates the infinitesimal increment of the integral length. The integral line l is normally set in the middle of the airgap and from the center of one stator slot to the center of the adjacent stator slot, as shown by the arc $\widehat{ab}$ in Fig. 7.1.

In general, the B_r and B_t data are collected in a manner with equal step Δl in the integral line from the FEA software. Therefore, the radial force can be further simplified to:

$$F_r = \frac{L_{stk}}{2\mu_0} \sum_{k=1}^{M} (B_r^2(k) - B_t^2(k)) \Delta l \tag{7.4}$$

where M is the total sampled points in the integral line. It is noted that the B_r and B_t information utilized in this section is collected from the nominal airgap length FEA model.

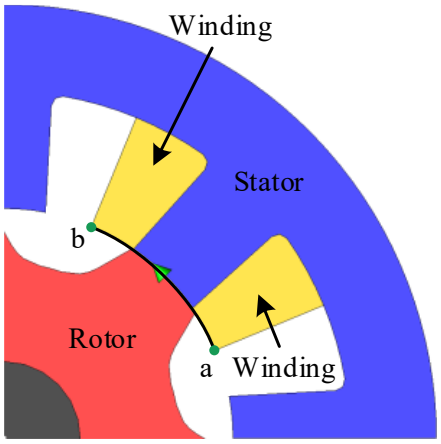

Figure 7.1: Description of the integral line.

With the collected flux density information, the phase flux-linkage can be estimated as (7.5) if the leakage flux is neglected. The N_t in (7.5) represents the turn number of one phase winding.

$$\psi_{ph} = N_t L_{stk} \sum_{k=1}^{M} B_r(k) \Delta l \tag{7.5}$$

Based on equations (7.4) and (7.5), the relationship between the radial force and the flux-linkage can be studied. Since the tangential flux density B_t is zero at the aligned position θ_{al}, the relationship at this position can be studied first. Observing (7.4) and (7.5), it is intuitive to check the ratio between the square root of the radial force and the flux-linkage, as shown in (7.6). From this expression, we can infer that the ratio $K_u(\theta_{al})$ keeps constant if the shape of the B_r is not changed under different current excitation. The unchanged shape of B_r means that the B_r at different current excitation can be expressed as $h(i)B_r(\theta)$, and the coefficient $h(i)$ only varies with current. In this case, $h(i)$ is a common coefficient in the numerator and denominator of (7.6), so it can be canceled out. Fig. 7.2(a) shows the contour plot and flux lines at

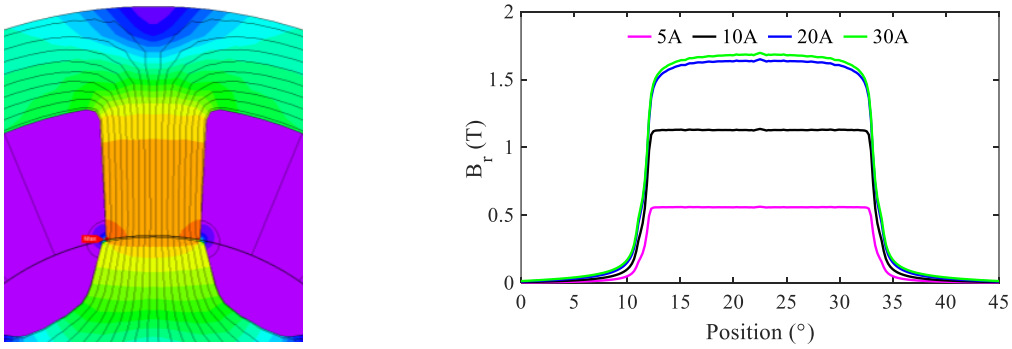

(a) (b)

Figure 7.2: (a) Contour plot and flux lines at 20 A current excitation and (b) Radial flux density B_r at the aligned position θ_{al} for the studied 8/6 SRM.

the aligned position θ_{al} for the studied 8/6 SRM. Due to the double salient structure of SRMs, the B_r component concentrates on the overlapping area. Fig. 7.2(b) shows the corresponding B_r waveforms under different current excitation. It is found that these profiles indeed show much higher magnitude on the overlapping area and can roughly be approximated as the rectangular shapes. Based on the above reasons, the condition of the unchanged-shape B_r can roughly be met.

$$K_u(\theta_{al}) = \frac{\sqrt{F_r(\theta_{al})}}{\psi_{ph}(\theta_{al})} = \frac{\sqrt{L_{stk}/2\mu_0 \times \sum_{k=1}^{M} B_r^2(k)\Delta l}}{N_t L_{stk} \sum_{k=1}^{M} B_r(k)\Delta l} \tag{7.6}$$

Fig. 7.5 shows the square root of the radial force and the scaled flux-linkage profiles at the aligned position θ_{al} for the above-mentioned four-phase 8/6 SRM and another three-phase 12/8 SRM. Fig. 2.1(b) shows the cross section of this 12/8 SRM. The ratio $K_u(\theta_{al})$ is 230.5 for the 8/6 SRM and 191.5 for the 12/8 SRM. From the figure, it is observed that the square root of the radial force perfectly coincides with the scaled flux-linkage profile at all current excitation levels, which verifies the above analysis.

At other rotor positions, since the tangential flux density B_t is not zero, the ratio

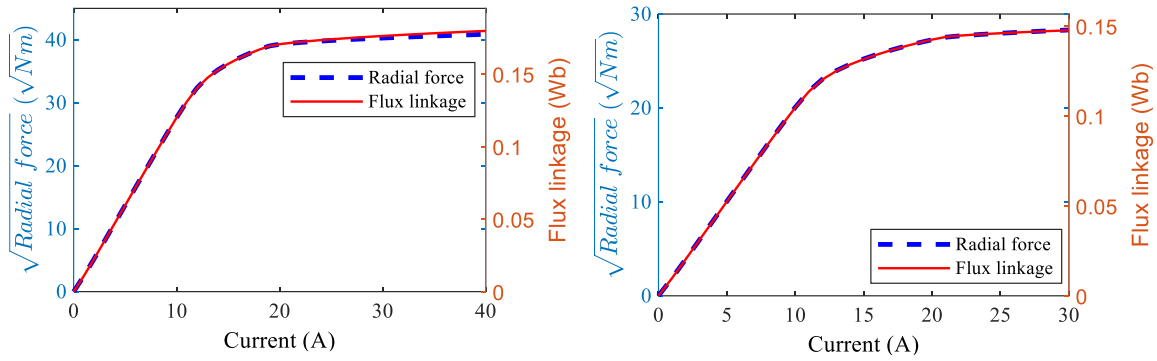

Figure 7.3: Root of radial force and scaled flux-linkage profiles at aligned position θ_{al} for the (a) four phase 8/6 SRM and (b) three phase 12/8 SRM.

between the square root of the radial force and the flux-linkage is modified as (7.7).

$$K_u(\theta_{al}) = \frac{\sqrt{L_{stk}/2\mu_0 \times \sum_{k=1}^{M}(B_r^2(k) - B_t^2(k))\Delta l}}{N_t L_{stk} \sum_{k=1}^{M} B_r(k)\Delta l} \tag{7.7}$$

It is observed that both B_r and B_t components contribute to the radial force. Because the double salient structure of the SRMs, the magnitude of B_r is much higher that of B_t, so B_r component dominates the magnitude of the radial force. Besides, as in the case at the aligned position, the condition that the unchanged-shape B_r is still assumed to be held in this situation. This assumption can be justified as below. Fig. 7.4(a) shows the contour plot and flux lines at 15° for the 8/6 SRM. It is found that the B_r component still concentrates on the overlapping region due to the lower reluctance in this region. In this case, the B_r waveforms is shown as Fig. 7.4(b) and the B_r component shows much higher magnitude in the overlapping region. If smaller B_r is neglected, the shape of the B_r under this situation can also be approximated as rectangular shapes and the above assumption can be roughly held.

As for the ratio $K_u(\theta)$ in this situation, it can be discussed based on the excitation

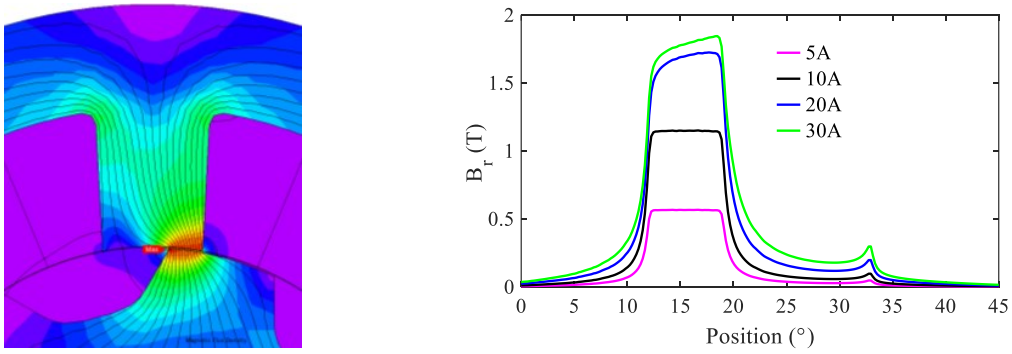

(a) (b)

Figure 7.4: (a) Contour plot and flux lines at 20 A current excitation and (b) Radial flux density B_r at the aligned position θ_{al} for the studied 8/6 SRM.

current level. When the current is small, the B_t is small and we can ignore this part. In this case, under the assumption that B_r has the same shape, the ratio $K_u(\theta)$ will keep constant. On the other hand, when the excitation current becomes higher and B_t cannot be ignored, the $K_u(\theta)$ will be affected. This effect can be discussed according to Fig. 7.5.

Fig. 7.5 shows the square root of the radial force and the scaled flux-linkage profiles at 15° for the 8/6 SRM and at 12° for the 12/8 SRM. The ratio $K_u(\theta)$ is 312 for the 8/6 SRM and 257 for the 12/8 SRM. From these two figures, the following points can be summarized:

a) The root of the radial force and the flux-linkage profile have the same saturation point. This is due to the fact that B_r is much higher than B_t so B_r dominates the magnitude of the radial force F_r and determines phase flux-linkage ψ_{ph}.

b) When the current is smaller than saturation point I_s, the ratio $K_u(\theta)$ keeps the same and the square root of the radial force profile aligns perfectly with the scaled flux-linkage profile.

c) When the current is higher than the saturation point I_s, there is deviation

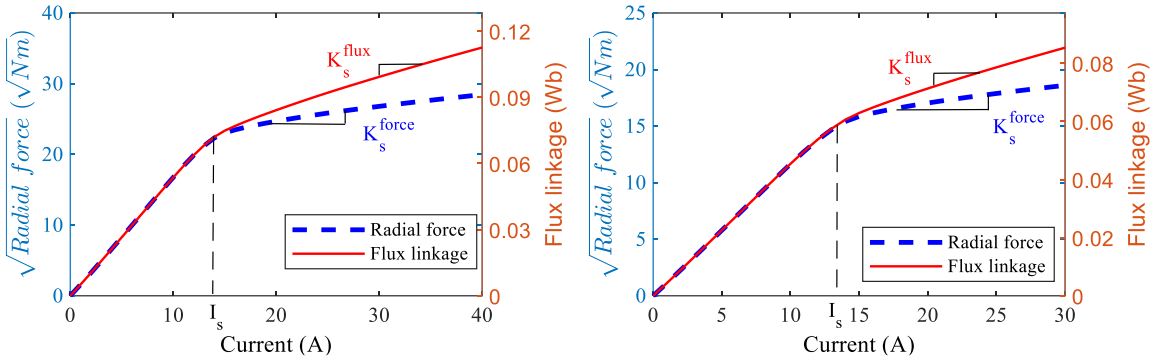

Figure 7.5: Root of radial force and scaled flux-linkage profiles at (a) 15° for the four phase 8/6 SRM and (b) 15° for the three phase 12/8 SRM.

between the square root of the radial force and the scaled flux-linkage profiles. This deviation is caused by the B_t component. Besides, the square root of radial force can be approximated as a straight line with slope K_s^{force} and the flux-linkage can be approximated as a straight line with slope K_s^{flux} in this region.

Although the above observations on the relationship between the radial force and flux-linkage is based on the nominal airgap length, these observations are assumed to be kept when the airgap length varies. The reasons for such assumption are: (a) the B_r component dominates the radial force regardless of the airgap length variation and (b) it always shows much higher amplitude on the overlapping region due to the double salient structures of SRMs. The simulation results shown in the latter section will prove this assumption is reasonable.

7.2.3 Radial Force Characteristics Estimation under Varied Airgap Length Condition

According to the relationship between the radial force and the flux-linkage discussed above, the radial force can be estimated from the actual measured flux-linkage profiles regardless of the possible airgap length variation. The flow chart of this estimation process is shown in Fig. 7.6, and it can be described as below:

a) Firstly, the FEA software is utilized to obtain the flux-linkage characteristics ψ_{FEA} and radial force characteristics F_{r_FEA} at the nominal airgap length. And measure the actual flux-linkage characteristics ψ_{ExpM} by experimental tests.

b) Compare the simulated flux-linkage characteristics ψ_{FEA} and the measured ones

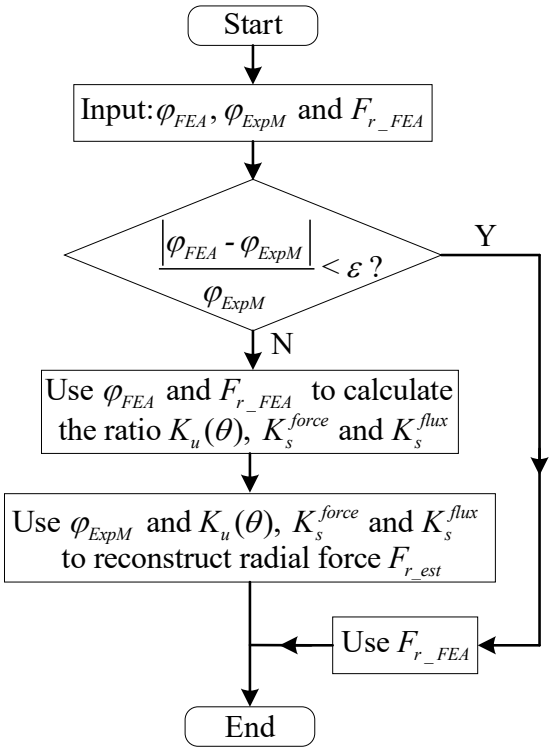

Figure 7.6: Flow chart of the proposed radial force characteristic estimation method.

ψ_{ExpM}. If the errors between them are with an acceptable threshold ϵ, it means that the air gap length is barely varied during the manufacturing process. In this case, the simulated radial force F_{r_FEA} can be utilized directly. Otherwise, the following reconstruction step is required.

c) Calculate the ratio $K_u(\theta)$, $K_s^{force}(\theta)$, and $K_s^{flux}(\theta)$ for all the rotor positions from the simulated ψ_{FEA} and F_{r_FEA} data. In the region where the current is smaller than the saturation point I_s, the radial force is reconstructed with $K_u(\theta)$ and measured flux-linkage profiles ψ_{ExpM}. In the region where the current is higher than I_s, the radial force is reconstructed with the ψ_{ExpM}, $K_u(\theta)$, $K_s^{force}(\theta)$, and $K_s^{flux}(\theta)$.

7.3 Simulation Verification

In order to verify the above-proposed radial force estimation method, the simulation tests are carried out in the mentioned 8/6 SRM and 12/8 SRM. It is noted that the nominal airgap length for the 8/6 SRM is 0.35 mm and the nominal airgap length for the 12/8 SRM is 0.3 mm. To imitate the possible airgap length variation for the actual SRM during the manufacturing process, the airgap length is deliberately reduced or increased to verify the effectiveness of the proposed method.

Notably, the flux-linkage characteristics at the varied (reduced or increased) air gap length obtained from the FEA imitate the actually measured flux-linkage ψ_{ExpM}. These curves reflect the effects of the possible airgap length variation during the manufacturing process. On the other hand, the radial force characteristics at the nominal airgap length obtained from the FEA represent the results of the conventional method since this is the way mostly employed in the literature. The radial force

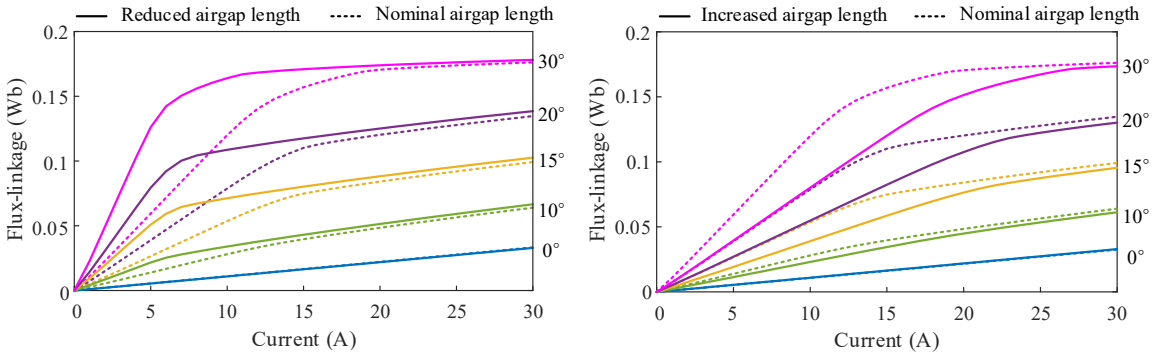

Figure 7.7: Flux linkage characteristics for the 8/6 SRM (a) when the airgap length is decreased to 0.15 mm and (b) when the airgap length is increased to 0.55 mm. (Note: the results represented by solid lines imitate ψ_{ExpM}.)

characteristics reconstructed from the ψ_{ExpM} and the above-mentioned relationship are the results of the proposed method. This relationship between the radial force and the flux-linkage is obtained at the nominal airgap length from the FEA simulation.

The simulation tests are carried out on the 8/6 SRM first. Two possible scenarios are considered: (a) the airgap length is deliberately increased to 0.55 mm from the nominal value 0.35 mm, and (b) the airgap length is deliberately decreased to 0.15 mm from the nominal value 0.35 mm.

Fig. 7.7 shows the flux-linkage characteristics at 0°, 10°, 15°, 20°, and 30° for the 8/6 SRM when the airgap length varies as described above. It is noted that the solid curves shown in Fig. 7.7 represent the flux-linkage profiles for the varied-airgap-length SRM. And these solid curves imitate the measured flux-linkage ψ_{ExpM} for the SRM which has airgap length variation during the manufacturing process. The dash lines are the flux-linage curves at the nominal airgap length, which are the data we can collect from FEA since the variation of the airgap length is unknown in normal case. From the presented curves, it is observed that the flux-linkage curves

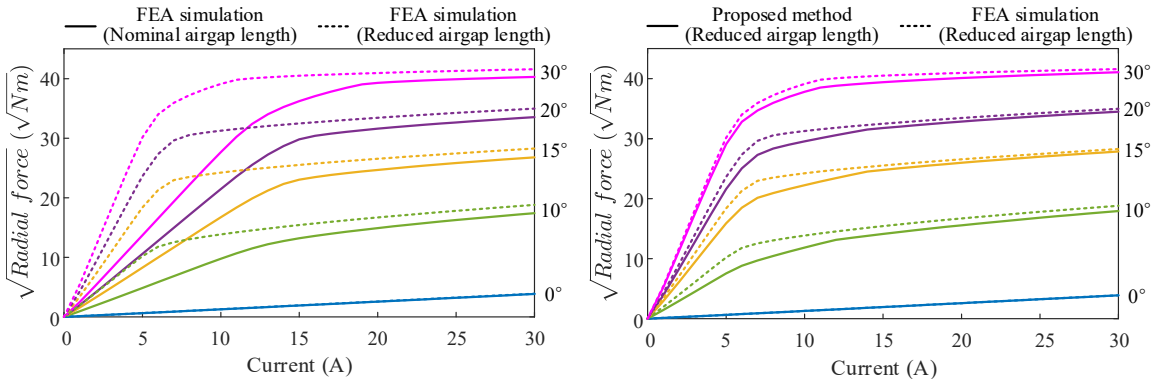

Figure 7.8: Radial force characteristics for the 8/6 SRM (a) when the simulated profiles at the nominal airgap length are used (conventional method) and (b) when the proposed method is used at the reduced airgap length situation. (Note: the results represented by dash lines are the real values of radial force.)

change significantly if the airgap length varies, especially at the positions close to the aligned position. Such flux-linkage variation indeed exists for the actual SRM due to the varied airgap length during the manufacturing process, as reported in (Ge *et al.*, 2020). And this airgap variation will inevitably affect the radial force characteristics, so there will be significant errors for radial force characteristics if the simulated ones at the nominal airgap length is used.

Fig. 7.8(a) compares the radial force profiles obtained from the conventional method and the real radial force values. In the picture, the dash lines represent the real radial force values for the varied-airgap-length SRM. And the solid lines in Fig. 7.8(a) are the radial force obtained from the FEA at the nominal airgap length, which is regarded as the conventional method since the variation of the airgap length is unknown. Not surprisingly, these two radial force characteristics show large deviations when the airgap length varies. If the airgap length is reduced for the actual SRM due to the manufacturing and the radial force from the conventional method

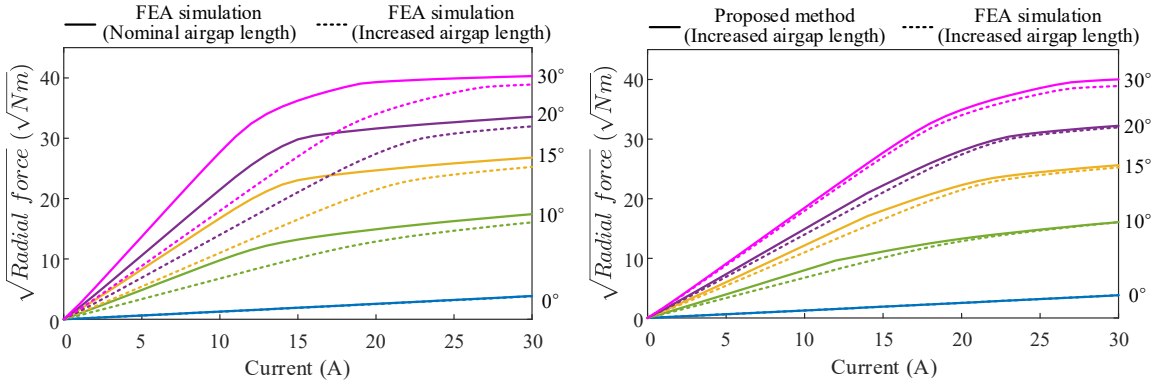

Figure 7.9: Radial force characteristics for the 8/6 SRM (a) when the simulated profiles at the nominal airgap length are used (conventional method) and (b) when the proposed method is used at the increased airgap length situation. (Note: the results represented by dash lines are the real values of radial force.)

is used, the resulted radial force errors will definitely affect the effectiveness of the acoustic noised reduction control methods.

On the other hand, the solid lines in Fig. 7.8(b) shows the reconstructed radial force by the proposed method at the reduced airgap length condition. The flux-linkage shown as the solid lines in Fig. 7.7(a) are employed in this reconstruction process. It is found that the reconstructed radial force profiles closely follow the real values (the dash lines), which proves the superiority and effectiveness of the proposed method.

Fig. 7.9 shows the radial force characteristics comparison when the airgap length is deliberately increased for the 8/6 SRM. From the presented results, it is observed that the reconstructed radial force profiles by the proposed method again follow the real values (dash lines) closely and show much more accurate values compared to the results obtained by conventional method (FEA results at the nominal airgap length).

To further validate the proposed radial force reconstruction method, the airgap

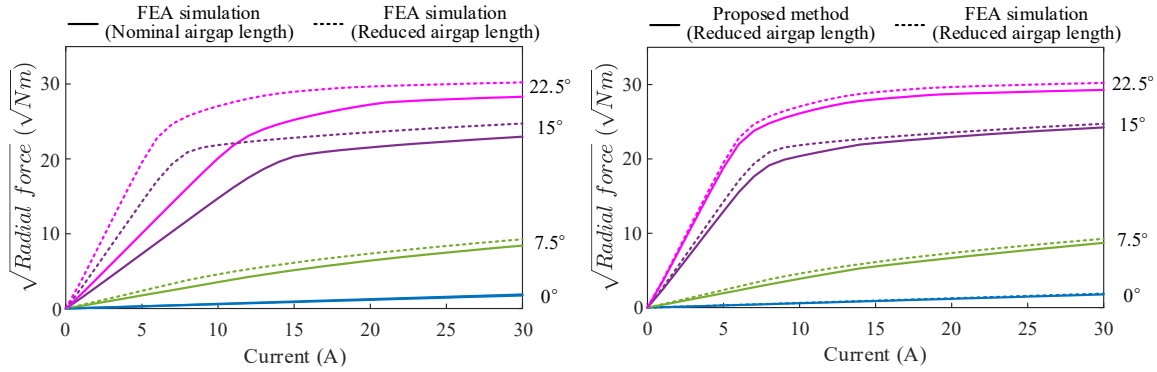

Figure 7.10: Radial force characteristics for the 12/8 SRM (a) when the simulated profiles at the nominal airgap length are used (conventional method) and (b) when the proposed method is used at the reduced airgap length situation. (Note: the results represented by dash lines are the real values of radial force.)

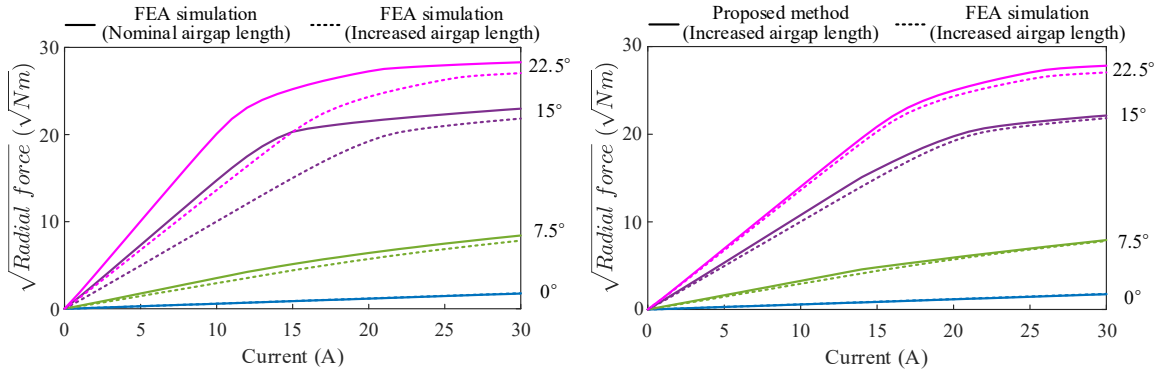

Figure 7.11: Radial force characteristics for the 12/8 SRM (a) when the simulated profiles at the nominal airgap length are used (conventional method) and (b) when the proposed method is used at the increased airgap length situation. (Note: the results represented by dash lines are the real values of radial force.)

length of the 12/8 SRM is also changed deliberately. Similarly, two scenarios are considered for this 12/8 SRM: (a) the airgap length is deliberately increased to 0.45 mm from the nominal value 0.3 mm, and (b) the airgap length is deliberately decreased to 0.15 mm from the nominal value 0.3 mm.

Fig. 7.10 and Fig. 7.11 show the simulation results at the above mentioned two

situations. The dash lines again represent the real radial force values at the varied-airgap-length condition. The solid lines in Fig. 7.10(a) and Fig. 7.11(a) are the estimation results obtained by the FEA simulation at the nominal airgap length, which is regarded as the results for the conventional method. And the solid lines shown in Fig. 7.10(b) and Fig. 7.11(b) are the reconstructed radial force by the proposed method. It is observed in both figures that the proposed method is able to provide accurate radial force estimation regardless of the airgap length variation for the 12/8 SRM.

The simulation results at two different SRMs shown above prove the effectiveness of the proposed radial force estimation method and reveals that it can be applied to SRMs with different configurations.

7.4 Conclusion

Acoustic noise is one of the main issues for the SRMs. Many advanced control methods shape the radial force to suppress the acoustic noise. The accurate radial force characteristics is vital for such methods, especially considering the airgap length variation during the manufacturing process. By analyzing the relationship between the radial force and the flux linkage, this chapter presents a simple and accurate method to reconstruct the radial force characteristics. Simulation results on two different SRMs, namely the 8/6 SRM and the 12/8 SRM, prove that the proposed method is able to provide good radial force estimation when the airgap length is decreased or reduced up to 50%.

Chapter 8

Conclusions and future work

8.1 Conclusions

Torque ripples and acoustic noise are two main drawbacks for SRMs, and these disadvantages prevent the wide applications of SRMs in the industrial sector. To ease these issues and enhance the control performance of the SRM drives, this thesis first presents several torque ripple suppression methods from the perspective of the proposed equivalent linear SRM model. It later shows two techniques that can be used to enhance the control performance of the advanced acoustic noise reduction methods.

A thorough review of the advanced torque control methods is firstly presented in chapter 2.

Although the existed numerical TSF methods could effectively generate the reference currents which not only reduce the torque ripples but also optimize the copper losses, the off-line optimization time is significantly long due to the high nonlinearity of the SRMs. Chapter 3 takes advantage of the simple linear model and utilizes the

equivalent linear torque model to generate the reference currents to significantly reduce the time consumption of the bi-objective optimization algorithm. The mapping between the equivalent linear torque model and the nonlinear torque model is developed to convert the generated current references to be applicable for the saturated SRMs. Compared to the traditional method that only adopts the nonlinear SRM model, the proposed method saves more than 70% time consumed by the traditional method for the bi-objective optimization problem but possesses a similar torque ripple reduction performance.

Since the MPTC method is capable to optimize the torque tracking error, the copper losses, and even the switching losses by a simple scalar function in an online manner, it becomes attractive for the SRM drives. Chapter 4 presents a new FCS MPTC method that uses the equivalent linear flux-linkage model and equivalent linear torque model to predict the behavior of the SRMs and achieve the MPTC algorithm. The corresponding transformations between the linear and nonlinear models are presented in detail. This technique significantly saves storage space. Furthermore, the improved switching table not only reduces the computational burden but also enhances the torque control performance in the high-speed range. To further enhance the torque control performance and reduce the high-frequency torque ripples, a CCS MPTC method is presented in Chapter 5. The challenges in developing the CCS MPTC method incurred from the high nonlinearity of SRMs are innovatively addressed by the introduction of the equivalent linear SRM model and proper modifications on the cost function. Extensive simulation and experimental results reveal that the proposed CCS MPTC method has outstanding performance on the torque ripple reduction in a wide speed range.

Apart from the torque ripple demerit, the acoustic noise issue also needs to be addressed. The current profiling technique is regarded as an effective method to suppress both the torque ripple and acoustic noise. In such techniques, a high-performance current controller is required. Chapter 6 presents a robust current controller regardless of the possible deviation of the measured flux-linkage characteristics. The expected duty cycle for the next control period under a certain reference current is calculated based on the proposed intersection method. Experimental results prove the good tracking performance and robustness of the proposed method. Another important information for the above-mentioned current profiling method is the radial force characteristics. However, it is barely possible to measure it directly, so the FEA software is normally employed to obtain this information. The issue is that the air-gap length possibly varies for the manufactured SRMs in the manufacturing process, which can be reflected from the deviation between the measured flux-linkage curves and the simulated flux-linkage curves. To improve the accuracy of the radial force characteristics, chapter 7 presents a simple and practical method to reconstruct the radial force characteristics from the measured flux-linkage curves. The relationship between the square root of the radial force and the flux-linkage is explained in detail. The good accuracy of the radial force information provides a solid basis for the advanced acoustics noise reduction method.

8.2 Future work

In Chapter 3, only the equivalent linear torque model is used to generate the current reference. The inequality constraints constructed from the voltage equation is not perfect since the current with equal torque differs with the current with equal

flux-linkage. To further enhance the performance of the method in chapter 3, the equivalent linear flux-linkage equation and the corresponding transformations should also be included.

Although the torque performance is significantly enhanced in a wide speed range by the proposed FCS MPTC and CCS MPTC methods, it still has the potential to further smooth the output torque at a speed that closes to the rated speed. Besides, with the aid of the radial force estimation technique developed in chapter 7, the MPTC method has the potential to reduce the torque ripples and suppress the acoustics simultaneously by inculpating the related constraint.

Since the developed torque control methods in chapter 3, chapter 4, and chapter 5 heavily rely on the torque and flux-linkage transformations, the possible inaccuracy of these transformations will degrade the control performance of the proposed methods. Therefore, it is necessary to develop a method to obtain the above important transformations in a robust way.

8.3 Publications

This thesis contributes to the following publications:

G. Fang, F. P. Scalcon, D. Xiao, R. P. Vieira, H. A. Gründling and A. Emadi, "Advanced Control of Switched Reluctance Motors (SRMs): A Review on Current Regulation, Torque Control and Vibration Suppression," in IEEE Open Journal of the Industrial Electronics Society, vol. 2, pp. 280-301, 2021. (Corresponding to chapter 2)

G. Fang, J. Ye, D. Xiao, Z. Xia, X. Wang and A. Emadi, "Time-Efficient Torque Shaping for Switched Reluctance Machines From Linear Space," in IEEE Transactions

on Power Electronics, vol. 36, no. 8, pp. 9361-9371, Aug. 2021. (Corresponding to chapter 3)

G. Fang, J. Ye, D. Xiao, Z. Xia and A. Emadi, "Computational-efficient Model Predictive Torque Control for Switched Reluctance Machines with Linear-Model-based Equivalent Transformations," in IEEE Transactions on Industrial Electronics, doi: 10.1109/TIE.2021.3091918. (Corresponding to chapter 4)

G. Fang, J. Ye, D. Xiao, Z. Xia and A. Emadi, "Low-Ripple Continuous Control Set Model Predictive Torque Control for Switched Reluctance Machines Based on Equivalent Linear SRM Model," in IEEE Transactions on Industrial Electronics. (Minor revision, corresponding to chapter 5)

G. Fang et al., "An Intersection-Method Based Current Controller for Switched Reluctance Machines with Robust Tracking Performance," in IEEE Transactions on Transportation Electrification, doi: 10.1109/TTE.2021.3086012. (Corresponding to chapter 6)

G. Fang, J. Ye, D. Xiao, Z. Xia and A. Emadi, "Lumped Radial Force Characteristics Reconstruction for Switched Reluctance Machines through Scaling Flux-linkage Characteristics," in IEEE Transactions on Magnetics. (Under review, corresponding to chapter 7)

Bibliography

Ahmad, S. S. and Narayanan, G. (2016). Linearized modeling of switched reluctance motor for closed-loop current control. *IEEE Transactions on Industry Applications*, **52**(4), 3146–3158.

Ai-De, X., Xianchao, Z., Kunlun, H., and Yuzhao, C. (2018). Torque-ripple reduction of srm using optimised voltage vector in dtc. *IET Electrical Systems in Transportation*, **8**(1), 35–43.

Bakr, M. (2013). *Nonlinear optimization in electrical engineering with applications in MATLAB*. The Institution of Engineering and Technology.

Bilgin, B., Jiang, J., and Emadi, A. (2019). *Switched Reluctance Motor Drives: Fundamentals to Applications*. CRC Press.

Bilgin, B., Howey, B., Callegaro, A. D., Liang, J., Kordic, M., Taylor, J., and Emadi, A. (2020). Making the case for switched reluctance motors for propulsion applications. *IEEE Transactions on Vehicular Technology*, **69**(7), 7172–7186.

Brauer, H. J., Hennen, M. D., and De Doncker, R. W. (2011). Control for polyphase switched reluctance machines to minimize torque ripple and decrease ohmic machine losses. *IEEE Transactions on Power Electronics*, **27**(1), 370–378.

Chai, J. and Liaw, C. (2010). Reduction of speed ripple and vibration for switched reluctance motor drive via intelligent current profiling. *IET Electric Power Applications*, **4**(5), 380–396.

Changhwan Choi, Seungho Kim, Yongdae Kim, and Kyihwan Park (2002). A new torque control method of a switched reluctance motor using a torque-sharing function. *IEEE Transactions on Magnetics*, **38**(5), 3288–3290.

Chapman, P. L. and Sudhoff, S. D. (2002). Design and precise realization of optimized current waveforms for an 8/6 switched reluctance drive. *IEEE Transactions on Power Electronics*, **17**(1), 76–83.

Cheok, A. D. and Fukuda, Y. (2002). A new torque and flux control method for switched reluctance motor drives. *IEEE Transactions on Power Electronics*, **17**(4), 543–557.

d. Paula, M. V. and Dos Santos Barros, T. A. (2021). A sliding mode ditc cruise control for srm with steepest descent minimum torque ripple point tracking. *IEEE Transactions on Industrial Electronics*, pages 1–1.

de Paula, M. V., d. S. Barros, T. A., Moreira, H. S., Catata, E. H., Villalva, M. G., and Filho, E. R. (2020). A dahlin cruise control design method for switched reluctance motors with minimum torque ripple point tracking applied in electric vehicles. *IEEE Transactions on Transportation Electrification*, pages 1–1.

Deng, X., Mecrow, B., Wu, H., and Martin, R. (2017). Design and development of low torque ripple variable-speed drive system with six-phase switched reluctance motors. *IEEE Transactions on Energy Conversion*, **33**(1), 420–429.

Ding, W., Liu, G., and Li, P. (2019). A hybrid control strategy of hybrid-excitation switched reluctance motor for torque ripple reduction and constant power extension. *IEEE Transactions on Industrial Electronics*, **67**(1), 38–48.

Dowlatshahi, M., Nejad, S. M. S., and Ahn, J. (2013). Torque ripple minimization of switched reluctance motor using modified torque sharing function. In *2013 21st Iranian Conference on Electrical Engineering (ICEE)*, pages 1–6.

Fang, G., Ye, J., Xiao, D., Xia, Z., and Emadi, A. (2021a). Computational-efficient model predictive torque control for switched reluctance machines with linear-model-based equivalent transformations. *IEEE Transactions on Industrial Electronics*, pages 1–1.

Fang, G., Ye, J., Xiao, D., Xia, Z., Wang, X., and Emadi, A. (2021b). Time-efficient torque shaping for switched reluctance machines from linear space. *IEEE Transactions on Power Electronics*, **36**(8), 9361–9371.

Fuengwarodsakul, N. H., Menne, M., Inderka, R. B., and De Doncker, R. W. (2005). High-dynamic four-quadrant switched reluctance drive based on ditc. *IEEE transactions On Industry applications*, **41**(5), 1232–1242.

Gan, C., Wu, J., Sun, Q., Yang, S., Hu, Y., and Jin, L. (2016). Low-cost direct instantaneous torque control for switched reluctance motors with bus current detection under soft-chopping mode. *IET Power Electronics*, **9**(3), 482–490.

Gan, C., Wu, J., Sun, Q., Kong, W., Li, H., and Hu, Y. (2018). A review on machine topologies and control techniques for low-noise switched reluctance motors in electric vehicle applications. *IEEE Access*, **6**, 31430–31443.

Gan, C., Sun, Q., Chen, Y., Si, J., Wu, J., and Hu, Y. (2020). A position sensorless torque control strategy for switched reluctance machines with fewer current sensors. *IEEE/ASME Transactions on Mechatronics*, pages 1–1.

Ge, L., Ralev, I., Klein-Hessling, A., Song, S., and De Doncker, R. W. (2020). A simple reluctance calibration strategy to obtain the flux-linkage characteristics of switched reluctance machines. *IEEE Transactions on Power Electronics*, **35**(3), 2787–2798.

Gobbi, R., Sahoo, N. C., and Vejian, R. (2008). Experimental investigations on computer-based methods for determination of static electromagnetic characteristics of switched reluctance motors. *IEEE Transactions on Instrumentation and Measurement*, **57**(10), 2196–2211.

Gundogmus, O., Sozer, Y., Vadamodala, L., Kutz, J., Tylenda, J., and Wright, R. L. (2019). Current harmonics injection method for simultaneous torque and radial force ripple mitigation to reduce acoustic noise and vibration in srms. In *2019 IEEE Energy Conversion Congress and Exposition (ECCE)*, pages 7091–7097.

Guo, H.-J. (2006). Considerations of direct torque control for switched reluctance motors. In *2006 IEEE International Symposium on Industrial Electronics*, volume 3, pages 2321–2325.

Henriques, L. O. d. A. P., Branco, P. C., Rolim, L. G. B., and Suemitsu, W. I. (2002). Proposition of an offline learning current modulation for torque-ripple reduction in switched reluctance motors: design and experimental evaluation. *IEEE Transactions on Industrial Electronics*, **49**(3), 665–676.

Hu, H., Cao, X., Yan, N., and Deng, Z. (2019). A new predictive torque control based torque sharing function for switched reluctance motors. In *2019 22nd International Conference on Electrical Machines and Systems (ICEMS)*, pages 1–5.

Husain, I. and Ehsani, M. (1996). Torque ripple minimization in switched reluctance motor drives by pwm current control. *IEEE Transactions on Power Electronics*, **11**(1), 83–88.

Husain, T., Elrayyah, A., Sozer, Y., and Husain, I. (2015). Flux-weakening control of switched reluctance machines in rotating reference frame. *IEEE Transactions on Industry Applications*, **52**(1), 267–277.

Husain, T., Elrayyah, A., Sozer, Y., and Husain, I. (2018). Unified control for switched reluctance motors for wide speed operation. *IEEE Transactions on Industrial Electronics*, **66**(5), 3401–3411.

Ilić-Spong, M., Miller, T. J. E., MacMinn, S. R., and Thorp, J. S. (1985). Instantaneous torque control of electric motor drives. In *1985 IEEE Power Electronics Specialists Conference*, pages 42–48.

Inderka, R. and De Doncker, R. (2002). Ditc-direct instantaneous torque control of switched reluctance drives. In *Conference Record of the 2002 IEEE Industry Applications Conference. 37th IAS Annual Meeting (Cat. No. 02CH37344)*, volume 3, pages 1605–1609.

Inderka, R. B. and De Doncker, R. W. (2003). Ditc-direct instantaneous torque control of switched reluctance drives. *IEEE Transactions on Industry Applications*, **39**(4), 1046–1051.

Kim, J. and Krishnan, R. (2009). Novel two-switch-based switched reluctance motor drive for low-cost high-volume applications. *IEEE Transactions on Industry Applications*, **45**(4), 1241–1248.

Kuai, S., Zhang, H., Xia, X., and Li, K. (2018). Unipolar sinusoidal excited switched reluctance motor control based on voltage space vector. *IET Electric Power Applications*, **13**(5), 670–675.

Kuai, S., Xia, X., Zhang, H., and Hu, K. (2020). Low-torque ripple control of srm based on current vector. *IET Electric Power Applications*, **14**(4), 723–730.

Kusumi, T., Hara, T., Umetani, K., and Hiraki, E. (2020). Simultaneous tuning of rotor shape and phase current of switched reluctance motors for eliminating input current and torque ripples with reduced copper loss. *IEEE Transactions on Industry Applications*, **56**(6), 6384–6398.

Lee, D., Liang, J., Lee, Z., and Ahn, J. (2009). A simple nonlinear logical torque sharing function for low-torque ripple sr drive. *IEEE Transactions on Industrial Electronics*, **56**(8), 3021–3028.

Lee, D., So-Yeon Ahn, Ahn, J., and Jang-Mok Kim (2011). Modified tsf for the high speed switched reluctance motor. In *2011 IEEE International Symposium on Industrial Electronics*, pages 655–660.

Li, C., Wang, G., Li, Y., and Xu, A. (2017). An improved finite-state predictive torque control for switched reluctance motor drive. *IET Electric Power Applications*, **12**(1), 144–151.

Li, H., Bilgin, B., and Emadi, A. (2019). An improved torque sharing function for torque ripple reduction in switched reluctance machines. *IEEE Transactions on Power Electronics*, **34**(2), 1635–1644.

Liang, J., Lee, D.-H., and Ahn, J.-W. (2009). Direct instantaneous torque control of switched reluctance machines using 4-level converters. *IET electric power applications*, **3**(4), 313–323.

Lin, Z., Reay, D. S., Williams, B. W., and He, X. (2006). Torque ripple reduction in switched reluctance motor drives using b-spline neural networks. *IEEE Transactions on Industry Applications*, **42**(6), 1445–1453.

Liu, X., Zhu, Z., Hasegawa, M., Pride, A., Deodhar, R., Maruyama, T., and Chen, Z. (2011). Performance comparison between unipolar and bipolar excitations in switched reluctance machine with sinusoidal and rectangular waveforms. In *2011 IEEE Energy Conversion Congress and Exposition*, pages 1590–1595.

Liu, X., Zhu, Z., and Pan, Z. (2012). Analysis of electromagnetic torque in sinusoidal excited switched reluctance machines having dc bias in excitation. In *2012 XXth International Conference on Electrical Machines*, pages 2882–2888.

Liu, X. Z., Verghese, G. C., Lang, J. H., and Onder, M. (1989). Generalizing the blondel-park transformation of electrical machines: Necessary and sufficient conditions. *IEEE Transactions on Circuits and Systems*, **36**(8), 1058–1067.

Lovatt, H. and Stephenson, J. (1997). Computer-optimised smooth-torque current waveforms for switched-reluctance motors. *IEE Proceedings-Electric Power Applications*, **144**(5), 310–316.

Ma, C., Qu, L., Mitra, R., Pramod, P., and Islam, R. (2016). Vibration and torque ripple reduction of switched reluctance motors through current profile optimization. In *2016 IEEE Applied Power Electronics Conference and Exposition (APEC)*, pages 3279–3285.

Ma, M., Ling, F., Li, F., and Liu, F. (2019). Torque ripple suppression of switched reluctance motor by segmented harmonic currents injection based on adaptive fuzzy logic control. *IET Electric Power Applications*, **14**(2), 325–335.

Mehta, S., Kabir, M. A., and Husain, I. (2018). Extended speed current profiling algorithm for low torque ripple srm using model predictive control. In *2018 IEEE Energy Conversion Congress and Exposition (ECCE)*, pages 4558–4563.

Mikail, R., Husain, I., Sozer, Y., Islam, M. S., and Sebastian, T. (2013). Torque-ripple minimization of switched reluctance machines through current profiling. *IEEE Transactions on Industry Applications*, **49**(3), 1258–1267.

Mikail, R., Husain, I., Sozer, Y., Islam, M. S., and Sebastian, T. (2014). A fixed switching frequency predictive current control method for switched reluctance machines. *IEEE Transactions on Industry Applications*, **50**(6), 3717–3726.

Mikail, R., Husain, I., Islam, M. S., Sozer, Y., and Sebastian, T. (2015). Four-quadrant torque ripple minimization of switched reluctance machine through current profiling with mitigation of rotor eccentricity problem and sensor errors. *IEEE Transactions on Industry Applications*, **51**(3), 2097–2104.

Miller, T. and McGilp, M. (1990). Nonlinear theory of the switched reluctance motor

for rapid computer-aided design. In *IEE Proceedings B (Electric Power Applications)*, volume 137, pages 337–347. IET.

Mir, S., Elbuluk, M. E., and Husain, I. (1999). Torque-ripple minimization in switched reluctance motors using adaptive fuzzy control. *IEEE Transactions on Industry Applications*, **35**(2), 461–468.

Nagel, N. J. and Lorenz, R. D. (1999). Complex rotating vector method for smooth torque control of a saturated switched reluctance motor. In *Conference Record of the 1999 IEEE Industry Applications Conference. Thirty-Forth IAS Annual Meeting (Cat. No. 99CH36370)*, volume 4, pages 2591–2598.

Nagel, N. J. and Lorenz, R. D. (2000). Rotating vector methods for smooth torque control of a switched reluctance motor drive. *IEEE Transactions on Industry Applications*, **36**(2), 540–548.

Nakao, N. and Akatsu, K. (2014a). Vector control for switched reluctance motor drives using an improved current controller. In *2014 IEEE Energy Conversion Congress and Exposition (ECCE)*, pages 1379–1386.

Nakao, N. and Akatsu, K. (2014b). Vector control specialized for switched reluctance motor drives. In *2014 International Conference on Electrical Machines (ICEM)*, pages 943–949.

Neuhaus, C. R., Fuengwarodsakul, N. H., and De Doncker, R. W. (2006). Predictive pwm-based direct instantaneous torque control of switched reluctance drives. In *2006 37th IEEE Power Electronics Specialists Conference*, pages 1–7.

Peng, F., Ye, J., and Emadi, A. (2016). A digital pwm current controller for switched reluctance motor drives. *IEEE Transactions on Power Electronics*, **31**(10), 7087–7098.

Peyrl, H., Papafotiou, G., and Morari, M. (2009). Model predictive torque control of a switched reluctance motor. In *2009 IEEE International Conference on Industrial Technology*, pages 1–6.

Rana, A. K. and Raviteja, A. (2021). A mathematical torque ripple minimization technique based on nonlinear modulating factor for switched reluctance motor drives. *IEEE Transactions on Industrial Electronics*.

Reddy, P. K., Ronanki, D., and Perumal, P. (2019). Efficiency improvement and torque ripple minimisation of four-phase switched reluctance motor drive using new direct torque control strategy. *IET Electric Power Applications*, **14**(1), 52–61.

Ro, H.-S., Lee, K.-G., Lee, J.-S., Jeong, H.-G., and Lee, K.-B. (2015). Torque ripple minimization scheme using torque sharing function based fuzzy logic control for a switched reluctance motor. *Journal of Electrical Engineering & Technology*, **10**(1), 118–127.

Rodriguez, J. and Cortes, P. (2012). *Predictive control of power converters and electrical drives*, volume 40. John Wiley & Sons.

Sahoo, N. C., Xu, J. X., and Panda, S. K. (1999). Determination of current waveforms for torque ripple minimisation in switched reluctance motors using iterative learning: an investigation. *IEE Proceedings - Electric Power Applications*, **146**(4), 369–377.

Sahoo, N. C., Xu, J. X., and Panda, S. K. (2001). Low torque ripple control of switched reluctance motors using iterative learning. *IEEE Transactions on Energy Conversion*, **16**(4), 318–326.

Sahoo, S. K., Panda, S. K., and Jian-Xin Xu (2005). Indirect torque control of switched reluctance motors using iterative learning control. *IEEE Transactions on Power Electronics*, **20**(1), 200–208.

Schramm, D. S., Williams, B. W., and Green, T. C. (1992). Torque ripple reduction of switched reluctance motors by phase current optimal profiling. In *PESC '92 Record. 23rd Annual IEEE Power Electronics Specialists Conference*, pages 857–860 vol.2.

Shaked, N. T. and Rabinovici, R. (2005). New procedures for minimizing the torque ripple in switched reluctance motors by optimizing the phase-current profile. *IEEE Transactions on Magnetics*, **41**(3), 1184–1192.

Shang, C., Reay, D., and Williams, B. (1999). Adapting cmac neural networks with constrained lms algorithm for efficient torque ripple reduction in switched reluctance motors. *IEEE transactions on control systems technology*, **7**(4), 401–413.

Song, S., Fang, G., Zhang, Z., Ma, R., and Liu, W. (2018). Unsaturated-inductance-based instantaneous torque online estimation of switched reluctance machine with locally linearized energy conversion loop. *IEEE Transactions on Industrial Electronics*, **65**(8), 6109–6119.

Song, S., Peng, C., Guo, Z., Ma, R., and Liu, W. (2019). Direct instantaneous torque

control of switched reluctance machine based on modular multi-level power converter. In *2019 22nd International Conference on Electrical Machines and Systems (ICEMS)*, pages 1–6.

Song, S., Hei, R., Ma, R., and Liu, W. (2020a). Model predictive control of switched reluctance starter/generator with torque sharing and compensation. *IEEE Transactions on Transportation Electrification*, **6**(4), 1519–1527.

Song, S., Fang, G., Hei, R., Jiang, J., Ma, R., and Liu, W. (2020b). Torque ripple and efficiency online optimization of switched reluctance machine based on torque per ampere characteristics. *IEEE Transactions on Power Electronics*, **35**(9), 9610–9618.

Stephenson, J., Hughes, A., and Mann, R. (2001). Torque ripple minimisation in a switched reluctance motor by optimum harmonic current injection. *IEE Proceedings-Electric Power Applications*, **148**(4), 322–328.

Stephenson, J., Hughes, A., and Mann, R. (2002). Online torque-ripple minimisation in a switched reluctance motor over a wide speed range. *IEE Proceedings-Electric Power Applications*, **149**(4), 261–267.

Sun, Q., Wu, J., Gan, C., Hu, Y., and Si, J. (2016). Octsf for torque ripple minimisation in srms. *IET Power Electronics*, **9**(14), 2741–2750.

Sun, Q., Wu, J., and Gan, C. (2020). Optimized direct instantaneous torque control for srms with efficiency improvement. *IEEE Transactions on Industrial Electronics*.

Sun, X., Wu, J., Lei, G., Guo, Y., and Zhu, J. (2020). Torque ripple reduction of

srm drive using improved direct torque control with sliding mode controller and observer. *IEEE Transactions on Industrial Electronics*, pages 1–1.

Tarvirdilu-Asl, R., Nalakath, S., Bilgin, B., and Emadi, A. (2019). A finite control set model predictive torque controlz for switched reluctance motor drives with adaptive turn-off angle. In *IECON 2019-45th Annual Conference of the IEEE Industrial Electronics Society*, volume 1, pages 840–845.

Tseng, K. J. and Shuyu Cao (2001). A srm variable speed drive with torque ripple minimization control. In *APEC 2001. Sixteenth Annual IEEE Applied Power Electronics Conference and Exposition (Cat. No.01CH37181)*, volume 2, pages 1083–1089 vol.2.

Valdivia, V., Todd, R., Bryan, F. J., Barrado, A., Lázaro, A., and Forsyth, A. J. (2014). Behavioral modeling of a switched reluctance generator for aircraft power systems. *IEEE Transactions on Industrial Electronics*, **61**(6), 2690–2699.

Villegas, J., Vazquez, S., Carrasco, J., and Gil, I. (2010). Model predictive control of a switched reluctance machine using discrete space vector modulation. In *2010 IEEE International Symposium on Industrial Electronics*, pages 3139–3144.

Vujičić, V. P. (2012). Minimization of torque ripple and copper losses in switched reluctance drive. *IEEE Transactions on Power Electronics*, **27**(1), 388–399.

Wallace, R. S. and Taylor, D. G. (1992). A balanced commutator for switched reluctance motors to reduce torque ripple. *IEEE Transactions on Power Electronics*, **7**(4), 617–626.

Wang, Y., Wu, H., Zhang, W., and Ma, Y. (2014). A high efficiency direct instantaneous torque control of srm using commutation angles control. In *2014 17th International Conference on Electrical Machines and Systems (ICEMS)*, pages 2863–2866.

Wiegand, C. (2018). F-35 air vehicle technology overview. In *2018 Aviation Technology, Integration, and Operations Conference*, page 3368.

Xia, Z., Bilgin, B., Nalakath, S., and Emadi, A. (2020). A new torque sharing function method for switched reluctance machines with lower current tracking error. *IEEE Transactions on Industrial Electronics*, pages 1–1.

Xu, A., Shang, C., Chen, J., Zhu, J., and Han, L. (2019). A new control method based on dtc and mpc to reduce torque ripple in srm. *IEEE Access*, **7**, 68584–68593.

Xue, X. D., Cheng, K. W. E., and Ho, S. L. (2009). Optimization and evaluation of torque-sharing functions for torque ripple minimization in switched reluctance motor drives. *IEEE Transactions on Power Electronics*, **24**(9), 2076–2090.

Yan, N., Cao, X., and Deng, Z. (2018). Direct torque control for switched reluctance motor to obtain high torque–ampere ratio. *IEEE Transactions on Industrial Electronics*, **66**(7), 5144–5152.

Yao, S. and Zhang, W. (2017). A simple strategy for parameters identification of srm direct instantaneous torque control. *IEEE Transactions on Power Electronics*, **33**(4), 3622–3630.

Ye, J., Bilgin, B., and Emadi, A. (2015a). An extended-speed low-ripple torque control of switched reluctance motor drives. *IEEE Transactions on Power Electronics*, **30**(3), 1457–1470.

Ye, J., Bilgin, B., and Emadi, A. (2015b). An offline torque sharing function for torque ripple reduction in switched reluctance motor drives. *IEEE Transactions on Energy Conversion*, **30**(2), 726–735.

Yu, Z., Gan, C., Chen, Y., and Qu, R. (2020). Dc-biased sinusoidal current excited switched reluctance motor drives based on flux modulation principle. *IEEE Transactions on Power Electronics*.

Zeng, H., Chen, H., and Shi, J. (2015). Direct instantaneous torque control with wide operating range for switched reluctance motors. *IET Electric Power Applications*, **9**(9), 578–585.

Zhang, W., Han, L., Wang, S., *et al.* (2019). Minimising torque ripple of srm by applying db-dtfc. *IET Electric Power Applications*, **13**(11), 1883–1890.

Zhao, X., Xu, A., and Zhang, W. (2017). Research on dtc system with variable flux for switched reluctance motor. *CES Transactions on Electrical Machines and Systems*, **1**(2), 199–206.

Zhu, Z. Q., Lee, B., Huang, L., and Chu, W. (2017). Contribution of current harmonics to average torque and torque ripple in switched reluctance machines. *IEEE Transactions on Magnetics*, **53**(3), 1–9.